

Hydro-Geomechanical Characterization of Inclined Heterolithic Stratification (IHS)

by

Masoud Khademi

A thesis submitted in partial fulfillment of the requirements for the degree of

Doctor of Philosophy

in

Geotechnical Engineering

Department of Civil and Environmental Engineering

University of Alberta

© Masoud Khademi, 2020

ABSTRACT

A sizeable portion of the Athabasca oil sand reservoir is classified as Inclined Heterolithic Stratification (IHS). IHS is a particular type of lithosome that is comprised of two alternating lithologies which are fluviially-dominated sand beds and brackish tidally-influenced mud beds. However, due to the significant heterogeneity of IHS and the minimal experimental studies performed on it, its hydro-geomechanical properties are relatively unknown. The main objectives of this study are investigating the geomechanical constitutive behavior of IHS and linking its geological and mechanical characteristics to their hydraulic behavior to estimate the permeability evolution of IHS during a Steam Assisted Gravity Drainage (SAGD) operation. To that end, a detailed methodology for reconstitution of analog IHS specimens was developed, and a microscopic comparative study was conducted between analog and in situ IHS samples. The SAGD-induced stress paths were experimentally simulated by running isotropic cyclic consolidation and drained triaxial shearing tests on analog IHS samples. Both series of experiments were performed in conjunction with permeability tests at different strain levels, flow rates, and stress states. Additionally, an analog sample with bioturbation was tested to examine the hydro-geomechanical effects of bioturbation. Furthermore, the hydro-mechanical characteristics of analog IHS were compared with its constituent layers (sand and mud). Finally, a geomechanical model was developed to numerically simulate the behavior of sand-dominated IHS with FLAC3D™ version 6.

The microscopic study showed that the layers' integration and grain size distribution are similar in analog and in situ IHS specimens. The results also revealed that the geomechanical properties of IHS, such as shear strength, bulk compressibility, Young's modulus, and dilation angle, are stress state dependent. In other words, elevating the effective confining stress could significantly

increase the strength and elastic modulus of a sample, while decreasing the compressibility and dilation angle. In contrast, the friction angle and Poisson's ratio are not very sensitive to changes in the isotropic confining stress. An important finding of this study is that the effect of an IHS sample's volume change on permeability is contingent on the stress state and stress path. Volume change during isotropic unloading-reloading resulted in permeability increases, and sample dilation during compression shearing resulted in permeability decreases, especially at high effective confining stresses. Moreover, the tests revealed that the existence of bioturbation dramatically improves permeability of IHS in comparison to equivalent non-bioturbated specimens but has negligible effects on its mechanical properties, which remain similar to non-bioturbated specimens. The results also showed that bioturbation has minimal impact on permeability changes during shearing. Lastly, experimental correlations were developed for each of the parameters mentioned above.

The numerical study performed in this thesis showed that the geomechanical model applied in the FLAC3D™ simulation can be a representative model for sand-dominated IHS. This numerical model used the Plastic Hardening constitutive model, with two separate sets of parameters for sand and mud layers. The required parameters for this geomechanical model were obtained through a series of triaxial tests on sand and mud specimens. For the first time, specialized experimental protocols have been developed that guide the infrastructure and processes required to reconstitute analog IHS specimens and conduct geomechanical testing on them. This study also delivered fundamental constitutive data to better understand the geomechanical behavior of the IHS reservoir and its permeability evolution during the in situ recovery processes. Such data can be used to capture the reservoir behavior and increase the efficiency of SAGD operations in IHS reservoirs.

PREFACE

Part of chapter 6 has been published in the SPE Annual Technical Conference and Exhibition 2019, and another paper has been accepted for publication in a future issue of SPE Journal. In both of these papers the first author was responsible for conducting the research and writing the manuscripts, and the second author was responsible for reviewing the papers and providing feedback.

Khademi M., Chalaturnyk R., (2019). Geomechanical Characterization of Inclined Heterolithic Stratification Lithosome and Its Permeability Evolution under SAGD Stress Paths, *SPE Annual Technical Conference and Exhibition*. Calgary: Society of Petroleum Engineers, <https://doi.org/10.2118/195968-MS>

Khademi M., Chalaturnyk R. Geomechanical Characterization of Inclined Heterolithic Stratification Lithosome and Its Permeability Evolution under SAGD Stress Paths, *SPE Journal*, Society of Petroleum Engineers, Accepted on February 2020, in press.

ACKNOWLEDGMENTS

First of all, I would like to thank my supervising professor, Dr. Rick Chalaturnyk, for his guidance, endless support, and encouragement throughout the course of this research work. Dr. Chalaturnyk is a highly perceptive supervisor who always generously helped me to shape my ideas. His scientific insight has been my greatest guide in finding the solution to many problems. I appreciate the patience and time he has devoted towards administering my work throughout this research, and I am grateful that he gave me the opportunity to learn from and work with him.

I would also like to thank Dr. Murray Gingras for his time and helpful comments. I would also like to express my sincere appreciation to the members of the Reservoir Geomechanics Research Group (RG²), past and present, for their contributions to this research. I would especially like to express my gratitude to Mr. Keivan Khalegi and Mr. Gilbert Wong for their guidance and support throughout this study.

I gratefully acknowledge the financial support of the Energi Simulation (formerly Foundation CMG) over the past five years of my Ph.D. education.

I would also thank Mr. Herbert Dixel and other personnel of the University of Alberta Machine Shop for their assistance in the fabrication of the experimental setup, and all RG² members who helped me while the experiments were conducted, especially Dr. Hossein Akbarzadeh, Dr. Amir-hosseini Haghi, Dr. Stephen Talman, Abel Sanchez Juncal, and Jakob Brandl.

I would also like to thank my parents who passed on to me a sense of great respect for education.

Finally, I would like to express deep gratitude to my wife Aniseh for her understanding, support, and love, without which all this would not have been accomplished.

TABLE OF CONTENTS

1. INTRODUCTION.....	1
1.1. Background.....	1
1.2. Statement of Problem.....	3
1.3. Research Objectives.....	4
1.4. Scope and Methodology.....	5
1.5. Organization of Thesis.....	6
2. LITERATURE REVIEW	9
2.1. Bitumen: a Promising Energy Source.....	9
2.1.1. What is Bitumen?.....	9
2.1.2. Role of Bitumen in Canada.....	9
2.1.3. Bitumen Reserves in Canada	10
2.1.4. Bitumen Recovery Techniques	10
2.2. Geology of the McMurray Formation.....	11
2.3. Sedimentology and Ichnology of IHS.....	14
2.3.1. Internal Architecture of IHS	15
2.3.2. Grain Size Distribution within IHS.....	16
2.3.3. Bioturbation Distribution within IHS	17
2.3.3.1. Bioturbation Index (BI).....	17

2.4.	SAGD Projects and Geomechanics.....	18
2.4.1.	Shear Strength and Stress-Strain Behavior of the Athabasca Oil Sand	18
2.4.1.1.	Problem of Sampling and Sample Disturbance.....	19
2.4.2.	Hydro-geomechanical Processes during SAGD	20
2.4.2.1.	Isotropic Process	20
2.4.2.2.	Deviatoric (Shear) Process.....	21
2.4.2.3.	Reservoir Stress Paths during SAGD.....	22
2.4.3.	IHS and SAGD	23
2.4.3.1.	SAGD Interval in IHS.....	23
2.4.3.2.	Effect of IHS Mud Layers.....	24
2.4.3.3.	Orientation of SAGD Well-pairs in IHS.....	25
3.	MATERIALS AND EXPERIMENTAL METHODS.....	26
3.1.	Test Materials.....	26
3.1.1.	Sand.....	26
3.1.1.1.	Grain Size Distribution	26
3.1.1.2.	Specific Gravity	27
3.1.1.3.	Porosity of Sand Specimen	29
3.1.2.	Mud.....	30
3.1.2.1.	Grain Size Distribution	30

3.1.2.2.	Silt-Clay Mixture Ratio.....	30
3.1.2.3.	Specific Gravity of Silt and Clay	31
3.1.2.4.	Porosity of Mud Specimen.....	31
3.1.3.	IHS	32
3.1.3.1.	Sample Configuration	32
3.1.3.2.	Grain Size Distribution and Density	33
3.1.3.3.	Average Porosity of IHS Specimen	33
3.2.	Development of Experimental Protocol to Reconstitute Analog IHS.....	34
3.2.1.	Sand Specimen Preparation Method.....	35
3.2.1.1.	Wet Tamping and Vibration.....	35
3.2.1.2.	Sand Packing Assembly.....	35
3.2.1.3.	Freezing, Extruding, and Trimming.....	36
3.2.1.4.	Mounting in the Triaxial Cell.....	37
3.2.2.	Mud Specimen Preparation Method.....	39
3.2.2.1.	Slurry Consolidation	39
3.2.2.2.	Mud Mold Preparation	40
3.2.2.3.	Freezing and Trimming.....	41
3.2.2.4.	Mounting in the Triaxial Cell.....	43
3.2.3.	Inclined Slicing Techniques for Sand and Mud Specimen	43

3.2.3.1.	Using 3-D Printed Rock.....	44
3.2.3.2.	Designing a Cutter Box.....	45
3.2.4.	Creating Bioturbation in Mud Layers	48
3.2.5.	Stacking Different IHS layers.....	50
3.2.6.	Consolidation of Analog IHS.....	52
3.3.	Microscopic Comparative Study of IHS.....	53
3.3.1.	Analog IHS Specimens	53
3.3.2.	In situ IHS Cores.....	55
3.4.	Experimental Setup for Hydro-geomechanical Testing.....	57
3.4.1.	Description of Experimental Apparatus.....	57
3.4.1.1.	ISCO® Pumps (Back Pump and Cell Pump).....	58
3.4.1.2.	Quizix® Pump	58
3.4.1.3.	INSTRON® Loading Frame with Environmental Chamber.....	59
3.4.1.4.	Triaxial Cell	60
3.4.1.5.	Instrumentation	61
3.4.1.5.1.	Gauges and Sensors	61
3.4.1.5.2.	Data Acquisition System.....	61
3.5.	Experimental Procedures	61
3.5.1.	Saturation of Test Specimens by Back Pressure.....	62

3.5.2.	B-test.....	63
3.5.3.	Isotropic Cyclic Consolidation Test.....	64
3.5.4.	Drained Triaxial Compression Test	65
3.5.4.1.	Strain Rate during Shearing	66
3.5.5.	Permeability Test	67
4.	HYDRO-MECHANICAL TESTING ON SAND LAYER.....	69
4.1.	Introduction.....	69
4.2.	B-test.....	69
4.3.	Isotropic Cyclic Consolidation Test.....	70
4.3.1.	Isotropic Bulk Compressibility	71
4.3.1.1.	Empirical Correlation for change in Bulk Compressibility	72
4.4.	Drained Triaxial Compression Test	73
4.4.1.	Stress-Strain Behavior.....	74
4.4.1.1.	Modulus of Elasticity.....	74
4.4.1.2.	Volumetric Behavior during Shearing	75
4.4.1.3.	Poisson’s Ratio.....	77
4.4.1.4.	Dilation Angle.....	77
4.4.1.5.	Specimens’ Deformation Patterns and Mode of Failure	80
4.4.2.	Drained Shear Strength	85

4.4.2.1.	Cohesion.....	86
4.4.2.2.	Friction Angle	86
4.4.2.3.	Axial and Volumetric Strains at Peak Shear Strength.....	87
4.5.	Permeability Test	89
4.5.1.	Absolute Permeability Evolution under SAGD Stress Paths	89
4.5.1.1.	Permeability Changes during Isotropic Unloading	90
4.5.1.2.	Permeability Changes during Triaxial Shearing	93
4.6.	Discussion and Conclusions.....	97
4.6.1.	Comparison with Previous Experimental Studies on Oil Sand.....	97
4.6.1.1.	Geomechanical Properties.....	97
4.6.1.1.1.	Stress-Strain Behavior.....	97
4.6.1.1.2.	Shear Strength.....	101
4.6.1.2.	Investigating the Applicability of Previous Empirical Permeability Relationships..	102
4.6.1.2.1.	Kozeny-Carman Model.....	102
4.6.1.2.2.	Chardabellas' Model.....	104
4.6.1.2.3.	Tortike's Model.....	105
4.6.1.2.4.	Touhidi-Baghini's Model.....	106
4.7.	Summary.....	109
5.	HYDRO-MECHANICAL TESTING ON MUD LAYER.....	111

5.1.	Introduction.....	111
5.2.	B-test.....	111
5.3.	Isotropic Cyclic Consolidation Test.....	112
5.3.1.	Isotropic Bulk Compressibility	114
5.3.1.1.	Empirical Correlation for change in Bulk Compressibility	115
5.4.	Drained Triaxial Compression Test	115
5.4.1.	Stress-Strain Behavior.....	116
5.4.1.1.	Modulus of Elasticity.....	116
5.4.1.2.	Volumetric Behavior during Shearing	117
5.4.1.3.	Poisson’s Ratio.....	118
5.4.1.4.	Dilation Angle.....	119
5.4.1.5.	Specimens’ Deformation Patterns and Mode of Failure	119
5.4.2.	Drained Shear Strength	122
5.4.2.1.	Cohesion.....	123
5.4.2.2.	Friction Angle	123
5.4.2.3.	Axial and Volumetric Strains at Peak Shear Strength.....	123
5.5.	Permeability Test	125
5.5.1.	Absolute Permeability Evolution under SAGD Stress Paths	125
5.5.1.1.	Permeability Changes during Isotropic Unloading	126

5.5.1.2.	Permeability Changes during Triaxial shearing	129
5.6.	Discussion and Conclusions.....	133
5.6.1.	Comparison with Previous Experimental Studies on Shale and Silt-Clay Mixtures	133
5.6.1.1.	Geomechanical Properties.....	133
5.6.1.1.1.	Stress-Strain Behavior.....	133
5.6.1.1.2.	Shear Strength.....	136
5.6.1.2.	Absolute Permeability.....	139
5.7.	Summary.....	142
6.	HYDRO-MECHANICAL TESTING ON IHS SPECIMEN	144
6.1.	Introduction.....	144
6.2.	B-test.....	144
6.3.	Isotropic Cyclic Consolidation Test.....	145
6.3.1.	Isotropic Bulk Compressibility	147
6.3.1.1.	Empirical Correlation for change in Bulk Compressibility	148
6.4.	Drained Triaxial Compression Test	148
6.4.1.	Stress-Strain Behavior.....	149
6.4.1.1.	Modulus of Elasticity	149
6.4.1.2.	Volumetric Behavior during Shearing	150
6.4.1.3.	Poisson's Ratio.....	152

6.4.1.4.	Dilation Angle.....	152
6.4.1.5.	Specimens' Deformation Patterns and Mode of Failure	153
6.4.2.	Drained Shear Strength	156
6.4.2.1.	Cohesion and Friction Angle	157
6.4.2.2.	Axial and Volumetric Strains at Peak Shear Strength.....	158
6.5.	Permeability Test	159
6.5.1.	Absolute Permeability Evolution under SAGD Stress Paths	159
6.5.1.1.	Permeability Changes during Isotropic Unloading	160
6.5.1.2.	Permeability Changes during Triaxial Shearing	164
6.6.	Discussion and Conclusions.....	167
6.6.1.	Sand-Mud-IHS Comparison	168
6.6.1.1.	Compressibility	168
6.6.1.2.	Shear Strength.....	168
6.6.1.3.	Modulus of Elasticity	170
6.6.1.4.	Poisson's Ratio, Cohesion, and Friction Angle	171
6.6.1.5.	Volumetric Behavior and Dilation Angle	171
6.6.1.6.	Permeability Evolution under SAGD Stress Paths	174
6.6.2.	Investigating the Applicability of Previous Empirical Permeability Relationships.....	174
6.6.2.1.	Kozeny-Carman Model.....	174

6.6.2.2.	Chardabellas' Model	175
6.6.2.3.	Tortike's Model.....	176
6.6.2.4.	Touhidi-Baghini's Model.....	177
6.6.3.	Empirical Correlations for Changes in Absolute Permeability	178
6.7.	Summary.....	181
7.	NUMERICAL SIMULATION OF IHS GEOMECHANICAL BEHAVIOR	183
7.1.	Introduction.....	183
7.2.	FLAC3D™	183
7.3.	Constitutive Model.....	184
7.4.	Numerical Analysis.....	188
7.4.1.	FLAC3D™ Numerical Experiments of Laboratory Tests on Sand Layer	189
7.4.2.	FLAC3D™ Numerical Experiments of Laboratory Tests on Mud Layer	195
7.4.3.	FLAC3D™ Numerical Experiments of Laboratory Tests on IHS	201
7.4.3.1.	Geomechanical Model of IHS.....	207
7.5.	Summary.....	208
8.	CONCLUSIONS AND RECOMMENDATIONS.....	210
8.1.	Summary.....	210
8.2.	Conclusions.....	211
8.2.1.	Sand, Mud, and IHS Samples Preparation	211

8.2.2. Geomechanical Properties of Sand, Mud, and IHS..... 212

8.2.3. Absolute Permeability Changes of Sand, Mud, and IHS 215

8.3. Recommendations for Future Research 217

REFERENCES..... 219

LIST OF TABLES

Table 3-1 Sand grain size distribution properties	27
Table 3-2 Porosity of the Athabasca oil sand cores and reconstituted samples	29
Table 3-3 IHS samples' configuration.....	33
Table 3-4 IHS samples' initial porosity.....	34
Table 3-5 Quizix [®] -QX 6000 (Chandler Engineering, 2017).....	59
Table 4-1 Isotropically consolidated drained triaxial compression tests data for analog sand samples	89
Table 5-1 Isotropically consolidated drained triaxial compression tests data for analog mud samples...	125
Table 5-2 In situ shale cores and analog mud samples' strength parameters (Suncor Energy, 2005; Suncor Energy 2009; Chalaturnyk, 1996).....	133
Table 6-1 Isotropically consolidated drained triaxial compression tests data for analog IHS samples ...	159
Table 8-1 Compressibility equation constants	212
Table 8-2 Modulus number and modulus exponent for different types of sample	213

LIST OF FIGURES

Figure 1-1 Alberta oil sand areas (Government of Alberta, 2017)	2
Figure 2-1 Stratigraphic setting of northern Alberta (Ranger & Gingras, 2003).....	12
Figure 2-2 Stratigraphic setting of the Lower Cretaceous McMurray Formation (Jablonski & Dalrymple, 2016)	15
Figure 2-3 Major stress paths followed within a reservoir during the SAGD process (Touhidi-Baghini, 1998)	23
Figure 2-4 Schematic diagram of SAGD and how the steam chamber development is slowed down by IHS mudstones (Dahl et al., 2010)	25
Figure 3-1 Grain size distribution curves of the Athabasca oil sand cores and reconstituted samples	27
Figure 3-2 Volumetric flask filled with water (left) and sand-water mixture (right).....	28
Figure 3-3 grain size distribution curve of silt (Sil Flour 325 ®)	30
Figure 3-4 Volumetric flask filled with silt-water mixture (left) and clay-water mixture (right).....	31
Figure 3-5 Analog IHS reconstitution flowchart	34
Figure 3-6 Sand packing assembly	36
Figure 3-7 Freezing sand packing assembly (a), Extruding frozen sample using INSTRON® (b), Frozen sand sample (c)	37
Figure 3-8 Preparation of analog sand sample for hydro-mechanical testing.....	38
Figure 3-9 Silt and kaolinite mixture (a), Silt-kaolinite slurry (b), Soaking stage (c)	40
Figure 3-10 Mud samples’ mold preparation using a Dremel rotary cutter.....	41
Figure 3-11 Filling the mud molds on the vibrating table (a) Mud samples inside the freezer (b).....	42

Figure 3-12 Cutting the mold using a cutter (a), Trimming a frozen mud sample using a masonry saw (b)	43
Figure 3-13 Masonry saw with a gauged rotary table inside the walk-in freezer	44
Figure 3-14 Sliced 3-D printed sandstone sample	45
Figure 3-15 Sliced analog sand sample (a), Wrapped sand slices (b).....	45
Figure 3-16 Mudstone cutter box (38.1 millimeters diameter)	47
Figure 3-17 Mudstone cutter box (63.5 millimeters diameter)	47
Figure 3-18 Wire saw (a), Mud slices (38.1 millimeters diameter) (b)	48
Figure 3-19 In situ IHS core with bioturbation	48
Figure 3-20 Penetrating a mud layer using a power drill.....	49
Figure 3-21 Sand filling of a penetrated mud layer	50
Figure 3-22 IHS layers stacking process.....	51
Figure 3-23 Staking IHS mud layer for bioturbated sample	52
Figure 3-24 Consolidation of analog IHS sample.....	53
Figure 3-25 Half cutting frozen analog IHS sample	54
Figure 3-26 Microscopic images of the sand-silt interface in analog IHS sample	55
Figure 3-27 McMurray Formation half-cut IHS cores.....	56
Figure 3-28 Microscopic images of the sand-silt interface in in situ IHS core.....	56
Figure 3-29 Schematic diagram of the triaxial system for permeability measurement	57
Figure 3-30 ISCO® 260D syringe pump (Teledyne ISCO®, 2017)	58

Figure 3-31 INSTRON® 5988 Floor Model testing system (Instron®, 2017).....	60
Figure 3-32 Triaxial Cell	60
Figure 4-1 B-tests on analog sand samples	70
Figure 4-2 Bulk volume change of analog sand samples.....	71
Figure 4-3 Coefficient of isotropic bulk compressibility of analog sand samples.....	72
Figure 4-4 Isotropically consolidated drained triaxial compression tests on analog sand samples	74
Figure 4-5 Variation of modulus of elasticity versus effective confining stress for analog sand samples .	75
Figure 4-6 Volumetric behavior of analog sand samples during drained triaxial compression tests.....	76
Figure 4-7 Typical plot of axial strain versus volumetric strain for an oil sand sample (modified from Touhidi-Baghini, 1998).....	79
Figure 4-8 Variation of dilation angle with effective confining stress for analog sand samples	79
Figure 4-9 Deformed shapes of specimens during hydrostatic loading (Ehrgott, 1970)	81
Figure 4-10 Shapes of failed specimens after a shear test (Ehrgott, 1970).....	81
Figure 4-11 Classification of failure modes of specimens loaded in a triaxial compression setup (Hatibu & Hettiaratchi, 1993)	82
Figure 4-12 Specimen deformation during an isotropically consolidated shear test (Ehrgott, 1970).....	83
Figure 4-13 Sand sample loaded in an isotropically consolidated drained shear test under σ_3' of 3.5 MPa	84
Figure 4-14 Sand sample loaded in an isotropically consolidated drained shear test under σ_3' of 1 MPa.	84
Figure 4-15 Sand sample loaded in an isotropically consolidated drained shear test under σ_3' of 0.5 MPa	85

Figure 4-16 Drained triaxial compression tests stress paths and failure envelope for analog sand samples	86
Figure 4-17 Peak axial strain for analog sand samples	88
Figure 4-18 Peak volumetric strain for analog sand samples	88
Figure 4-19 Volume change during isotropic unloading of analog sand samples	91
Figure 4-20 Normalized absolute permeability versus effective confining stress for analog sand samples	91
Figure 4-21 Normalized absolute permeability versus volume change for analog sand samples during isotropic unloading.....	92
Figure 4-22 Normalized absolute permeability versus normalized porosity for analog sand samples during isotropic unloading.....	93
Figure 4-23 Normalized absolute permeability versus axial strain for analog sand samples during triaxial shearing.....	94
Figure 4-24 Normalized absolute permeability versus volumetric strain for analog sand samples during triaxial shearing.....	95
Figure 4-25 Normalized absolute permeability versus normalized porosity for analog sand samples during triaxial shearing.....	96
Figure 4-26 Peak failure envelope for McMurray Formation oil sands.....	98
Figure 4-27 Modulus of elasticity versus effective confining stress for McMurray Formation oil sands	100
Figure 4-28 Normalized deviatoric stress versus axial strain for McMurray Formation oil sand	101
Figure 4-29 Prediction of absolute permeability alteration during isotropic unloading using the Kozeny-Carman equation	103
Figure 4-30 Prediction of absolute permeability alteration during triaxial shearing using the Kozeny-Carman equation	104

Figure 4-31 Prediction of absolute permeability alteration during isotropic unloading using Chardabellas' equation.....	105
Figure 4-32 Prediction of absolute permeability alteration during isotropic unloading using Tortike's equation.....	106
Figure 4-33 Prediction of absolute permeability alteration during isotropic unloading using Touhidi-Baghini's equation	108
Figure 4-34 Prediction of absolute permeability alteration during isotropic unloading using Touhidi-Baghini's equation, B=7	108
Figure 5-1 B-tests on analog mud samples	112
Figure 5-2 Bulk volume change of analog mud samples	113
Figure 5-3 Coefficient of isotropic bulk compressibility of analog mud samples	114
Figure 5-4 Isotropically consolidated drained triaxial compression tests on analog mud samples	116
Figure 5-5 Variation of modulus of elasticity versus effective confining stress for analog mud samples	117
Figure 5-6 Volumetric behavior of analog mud samples during drained triaxial compression tests.....	118
Figure 5-7 Variation of dilation angle with effective confining stress for analog mud samples	119
Figure 5-8 Mud sample loaded in an isotropically consolidated drained shear test under σ_3' of 3.5 MPa	121
Figure 5-9 Mud sample loaded in an isotropically consolidated drained shear test under σ_3' of 1 MPa. 121	
Figure 5-10 Mud sample loaded in an isotropically consolidated drained shear test under σ_3' of 0.5 MPa	121
Figure 5-11 Drained triaxial compression tests stress paths and failure envelope for analog mud samples	122

Figure 5-12 Peak axial strain for analog mud samples	124
Figure 5-13 Peak volumetric strain for analog mud samples.....	124
Figure 5-14 Volume change during isotropic unloading of analog mud samples	126
Figure 5-15 Normalized absolute permeability versus effective confining stress for analog mud samples	127
Figure 5-16 Normalized absolute permeability versus volume change for analog mud samples during isotropic unloading.....	128
Figure 5-17 Normalized absolute permeability versus porosity for analog mud samples during isotropic unloading	129
Figure 5-18 Normalized absolute permeability versus axial strain for analog mud samples during triaxial shearing.....	130
Figure 5-19 Normalized absolute permeability versus volumetric strain for analog mud samples during triaxial shearing.....	131
Figure 5-20 Normalized absolute permeability versus porosity for analog mud samples during triaxial shearing.....	132
Figure 5-21 Peak failure envelope for in situ shale cores and analog mud samples.....	134
Figure 5-22 Modulus of elasticity versus effective confining stress for in situ shale cores and analog mud samples.....	136
Figure 5-23 Normalized deviatoric stress versus axial strain for Clearwater shale (Suncor Energy, 2009)	137
Figure 5-24 Normalized deviatoric stress versus axial strain for Wabiskaw shale (Suncor Energy, 2005)	137

Figure 5-25 Normalized deviatoric stress versus axial strain for Wabiskaw shale (Suncor Energy, 2009)	138
Figure 5-26 Normalized deviatoric stress versus axial strain for Upper and Lower McMurray shale (Chalaturnyk, 1996).....	138
Figure 5-27 Normalized deviatoric stress versus axial strain for analog mud samples	139
Figure 5-28 Porosity versus vertical effective stress for Mondol’s synthetic mudstones and analog mud samples.....	140
Figure 5-29 Absolute permeability versus porosity for Mondol’s synthetic mudstones and analog mud samples.....	141
Figure 6-1 B-tests on analog IHS samples.....	145
Figure 6-2 Bulk volume change of analog IHS samples.....	146
Figure 6-3 Coefficient of isotropic bulk compressibility of analog IHS samples.....	147
Figure 6-4 Isotropically consolidated drained triaxial compression tests on analog IHS samples	149
Figure 6-5 Variation of modulus of elasticity versus effective confining stress for analog IHS samples	150
Figure 6-6 Volumetric behavior of analog IHS samples during drained triaxial compression tests.....	152
Figure 6-7 Variation of dilation angle with effective confining stress for analog IHS samples	153
Figure 6-8 IHS sample loaded in an isotropically consolidated drained shear test under σ_3' of 3.5 MPa	154
Figure 6-9 IHS sample loaded in an isotropically consolidated drained shear test under σ_3' of 1 MPa..	155
Figure 6-10 IHS sample loaded in an isotropically consolidated drained shear test under σ_3' of 0.5 MPa	155
Figure 6-11 Bioturbated IHS sample loaded in an isotropically consolidated drained shear test under σ_3' of 0.5 MPa.....	155

Figure 6-12 Drained triaxial compression tests stress paths and failure envelope for analog IHS samples	156
Figure 6-13 Drained triaxial compression tests stress paths for bioturbated and non-bioturbated analog IHS samples.....	157
Figure 6-14 Peak axial strain for analog IHS samples	158
Figure 6-15 Peak volumetric strain for analog IHS samples	159
Figure 6-16 Bulk volume change during isotropic unloading of analog IHS samples	161
Figure 6-17 Normalized absolute permeability versus effective confining stress for analog IHS samples	161
Figure 6-18 Normalized absolute permeability versus volume change for analog IHS samples during isotropic unloading.....	162
Figure 6-19 Typical normalized absolute evolution for an analog IHS sample during isotropic unloading	163
Figure 6-20 Normalized absolute permeability versus normalized porosity for analog IHS samples during isotropic unloading.....	164
Figure 6-21 Normalized absolute permeability versus axial strain for analog IHS samples during triaxial shearing.....	165
Figure 6-22 Normalized absolute permeability versus volumetric strain for analog IHS samples during triaxial shearing.....	166
Figure 6-23 Normalized absolute permeability versus normalized porosity for analog IHS samples during triaxial shearing.....	166
Figure 6-24 Stress-strain curves of analog sand, mud, and IHS samples under σ_3' of 3.5 MPa.....	169
Figure 6-25 Stress-strain curves of analog sand, mud, and IHS samples under σ_3' of 1 MPa.....	169

Figure 6-26 Stress-strain curves of analog sand, mud, and IHS samples under σ_3' of 0.5 MPa.....	170
Figure 6-27 Volumetric behavior of analog sand, mud, and IHS samples during drained triaxial shearing under σ_3' of 3.5 MPa.....	172
Figure 6-28 Volumetric behavior of analog sand, mud, and IHS samples during drained triaxial shearing under σ_3' of 1 MPa.....	173
Figure 6-29 Volumetric behavior of analog sand, mud, and IHS samples during drained triaxial shearing under σ_3' of 0.5 MPa.....	173
Figure 6-30 Prediction of absolute permeability alteration of IHS during isotropic unloading using the Kozeny-Carman equation	175
Figure 6-31 Prediction of absolute permeability alteration of IHS during isotropic unloading using Chardabellas' equation.....	176
Figure 6-32 Prediction of absolute permeability alteration of IHS during isotropic unloading using Tortike's equation	177
Figure 6-33 Prediction of absolute permeability alteration of IHS during isotropic unloading using Touhidi-Baghini's equation	178
Figure 6-34 Normalized absolute permeability correlation for non-bioturbated IHS samples.....	180
Figure 6-35 Normalized absolute permeability correlation for bioturbated IHS samples	180
Figure 7-1 Hyperbolic stress-strain relation (Itasca, 2017).....	187
Figure 7-2 Geometry of the problems and the assumed grid sizes for sand (a), mud (a), and IHS (b) samples	189
Figure 7-3 Deviatoric stress versus axial strain for sand samples (Lab tests simulated by FLAC3D™) 190	
Figure 7-4 Volumetric strain versus axial strain for sand samples (Lab tests simulated by FLAC3D™)191	

Figure 7-5 Contours of volumetric strain (a), contours of shear strain (b), CT Scan (c), and digital image (d) of Sand No. 1 ($\sigma_3' = 3.5$ MPa).....	192
Figure 7-6 Contours of volumetric strain (a), contours of shear strain (b), CT Scan (c), and digital image (d) of Sand No. 2 ($\sigma_3' = 1$ MPa).....	193
Figure 7-7 Contours of volumetric strain (a), contours of shear strain (b), CT Scan (c), and digital image (d) of Sand No. 3 ($\sigma_3' = 0.5$ MPa).....	194
Figure 7-8 Deviatoric stress versus axial strain for mud samples (Lab tests simulated by FLAC3D™)	195
Figure 7-9 Volumetric strain versus axial strain for mud samples (Lab tests simulated by FLAC3D™)	197
Figure 7-10 Contours of volumetric strain (a), contours of shear strain (b), CT Scan (c), and digital image (d) of Mud No. 1 ($\sigma_3' = 3.5$ MPa).....	198
Figure 7-11 Contours of volumetric strain (a), contours of shear strain (b), and digital image (c) of Mud No. 1 ($\sigma_3' = 1$ MPa).....	199
Figure 7-12 Contours of volumetric strain (a), contours of shear strain (b), CT Scan (c), and digital image (d) of Mud No. 3 ($\sigma_3' = 0.5$ MPa).....	200
Figure 7-13 Deviatoric stress versus axial strain for IHS samples (Lab tests simulated by FLAC3D™)	202
Figure 7-14 Volumetric strain versus axial strain for IHS samples (Lab tests simulated by FLAC3D™)	203
Figure 7-15 Contours of volumetric strain (a), contours of shear strain (b), CT Scan (c), and digital image (d) of IHS No. 1 ($\sigma_3' = 3.5$ MPa).....	204
Figure 7-16 Contours of volumetric strain (a), contours of shear strain (b), CT Scan (c), and digital image (d) of IHS No. 2 ($\sigma_3' = 1$ MPa).....	205
Figure 7-17 Contours of volumetric strain (a), contours of shear strain (b), CT Scan (c), and digital image (d) of IHS No. 3 ($\sigma_3' = 0.5$ MPa).....	206

NOMENCLATURE

u	Pore pressure
σ_c	Isotropic confining stress
B	Skempton's pore pressure parameter
C_b	Coefficient of isotropic bulk compressibility
σ_3'	Effective confining stress
ε_v	Volumetric strain
ε_a	Axial strain
ψ	Dilation angle
$d\gamma$	Rate of plastic distortion
$d\varepsilon_v$	Rate of plastic volumetric strain
$d\varepsilon_a$	Rate of axial strain
ν	Poisson's ratio
E	Young's modulus
φ	Friction angle
K_a	Absolute permeability
n	Porosity

D_s	Mean particle size
K_0	Initial absolute permeability
φ_0	Initial porosity
SAGD	Steam Assisted Gravity Drainage
IHS	Inclined Heterolithic Stratification

1. INTRODUCTION

1.1. Background

Oil sand reservoirs exist in several locations around the world, such as in the USA, Russia, Venezuela, and Canada. Among these oil sand regions, the Athabasca deposit in Alberta, Canada is the largest (Government of Alberta, 2017). Considering the current established 165 billion barrel of oil sand reserves in northern Alberta, Canada has the third largest reserves of crude oil in the world. As depicted in Figure 1-1, oil sand reservoirs are located in three main regions within northern Alberta and underlie 142,200 square kilometers (km²) of land in the Athabasca, Cold Lake, and Peace River areas. Among these three regions, the Athabasca reservoir has the largest bitumen reserve and production capacity (Alberta Energy Regulator, 2015). Furthermore, a sizeable portion of this reservoir in the Middle McMurray Formation is classified as Inclined Heterolithic Stratification (IHS) lithosomes, which has a significant capacity of recoverable crude bitumen (Strobl et al., 1997; Jablonski, 2012)

When seeking to extract this bitumen using currently available technology, approximately 80% of oil sands are recoverable through in situ production, and 20% by mining. Four major production techniques which are currently used in Alberta are Primary/Enhanced Recovery, Cyclic Steam Stimulation, Steam Assisted Gravity Drainage (SAGD), and Surface Mining. It is worth noting that the bitumen recovery rate for each of these extraction methods is different. Surface mining and SAGD have the highest recovery rates, at 90% and 50-60% respectively. However, only three percent of this massive oil sand land (4,800 km²) is surface minable, which makes SAGD the most appropriate and promising method of bitumen extraction (Government of Alberta, 2017; Alberta Energy Regulator, 2015; Edmunds, 1987).

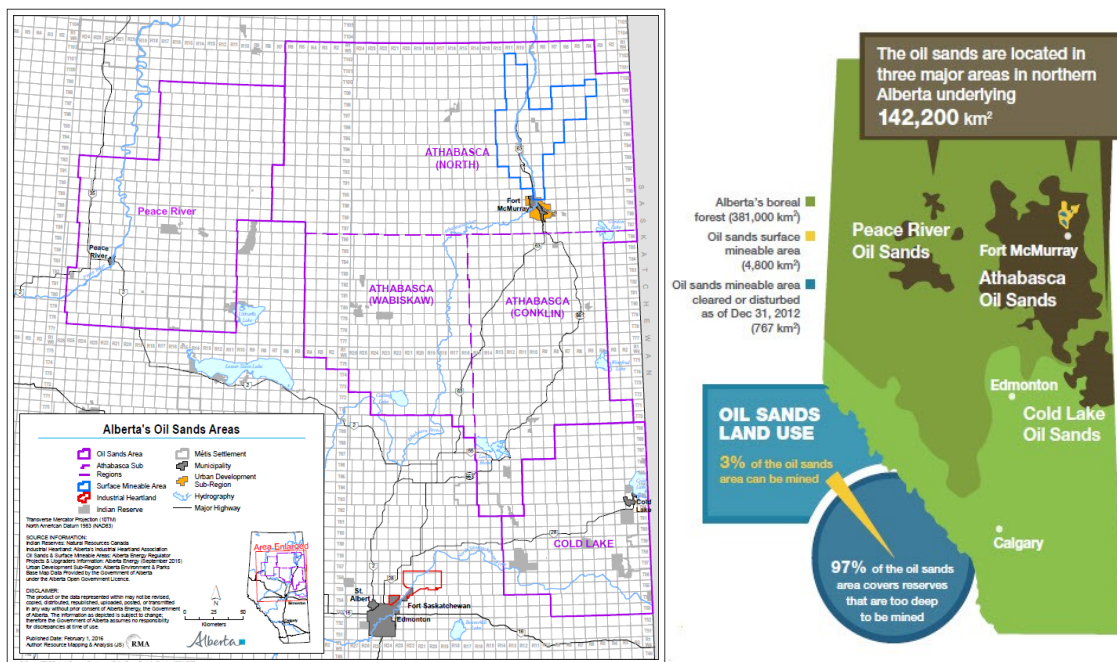


Figure 1-1 Alberta oil sand areas (Government of Alberta, 2017)

During the SAGD operation, the injection of high pressure and high temperature steam into the oil sand reservoir creates a complex interaction between the porous media, in situ fluid, and injected fluids. Geomechanical reactions to such fluid pressure and temperature changes lead to alterations in the stress state and deformation of the reservoir. In particular, the resulting variations in confining stress and shear stress affect the hydraulic properties of the reservoir, the stability of the underground opening, and the performance of the SAGD process (Chalaturnyk, 1996; Touhidi-Baghini, 1998). Some of the previous studies have shown that these changes are especially severe when tensile or shear yield happens (Touhidi-Baghini, 1998; Li, 2006).

In the case of the Athabasca region, the reservoir behavior during SAGD is greatly affected by the geology. A significant portion of the oil sand reservoir in the lower Cretaceous Middle McMurray Formation can be classified as Inclined Heterolithic Stratification lithosomes (Jablonski, 2012). The SAGD bitumen extraction interval is comprised of a cross-bedded clean sand sequence and 10 meters up to the sand-dominated IHS (Cenovus FCCL Ltd., 2013). This type of IHS lithosome has a large percentage of sand layers with high bitumen content (12% of the total mass in some

cases) (Strobl et al., 1997). The two other types of IHS (mixed IHS and mud-dominated IHS) cannot be classified as practical SAGD bitumen intervals because of their high mud content and presumed low permeability (Cenovus FCCL Ltd., 2013; Strobl et al., 1997).

In contrast to the abundance of experimental and numerical studies on the cross-bedded sand in the Athabasca reservoir, the published data on IHS is minimal. This is mainly due to the great heterogeneity of IHS facies in terms of sand and mud layer thickness, percentage, and inclination, as well as the contrasting and complex behavior of these layers. Because of the great heterogeneity of IHS and the minimal experimental studies on it, its hydro-geomechanical properties are relatively unknown, especially during SAGD operation.

For these reasons, the major goals of this research are investigating the geomechanical constitutive behavior of IHS as well as linking IHS' geological and mechanical characteristics to its hydraulic behavior. The findings of this study lead to a more accurate estimation of permeability changes in the IHS reservoir during the bitumen extraction process.

1.2. Statement of Problem

As declared in the previous sections, IHS lithosomes form a significant portion of heavy oil-bearing strata in Alberta, especially in the Athabasca Oil Sand Area (OSA). In the Middle McMurray Formation, IHS facies are located on top of clean cross-bedded sand facies. The bitumen saturation in sand layers of IHS is high, which makes the sand-dominated IHS a worthy target for future bitumen exploitation. However, numerical studies have shown that the existence of mud layers within the IHS creates severe flow baffle during SAGD operations, and delays steam chamber growth. These low permeability mud layers not only decrease the amount of bitumen recovery in current SAGD projects, but also make any future development plans in IHS facies economically undesirable.

Currently, due to the minimal published experimental data on IHS, there is no clear understanding of either the hydraulic characteristics or the constitutive behavior of these lithosomes, particularly when they are subjected to a SAGD operation. Moreover, the lack of experimental data on this type of lithology makes it infeasible to validate the previous numerical research.

One of the biggest challenges regarding the IHS is its high degree of heterogeneity in terms of sand and mud layer thickness, orientation, and distribution. Moreover, the physical characteristics of IHS beds contrast with each other. For example, their grain size, porosity, permeability, bioturbation, and horizontal continuity are very different (Jablonski & Dalrymple, 2016). Such great heterogeneity makes undisturbed in situ IHS samples (cores) unsuitable for laboratory testing. Therefore, the development of a technique to reconstitute analog IHS specimens becomes a necessity for any kind of experimental study on this type of lithology.

For these reasons, this study aims to conduct a series of extensive laboratory experiments on analog IHS samples to link their geological characteristics to their hydro-mechanical behavior under various stress states. These stress states are designed to simulate the reservoir's stress paths during the SAGD operation.

1.3. Research Objectives

The overarching objective of this research is to investigate the geomechanical constitutive behavior of IHS. The other major goal of this research is to link geological and mechanical characteristics of the IHS to its hydraulic behavior in order to estimate the permeability evolution of the IHS reservoir during a SAGD operation. To that end, the different phases of this study are summarized as follows:

- Characterizing the geomechanical behavior of sand and mud layers of IHS separately.
- Characterizing the IHS samples; in other words, determining their physical, mechanical, and hydraulic properties.

- Investigating the evolution of absolute permeability in sand, mud, and IHS samples under the SAGD-induced stress paths.
- Investigating the hydro-mechanical effects of bioturbation on IHS.
- Developing empirical correlations for predicting the geomechanical parameters of sand, mud, and IHS samples at various stress states.
- Developing empirical correlations relating the absolute permeability of IHS to its stress state and deformation.
- Exploring the possibility of permeability enhancement mechanisms under various stress states.

In order to achieve the above-mentioned objectives, the following laboratory goals must be accomplished.

- Developing a methodology to reconstitute similar analog sand and mud samples.
- Developing a methodology to reconstitute similar analog IHS samples with and without bioturbation.
- Developing a triaxial test setup with which the hydro-mechanical tests can be performed.
- Devising test procedures to experimentally simulate the SAGD-induced stress paths.

1.4. Scope and Methodology

This research introduces the concept of IHS from sedimentological and ichnological perspectives and explains the geological position of IHS facies with respect to the Athabasca oil sand reservoir. It also illuminates the need for and role of reservoir geomechanical studies on IHS, particularly during a SAGD operation. In this regard, in order to experimentally investigate the geomechanical constitutive behavior of IHS and link its geological and mechanical characteristics to its hydraulic behavior, several similar IHS samples are required.

However, in situ IHS specimens (cores) are too heterogeneous in terms of layer thickness, distribution, and inclination to provide a reliable sample. Furthermore, they have high degree of

fabric (microstructure) disturbance which is the result of coring, sampling, and evolution of dissolved gas (for bitumen-saturated samples) (McKay, 1989; Touhidi-Baghini, 1998; Scott, 1992)

The high number of changeable parameters in addition to the high degree of fabric disturbance makes the oil saturated in situ IHS specimens challenging for experimental studies. Therefore, during this study, all the tests were performed on oil-free analog specimens. Using reconstituted analog specimens not only enables the production of high-quality similar samples, but also assures the repeatability of results. The issues associated with using in situ bitumen saturated samples are discussed in more detail in section 3.2.1.1.

In order to achieve the research objectives explained in section 1.3, a detailed methodology for reconstitution of analog IHS specimens was developed, and a microscopic comparative study was conducted between analog and in situ IHS samples. This step included creating analog sand and mud samples, which required the design and manufacture of several tools and the development of several techniques.

In addition, an extensive laboratory testing program was designed to investigate the constitutive behavior of IHS. In this program, the SAGD-induced stress paths were experimentally simulated by running isotropic cyclic consolidation and drained triaxial shearing tests. Both series of tests were performed in conjunction with permeability tests at different strain levels, flow rates, and stress states.

Additionally, an analog bioturbated IHS sample was tested to examine the hydro-geomechanical effects of bioturbation. Moreover, the hydro-mechanical characteristics of analog IHS were compared with their constituent layers (sand and mud samples). Finally, a numerical model for sand dominated IHS was built to match the experimental data produced during this program.

1.5. Organization of Thesis

Chapter 2 illustrates the extent of bitumen reserves in Canada and describes the current bitumen recovery techniques. It also explains the geology of the McMurray Formation with a focus on IHS

lithosomes' sedimentology and internal architecture. Additionally, it delineates the need for and role of geomechanical studies on IHS lithology, especially during a SAGD project. Finally, it summarizes the findings of previous reservoir geomechanical studies that have been done on oil sand reservoirs.

Chapter 3 describes the materials used in this study to create analog samples. It also explains the experimental protocols that were developed to reconstitute analog sand, mud, and IHS specimens. Moreover, it illuminates the result of a microscopic comparative study on in situ and analog IHS samples. In addition, it describes the experimental setup that was used to run hydro-geomechanical testing and elaborates on the specification of the major component of the setup. Lastly, it presents the experimental procedures of the testing program that was conducted on sand, mud, and IHS samples.

Chapter 4 presents the results of the tests performed on the sand samples. These include the B-test, the isotropic cyclic consolidation test, the drained triaxial compression test, and the permeability test. As part of the test results analysis, isotropic bulk compressibility, stress-strain behavior, shear strength, and permeability evolution of the sand specimens under the SAGD-induced stress paths were discussed. In addition, the geomechanical properties of the analog samples were compared with previous experimental studies on oil sand, and a number of experimental correlations were developed for some of these parameters. Finally, the applicability of former empirical permeability relationships was investigated.

Chapter 5 presents the results of the tests performed on the mud samples. These include the B-test, the isotropic cyclic consolidation test, the drained triaxial compression test, and the permeability test. As part of the test results analysis, isotropic bulk compressibility, stress-strain behavior, shear strength, and permeability evolution of the mud specimens under the SAGD-induced stress paths were discussed. In addition, the geomechanical properties of the tested mud samples were compared with previous experimental studies on McMurray mudstone and other silt-clay mixtures, and several experimental correlations were developed for some of these parameters.

Chapter 6 presents the results of the tests performed on the IHS samples. These include the B-test, the isotropic cyclic consolidation test, the drained triaxial compression test, and the permeability

test. As part of the test results analysis, isotropic bulk compressibility, stress-strain behavior, shear strength, and absolute permeability and its evolution under SAGD-induced stress paths for the IHS specimens were compared with sand and mud samples. In addition, a variety of experimental correlations were developed for the geomechanical properties of the tested IHS samples. Lastly, a series of empirical correlations that relates the absolute permeability of IHS to its stress state and deformation was proposed for bioturbated and non-bioturbated samples.

Chapter 7 describes the numerical model that was built to simulate the geomechanical behavior of sand-dominated IHS. It also explains the numerical simulator, the constitutive model, and the material properties that were used in building this model. The results obtained in chapters 4 and 5 were used as the materials' input functions in the developed model. In addition, to assure the accuracy of the developed model, the outcomes of laboratory testing on IHS samples were compared with the numerical results.

Chapter 8 summarizes the findings of this research and draws conclusions on both the hydro-geomechanical properties of sand, mud, and IHS samples, and their permeability evolution under SAGD-induced stress paths. Finally, it identifies and delineates the areas of further research.

2. LITERATURE REVIEW

2.1. Bitumen: a Promising Energy Source

2.1.1. What is Bitumen?

Bitumen can be defined as a combination of several viscous organic liquids which are sticky, black, and soluble in carbon disulfide (CS₂) (Shivam Tar Products, 2017). As a viscous, super-heavy oil, bitumen does not flow in its natural state (Alberta Energy Regulator, 2015). In northern Alberta, it is embedded in sand (clastic) and carbonate formations. Crude bitumen, and the rock fabric which contains it, together with all other associated mineral materials except natural gas, are called oil sands (Alberta Energy Regulator, 2015). From a chemical perspective, Alberta oil sand bitumen is composed of a variety of organic molecules which have paraffinic, aromatic and heterocyclic structures (Strausz & Lown, 2003). Moreover, bitumen differs from typical petroleum, owing to its high concentration of heavy polymeric materials (Strausz & Lown, 2003).

2.1.2. Role of Bitumen in Canada

The non-renewable energy sector is one of the pivotal driving forces behind the Canadian economy, at both the provincial and federal levels. As an illustration, in 2015, the oil sand industry directly created 151,000 jobs and boosted the economy by \$23 billion. Based on a projection by the Canadian Association of Petroleum Producers (CAPP) and the Canadian Energy Research Institute (CERI), over the next 20 years, the oil sand sector will contribute \$1.2 trillion to the Canadian economy (Canadian Energy Research Institute, 2017; Canadian Association of Petroleum Producers, 2017). This huge contribution will be made through corporate and personal income taxes (federal and provincial), royalties, land sales, job creation, etc. As a case in point, in the 2013-14 fiscal year, 55% of Alberta's non-renewable resource revenue (\$5.2 billion) came from bitumen and synthetic crude oil royalties (Government of Alberta, 2017).

2.1.3. Bitumen Reserves in Canada

Oil sands areas (OSAs) are defined as the geological formations and the geographical areas in which crude bitumen is located. As presented in Figure 1-1, in northern Alberta, there are three major OSAs: Athabasca, Cold Lake, and Peace River. Within these OSAs, the Athabasca Wabiskaw-McMurray and Athabasca Grosmont oil sand deposits are the largest (Wightman et al., 1989). The Alberta Energy Regulator's most recent statistics show that the remaining established bitumen reserves equal about 26.43 billion cubic meters (Aherne & Maini, 2008; Alberta Energy Regulator, 2017).

2.1.4. Bitumen Recovery Techniques

There are four methods to extract bitumen from oil sand reservoirs: i) Primary/Enhanced Recovery, ii) Cyclic Steam Stimulation, iii) Steam Assisted Gravity Drainage (SAGD), and iv) Surface Mining. The quality and location (depth) of the reservoir determines which of these methods should be used. Shallow reservoirs can be surface mined, but only 3% of OSAs are surface minable. Among the other in situ recovery techniques, SAGD is the most common. In 2014, for example, approximately 60% of the total in situ bitumen production was recovered through the SAGD process (Alberta Energy Regulator, 2015; Holly et al., 2016).

During a SAGD operation, which is a thermal recovery method, two horizontal parallel wells (a "well-pair") are used. Steam is supplied through the top well (the "injection-well"), and oil and condensate are collected from the bottom-well (the "production well"). The steam injected in the top well creates a growing steam chamber which heats a thin layer of the bitumen-saturated reservoir (and reduces the viscosity of bitumen), then condensates drain to the bottom of the steam chamber. To keep the pressure of the growing chamber constant, steam is continuously injected into the top well during this process. Once the front edge of the heated zone reaches the production well, condensate and bitumen are produced from the bottom well (Holly et al., 2016; Strobl et al., 1997; Edmunds, 1987).

2.2. Geology of the McMurray Formation

One of the most distinctive characteristics of the McMurray Formation is its complex geological heterogeneity. This formation, which embodies the majority of heavy oil deposits in the Athabasca oil sands region, belongs to the Mannville Group of Northern Alberta. As depicted in Figure 2-1, the lower section of the Mannville Group includes the McMurray Formation, and the upper section encompasses the Wabiskaw Member, the Clearwater Formation, and the Grand Rapids Formation (Ranger & Gingras, 2003).

In the Athabasca OSA, the overburden thickness ranges from zero meters along the Athabasca river outcrop to 450 meters at the southwest region of the deposit. The thickness of the McMurray Formation itself varies from zero to 110 meters. This formation is overlaid by the Glauconitic shoreface sands of the Wabiskaw Member, which is the basal unit of Clearwater Formation (Jablonski, 2012; Ranger & Gingras, 2003).

The deposition of the McMurray Formation occurred on top of the Devonian evaporates and carbonates, and created a sharp unconformity surface. Prior to that, the Devonian carbonate and underlying Middle Devonian Elk Point Group evaporates experienced many erosions and salt dissolutions, and a structural collapse which led to the creation of a broad north-south trending valley known as the McMurray subbasin (Stewart & MacCallum, 1978). Afterward, due to the frequent transgressions of the Cretaceous Boreal sea (during the Aptian-Albian), the McMurray Formation was deposited in this valley (Flach, 1984). It should also be noted that the depositional environment was changing during the different periods of this process, which led to the development of a very heterogeneous heavy oil reservoir (Hassanpour, 2009).

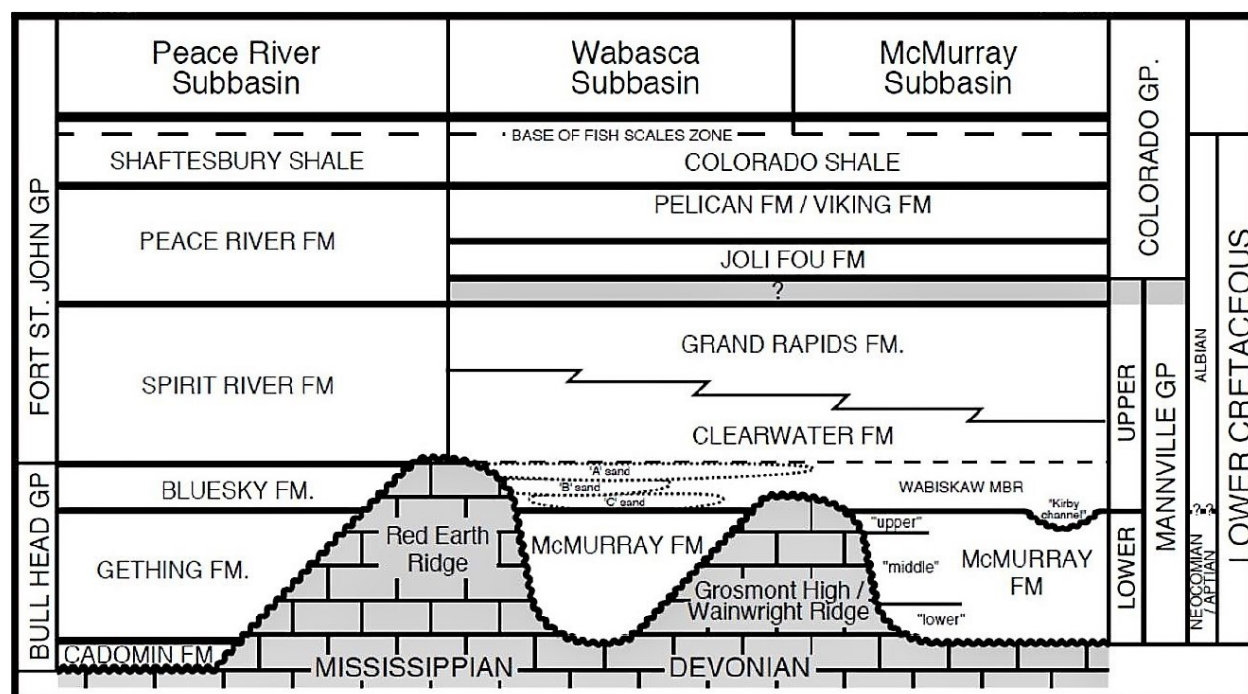


Figure 2-1 Stratigraphic setting of northern Alberta (Ranger & Gingras, 2003)

Because of the great regional diversity of lithological characteristics and thickness throughout the McMurray Formation, it has never been formally divided into sub-units. However, many researchers use an informal threefold stratigraphy to study this formation. The idea of subdividing the McMurray Formation into three units (Upper, Middle, and Lower McMurray) was initially introduced by Carrigy (Carrigy, 1959). He proposed that during the deposition of the McMurray Formation the Boreal Sea went through a third-order transgression which resulted in the creation of lower fluvial deposits, middle estuarine and point bar successions, and upper marine facies (Ranger & Gingras, 2003; Hein & Cotterill, 2006; Ranger et al., 2008).

The composition of the Lower McMurray Formation, which is laid on top of the sub-Cretaceous unconformity, includes quartz-dominated, medium to coarse-grained, and structureless to cross-bedded sand. This unit has poor to moderate sorting and contains a large number of subangular grains. In some locations, lenses of quartz-pebble conglomerate can be observed in this unit, which embodies the underlying Devonian carbonate clasts. The depositional environment for Lower McMurray is considered to be fluvial. Nevertheless, based on some of the other evidence such as the existence of coal horizons and a very limited amount of bioturbation within this unit, it can be

concluded that the Lower McMurray fluvial system was, in fact, the upper part of a bigger estuarine system (Ranger & Gingras, 2003).

Among the McMurray Formation subdivisions, the Middle McMurray is the thickest (30 to 60 meters) and most heterogeneous unit. The sand layers of this unit have the highest oil saturation and the best reservoir potential (Jablonski, 2012). The depositional environment of the Middle McMurray can be explained within a tidally-influenced, middle-to-outer estuarine system (Hassanpour, 2009). It should also be noted that in many regions, the contact of this unit with the underlying Lower McMurray is either minimal or non-existent, and the Middle McMurray lies immediately on the top of the sub-Cretaceous unconformity. When such a contact is observed, it is usually unconformable and can be distinguished with a sharp change in lithology between two units (Ranger & Gingras, 2003).

Within the Middle McMurray unit there are two distinctive reservoir facies which are i) large-scale cross-stratified sand, and ii) Inclined Heterolithic Stratification (IHS).

The former, which is located at the bottom of this unit, has a thickness of 10 to 30 meters and can be characterized by its high porosity, permeability, and bitumen saturation. This section is predominantly composed of lower medium to upper fine-grained quartz-dominated sand; it is comprised of bedsets (up to 0.5 meters in thickness) that have strong tidal indicators such as reverse flow ripples (Ranger & Gingras, 2003; Jablonski, 2012; Hassanpour, 2009).

The latter, which is located on top of the cross-bedded sand, has a thickness of 30 to 40 meters. This section is comprised of both sand and mud layers, and has a complex internal architecture (which is described later in this chapter). Although the sand layers of IHS have a current-ripple cross-laminated structure and include upper fine-grained sand, their general composition and bitumen saturation are very similar to basal Middle McMurray sand (Ranger & Gingras, 2003; Jablonski, 2012; Hassanpour, 2009). Developing an understating of the heterogeneity of IHS deposits has drawn a lot of interest over the past few years, due to the significant role it could play in the development of in situ bitumen recovery processes.

It is worth noting that the contact condition between cross-stratified sand and IHS within the Middle McMurray depends on its locality. In some areas, the contact is gradational; however, in others, it is sharp and erosional.

The Upper McMurray Formation, which is known for its horizontal strata, predominantly consists of marine deposits. The existence of i) wave-generated structures, ii) a variety of ichnogenera suites within the interbedded argillaceous fine-grained sand and silts, and iii) several meter-scale upward coarsening cycles all testify to its marine origins (Jablonski, 2012; Ranger & Gingras, 2003). As declared by Range and Gingras (2003), there are two coarsening cycles in the Upper McMurray Formation, and each of them has three lithofacies.

2.3. Sedimentology and Ichnology of IHS

As stated before, in the Athabasca OSA, the lower (early) Cretaceous McMurray Formation contains the majority of recoverable reserve. Over time, this oil sand region has experienced many fluvial and tidal currents. This process led to great heterogeneity in sediment distribution and deposition development, which created several distinct facies within the McMurray Formation. Currently, there are nine recognized facies in the Middle McMurray Formation, which can be classified into three main categories: i) Sand-dominated facies, ii) Inclined heterolithic stratification (IHS) facies, and iii) Mixed heterolithic facies (Jablonski, 2012; Thomas et al., 1987; Dabek et al., 2014; Mossop, 1980) (**Error! Reference source not found.**).

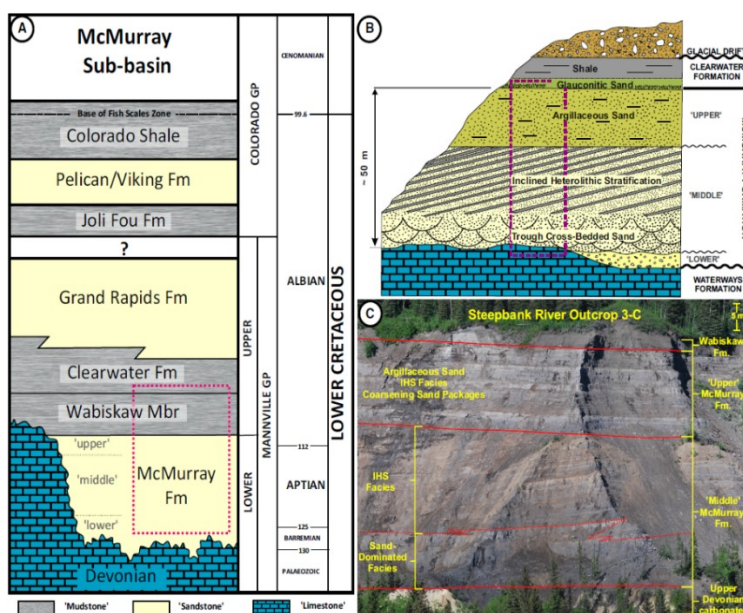


Figure 2-2 Stratigraphic setting of the Lower Cretaceous McMurray Formation (Jablonski & Dalrymple, 2016)

As noted earlier, IHS cover a large section of the McMurray Formation, and it is considered as potentially one of the richer bitumen extraction zones (a sand-dominated IHS). IHS lithosomes are made of sand and mud layers and can be subdivided into three categories based on their sand-mud percentage: Sand-dominated, Mixed, and Mud-dominated IHS (Bechtel et al., 1994).

Due to the substantial sedimentological differences among IHS layers, their permeability differs greatly. Such differences affected the bitumen migration pathway during the generation of the Athabasca oil sand reservoir. Consequently, different types of IHS have various reservoir potentials (Thomas et al. 1987; Ranger et al. 2012). The sections below describe the sedimentology of IHS in more detail.

2.3.1. Internal Architecture of IHS

A large number of IHS lithosomes are the result of lateral accretion within meandering channels of freshwater and tidally-influenced rivers (Thomas et al., 1987). In the case of the McMurray Formation, the IHS was built up on a point bar of deep continental-scale river in fluvial-marine

transition. IHS lithosomes are comprised of two alternating lithologies: fluvially-dominated sand beds alternating with brackish, tidally-influenced mud beds. Different beds are deposited according to the seasonal or annual fluctuations between the river-flood stage and low-flow stage. Sand beds are deposited quickly during river floods by unidirectional freshwater currents; therefore, little to no bioturbation can be seen in them. In contrast, fine-grained beds are severely bioturbated and include rare tidal structures. The deposition of fine-grained beds begins at the late flood stage and continues during the low-river flow period or inter-flood span (Jablonski & Dalrymple, 2016; Bechtel et al., 1994).

It is worth noting that the thickness of the sand beds is controlled by the magnitude and duration of the river-flood stage; larger and/or longer floods result in thicker sand beds (Jablonski, 2012). Also, the relative position of IHS within the fluvial-marine transition can be presumed to be landward since the large volume of IHS contains river flood deposits. In IHS, there are many meter-scale cycles (MSCs) of alteration between sandier and muddier layers which can be inferred as longer-term cyclicity in fluvial discharge due to ocean and/or solar dynamics. The typical characteristics of a MSC are: i) a sharp base, ii) an upward decrease in sand-bed thickness, iii) upward increases in the preservation of fine-grained beds, and iv) an upward increase in the intensity of bioturbation (Jablonski & Dalrymple, 2016; Bechtel et al., 1994; Lettley & Pemberton, 2004).

2.3.2. Grain Size Distribution within IHS

Sand beds of IHS, having a thickness of five to 150 cm, are mainly comprised of well-sorted, lower medium-grained to upper fine-grained quartzose sand. The primary structure of these sand beds is asymmetric current-ripple cross-lamination. Trough cross-stratification or structureless sand can be seen in thicker beds. Although sand beds are sand-dominated, containing more than 90% quartz sand, a small amount of lithological heterogeneity remains in the form of silt and very fine-grained sand. These heterogeneities occur within current-rippled beds (Jablonski & Dalrymple, 2016; Thomas et al., 1987). Fine-grained beds in IHS are mostly composed of silt-sized quartz, with small amounts of very fine-grained quartzose sand and clay (predominantly kaolinite). These beds

usually have a thickness in the range of 0.5 to 20 cm. In the absence of weathering in fine-grained beds, they show a plane-parallel laminated structure with 0.5 to 4.0 mm laminae thickness or a structureless internal form. Fine-grained beds thicker than 15 cm typically have an interbedding of rippled, very fine-grained sand with 1 cm bed thickness, and laminated to structureless silt (Jablonski & Dalrymple, 2016; Siiro, 2002).

2.3.3. Bioturbation Distribution within IHS

Bioturbation intensity in sand layers is a function of bed thickness and the vertical location of the bioturbation within the bed. Normally, when the thickness of a sand layer exceeds over 30 cm, little to no bioturbation is evident. However, a high concentration of *Cylindrichnus* burrows penetrating down from overlying fine-grained beds can be detected in the top part of such sand beds. This style of bioturbation is called “top-down” bioturbation, and it is restricted to one burrow length, which is 0.5 to 10 cm in penetration depth. In thicker sand beds, a gradational increase in bioturbation intensity in the upward direction can be observed. However, sand beds thinner than 30 cm show bioturbation (burrowing) throughout their thickness (Jablonski & Dalrymple, 2016).

Bioturbation in fine-grained beds is usually obscured due to weathering degradation. In the case of visible bioturbation, it usually consists of *Cylindrichnus* burrows that penetrate down into the underlying sand beds. In fine-grained beds, structureless sections show a high degree of bioturbation (BI = 3 to 6) and fresh surfaces show moderate to high bioturbation intensities (BI = 5 to 6). Another variable aspect of fine-grained beds is their lateral continuity in both strike and dip directions, which could be as short as 50 cm in some cases, and as long as 30 meters in others (Jablonski & Dalrymple, 2016).

2.3.3.1. *Bioturbation Index (BI)*

The bioturbation index (BI), a descriptive metric for the degree of bioturbation, is defined based on burrow density, burrow overlap, and sharpness of original sedimentary fabric. The range of BI is 0 to 6, and a higher BI value means a higher degree of bioturbation (Taylor & Goldring, 1993).

2.4. SAGD Projects and Geomechanics

2.4.1. Shear Strength and Stress-Strain Behavior of the Athabasca Oil Sand

In order to capture oil sand reservoir behavior during fluid injection, heating, and production, it is necessary to investigate its stress-strain relationship, peak shear strength behavior, and pore fluid flow characteristics. In the past few decades, several researchers have studied the unique geomechanical behavior of oil sands, which separates them from two conventional categories of cohesionless sands (dense and loose sands). Some of these features are i) high shear strength, ii) very stiff structure, iii) large degree of dilation at peak shear strength (especially at low confining stresses), and iv) no stress-dependent cohesion (Dusseault, 1977; Touhidi-Baghini, 1998; Chalaturnyk, 1996).

Dusseault and Morgenstern (1978) suggested that the interlocking structure (micro-fabric) of oil sands is the reason behind most of these features, and labelled oil sand “locked sand”. This term means oil sand grains have dense interpenetrative contacts which are the result of the solution and recrystallization of quartz in a diagenetic environment. This process not only reduces porosity and grain roundness, but also increases rugosity, shear strength, and degree of dilation at peak shear strength (Dusseault & Morgenstem, 1978)

The shear strength of oil sand is a function of several factors, such as the minimum effective confining stress and the initial fabric structure of the sample (porosity). For example, an increase in the minimum confining stress leads to a nonlinear increase in the shear strength; moreover, a very small increase in a sample’s porosity causes a noticeable drop in the measured shear strength. In addition, the shear strength of oil sand is stress path dependent. Based on Agar et al. (1987) experiments, heating the Athabasca oil sand up to 200°C in drained conditions does not have any substantial effects on its strength; however, the undrained heating causes a huge reduction in strength, especially in gas-rich oil sands, due to the thermal pore pressure generation.

One of the proper experimental methods to model the nonlinear stress-strain behavior of oil sands is the hyperbolic model, which is accurate up to 80% of the peak deviatoric stress level (Dusseault & Morgenstem, 1978; Agar et al., 1987).

2.4.1.1. *Problem of Sampling and Sample Disturbance*

In order to experimentally investigate the effects of mud and sand layers, link IHS' geomechanical behavior to its hydraulic behavior, and explore the possibility of permeability enhancement in IHS during a SAGD operation, several similar sand, mud, and IHS samples are required. As explained in section 2.1.1., the oil sand at its in situ condition can be characterized as a system of unconsolidated water-wet sand which is normally saturated with bitumen, water, and different amounts of dissolved gas. In most cases, the reservoir pore pressure is equal to the bubble pressure of dissolved gas (Touhidi-Baghini, 1998).

The decrease in the effective confining stress and pore pressure that happens during sampling and coring causes expansion of void spaces and evolution of dissolved gas, and subsequent disturbance of the sample's microstructures. Due to the very high viscosity of bitumen at the in situ temperature, its effective permeability to gas is extremely low. Therefore, the expanded evolved gases in bitumen cannot drain and muddle the grains' interlocking structures (Touhidi-Baghini, 1998; Agar, 1984). Such a phenomenon significantly affects the constitutive behavior of the uncemented oil sand and subsequently the IHS samples (Dusseault & Morgenstem, 1978; McKay, 1989). In fact, Dusseault (1977) declared that the geomechanical properties of oil sand such as elastic modulus, compressibility, permeability, shear strength, porosity, and saturation are very sensitive and can be negatively affected by sample disturbance.

Despite the recent improvements in sampling and coring techniques, the issue of sample disturbance due to dissolved gas evolution still exists. In order to avoid this problem, an oil-free material can be used instead. The concept of using an oil-free material to determine the constitutive behavior of an oil-saturated material was first introduced by Protulipac. He showed that the constitutive behavior of the oil-free St. Peter sandstone (that has a similar microstructure to the McMurray Formation) is similar to the constitutive behavior of the oil-saturated McMurray sand (Protulipac, 1991).

In addition to the issue of sample disturbance, in situ IHS specimens (cores) are too heterogeneous in terms of mud and sand layer thickness, distribution, and inclination depending on where the samples are cored. Consequently, it is almost impossible to recover two similar in situ IHS

samples. Having too many changeable parameters can cause huge variations in any laboratory-measured hydro-mechanical properties. In other words, such heterogeneity makes in situ IHS specimens challenging for any kind of experimental study.

In conclusion, to avoid the issues of heterogeneity and fabric disturbance, different methodologies for the reconstitution of oil-free analog sand, mud, and IHS specimens need to be developed. Chapter 3 describes such reconstitution protocols in detail.

It is also worth noting that one of the biggest challenges of using lab results in field-scale simulation is the issue of heterogeneity and scaling. As explained in this chapter, IHS lithosomes are very heterogeneous in term of their internal architecture. In addition, due to the geological heterogeneity of the McMurray Formation, the value of initial bitumen saturation for IHS varies at different locations within the reservoir. However, the tested samples in this study were bitumen-free and small. They also had a fixed and relatively simple geometry compared to the in situ IHS core. Although the fundamental constitutive data that was delivered in this study expands and improves our understand from geomechanical behavior of sand-dominated IHS, it should not be considered as equivalent field data for simulation of all types of IHS.

2.4.2. Hydro-geomechanical Processes during SAGD

Injection of high pressure and high temperature steam into the oil sand reservoir during a SAGD operation generates a complicated interaction between the injected fluid, in situ fluid, and the porous media. Such pressure and temperature variations trigger two major geomechanical reactions: isotropic stress and shear stress changes. These changes in the stress state lead to pore space, pore shape, and pore throat changes. Therefore, they could alter the permeability value of the reservoir (Li & Chalaturnyk, 2006).

2.4.2.1. *Isotropic Process*

Injection of high pressure steam into the reservoir (normally higher than the initial reservoir pressure) leads to isotropic unloading within the high pore pressure front of the reservoir. This

pore pressure increase in the drained zone and part of the partially drained zone of the reservoir leads to a decrease in the effective confining stress. As a result, the oil sand grains move apart from each other without any relative repositioning. This means the configuration of grains and their relative positions do not change during this process. Previous numerical and experimental works have shown that the volume change and permeability alteration/enhancement (both absolute and relative) due to isotropic unloading are smaller than those associated with the deviatoric (shearing) process, especially afterpeak shear strength (Abdallah, 2013; Oldakowski, 1994; Scott et al., 1994; Touhidi-Baghini, 1998; Li & Chalaturnyk, 2006; Li, 2006).

2.4.2.2. *Deviatoric (Shear) Process*

The main reason behind deviatoric (shear) stress changes within a reservoir is a change in total stress. During a SAGD operation, due to the high temperature of injected steam, the reservoir materials within the steam chamber undergo a substantial volumetric expansion. Consequently, the total stress increases and may initiate the shearing process. This process mainly occurs around the interface between the completely drained and partially drained zones of the reservoir (beyond the surface of the steam chamber). In other words, an inhomogeneous thermal expansion within the reservoir leads to an increase in the effective horizontal stresses and subsequent shearing of the reservoir materials. The shearing process can also occur because of an increase in pore pressure.

Shear dilation, in contrast to isotropic unloading, results in a considerable relative displacement of the sand grains and substantial changes in their pore geometry. This process contributes to porosity, compressibility, and permeability changes (Li, 2006). Previous field measurements showed a maximum volumetric strain of 2.5% within the reservoir, as a result of the SAGD process (Chalaturnyk, 1996). It is also worth noting that reservoir dilation or contraction during SAGD could cause surface uplift or subsidence as well. Recent numerical studies have shown that stiffer overburden rock, a smaller lateral stress ratio, a smaller dilation angle, and a larger Poisson's ratio correspond to a smaller magnitude of shear dilation and permeability enchantment in oil sand reservoirs (Yin et al., 2009).

Since geomechanically-induced absolute permeability changes are one of the critical factors in the efficiency of a SAGD operation, several researchers such as Oldakowski (1994), Touhidi-Baghini (1998), and Abdullah (2012) have developed empirical correlations to link the absolute permeability of oil sand to its geomechanical parameters.

2.4.2.3. Reservoir Stress Paths during SAGD

Plotting stress path is a significant geomechanics methodology used to identify and model the principal mechanisms that occur within a reservoir during a specific period, such as a SAGD operation. This method also enables us to divide the complex SAGD process into different, straightforward stress paths that can be simulated in laboratory experiments (Touhidi-Baghini, 1998; Abdallah, 2013).

As stated earlier, the stress-strain responses of the reservoir materials are stress path dependent. As explained in sections 2.4.2.1 and 2.4.2.2, two principal stress paths are followed by the reservoirs during the SAGD process:

- i) Decreasing mean effective stress due to the pore pressure increase. In $p-q'$ space, the path is horizontal, since σ'_1 and σ'_3 decrease equally, and $\sigma'_1 - \sigma'_3$ is constant.
- ii) Increasing mean effective stress and deviatoric stress due to thermal expansion. This increase is predominantly because of an increase in total horizontal stresses.

In shallow reservoirs, the vertical stress stays relatively constant during SAGD; however, in deep reservoirs, it can be increased due to the increase in confinement. As depicted in Figure 2-3, in the in situ condition, the reservoir could follow a stress path which is a combination of the two above-mentioned paths (Chalaturnyk, 1996; Touhidi-Baghini, 1998). As explained by Yaich (2008), such combined stress paths during a SAGD operation can be replicated in the laboratory through a radial extension test. It should also be noted that the stress path followed by different parts of the reservoir is not the same. The true combined stress path for each section of the reservoir depends on its

distance from the injection or production well and the value of water or steam mobility within that particular section of the reservoir.

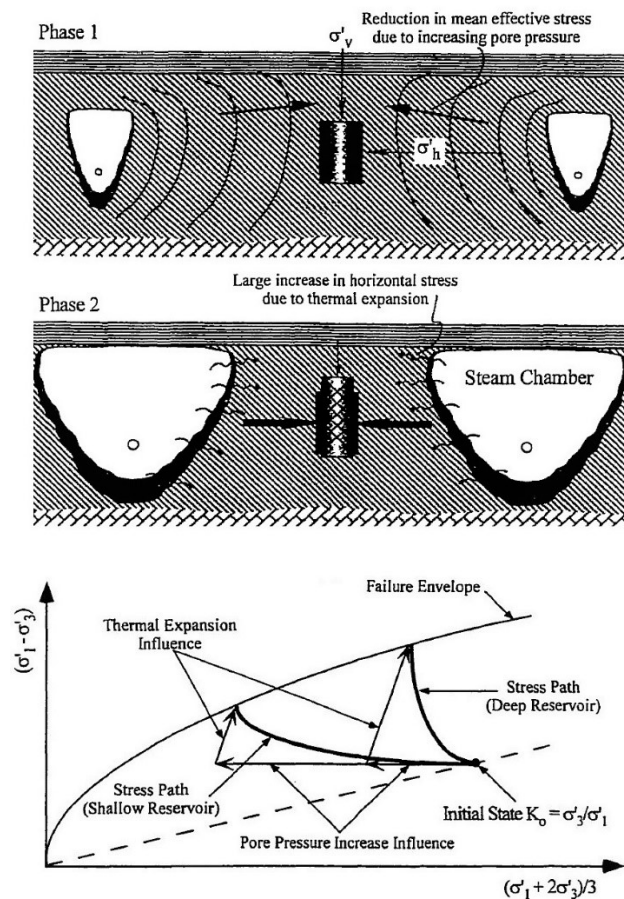


Figure 2-3 Major stress paths followed within a reservoir during the SAGD process (Touhidi-Baghini, 1998)

2.4.3. IHS and SAGD

2.4.3.1. SAGD Interval in IHS

As discussed earlier, IHS constitutes a substantial portion of the heavy oil reservoir within the Athabasca oil sand region (Jablonski, 2012). Within the Middle McMurray Formation, the cross-bedded clean sand sequence plus ten meters up to the sand-dominated IHS are considered to be the major SAGD bitumen extraction intervals (Cenovus FCCL Ltd., 2013).

Among the different types of IHS, the sand-dominated ones contain a large percentage of sand layers (more than 85%) with high bitumen saturation. The bitumen content in these layers in some cases could be as high as 12% of the total mass (Strobl et al., 1997). From a practical point of view, due to the high mud content and presumed low permeability values of the two other IHS categories (Mixed IHS and Mud-dominated IHS), they cannot be classified as SAGD bitumen extraction intervals (Cenovus FCCL Ltd., 2013; Strobl et al., 1997). Nonetheless, running a SAGD project even in sand-dominated IHS intervals is a complicated task, since this lithosome has two substantially different layers (sand and mud) with complex and contrasting hydro-mechanical behavior.

2.4.3.2. *Effect of IHS Mud Layers*

Previous numerical studies on IHS reservoirs and the data from temperature observation wells have shown that the existence of low permeability mud layers within the IHS acts as a severe flow baffle during SAGD operations, hindering both the temperature rise and the advancement of the steam chamber. This, therefore, has a detrimental effect on the amount of bitumen recovery (Figure 2-4) (Dahl et al., 2010; Strobl et al., 1997). In this regard, Strobl et al. declared that the value of absolute permeability differs up to three orders of magnitude between high porosity sand in a trough cross-bedded unit compared to mud layers associated with the IHS unit (Strobl et al., 1997).

Other numerical studies have suggested that breaking such flow baffles during a SAGD operation can potentially increase the production rate drastically (Li, 2006; Gu et al., 2011). Hence, to reach the ideal steam circulation and bitumen recovery during a SAGD operation in IHS, the fluid flow path within IHS layers and their hydro-geomechanical characteristics and responses should be well researched and analyzed.

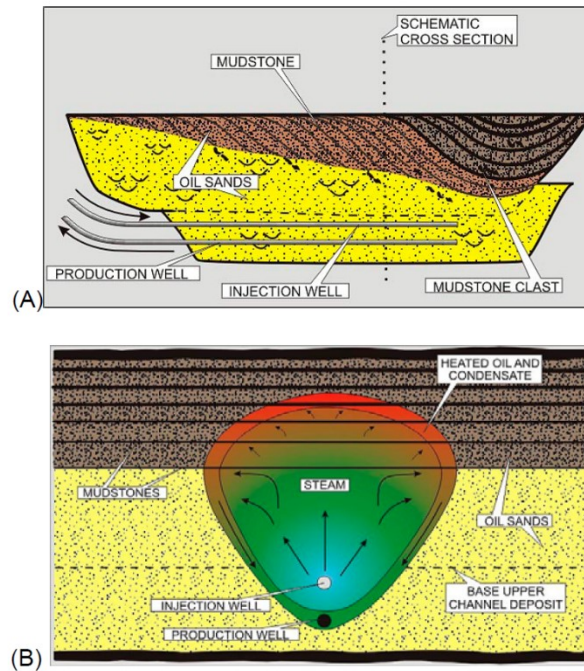


Figure 2-4 Schematic diagram of SAGD and how the steam chamber development is slowed down by IHS mudstones (Dahl et al., 2010)

2.4.3.3. Orientation of SAGD Well-pairs in IHS

Due to the great difference in the permeability of IHS layers, several numerical studies have been conducted to find the optimum orientation of the SAGD well-pairs with respect to the IHS bedding. These studies have shown that by placing the wells perpendicular to the IHS beds' dip direction, they can create a large number of breakthrough points for steam injection, and have maximum cross-sectional cuts with IHS layers. Therefore, the injected steam can sweep the reservoir more efficiently, and the bitumen can flow more easily to the production well (Strobl et al., 1997; Wang et al., 2013). Similarly, the performance of the well-pairs was reported to be minimum when they were oriented aligned with the IHS bedding plane (Wang et al., 2013).

3. MATERIALS AND EXPERIMENTAL METHODS

3.1. Test Materials

In this research program, three different types of specimens (sand, mud, and IHS) were reconstituted. The following sections describe some of the fundamental characteristics of the materials used and the physical properties of the created samples.

3.1.1. Sand

3.1.1.1. Grain Size Distribution

In order to build the analog sand sample, McMurray Formation tailing sand was used. This sand is a by-product of the extraction of bitumen from oil sand and has the closest grain size distribution and composition to in situ oil sand cores. Figure 3-1 shows the grain size distribution curves for the reconstituted samples as well as for in situ oil sand cores. The yellow curves in this figure are plotted based on the data from Rottenfusser et al. (1988), and represent the grain size domain of McMurray Formation rich oil sand. The gray and red curves show the results of sieve and laser analyses on the Athabasca oil sand core respectively (Delage et al., 2013). As can be seen in Figure 3-1, the reconstituted samples and in situ cores have nearly the same grain size distribution. Using Equation 3-1 and Equation 3-2, the coefficients of uniformity (C_u) and curvature (C_c) were calculated. The results show that the sand used is uniformly graded (Table 3-1).

$$C_u = \frac{D_{60}}{D_{10}} \quad \text{Equation 3-1}$$

$$C_c = \frac{D_{30}^2}{D_{10} \times D_{60}} \quad \text{Equation 3-2}$$

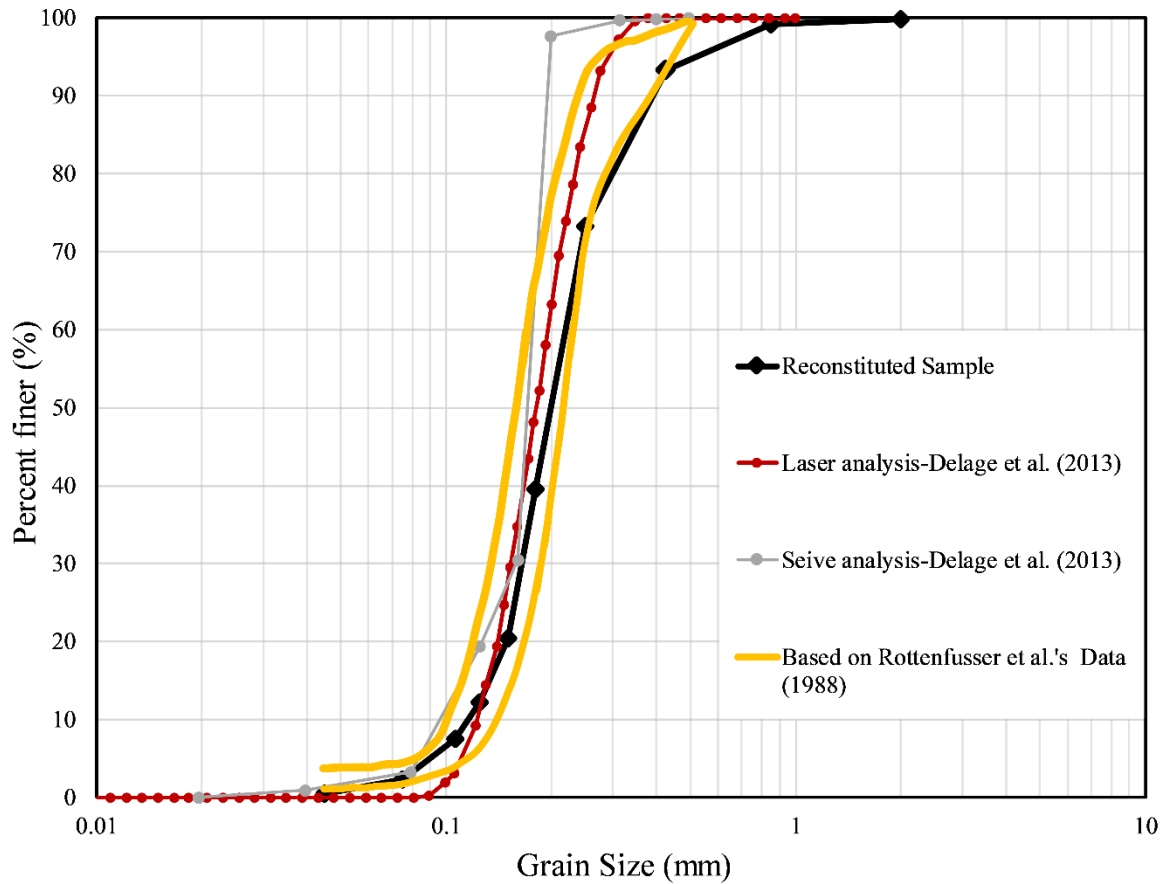


Figure 3-1 Grain size distribution curves of the Athabasca oil sand cores and reconstituted samples

Table 3-1 Sand grain size distribution properties

D ₁₀ (mm)	D ₃₀ (mm)	D ₅₀ (mm)	D ₆₀ (mm)	C _u	C _c	S.G.
0.125	0.160	0.200	0.220	1.76	0.93	2.65

3.1.1.2. Specific Gravity

Specific gravity is one of the important properties of the sand used, which needs to be determined in a laboratory. Specific gravity is defined as the ratio of an object's density to the density of water.

Considering the density of water to be equal to 1 gr/cm^3 , the value of sand's specific gravity is equal to the density of the sand grains.

Using the ASTM D-854, the procedure for measuring the density of sand grains starts with weighting an empty and air-dried clear-glass volumetric flask. After recording the weight of the flask, it was filled with water up to its graduation mark (ring), and was weighted again (Figure 3-2). The difference of these two weights (empty and full flask weights) is divided by the density of water to calculate the exact volume of the flask. In the next step, a specific amount of sand was put in the oven for 24 hours to dry completely. After measuring the weight of the dried sand, it was mixed with water inside the volumetric flask, and the mixture was boiled for 20 minutes to ensure that all the trapped air between the sand grains was released.

After cooling the sand-water mixture to room temperature, the flask was topped up with water to its graduation mark and was weighted again (Figure 3-2). By subtracting the weights of the empty flask and used sand from the total weight, and dividing the result by the density of water, the volume of water in the sand-water mixture was calculated. The difference between the volume of the water when it alone filled the flask and when it was mixed with sand gives the exact volume of the sand grains. Finally, by dividing the weight of sand grains by their volume, the density of sand was calculated to be 2.65 gr/cm^3 .



Figure 3-2 Volumetric flask filled with water (left) and sand-water mixture (right)

3.1.1.3. Porosity of Sand Specimen

In order to determine the porosity of the reconstituted samples, their dry density (ρ_d) was first evaluated. To compute ρ_d , the volume of the reconstituted samples and the amount of sand that had been used to create them were measured. Then, using Equation 3-3 and Equation 3-4, their porosity values were calculated.

$$\rho_d = \frac{G_s \gamma_w}{1 + e} \quad \text{Equation 3-3}$$

$$n = \frac{e}{1 + e} \quad \text{Equation 3-4}$$

where G_s is specific gravity, γ_w is the water unit weight, e is the void ratio, and n is the porosity.

As can be seen in **Error! Reference source not found.**, the average porosity value of the reconstituted oil-free specimens (ROS) in this study is similar to the other reconstituted sand samples and in situ oil sand cores that have been reported by other researchers.

Table 3-2 Porosity of the Athabasca oil sand cores and reconstituted samples

Reconstituted Samples	Oldakowski-Reconstituted (1994)	Oldakowski-in situ cores (1994)	Touhidi-Baghini - Reconstituted (1 st mix) (1998)	Touhidi-Baghini - Reconstituted (2 nd mix) (1998)	Touhidi-Baghini - Reconstituted (3 rd mix) (1998)	Touhidi-Baghini - in situ cores (1998)
ROS1 = 38						
ROS2 = 37						
ROS3 = 36	Max = 39	Max = 39	Max = 39	Max = 41	Max = 37	Max = 35
ROS4 = 36						
ROS5 = 36	Min = 36	Min = 35	Min = 34	Min = 38	Min = 32	Min = 33
ROS6 = 35						
ROS7 = 36						

3.1.2. Mud

3.1.2.1. Grain Size Distribution

Considering the IHS mud layer composition, which is mainly silt with a minor amount of very fine-grained sand and clay, a mixture of silt [Sil Industrial Minerals Flour 325 ®] and clay was used to make the mud samples. The silt flour used is mainly composed of quartz and has a particle size distribution shown in Figure 3-3. It can be seen that the Sil Industrial Minerals Flour 325 contained a small amount of fine-grained sand which made it a close substitute for McMurray Formation silt.

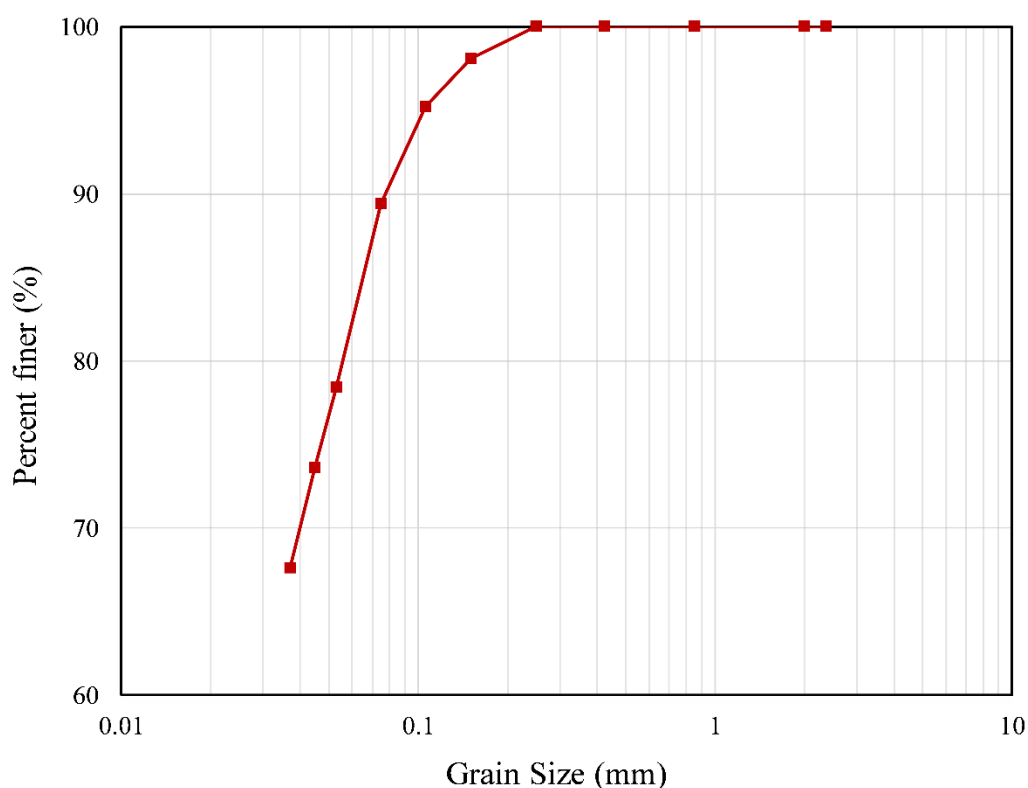


Figure 3-3 grain size distribution curve of silt (Sil Flour 325 ®)

3.1.2.2. Silt-Clay Mixture Ratio

Sirro (2002), in his analysis of McMurray Formation grain size distribution patterns, declared that the clay component of IHS mud layers is composed predominantly of kaolinite which constitutes

approximately 10% of the mud layer's total mass. The other 90% is composed of silt with a minor amount of sand. Therefore, in this study, to prepare the mud mixture, silt (Sil Industrial Minerals Flour 325 ®) and clay (kaolinite) were blended in a 9 to 1 mass ratio.

3.1.2.3. *Specific Gravity of Silt and Clay*

Following the same procedure that was explained in section 3.1.1.2, the specific gravity of the silt and clay flours were measure in the laboratory (Figure 3-4). The results showed that the values of specific gravity for silt and clay are equal to 2.68 and 2.67 respectively. Therefore, using the weighted average, the specific gravity of the mud mixture is equal to 2.68.



Figure 3-4 Volumetric flask filled with silt-water mixture (left) and clay-water mixture (right)

3.1.2.4. *Porosity of Mud Specimen*

Following the same procedure described in section 3.1.1.3, the porosity of reconstituted mud samples was calculated. It should also be noted that the porosity value of all analog mud samples was assumed to be the same because they were made from the same patch of slurry and their reconstitution process was identical.

In order to determine the dry density of a specimen, its volume and dry weight are needed. The process of measuring dry weight for the sand and mud samples was dissimilar since these samples were reconstituted differently. For sand samples, the dry weight was calculated using the initial and remaining amount of sand in the sand boiling bucket, whereas for mud samples it was measured by oven drying (for 48 hours) a water-saturated sample and determining its final weight. The methodologies used to create analog sand and mud samples are discussed in more detail in sections 3.2.1 and 3.2.2.

Using the described method, the initial porosity value for the reconstituted analog mud samples was calculated to be 45%. The consolidation test results showed that the pre-shear porosity value for mud samples could be as low as 33% when they are subjected to high effective confining stresses. Likewise, the results of neutron-logs in the Athabasca Wabiskaw-McMurray succession revealed 36% to 45% porosity range for the mud layers of IHS, which is very close to that obtained for reconstituted mud specimens in this study (Hein & Cotterill, 2006).

3.1.3. IHS

3.1.3.1. *Sample Configuration*

As explained in section 2.4.3, the focus of this research is on sand-dominated IHS because of its significant bitumen content and high reservoir potentials. In this class of IHS, sand layers comprise more than 85% of the lithosome; moreover, the dip angle of sand and mud layers varies from 4 to 22 degrees. As explained in chapter 2 the sand-mud contact angle of inclination is not constant at different locations within the McMurray Formation. However, the dip angle of 10 degrees for sand and mud layers could represent a high percentage of sand-dominated IHS lithosomes in the McMurray Formation (Bechtel et al. , 1994; Strobl et al., 1997; Hassanpour, 2009; Jablonski, 2012).

Therefore, considering the internal architecture of sand-dominated IHS, and also with a view to making the analog IHS samples similar, the following configuration was applied to all reconstituted specimens (Table 3-3).

Table 3-3 IHS samples' configuration

Type of IHS	Sand Content (%)	Mud Content (%)	Number of Mud Layers	Height (mm)	Diameter (mm)	Sand–Mud Contact Angle of Inclination
Sand-dominated	88	12	3	127	63.5	10

In addition, to create analog bioturbated samples, 10% of the mud layers' cross-section areas were penetrated to accommodate the appropriate amount of bioturbation index. More details on the reconstitution of bioturbated samples can be found in section 3.2.4.

3.1.3.2. Grain Size Distribution and Density

Unlike the sand and mud samples, the density and grain size distribution are not constant along the length of an IHS specimen. As explained later in this chapter, analog sand and mud samples were used to create the IHS specimens. Therefore, the grain size distribution and density of IHS constituent layers are identical to the sand and mud samples which were used in the reconstitution process.

3.1.3.3. Average Porosity of IHS Specimen

Porosity is one of the factors that has a significant influence on both the geomechanical properties and the hydraulic behavior of a sample. However, assigning a single value to the porosity of an IHS specimen is very complicated because the initial porosity of sand and mud layers are very different. Furthermore, the value of such a difference might change during the consolidation process. For this study, the volumetric average between the porosity values of the constituent sand and mud layers was adopted to describe the porosity of an IHS sample. As explained in section 3.1.3.1, sand and mud layers form 88% and 12% of any IHS sample, respectively. Consequently, the porosity of IHS samples can be computed using the porosity of sand and mud samples which were used to create them (Table 3-4).

Table 3-4 IHS samples' initial porosity

IHS 1	IHS 2	IHS 3	IHS 4
37%	37%	36%	37%

The minimal discrepancy that was observed in the IHS samples' porosity values is due to the difference in the initial porosity of used sand samples.

3.2. Development of Experimental Protocol to Reconstitute Analog IHS

As explained in section 2.4.1.1, there are many problems associated with using in situ IHS specimens (such as having too many changeable parameters and a high degree of fabric disturbance) which make them unsuitable for any kinds of experimental study. Therefore, the development of a specialized protocol to reconstitute analog IHS is necessary for any laboratory studies on this type of lithology. This section frames the overall structure of such protocols (Figure 3-5), and presents all of the related infrastructure and processes required to reconstitute analog sand, mud, and IHS specimens.

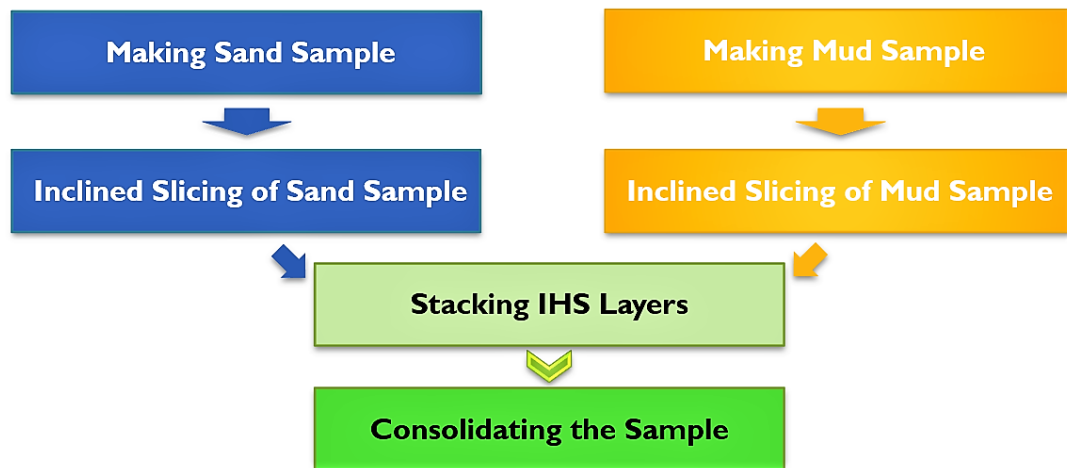


Figure 3-5 Analog IHS reconstitution flowchart

The developed methodology can be used to reconstitute all types of IHS in any desired sizes of samples. Nevertheless, considering the focus of this research and the physical properties of the tests' setup, only sand-dominated IHS of 63.5-mm diameter by 127-mm height were reconstituted

with the exclusion of one small size IHS sample (38.1-mm diameter by 76.2-mm height) which was built to confirm the practicality of the suggested method.

3.2.1. Sand Specimen Preparation Method

3.2.1.1. *Wet Tamping and Vibration*

There are several techniques available to construct reconstituted sand samples, such as dry and moist tamping, water pluviation, slurry deposition, and wet vibration (Kuerbis & Vaid, 1988; Vaid & Negussey, 1984; Touhidi-Baghini, 1998). Each of these methods produces samples with different density values and levels of homogeneity. In this study, in order to replicate the in situ density and porosity of oil sand specimens, a modified combination of moist tamping and wet vibration methods was used. This improved new technique helped to create more homogeneous specimens with a higher degree of initial saturation.

The main procedure for reconstituting samples started by boiling the dry sand for 30 minutes in de-aired distilled water to fully saturate the sand and clear out any impurities that might have been mixed with the sand grains. This step also helped to make the sand grains more water wet. After cooling down the sand to room temperature, the wet sand was poured into a sand packing assembly (Figure 3-6) which was mounted on a vibrating table. Filling the cylindrical former was done gradually and in many soil increments using a scoop. In each increment, the frequency of the vibrating table was adjusted to avoid excessive liquefaction of the sand, and in the meantime, the cylindrical former's wall was tapped gently using a hammer. After filling and closing the former, the sample was flushed with the de-aired water to displace any trapped air and maximize saturation.

3.2.1.2. *Sand Packing Assembly*

As stated in section 3.2.1.1, to make the analog sand samples, a sand packing assembly was engineered (Figure 3-6). This set up has four major components: i) top and bottom pedestals (end caps), ii) middle cylindrical former, iii) four long bolts and nuts, and iv) two porous disks. Both

end caps have two distinct drainage ports with separate valves. These drainage lines help to empty out any excess water on the soil's surface while filling the former. They also can be used to flush the sample after closing and sealing the sand packing assembly.

The pedestals are attached to the former using the bolts and nuts. Furthermore, each endcap is grooved on its side, and two vacuum greased O-rings circle each for sealing purposes. The surface of the pedestal is also grooved for homogeneous distribution of water during flushing of the specimens. In this setup, the porous disks were immediately placed at the bottom and top of the sample. It should also be noted that before using the porous disks, they were fully saturated by boiling in de-aired distilled water for 30 minutes and cooled to room temperature.



Figure 3-6 Sand packing assembly

3.2.1.3. Freezing, Extruding, and Trimming

After flushing the sample, the whole assembly was placed in a container full of dry ice for 30 to 45 minutes to freeze the sand specimens (Figure 3-7-a). An INSTRON[®] load frame was then used to extrude the frozen water-saturated sand sample (Figure 3-7-b). At that point, the sample was trimmed to the desired size inside a walk-in freezer using a masonry saw. It was then wrapped with plastic stretch wrap and stored in the freezer (Figure 3-7-c).

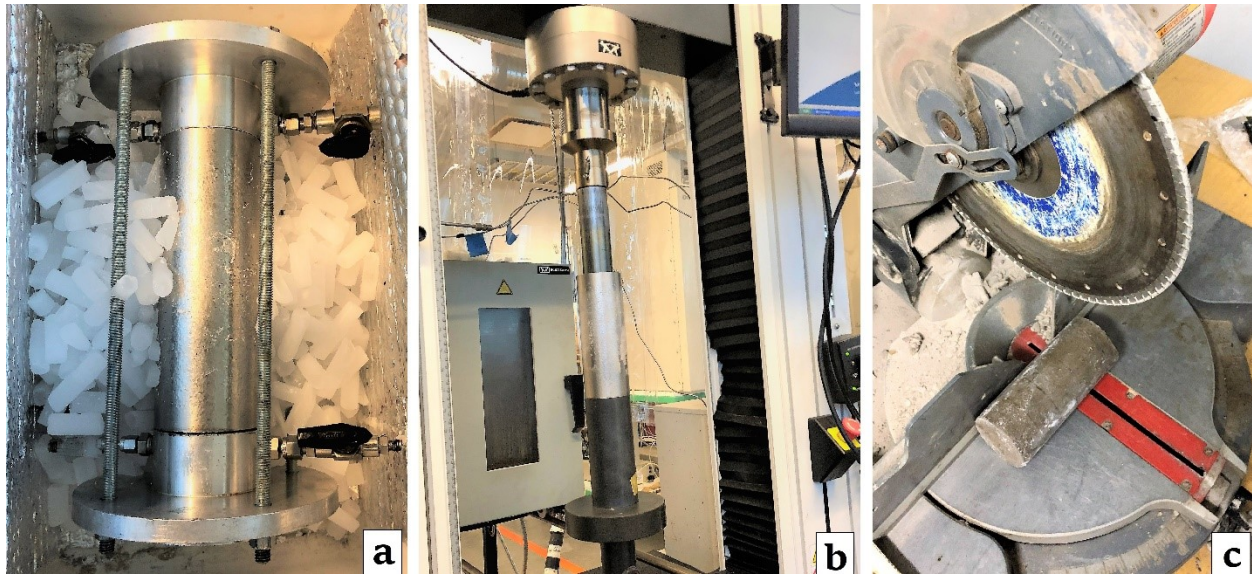


Figure 3-7 Freezing sand packing assembly (a), Extruding frozen sample using INSTRON[®] (b), Frozen sand sample (c)

3.2.1.4. *Mounting in the Triaxial Cell*

Positioning a sand sample inside the triaxial cell and attaching the internal sensors to the specimen is a delicate and lengthy procedure. Therefore, to minimize the disturbance on the samples during this process, the base of the cell was brought into the walk-in freezer, and the whole operation was performed inside the freezer.

The process started by placing a water-saturated porous disk on the base of the cell. Afterward, a filter paper, that was previously cut and saturated, was gently placed across the porous disk from its side. Then, a 3 millimeters thick Viton[®] membrane, trimmed to the appropriate size, was placed over the bottom platen of the cell. At that point, the frozen sand sample was taken out of the plastic stretch wrap and pushed into the membrane. After that, another water-saturated filter paper and porous disk were placed immediately on top of the sample. Finally, the top cap was pushed into the membrane and placed on top of the porous disk.

In order to secure the sample inside the cell and seal it inside the Viton[®] membrane, two hose clamps were used at the top and bottom of the sample where the membrane attached to the platens

(Figure 3-8). In order to avoid membrane damage during the tightening of the hose clamps, two Viton[®] rubber bands were used underneath the clamps. It should also be noted that the platens were grooved with an O-ring to help the sealing process.

In addition, before bringing the cell into the walk-in freezer, all of its flow lines needed to be saturated with de-aired distilled water. This step minimized the transference of any air trapped in the lines into the sample itself. Moreover, the channels for internal sensors needed to be checked before each test because after closing the cell and filling it with confining fluid, there was no way to fix those connections without losing the sample and dismantling the cell.

In the end, as displayed in Figure 3-8, the axial displacement and radial extension sensors were installed on the sample. More details on instrumentation inside the triaxial cell can be found in section 3.4.1.5.



Figure 3-8 Preparation of analog sand sample for hydro-mechanical testing

3.2.2. Mud Specimen Preparation Method

3.2.2.1. *Slurry Consolidation*

The first step in making the mud sample was to mix specific amounts of silt and clay powders using the mixture ratio which was explained in section 3.1.2.2. As can be seen in Figure 3-9-a, a lift-stand professional mixer was used to mix this combination for ten minutes. Afterward, the slurry molding method was followed. This method is an improved version of what was called the “slurry consolidation approach” by Wang et al. (2011). In this modified method of creating a uniform mud slurry, a specific amount of water (1.5 times of mixture’s liquid limit) was added to the silt-kaolinite blend, then mixed thoroughly for 15 minutes (Figure 3-9-b). It is worth noting that the slurry was mixed slowly in order to minimize the air entrapment during the mixing process. In the end, the slurry was wrapped with plastic stretch wrap, and stored in the moisture room for 24 hours. This step, which is known as a soaking stage, assures the full absorption of water by the mud mixture (Figure 3-9-c).



Figure 3-9 Silt and kaolinite mixture (a), Silt-kaolinite slurry (b), Soaking stage (c)

3.2.2.2. *Mud Mold Preparation*

In order to build 63.5-mm diameter by 127-mm height mud samples, a cylindrical former (mold) was needed. After trying different methods, a beverage can having the exact required internal dimensions was selected as a mold to make the mud samples. In order to prepare this mold, the beverage can was cleaned and its stay-tab lid was removed using a Dremel rotary cutter (Figure 3-10). Finally, the cut surface was smoothed using a Dremel rotary grinding stone and grit finishing set.



Figure 3-10 Mud samples' mold preparation using a Dremel rotary cutter

3.2.2.3. *Freezing and Trimming*

The next step in the reconstitution process of mud samples was filling molds mounted on a vibrating table (Figure 3-11-a). It should be noted that, before the slurry was poured into the molds,

it was mixed for another 15 minutes to ensure the consistency of the blend. Similar to the process described in section 3.2.1.1, filling the mold was carried out gradually and in many soil increments. In each increment, the frequency of the vibrating table was adjusted to avoid air entrapment. After filling and closing all the molds using plastic stretch wrap, the samples were placed in the freezer (Figure 3-11-b).

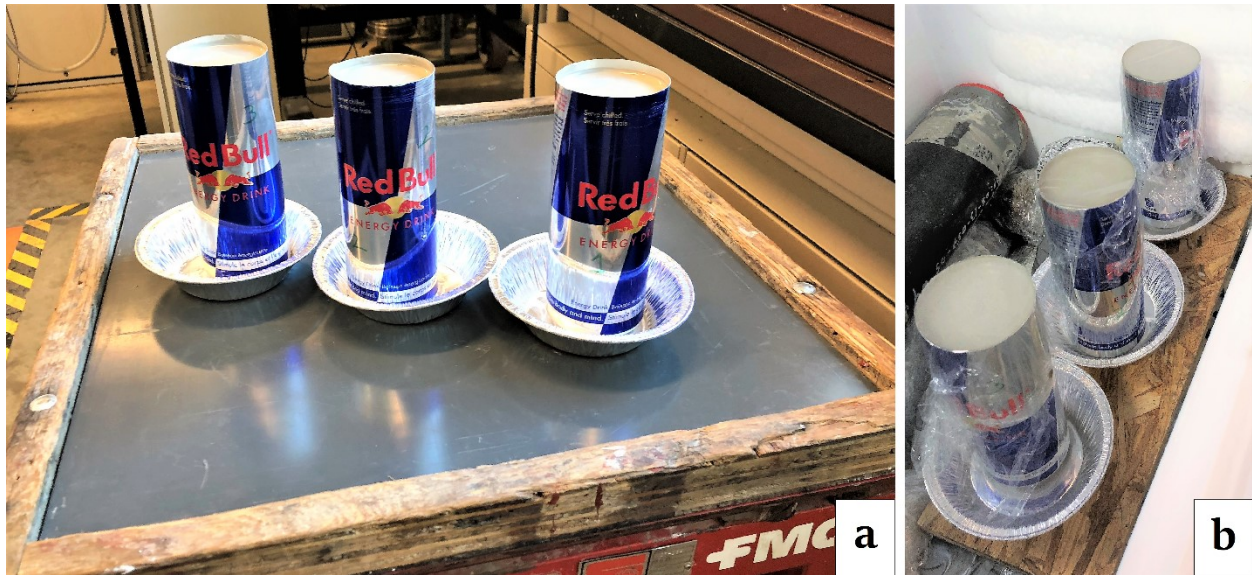


Figure 3-11 Filling the mud molds on the vibrating table (a) Mud samples inside the freezer (b)

After freezing, a snap-blade knife was used to open the mold and remove the sample (Figure 3-12-a). When the samples were taken out, they were wrapped with plastic stretch wrap and placed in a container full of dry ice for half an hour. At that point, they were trimmed to the desired size inside a walk-in freezer using a masonry saw, wrapped again with plastic stretch wrap, and stored in the freezer (Figure 3-12-b). The use of beverage cans as mud molds had several benefits such as i) convenience in removing them from the samples, and ii) provoking minimal sample disturbance during the reconstitution process.



Figure 3-12 Cutting the mold using a cutter (a), Trimming a frozen mud sample using a masonry saw (b)

3.2.2.4. *Mounting in the Triaxial Cell*

The installation of a mud sample and associated internal measuring devices in the triaxial cell was performed following the same procedure explained in section 3.2.1.4.

3.2.3. *Inclined Slicing Techniques for Sand and Mud Specimen*

In order to build an IHS specimen, the reconstituted sand and mud samples needed to be cut into thin inclined slices. To put this aim into practice, specific procedures were designed depending on the samples' size, material, and condition.

3.2.3.1. Using 3-D Printed Rock

In order to cut the frozen, water-saturated sand samples into thin slices at a certain angle, a masonry saw with a gauged rotary table was used inside a walk-in freezer. Also, several sample holders with specific angles were built. The angles of the sample holders were selected based on the range of sand-mud contact angle of inclination in the McMurray Formation IHS. After preparing the required equipment, several 3-D printed sandstones were cut to test the feasibility and accuracy of the developed method (Figure 3-13 and Figure 3-14). The results were quite satisfactory, so the same procedure was applied to the frozen sand samples (Figure 3-15-a). After cutting each slice, it was wrapped, placed in dry ice, and stored in the freezer (Figure 3-15-b).



Figure 3-13 Masonry saw with a gauged rotary table inside the walk-in freezer

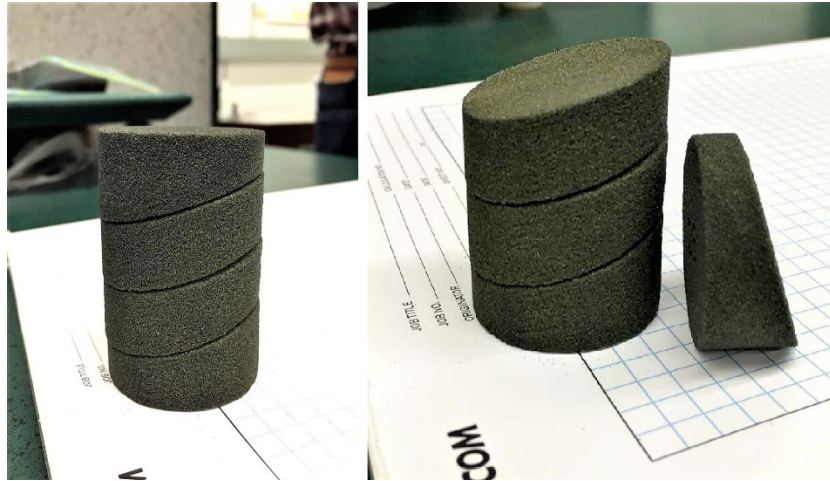


Figure 3-14 Sliced 3-D printed sandstone sample



Figure 3-15 Sliced analog sand sample (a), Wrapped sand slices (b)

3.2.3.2. *Designing a Cutter Box*

Unlike the analog sand specimen, using the masonry machine saw to slice the mud samples came with its own limitations, such as the size of the samples and the thickness of the mud slices. Due to the soft nature of the mud samples and the thinness of the mud slices, the masonry saw could not be used to slice the small-sized mud specimens. In fact, the heat generated during the cutting

process significantly disturbed the small size samples. Moreover, due to the thickness of the masonry saw blades, cutting slices thinner than 5 millimeters was practically impossible.

Therefore, special cutter boxes for use with a wire saw were designed to cut the mud samples at a wide range of angles. Similar to the process explained in the previous section, the range of angles in these cutter boxes was selected based on the observed dip angles in the McMurray IHS' sand and mud layers (Figure 3-16 Figure 3-17).

As stated earlier, during the feasibility stage of this study, an IHS sample of 38.1-mm diameter by 76.2-mm height was made to verify the accuracy of the proposed method. In order to prepare the mud layers for this small size IHS sample, the 38.1-mm diameter cutter box was used. After slicing the mud sample, the slices were wrapped and stored in the moisture room (Figure 3-18-b). When slicing the 63.5-mm diameter mud samples, it was found that both the bigger size cutter box and masonry saw can be utilized. It should also be noted that the dimensions of the existing slots on these cutter boxes were designed based on the proposed configuration of IHS samples, explained in section 3.1.3.1. Finally, it is worth noting that the slicing of mud samples using the cutter box was carried out at room temperature, whereas the masonry saw was used inside the walk-in freezer.

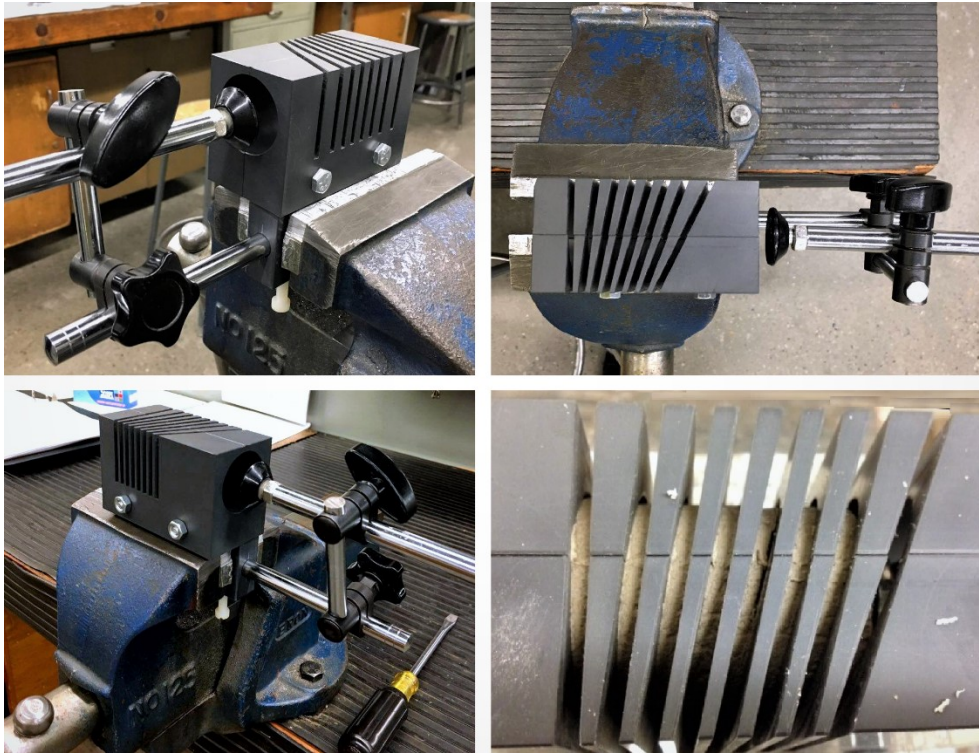


Figure 3-16 Mudstone cutter box (38.1 millimeters diameter)



Figure 3-17 Mudstone cutter box (63.5 millimeters diameter)

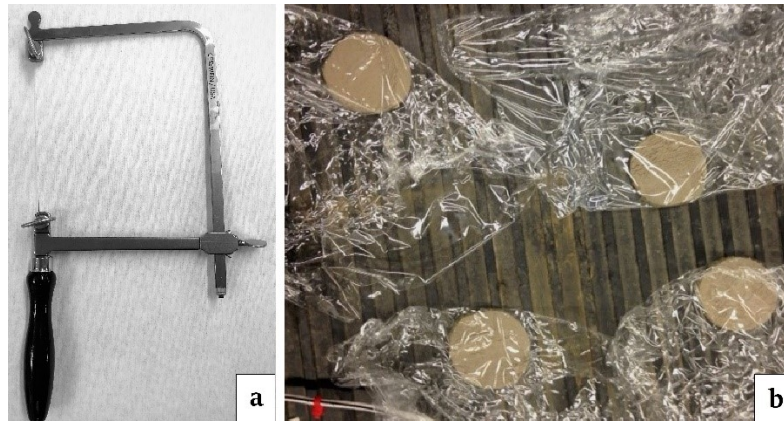


Figure 3-18 Wire saw (a), Mud slices (38.1 millimeters diameter) (b)

3.2.4. Creating Bioturbation in Mud Layers

As discussed in Chapter 2, one of the interesting aspects of the McMurray Formation IHS is that approximately 50% of the beds contain bioturbation. Such bioturbation primarily occurs in the mud layers of IHS, in the form of burrows of worms, clams, and shrimp which later were filled with sand from the adjacent layers (Figure 3-19) (Jablonski & Dalrymple, 2016).

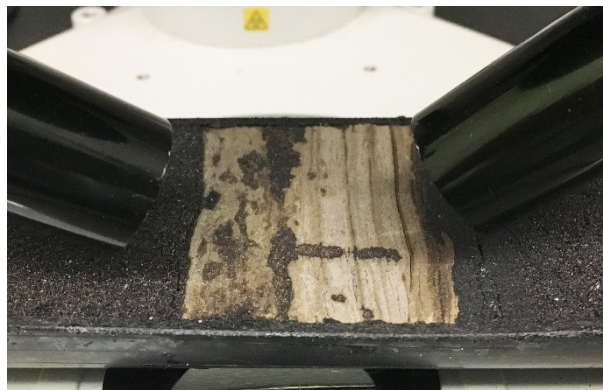


Figure 3-19 In situ IHS core with bioturbation

In order to experimentally investigate the hydro-mechanical effects of the bioturbation, we decided to create bioturbated mud layers and reconstitute a bioturbated IHS sample. Therefore, several holes were drilling in the frozen mud layers using a power drill with titanium drill bits (Figure 3-20). These holes were later filled with water-saturated McMurray sand, the same material used

to create analog sand samples (Figure 3-21). In this process, the diameter of drill bit was determined considering the IHS' bioturbation index, the cross-section area of the sample, and an estimation of the maximum practical number of holes that can be drilled in a thin mud layer without breaking or significantly disturbing it. It should also be noted that the whole procedure was performed inside the walk-in freezer to minimize the disturbance on the mud layers.

In this protocol, the bioturbated cross-section area and the number and diameter of the holes can be changed based on the IHS type and its degree of bioturbation. For the scope of this research, to accommodate the appropriate amount of bioturbation index in the sand-dominated IHS, the bioturbated cross-section area was 10% of the mud layers.



Figure 3-20 Penetrating a mud layer using a power drill



Figure 3-21 Sand filling of a penetrated mud layer

3.2.5. Stacking Different IHS layers

After sand and mud slices were prepared, they needed to be stacked to make an IHS sample. In this method, the number, inclination, and thickness of the sand and mud layers were selected based on the type of IHS. Throughout this study, the configuration described in Table 3-3 was used to build the IHS specimens.

The stacking process started by placing the sand and mud layers in a container full of dry ice for thirty minutes (Figure 3-22-a). This step helped to keep these layers undisturbed during the sample assembly. After taking the layers out of the container and unwrapping them, the first sand piece was placed on a flat, non-stick surface (Figure 3-22-b). Afterward, a fixed number of mud layers were placed between the sand layers up to a predetermined height (Figure 3-22-c). During this process, the sand and mud layers needed to be slightly rotated to become perfectly aligned and fit together (Figure 3-22-d).

After placing the top sand piece on the last mud layer, a spray bottle was used to cover the surface of the sample with tiny drops of water. Following that, the sample was left in the walk-in freezer for five minutes (Figure 3-22-e). At that point, it was taken off the flat surface and gently positioned inside the triaxial cell following the exact procedure described in section 3.2.1.4 (Figure

3-22-f). The implementation of this method has shown that spraying water gives an IHS sample the cohesion it needs (particularly at the interface regions of its layers) to be pushed into the Viton[®] membrane without requiring repositioning of its layers.

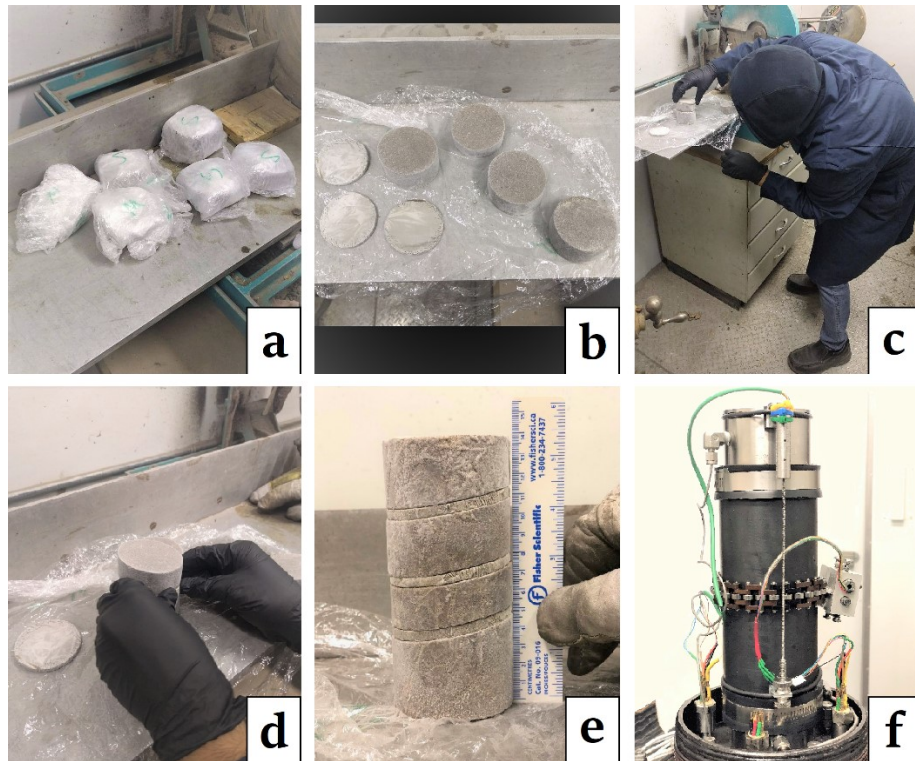


Figure 3-22 IHS layers stacking process

With regard to creating the bioturbated IHS sample, the same methodology can be implemented. The only difference is that the ordinary mud layers need to be substituted with bioturbated ones (Figure 3-23).



Figure 3-23 Staking IHS mud layer for bioturbated sample

3.2.6. Consolidation of Analog IHS

The final stage in reconstituting an analog IHS is consolidation. Consolidating an IHS sample leads to compaction of its layers and production of a seamlessly integrated specimen. Therefore, after placing the IHS sample inside the triaxial cell, the cell was filled with white silicone oil (Figure 3-24-a). It should be noted that the silicone oil container was put in the freezer overnight. Filling the cell with freezing cold silicone oil helped to keep the sample undisturbed during the time the cell was in transition between the walk-in freezer and the main lab, and also during the time when the cell's electric and hydraulic lines were being connected to the main setup. After attaching all these lines and positioning the cell inside the load frame's environmental chamber, the cell was pressurized to a predetermined value (Figure 3-24-b).

It is worth noting that before consolidating the sample under isotropic confining stress, it sat in the cell for saturation for 24 to 48 hours. Afterward, a pore pressure coefficient B-test was conducted. The saturation process helped to displace and dissolve any trapped air within the sample. More detail on the saturation and consolidation processes can be found in section 3.5.



Figure 3-24 Consolidation of analog IHS sample

3.3. Microscopic Comparative Study of IHS

One of the most important factors that assures the resemblance between analog and in situ IHS specimens is the mud-sand interface condition. This condition refers to the degree of integration and compaction between the sand and mud layers. Consequently, in order to investigate the mud-sand interface and examine the grain size and material changes within both analog and in situ IHS samples, a microscopic comparative study was conducted.

3.3.1. Analog IHS Specimens

With regard to the reconstituted analog IHS specimens, after finishing the consolidation process, the sample was taken out of the triaxial cell to perform the microscopic analysis. In order to do that, the chamber cylinder was taken off the triaxial cell and dry ice was used to freeze the sample (Figure 3-25). Then, using a snap-blade knife, the Viton[®] membrane was opened. Following that, the sample was wrapped and placed in the container full of dry ice for an hour. Then it was cut in half using a masonry saw (Figure 3-25). Finally, a high-resolution optical microscope was used to take pictures of the mud-sand interface region (Figure 3-26).

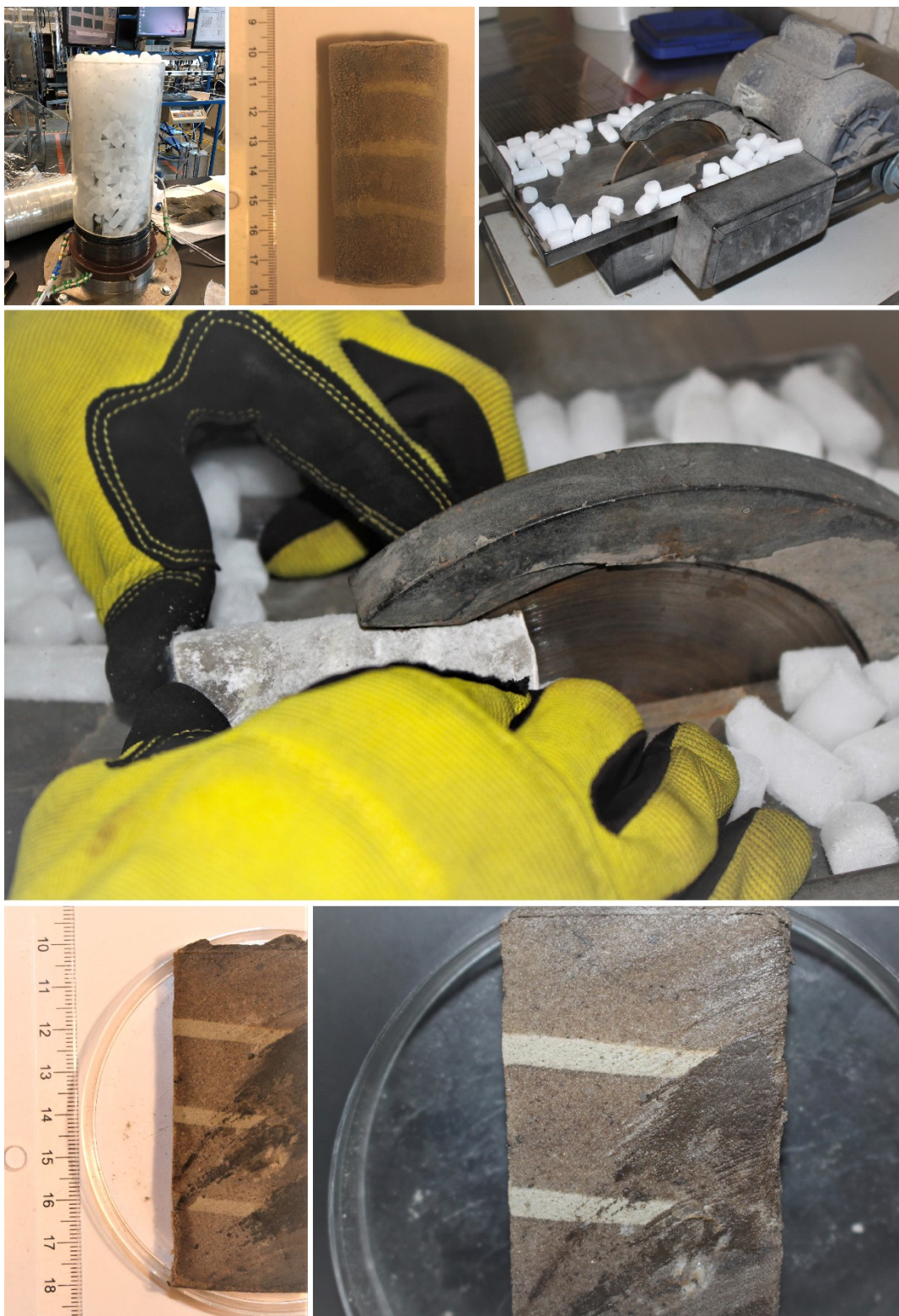


Figure 3-25 Half cutting frozen analog IHS sample

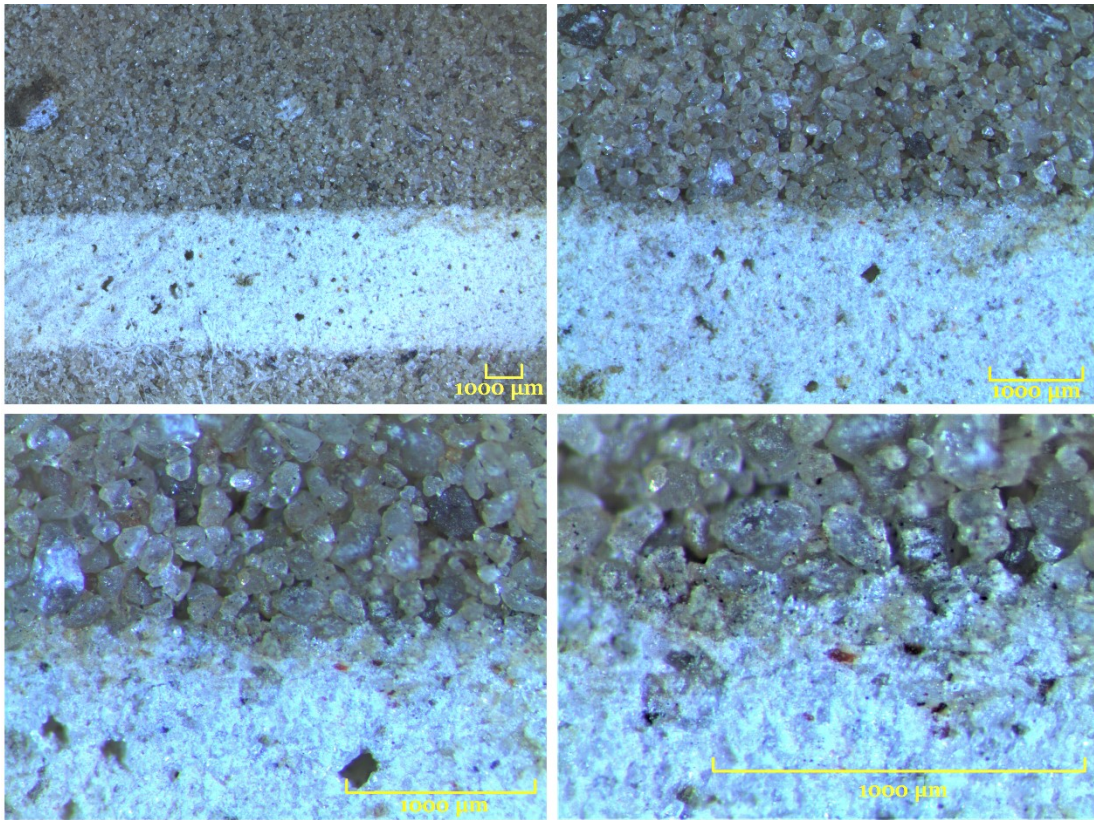


Figure 3-26 Microscopic images of the sand-silt interface in analog IHS sample

3.3.2. In situ IHS Cores

The same series of pictures was taken from the McMurray Formation bitumen saturated IHS cores (Figure 3-27). It should be noted that these cores were originally cut in half; in other words, no cutting job was performed on in situ IHS cores.

Comparing Figure 3-26 with Figure 3-28, it is clear that both layers' integration and grain size distribution are very similar in the analog and in situ IHS specimens.



Figure 3-27 McMurray Formation half-cut IHS cores

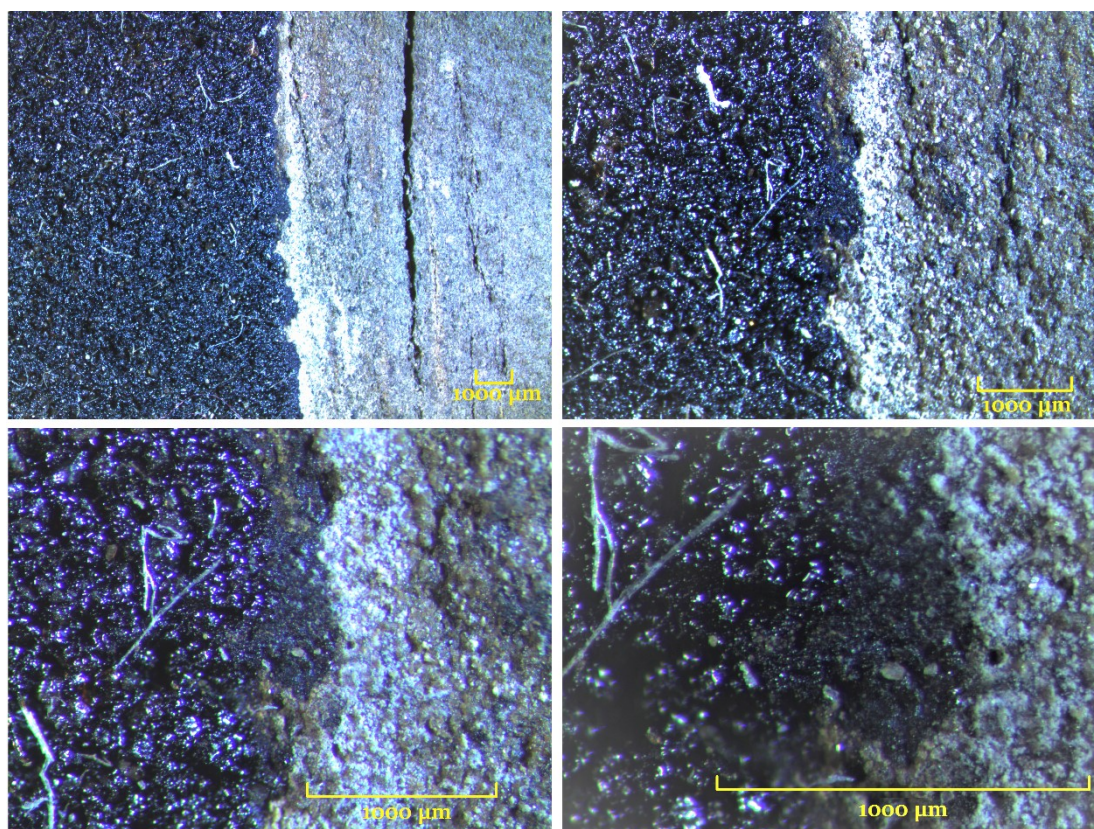


Figure 3-28 Microscopic images of the sand-silt interface in in situ IHS core

3.4. Experimental Setup for Hydro-geomechanical Testing

Throughout the course of this study, a triaxial test setup, which was mounted on a 400 kN INSTRON® load frame, was used to run the hydro-geomechanical testing. Figure 3-29 schematically shows the different apparatus and instrumentation utilized in this setup.

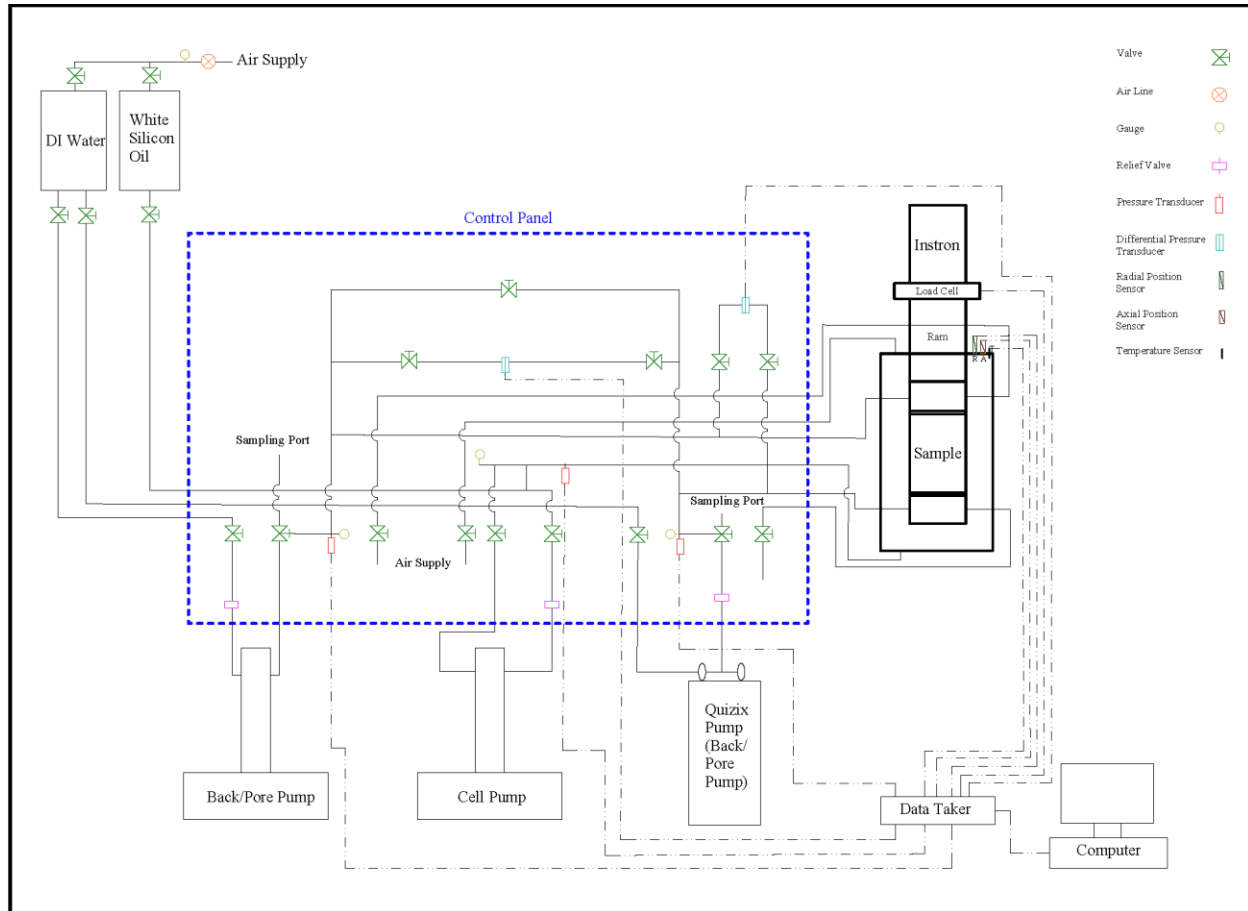


Figure 3-29 Schematic diagram of the triaxial system for permeability measurement

3.4.1. Description of Experimental Apparatus

As can be seen in Figure 3-29, the experimental setup is comprised of many different components. The following sections briefly describe the specifications of the major components of this system.

3.4.1.1. ISCO® Pumps (Back Pump and Cell Pump)

In the triaxial test setup, to control pore (back) pressure and confining cell pressure, two separate ISCO® pumps were used (Figure 3-30). Although the pump model for both of these pumps is the same (ISCO® 260D syringe pump), the back pump controls pore pressure by pumping water, while the cell pump adjusts the confining cell pressure by pumping white silicone oil. These pumps provide precise and predictable flow rate and pressure control for a wide range of flow rates and pressures. The operating pressure for these pumps ranges from 10 to 7500 psi, and their flow rate varies from 0.001 to 107 mL/min. It is also worth noting that the volume changes of a sample during a test can be measured by monitoring the reservoir's volume of the back pressure pump.

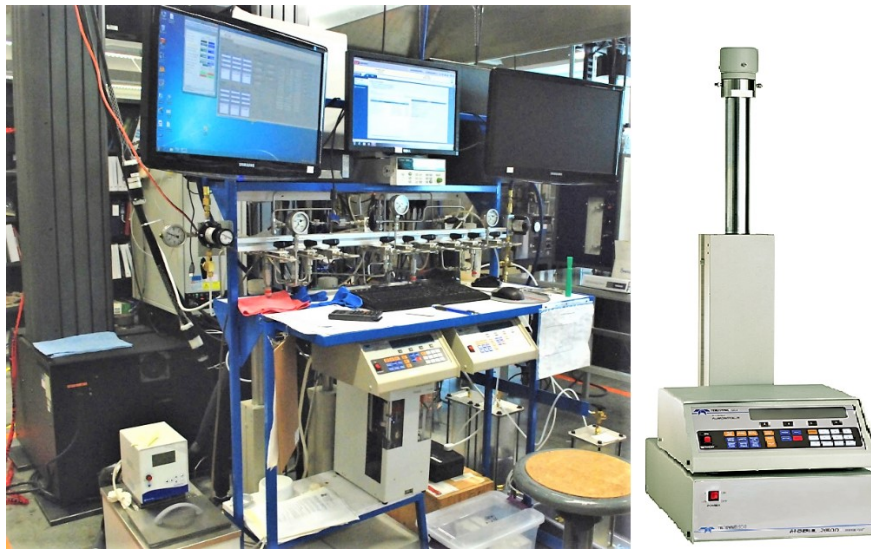


Figure 3-30 ISCO® 260D syringe pump (Teledyne ISCO®, 2017)

3.4.1.2. Quizix® Pump

In order to run the permeability tests in conjunction with other mechanical tests, a Quizix® pump was needed. This pump allowed control of the pore pressure at the top and bottom of the sample independently with two different pumps. In fact, the top of the sample was connected to the ISCO® (back) pump, and the bottom of the sample was connected to the Quizix® pump (Figure 3-29). Having two separate pumps made it possible to run the permeability tests at both constant flow

rate and constant differential pressure modes. It should also be noted that the Quizix[®] pump used is highly accurate in controlling both pressure and flow rate. Some of the specifications of this pump are presented in Table 3-5.

Table 3-5 Quizix[®]-QX 6000 (Chandler Engineering, 2017)

Model	Max Pressure	Max Flow Rate	Cylinder Stroke Volume	Min Flow Rate	
QX-6000	6,000 psi	50 mL/min	12.3 mL	0.001 mL/min	

3.4.1.3. INSTRON[®] Loading Frame with Environmental Chamber

In order to apply an axial load in triaxial shearing tests, an INSTRON[®] 5988 Floor Model testing system was utilized in the experimental setup (Figure 3-31). This loading frame has 400 kN load capacity, and a built-in load cell with a measurement accuracy of +/- 2 N. The speed of its ram ranges from 0.00005 to 1016 mm/min, and it has a 2050 mm vertical test space.

In addition, this setup has an environmental chamber built into it which provides a confined space for the triaxial cell. Because the sample's volume change and pore pressure are very sensitive to temperature changes, this heating (environmental) chamber was used to keep the temperature constant at a predetermined value throughout the tests. Finally, Bluehill[®] Universal software was used to control the testing system and collect the load frame data.



Figure 3-31 INSTRON® 5988 Floor Model testing system (Instron®, 2017)

3.4.1.4. *Triaxial Cell*

A triaxial cell with internal instrumentation capability was used in this testing program (Figure 3-32). The maximum operating pressure and temperature for this cell are 50 MPa and 60° celsius respectively. The material of construction for structural members of this cell is the quenched and tempered AISI 4140, which has a minimum yield stress of 110,000 psi.



Figure 3-32 Triaxial Cell

3.4.1.5. Instrumentation

3.4.1.5.1. Gauges and Sensors

The triaxial system has many gauges and sensors which were used to monitor and record the major parameters of the tests, including pore pressure, confining stress, sample volume change, temperature, flow rate, axial and radial displacements, axial load, and differential pressure.

Figure 3-29 illustrates the position of these sensors and gauges. As can be seen in this picture, all measuring devices were situated outside the triaxial cell except the thermocouple, axial LVDT, and radial displacement sensor, which were installed inside the cell. It is also worth noting that the three pumps used in this system have built-in pressure and flow rate sensors. This allows a researcher to cross-check the reading of external pressure transducers and flow meters.

3.4.1.5.2. Data Acquisition System

Agilent data logger and LabVIEW™ software were used to record the data and adjust the test parameters. This data acquisition system has 22 bits of resolution and ultra-low reading noise. Furthermore, it has a scan rate capacity of up to 250 channels per second. That being said, the logging rate was not constant throughout the tests; in other words, it was adjusted accordingly during different stages of the experiments.

3.5. Experimental Procedures

During a SAGD operation, an oil sand reservoir undergoes significant stress state changes which affect the reservoir's geomechanical and hydraulic properties. As explained in Chapter 2, the two principal stress paths followed by the reservoirs during a SAGD process are: i) decreasing mean effective stress due to the pore pressure increase, and ii) increasing mean effective stress and deviatoric stress due to the thermal expansion. In this study, these stress paths were experimentally

simulated by running isotropic unloading and triaxial shearing tests respectively. In addition, a series of permeability tests were conducted along all of these stress paths.

This section presents the experimental procedures adopted for the above-mentioned tests on reconstituted sand, mud, and IHS specimens. Saturation and consolidation procedures are also described in this module.

3.5.1. Saturation of Test Specimens by Back Pressure

Initial saturation of the test specimens used for triaxial testing was performed by applying an elevated back pressure to the pore fluid lines. As explained in section 3.2, during the samples' reconstitution process, some efforts were made to saturate the specimens. Therefore, applying back pressure can be considered as an additional step to assure a sample reaches its highest possible level of saturation.

Before starting the saturation process, the pore and confining fluid reservoirs were filled with deaired distilled water and white silicone oil respectively. Then, all the tubing was flushed with fluids to displace and remove any trapped air from the lines. At that point, the triaxial cell body was placed inside the environmental chamber, and the loading piston was brought in touch with the top cap. Finally, the pressure readings in all pumps were reset to zero before connecting the lines to the cell.

In order to saturate a sample using this method, immediately after assembling the triaxial cell, the cell pressure was increased to 250 kPa, and subsequently, the back pressure was raised to 50 kPa. Following that, both the confining stress and back pressure were incrementally increased to 3.2 MPa, and 3 MPa respectively, and the sample was left for 48 hours to saturate in this condition. It should also be noted that throughout this process, the effective confining stress on the samples was kept at 200 kPa. Maintaining such a low effective confining stress during the saturation process was assumed to have a negligible effect on the sand samples' volume.

Using an elevated back pressure to saturate a sample has several advantages such as: i) helping the trapped gas (air) inside the specimen and between the membrane and the specimen to dissolve in water more quickly and easily, ii) avoiding the air bubbles impediment in the pore fluid lines by eliminating any residual bubbles in the tubing, iii) enhancing the pore pressure response time, iv) facilitating the water imbibition by the specimen during a drained shear dilation by removing the risk of an airlock, and v) improving the reliability of permeability measurements (Touhidi-Baghini, 1998; Head & Epps, 2006).

3.5.2. B-test

After leaving the sample under back pressure of 3 MPa for 48 hours, the B-test needed to be carried out to assure the full saturation of the specimen. In order to do that, first, the pore pressure and confining stress values were recorded. Then the pore pressure pump was stopped. This step is equivalent to closing the pore fluid drainage valves. Afterward, using the cell pressure pump, the confining stress was increased to 5700 kPa in five consecutive increments of 500 kPa. At the end of each confining stress increment, the undrained pore pressure increase was measured. The ratio of this pore pressure increase to the confining stress increment is the B value (Equation 3-5) (Bishop & Henkel, 1962; ASTM International, 2016)

$$B = \frac{\Delta u}{\Delta \sigma_c} \quad \text{Equation 3-5}$$

where u is pore water pressure and σ_c is confining stress.

Getting constant and close to unity B values for at least three consecutive load increments confirmed the full saturation of the samples. In other words, the plot of B values versus back pressure should be flat with increasing back pressure for a saturated sample (Chaney et al., 1979).

It is also worth noting that during this experiment, each confining load increment proceeded when the pore pressure value for that step of the test was completely stabilized. The pore pressure

stabilization process normally takes between three to ten minutes depending on the type of sample being tested.

3.5.3. Isotropic Cyclic Consolidation Test

The isotropic cyclic consolidation test was performed on reconstituted samples to measure their bulk compressibility, and also to simulate the first component of a SAGD-induced stress path which is decreasing mean effective stress. During the cyclic consolidation tests, the effective confining stress ranged from 0.2 to 7 MPa, which covers the range of interest for a large number of SAGD projects. During this test, each sample went through two full cycles of loading and unloading. Then the volumetric strain changes were measured and plotted versus effective confining stresses. It should also be noted that the last unloading phase for each test was continued down to the effective isotropic stress in which the sample needed to be sheared.

Each of these cycles comprised several loading or unloading increments, and the volumetric strain and compressibility for each of these increments were computed using the following equations:

$$\varepsilon_v = \frac{\Delta V_c}{V_0} \quad \text{Equation 3-6}$$

$$C_b = \frac{\Delta \varepsilon_v}{\Delta \sigma'_3} \quad \text{Equation 3-7}$$

where ε_v is the volumetric strain, ΔV_c is the volume change due to consolidation, V_0 is the sample's initial volume, C_b is bulk compressibility, $\Delta \sigma'_3$ is an increment of effective confining stress, and $\Delta \varepsilon_v$ is corresponding volumetric strain due to $\Delta \sigma'_3$.

At the end of consolidation, the sample's length and cross-section area were corrected using the equations below:

$$L_c = L_0 \left(1 - \frac{1}{3} \frac{\Delta V_c}{V_0} \right) \quad \text{Equation 3-8}$$

$$A_c = \frac{V_0 - \Delta V_c}{L_c} \quad \text{Equation 3-9}$$

where L_0 is the initial length of the sample, L_c is the corrected length of the sample, A_c is the corrected cross-section area of the sample, ΔV_c is the volume change due to consolidation, and V_0 is the sample's initial volume.

As stated in section 3.4, during consolidation, the samples' volume changes were measured by monitoring the volume of the pore pressure pump's reservoir. In this regard, each step of consolidation (or unloading) was considered to be complete when the volume of the reservoir did not change over a long period of time; in other words, when no significant movement of the water took place. In addition, throughout this test, the pore pressure was kept constant at 3 MPa, and the effective stress was changed by altering the confining stress. Decreasing the effective confining stress by lowering the cell pressure is equivalent to the isotropic unloading process that happens within a reservoir due to the pore pressure increase in a SAGD operation.

3.5.4. Drained Triaxial Compression Test

In order to simulate the second component of the SAGD-induced stress path, which consists of increasing mean effective stress and deviatoric stress, several drained triaxial shear tests were conducted on the sand, mud, and IHS samples. In these tests, the specimens underwent compressive shear loading at three different effective confining stresses of 0.5, 1, and 3.5 MPa, after which their stress-strain behavior was examined. These effective stresses would represent reservoir depths of 22, 45, and 159 meters respectively if the average overburden unit weight is assumed to be 22 kN/m³. As explained in Chapter 2, the samples' strength is highly dependent on the effective confining stress in which it is being sheared. In fact, increasing effective confining

stress leads to a rise in shear strength. It should also be noted that in this study, the Mohr-Coulomb model was used as the failure criterion, represented by the following formula:

$$\sigma_1 = \sigma_3 \tan^2\left(45 + \frac{\varphi}{2}\right) + 2c \tan\left(45 + \frac{\varphi}{2}\right) \quad \text{Equation 3-10}$$

$$\tau_f = c + \sigma_n \tan \varphi$$

where σ_1 and σ_3 are principal stresses, τ_f is shear strength per unit area, c is cohesion, σ_n is the normal stress on the shear plane, and φ is the friction angle.

As stated before, in this testing program, the specimens were initially consolidated under an isotropic confining stress. Then, they were sheared in compression by increasing the axial load applied to them via an INSTRON® load frame. It is also worth mentioning that during the shearing process, the drainage paths were open to allow the samples to fail under full drainage conditions.

3.5.4.1. *Strain Rate during Shearing*

Two common methods to shear a sample in a triaxial cell are: i) strain-control shearing, and ii) stress-control shearing. In this study, the former approach was chosen to fail the samples. Since all the shearing tests were conducted in a drained condition, the rate of deformation (strain) was slow enough to allow any excess pore water pressure to dissipate at any time during the shearing (Bishop & Henkel, 1962).

Using the Manual of Soil Laboratory Testing (Head & Epps, 2006) the maximum rate of axial strain can be calculated using Equation 3-11 Equation 3-12. These equations are only valid for drained triaxial compression tests on specimens that do not have side drains.

$$t_f = 8.5t_{100} \quad \text{Equation 3-11}$$

$$v_{max} = \frac{\varepsilon_f L}{100t_f} \quad \text{Equation 3-12}$$

where t_f is the time to failure, ε_f is the strain at peak shear strength, L is the length of specimen, v_{max} is the maximum rate of axial displacement (maximum speed of INSTRON[®] ram), and t_{100} is the time of 100% consolidation, which is a function of the samples' permeability and can be derived from the consolidation curves.

It should also be noted that if the calculated t_f using Equation 3-11 is less than 120 minutes, the actual time to reach peak shear strength should not be less than two hours. Furthermore, for the first sample, the ε_f needs to be estimated based on the sample's type and condition; however, for the rest of the specimens of the same type, the ε_f value from the first test can be substituted into Equation 3-12.

3.5.5. Permeability Test

To study the absolute permeability of sand, mud, and IHS samples and their alteration during a SAGD operation, a series of permeability tests were conducted on them. Such tests were performed during the isotropic unloading and triaxial shearing of the specimens which respectively represent the two major stress paths followed by the reservoir during a SAGD operation.

During isotropic unloading, the test was stopped at different effective confining stresses to perform permeability tests. Similarly, shearing of the samples was paused at several axial strain levels, and the permeability tests were carried out in those rest intervals.

The permeability test started by closing the bypass valve that connects the top and bottom of the sample. Afterward, the Quizix[®] pump, which is known for its precise and pulse-free delivery of liquids, was utilized to deliver a constant flow rate through the sample while it was subjected to a controlled effective stress path. Then, the pressure difference between the top and bottom of the

sample was measured. Finally, Darcy's law (Equation 3-13) was used to calculate the absolute permeability of the specimen.

$$v = K \frac{\Delta H \rho g}{\eta L} \times 10^{-12}$$

Equation 3-13

$$v = ki \quad i = \frac{\Delta H}{L}$$

where i is the hydraulic gradient, ΔH is the total head difference, L is the flow length, k is the hydraulic conductivity, v is the discharge velocity, ρ is the fluid density, η is the dynamic viscosity of the fluid, g is acceleration due to gravity, and K is absolute permeability.

The pressure difference was measured using two differential pressure transducers (Figure 3-29). This value was also cross-checked with the subtraction of pressure readings by two separate pressure transducers installed on the fluid lines at both ends of the sample (Figure 3-29), and also with the deducting of the pressure readings from the ISCO® and Quizix® pumps.

It should be noted that, in each step, the permeability tests were conducted at three different flow rates depending on the type of sample. For sand samples, the permeability tests were run at 3, 5, and 7 ml/min. For mud specimens, they were conducted at 0.01, 0.02, and 0.03 ml/min. And finally, for IHS samples, flow rates of 0.2, 0.3, and 0.4 ml/min were used to perform these tests. Normally, the test at each flow rate continued until the differential pressure reached a steady state condition (fixed value) and maintained that condition for a significant amount of time.

In order to avoid fine-grained soil migration during the permeability tests, the direction of the flow was decided to be upward, and the tests were conducted at low flow rates. Another important criterion for selecting an appropriate flow rate was the amount of pressure difference it creates between both ends of the specimen. This was very important because excessive pressure difference (higher than 20% of the effective confining stress) could significantly disturb the sample's structure (ASTM International, 2006).

4. HYDRO-MECHANICAL TESTING ON SAND LAYER

4.1. Introduction

In order to investigate the geomechanical constitutive behavior of oil sand and its permeability evolution under SAGD-induced stress paths, a series of tests was performed on reconstituted oil-free sand specimens (ROs). Chapter 4 presents and analyzes the results of these experiments, which include B-test, isotropic cyclic consolidation test, drained triaxial compression test, and permeability test.

In addition, this chapter discusses the outcomes of previous experimental studies on oil sand to ensure the resemblance between ROs and in situ oil sand samples in terms of their geomechanical properties. It also investigates the applicability of former empirical permeability relationships.

4.2. B-test

Measuring the B value for a soil specimen is the most common method of determining its degree of saturation. Chaney et al. (1979) declared that if the calculated B value for three consecutive B tests on a sample was quite constant, it could safely be assumed that the sample is fully saturated.

Figure 4-1 shows the results of B-tests on three analog sand samples. As can be seen, the plots of undrained pore pressure increase versus isotropic confining stress increments are completely linear for all samples. This indicates that the B value is constant and independent of the magnitude of the back pressure. Therefore, according to the method suggested by Chaney et al. (1979), all sand samples are fully saturated.

The relationships between pore pressure (u) and isotropic confining stress (σ_c) for sand samples are also displayed on the graph, reconfirming a saturated value of B of unity.

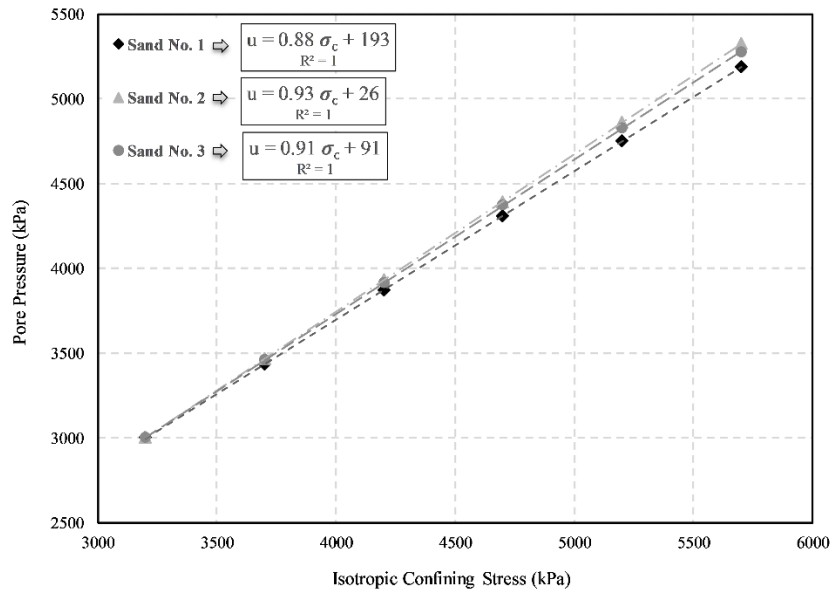


Figure 4-1 B-tests on analog sand samples

4.3. Isotropic Cyclic Consolidation Test

The isotropic cyclic consolidation test was performed on reconstituted sand samples in an attempt to measure the coefficient of bulk compressibility and to recompact the specimens before the drained shear tests.

As stated before, each specimen was saturated under an effective isotropic confining stress of 0.2 MPa with a pore pressure of 3 MPa. Afterward, the effective confining stress was cycled two times between 0.2 MPa and 7 MPa. For soils subjected exclusively to isotropic stress, the volume change is governed by effective stress rather than total stress. Figure 4-2 illustrates the bulk volume changes for ROS 2 and 3 with the effective confining stresses. Unfortunately, the test on ROS 1 did not yield satisfactory results due to a technical issue that occurred in the environmental chamber which led to significant temperature variations.

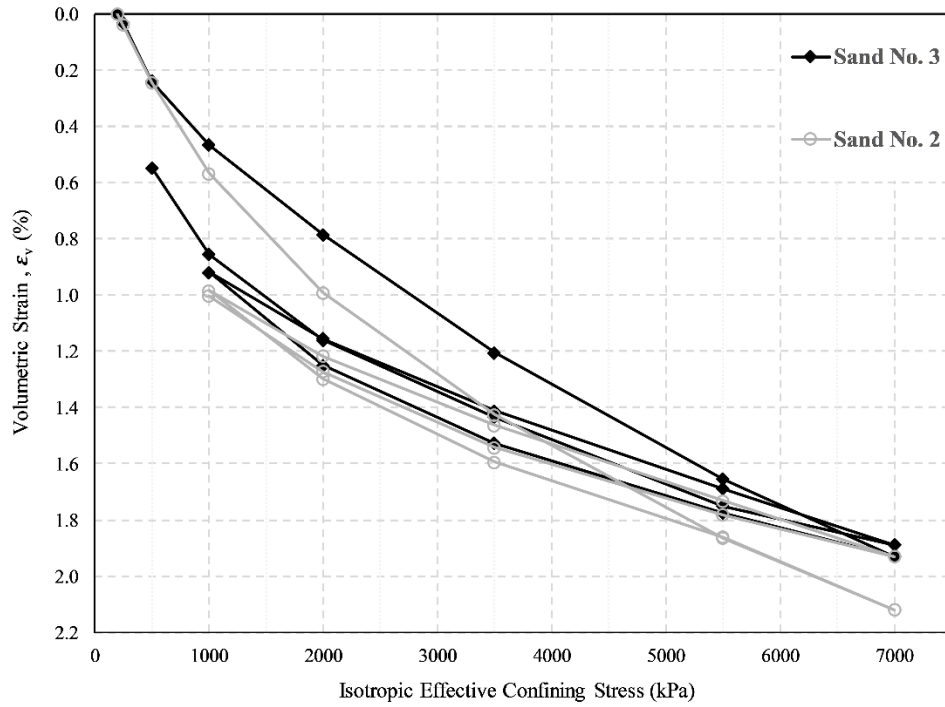


Figure 4-2 Bulk volume change of analog sand samples

The initial loading produced a significant amount of volume change as a result of initial grain rearrangement. Moreover, some small hysteresis loops can be observed in the consolidation curves because of the cycles of unloading and reloading.

4.3.1. Isotropic Bulk Compressibility

Figure 4-3 shows the variation of the coefficient of isotropic bulk compressibility (C_b) for ROSs. As shown in this figure, despite the observed hysteresis in consolidation curves, the computed compressibility values for each effective confining stress are very close.

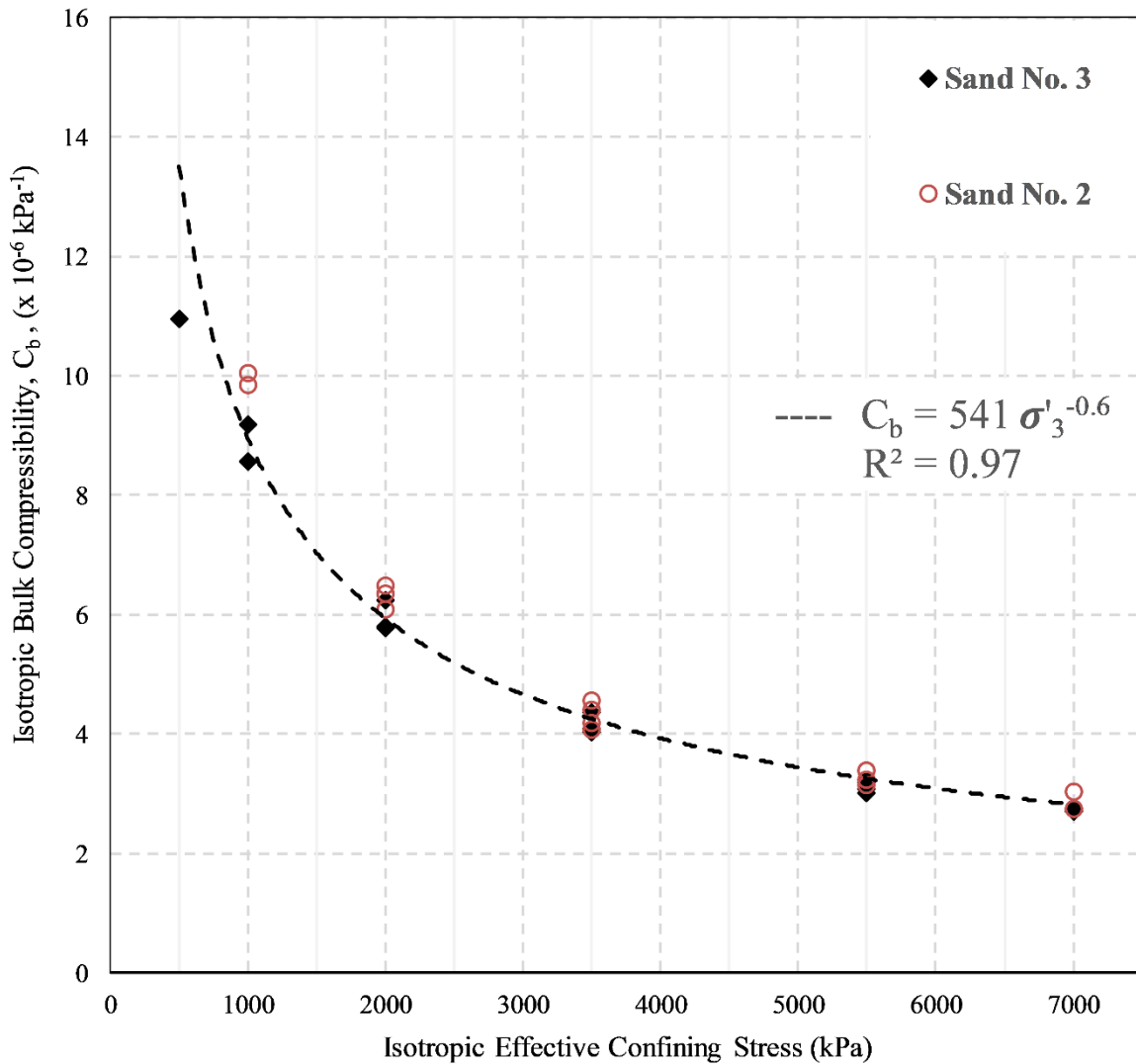


Figure 4-3 Coefficient of isotropic bulk compressibility of analog sand samples

4.3.1.1. Empirical Correlation for change in Bulk Compressibility

An analysis of the final results revealed that bulk compressibility is a strong function of effective confining stress, particularly at low stress levels (below 3 MPa). A power law function was established to capture the relationship between the compressibility and effective confining stress, which can be expressed as follows:

$$C_b = a\sigma_3'^b \quad \text{Equation 4-1}$$

where C_b is the coefficient of bulk compressibility ($\times 10^{-6} \text{ kPa}^{-1}$), σ_3' is the effective confining stress (kPa), and a and b are constants.

Using curve fitting techniques, the constants a and b can be determined for each test (and even for every single cycle of loading or unloading), but given the consistency of the constants for all tests, a single curve fit equation was developed. Figure 4-3 illustrates the power law curve fit for all data where the values of the constants a and b are 541 and -0.6 respectively.

Although this developed relationship can be used to estimate C_b based on effective confining stress levels, its applicability is limited to σ_m' ranging only from 0.2 MPa to 7 MPa. Therefore, extra caution needs to be exercised for any applications outside of this range.

4.4. Drained Triaxial Compression Test

The drained triaxial compression tests were conducted with effective confining stresses of 0.5, 1, and 3.5 MPa. A total of three tests were performed on analog sand samples. The results of these isotropically consolidated drained shear tests are plotted together in Figure 4-4. As can be seen in this figure, the samples' stress-strain behavior is strongly influenced by the confining stress. At all three confining stresses, semi-ductile failure was observed. Therefore, the deviatoric stress did not drop significantly after the peak shear strength was reached.

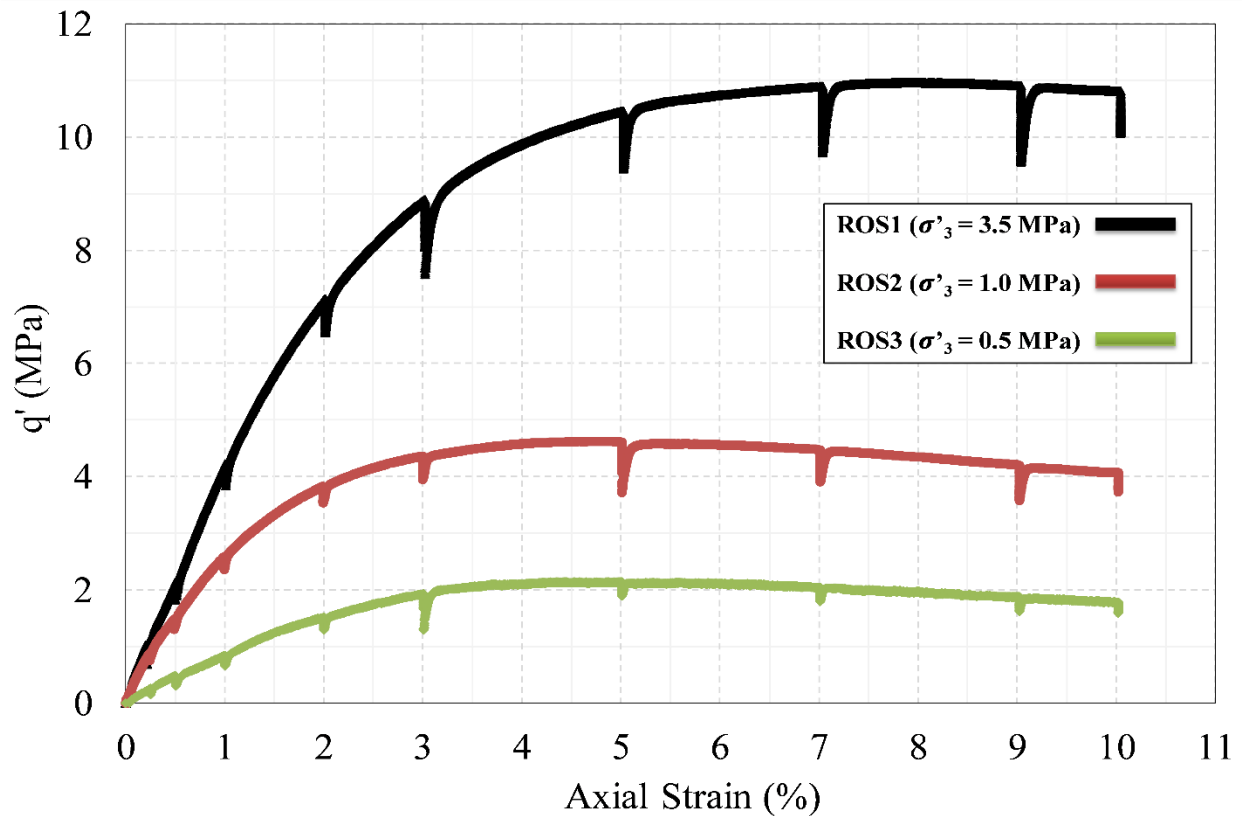


Figure 4-4 Isotropically consolidated drained triaxial compression tests on analog sand samples

4.4.1. Stress-Strain Behavior

4.4.1.1. Modulus of Elasticity

One of the most useful stiffness parameters in geomechanical studies is Young's modulus (E). Therefore, the value of Young's modulus was calculated for each specimen using its stress-strain curve and the average slope method (ASTM International, 2016). In this approach, the average slope of the linear portion of the stress-strain plot was computed by dividing the change in stress by the change in strain for that section of the plot.

Figure 4-5 shows Young's modulus of analog sand samples with effective confining stresses. As can be seen, the modulus of elasticity increases with an increase in effective confining stress, and its variation with σ_3' is nonlinear.

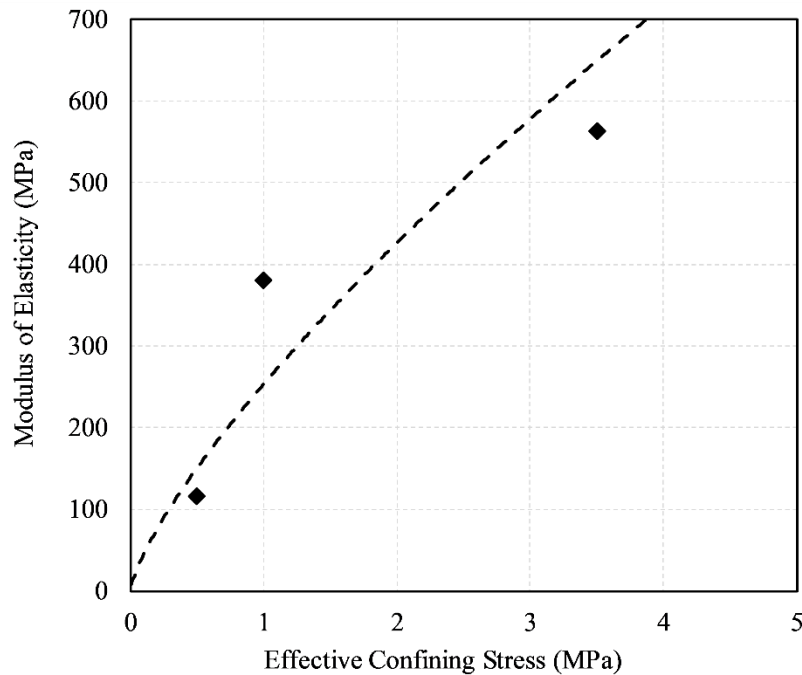


Figure 4-5 Variation of modulus of elasticity versus effective confining stress for analog sand samples

4.4.1.2. Volumetric Behavior during Shearing

Figure 4-6 illustrates the volumetric behavior during shearing for analog sand samples. It is clear from this graph that the dilative or contractive behavior of the sand specimens during shearing is predominantly controlled by the value of effective confining stress (σ_3'). In fact, all the tests displayed contraction to a certain level at the beginning of the shearing. Subsequently, different volume changes with an increase in axial strain depended on their confining stress. It was observed that under 3.5 MPa effective confining stress, contraction continued until 3% axial strain, then the sample dilated in shear. But in total, no significant volume changes occurred throughout the shearing in this test. On the other hand, for the samples under effective confining stresses of 1 and 0.5 MPa, after a short period of contraction at the beginning of the tests (which ended before the axial strain of 1%), both specimens dilated noticeably up to the end of shearing.

As stated before, all sand samples were isotropically consolidated resulting in a high pre-shear density, and consequently it was expected that volumetric dilation would occur during

compression shearing. Based on his research on oil sands, Scott (1992) declared that such behavior is due to the rolling and crushing of particles that occurs in the course of shearing. According to his theory, at low effective confining stresses, the sand grains can roll over each other during shearing, causing a volume expansion; at higher σ_3' values, they cannot overcome the confining stress to roll over each other, and inevitably will be broken by the shear force. As a result, these small broken particles will fill the voids inside the specimen which could not be filled before shearing. Consequently, volume contraction occurs in the sample and this influence on permeability is discussed subsequently.

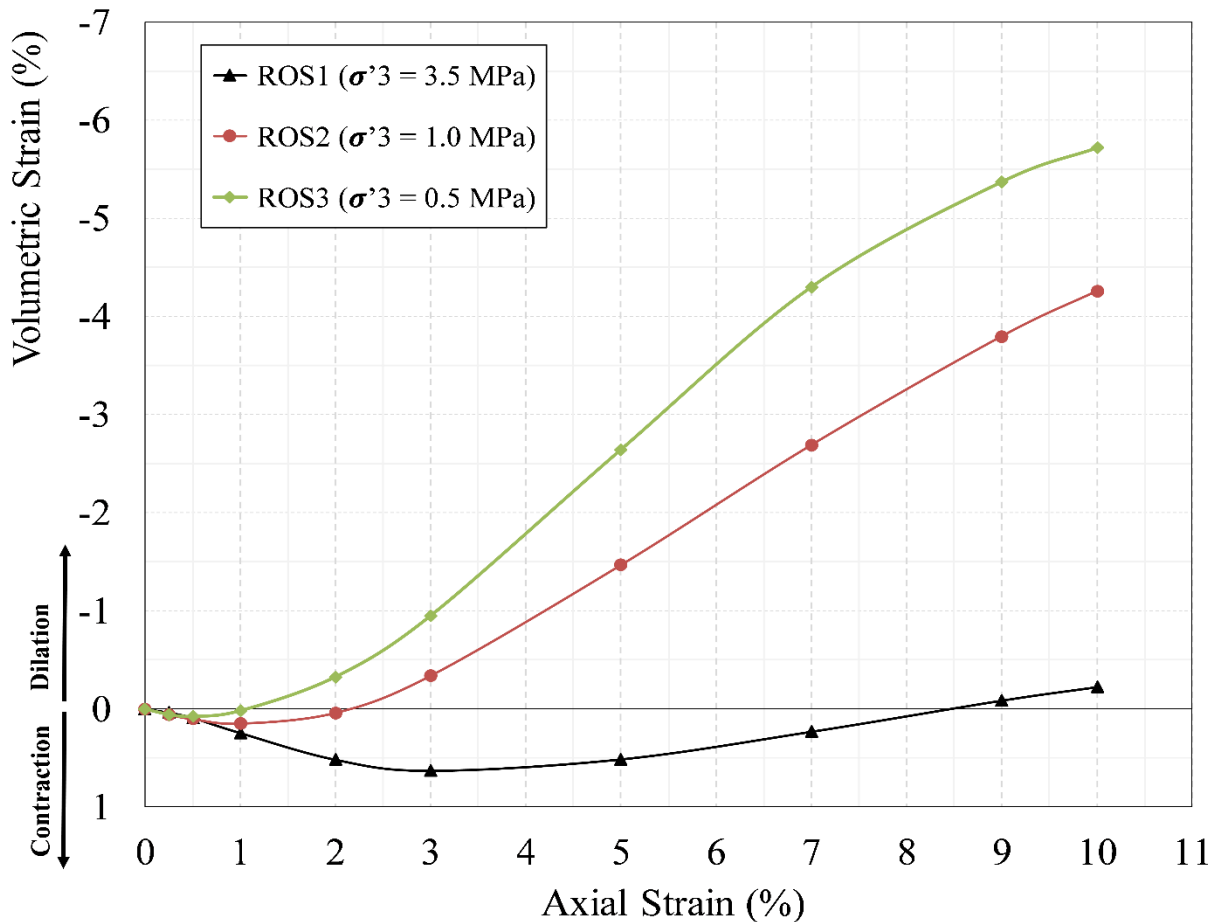


Figure 4-6 Volumetric behavior of analog sand samples during drained triaxial compression tests

4.4.1.3. Poisson's Ratio

Poisson's ratio, ν , is defined as the negative of the ratio of lateral strain to axial strain in a material. However, due to the dilatancy behavior in soil specimens, as well as nonlinearities in the axial and lateral stress-strain curves especially at low stress levels, measuring Poisson's ratio might not always be possible in soil testing. Consequently, in this study, Poisson's ratio was computed using a small axial strain of 0.25% and the corresponding volumetric strain before the dilatancy controls the sands' volumetric behavior. The expression used to calculate Poisson's ratio is as follows:

$$\nu = \frac{\varepsilon_a - \varepsilon_v}{2\varepsilon_a} \quad \text{Equation 4-2}$$

where ε_a is the axial strain, and ε_v is the volumetric strain.

As can be seen in Table 4-1, the calculated ν values for all sand samples are essentially the same.

4.4.1.4. Dilation Angle

Dilatancy is defined as the change in volume associated with shear distortion in a material. In order to characterize a dilatant material, its dilation angle (ψ) can be determined using the following expression:

$$\sin \psi = -\frac{d\varepsilon_v}{d\gamma} \quad \text{Equation 4-3}$$

where $d\varepsilon_v$ is the rate of plastic volumetric strain, and $d\gamma$ is the rate of plastic distortion.

This expression is only accurate for plane strain condition of simple shear; therefore, it could not be applied to assess ψ from triaxial tests (Vermeer & Borst, 1984). To fill this gap, Schanz and Vermeer (1996) proposed the following formula (Equation 4-4), derived using the concept of superposition and the triaxial strain conditions, which allows the direct evaluation of dilation angle from triaxial compression test data:

$$\sin \psi = \frac{1}{1 - \frac{2}{(d\varepsilon_v/d\varepsilon_a)}} \quad \text{Equation 4-4}$$

where $d\varepsilon_v$ is the rate of plastic volumetric strain, and $d\varepsilon_a$ is the rate of axial strain.

In order to use Equation 4-4 in a triaxial test, first, the plot of volumetric strain versus axial strain needs to be generated. Then, by determining the slope of any portion of this plot ($d\varepsilon_v/d\varepsilon_a$) and substituting it into the equation, the dilation angle for that section of the curve can be calculated. However, it should be noted that the initial slope of axial strain-volumetric strain curve cannot be used in measuring the dilation angle because it corresponds to elastic deformation, not the plastic deformation (Figure 4-7).

As illustrated in Figure 4-7, in a triaxial compression test on a soil sample, normally the relationship between volumetric and axial strain can be approximated by a bilinear curve fit model that represents the peak and residual dilation rate regions. The same method was used in this study. In fact, to determine the ψ , the slope of the line in the peak dilation rate region was substituted into the equation 4-4. This slope represents an average of the dilation rate from the beginning of dilation up to the start of the residual region. It is also worth adding that material will not dilate infinitely; indeed, after shearing to a certain degree, the dilatancy angle gradually decreases (Vermeer & Borst, 1984).

Figure 4-8 presents the dilation angles of analog sand samples with effective confining stress. As can be seen, the ψ decreases with the increase in effective confining stress, and its variation with σ_3' can be described using a power function.

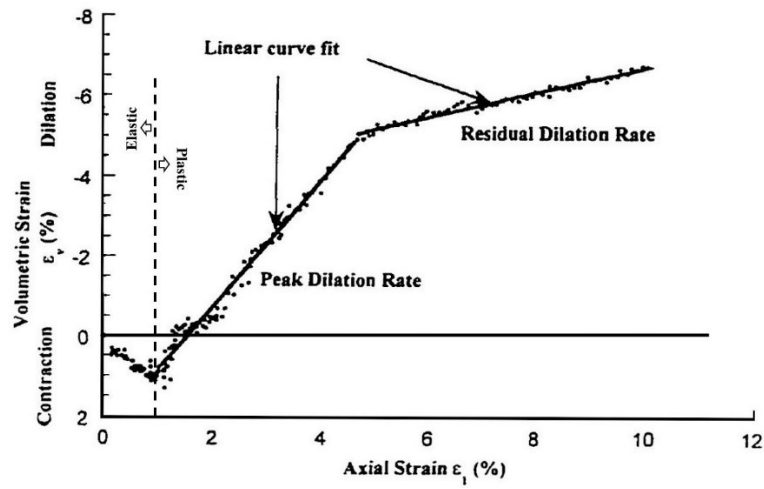


Figure 4-7 Typical plot of axial strain versus volumetric strain for an oil sand sample (modified from Touhidi-Baghini, 1998)

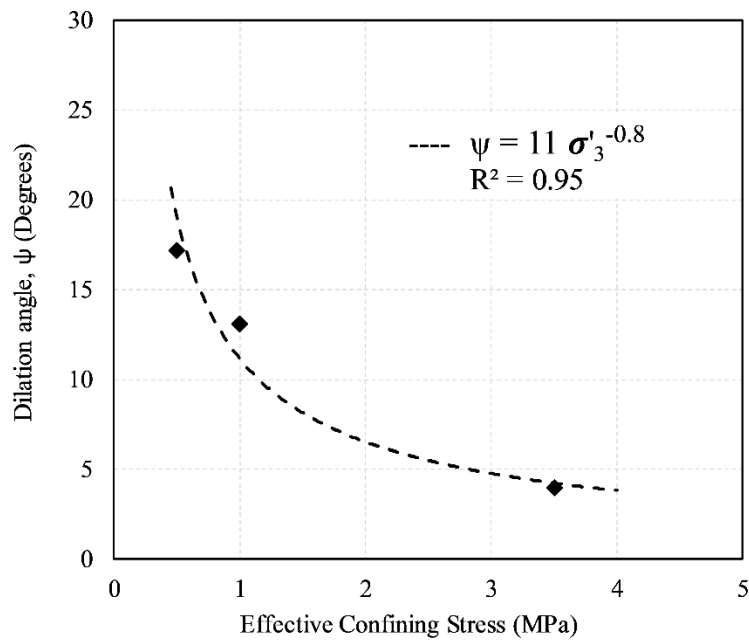


Figure 4-8 Variation of dilation angle with effective confining stress for analog sand samples

4.4.1.5. *Specimens' Deformation Patterns and Mode of Failure*

Mode of failure in soil and soft rock samples can be described on a spectrum with brittle and ductile failure representing opposite ends. A sample's mode of failure depends on the amount of plastic deformation it shows after the yield point. Indeed, a ductile material shows extensive plastic deformation after reaching a yield point, while plastic material fails with little to no plastic deformation (Mercier et al., 2003).

As explained earlier, the mode of failure can also be characterized using the stress-strain curve and the amount of stress drop after peak shear stress. To illustrate, the ductile material does not show any stress drop after peak strength and before residual strength, whereas in brittle material the amount of such a stress drop is considerable (Schöpfer et al., 2013).

Previous experimental studies on soil samples have shown that the failure mode is a function of several factors. These factors include the degree of cementation, moisture content, soil texture, particle size, microstructural state, rate of displacement, and effective confining stress under which the sample is sheared (Hatibu & Hettiaratchi, 1993; Asghari et al., 2004; Choo & Suna, 2018). For instance, Scott (1992) showed that increasing the effective confining stress could change the oil sands' mode failure from brittle to ductile.

One of the methods that can be used to determine the mode of failure in a shear test is investigating the state of the sample at the end of shearing. In order to analyze the shape of a failed specimen in a consolidated drained shear test, the sample's deformation should be broken down into two components: hydrostatic loading-induced deformation (consolidation phase), and triaxial compression-induced deformation (shearing phase). Normally, the latter has a more significant effect on the final shape of a failed specimen than the former.

As proposed by Ehrgott (1970), the soil sample's deformation during the application of hydrostatic loading could either have a double cone shape or a cylindrical shape depending on the amount of deformation restraint at the end-caps (Figure 4-9). Indeed, the impacts of end-platen friction are more severe in double cone deformation compared to that in the cylindrical one.

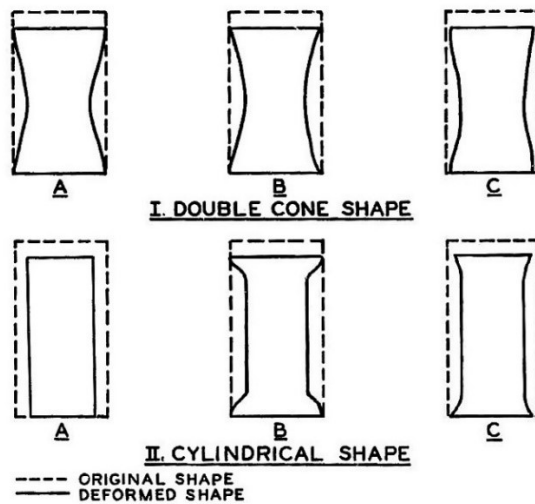


Figure 4-9 Deformed shapes of specimens during hydrostatic loading (Ehrgott, 1970)

Evaluating the sample deformation during the triaxial compression phase is very challenging because of the complicated shear zones which develop within the sample. Typically, the shear-induced deformation can be categorized into two master groups of ductile-type failures (Type I) with bulge and brittle-type failures with a shear plane (Ehrgott, 1970).

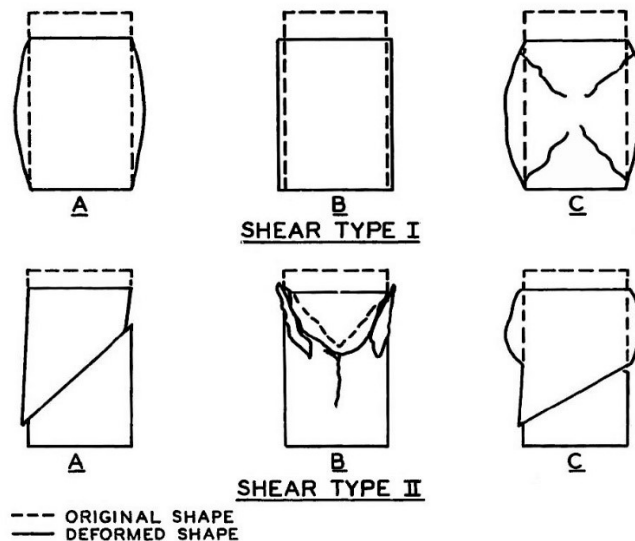


Figure 4-10 Shapes of failed specimens after a shear test (Ehrgott, 1970)

As schematically illustrated in Figure 4-10, in this classification, Type IA represents bulge-type failure with severe end-cap effects. Type IB shows the uniform ductile type failure without any

end-cap effect. Type IC indicates a semi-ductile failure with bulging-type deformation in the middle and cracking at both ends of the sample because of end-cap friction. These cracks create cone-shaped zones at both ends of the sample (Ehrgott, 1970). This type of failure is also known by other names, such as “barreling failure” or “ductile-faulting failure” (Hatibu & Hettiaratchi, 1993; Nandanwar, 2015; Asghari et al., 2004).

In addition, Type IIA shows a classic brittle failure with a clear-cut shear plane. Type IIB is a wedge-type failure. This type of failure normally has a vertical fracture along the axis of the sample. Finally, Type IIC shows composite type failure in which the sample is composed of two materials, and it fails either in both materials or only in the weaker one (Ehrgott, 1970).

In another attempt to determine the mode of failure using the state of the specimen at the end of shearing, Hatibu and Hettiaratchi (1993) introduced a qualitative method. As schematically depicted in Figure 4-11, they proposed seven distinctive modes of deformation to cover the full range from brittle to ductile failure behavior.

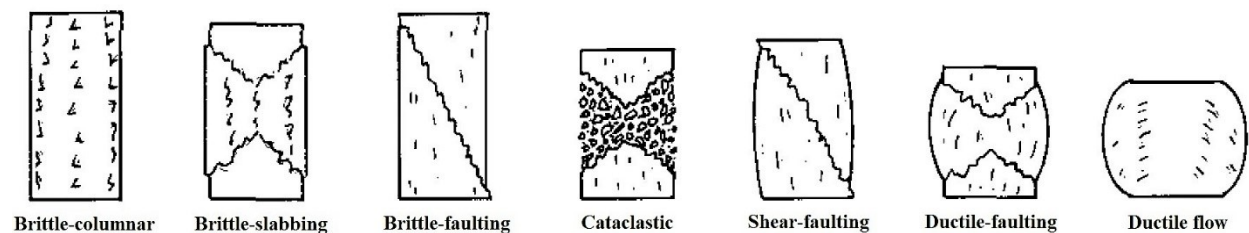


Figure 4-11 Classification of failure modes of specimens loaded in a triaxial compression setup (Hatibu & Hettiaratchi, 1993)

Considering the above-mentioned two components of sample deformation, the evolution of sample shape during a complete isotropically consolidated drained compression test is depicted in Figure 4-12 .

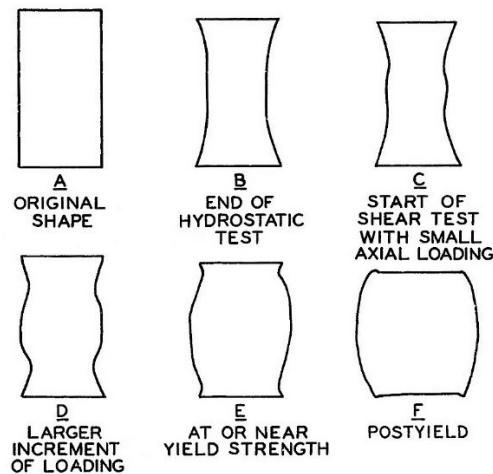


Figure 4-12 Specimen deformation during an isotropically consolidated shear test (Ehrgott, 1970)

In order to investigate the mode of failure in ROSs after finishing each test and removing the axial and confining stresses, the sample was frozen using dry ice and its picture was taken. The frozen samples were also scanned using a Toshiba Aquilion One X-ray CT scanner.

Figure 4-13 to Figure 4-15 show the ROSs after they were triaxially failed under effective confining stresses of 3.5, 1, and 0.5 MPa respectively. It is noted that the center of all three specimens slightly bulged outward, while the samples' ends remained relatively unaffected. By taking a closer look at the CT scan images, it can also be observed that some cracks were formed at either end of these samples. As explained earlier, these cracks formed because of the friction between loading platens and the sand samples. It should also be noted that normally some shape rebounding occurs in a sample upon the removal of axial and confining stresses, and this would mask some of the created cracks.

By comparing the deformed shape of ROSs with the deformation modes presented in Figure 4-10 and Figure 4-11, it can be concluded that the mode of failure for these samples is semi-ductile (Type IC) or barreling type. This phenomenon was corroborated by Nandanwar (2015) and Asghari et al. (2004), who observed that the dilation in reconstituted or uncemented sand samples occurs mainly at the center of the specimen. They also noticed some crack formation at the top or bottom of the sheared samples similar to that discerned for ROSs.

Because no clear shear failure lines were observed in the ROSs, obvious peaks of deviatoric stress were not observed on the stress-strain curves of these samples. This was consistent with the results obtained by Touhidi-Baghini (1998), Chalaturnyk (1996), and Oldakowski (1994), who ran triaxial compression tests on reconstituted and in situ oil sand samples.

It is also worth noting that since the isotropic consolidation-induced volume change in ROSs was not significant, the samples did not show considerable deformation during this phase.

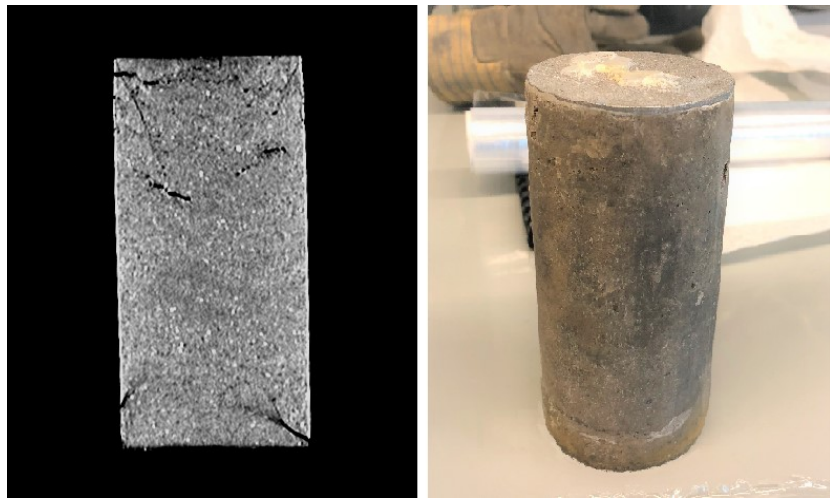


Figure 4-13 Sand sample loaded in an isotropically consolidated drained shear test under σ_3' of 3.5 MPa

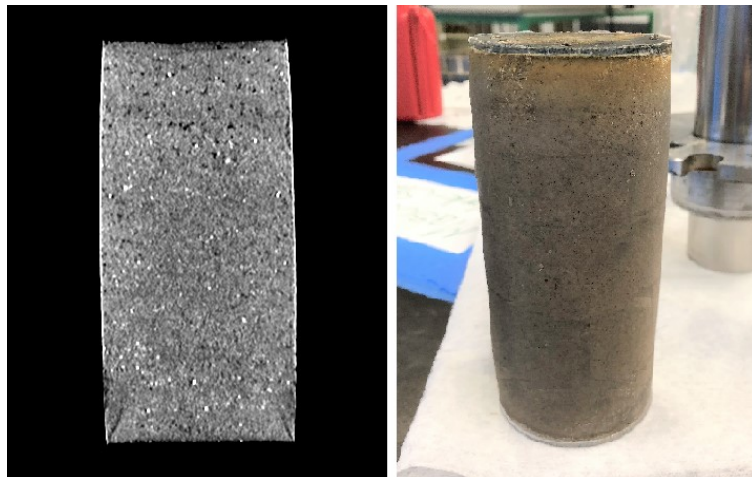


Figure 4-14 Sand sample loaded in an isotropically consolidated drained shear test under σ_3' of 1 MPa

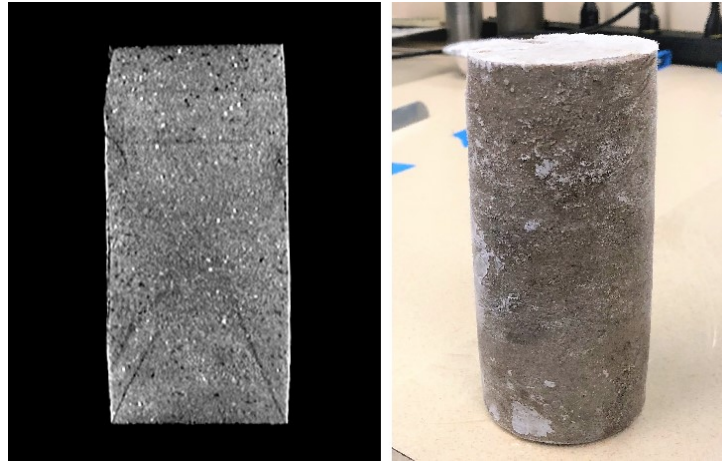


Figure 4-15 Sand sample loaded in an isotropically consolidated drained shear test under σ_3' of 0.5 MPa

4.4.2. Drained Shear Strength

From the stress-strain curves in Figure 4-4, it can be seen that the shear strength of sand samples is highly dependent on the effective confining stress. Indeed, increasing the effective confining stress leads to a rise in shear strength. In addition, for all tested analog sand samples, the post-peak stress reduction was not significant. Such a minor post-peak shear strength reduction is due to the relatively high confining stresses under which these specimens were tested, and also to the absence of interlocking structures within the reconstituted samples.

As stated earlier, the failure envelope describes the generalized stress state under which material will fail. Therefore, to develop the failure envelope for the reconstituted oil-free sand specimens (ROs), their stress paths were plotted in $s'-t$ space. As demonstrated in Figure 4-16, a polynomial equation can capture the relationship between t and s' over the effective stress range tested.

$$t = -0.01 s'^2 + 0.7 s' - 0.02$$

$$R^2 = 0.96$$

Equation 4-5

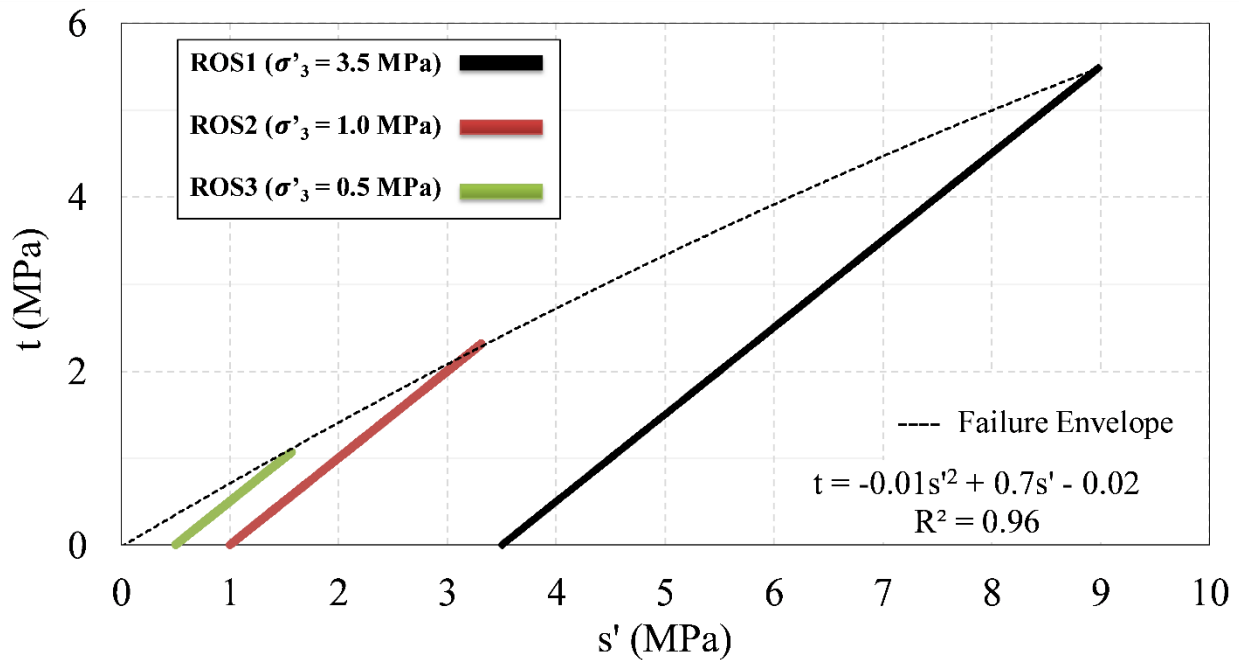


Figure 4-16 Drained triaxial compression tests stress paths and failure envelope for analog sand samples

It can be seen that the failure envelope has a slight curvature. This implies a mild reduction in the effective friction angle with an increase in the effective confining stress.

4.4.2.1. Cohesion

From the peak failure envelope in s' - t space (Figure 4-16), it can be concluded that the reconstituted analog sand sample is a cohesionless material. The same result was reported by other researchers for undisturbed oil sand cores and reconstituted oil sand samples.

4.4.2.2. Friction Angle

Using the peak failure envelope in s' - t space, a friction angle of 37° was computed for reconstituted oil-free sand specimens. It is also worth adding that the friction angle has direct relationships with

relative density and effective confining stress. In fact, the peak friction angle increases with the increase in relative density, and the decrease in effective confining stress.

4.4.2.3. *Axial and Volumetric Strains at Peak Shear Strength*

Figure 4-17 and Figure 4-18 show the axial and volumetric strains at peak shear strength with the effective confining stresses respectively. From these plots, it is clear that the rise in effective confining stress leads to an increase in the axial strain, while it decreases the volumetric strain. In fact, for the tests performed at low effective confining stresses, the volumetric strain at peak shear strength was negative. This means the samples' volume increased, whereas for high effective confining stresses, the volumetric strain at peak became positive, which represents volume decrease in the specimen (Table 4-1).

Therefore, at low confining stresses dilation is dominant, and at high effective stresses contraction is dominant. It is expected that an oil sand reservoir exhibits the same volumetric behavior during a SAGD operation when the reservoir undergoes shearing. As delineated in section 4.4.1.2, the reasons behind this phenomenon could be particles crushing and particles rolling at high and low effective confining stresses respectively.

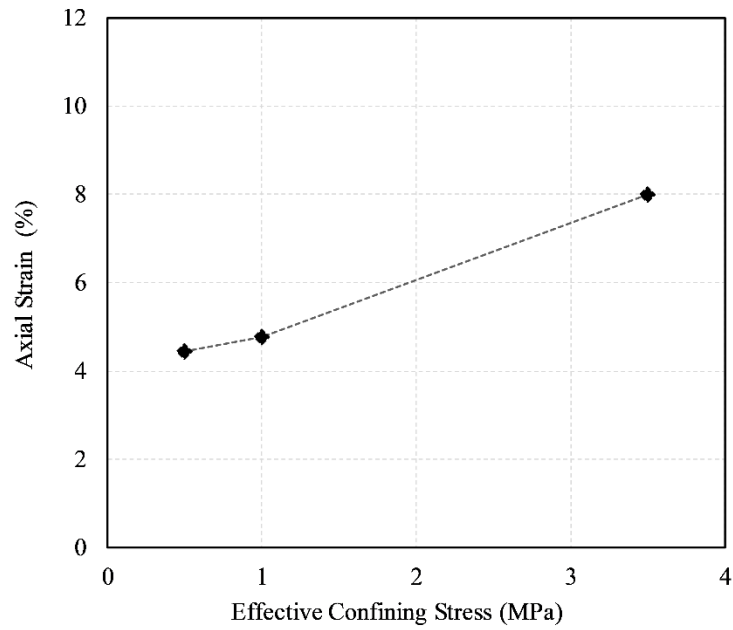


Figure 4-17 Peak axial strain for analog sand samples

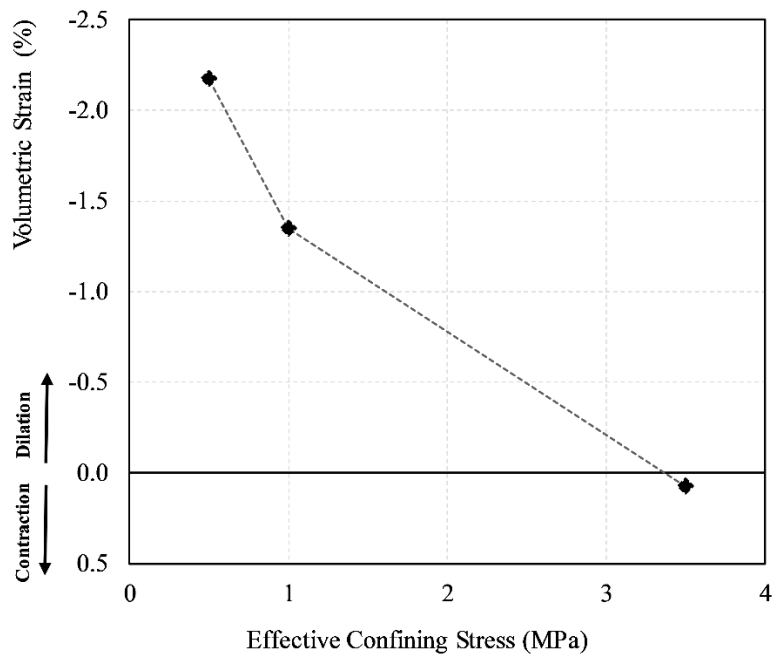


Figure 4-18 Peak volumetric strain for analog sand samples

Table 4-1 Isotropically consolidated drained triaxial compression tests data for analog sand samples

Test	Effective Confining Stress (MPa)	Back Pressure (MPa)	Deviatoric Stress at Peak Shear Strength (MPa)	Axial Strain at Peak Shear Strength (%)	Volumetric Strain at Peak Shear Strength (%)	Young Modulus @ $\varepsilon_a=1\%$ (MPa)	Young Modulus @ $\varepsilon_a=0.2\%$ (MPa)	Poisson's Ratio
ROS 1	3.5	3.0	10.9	8.0	0.1	411	562	0.39
ROS 2	1.0	3.0	4.6	4.8	-1.3	254	380	0.38
ROS 3	0.5	3.0	2.1	4.5	-2.2	84	116	0.39

4.5. Permeability Test

4.5.1. Absolute Permeability Evolution under SAGD Stress Paths

As explained in Chapter 2, the performance of a SAGD project depends on the permeability of the oil sand reservoir, particularly its absolute permeability (K_a), and its evolution throughout the operation. In fact, the injection of high pressure high temperature steam into the oil sand reservoir leads to two major geomechanical reactions – namely, mean effective stress and shear stress changes. These stress state changes cause reservoir deformations, and consequent absolute permeability alteration. Such changes in absolute permeability not only can significantly affect the amount of fluid drainage from the reservoir, but also can have major impacts on the extent of pore pressure migration within the reservoir (Chalaturnyk, 1996; Touhidi-Baghini, 1998).

Therefore, to understand the interrelation between permeability and strength deformation behavior of oil sands, a series of tests was performed on reconstituted analog sand samples to replicate the stress and pore pressure conditions of a SAGD process. It is worth noting that due to the geological heterogeneity of the McMurray Formation, the value of initial in situ absolute permeability for oil sands varies at different locations within the reservoir. Therefore, this study focuses on changes to the initial absolute permeability (under SAGD stress paths) rather than on calculating the true value of in situ permeability.

In addition, as explained in section 3.5.5, to calculate the permeability of sand samples, each test was performed at three different flow rates, and the differential pressure along the sample was

measured using three different methods. The final results show a minimal discrepancy between different flow rates and various differential pressure measurement techniques.

4.5.1.1. Permeability Changes during Isotropic Unloading

As explained earlier, the first component of the SAGD-induced stress path is decreasing mean effective stress due to the increase in pore pressure. This stress path was experimentally simulated through isotropic unloading of the samples. In other words, the effective confining stress was gradually decreased from 10 MPa to 4 MPa, while the pore pressure was kept constant at 3 MPa. During this process, the test was paused at different effective confining stresses to perform permeability tests.

Figure 4-19 and Figure 4-20 show the variations of volumetric strain and normalized absolute permeability of sand samples respectively with effective confining stresses during an isotropic unloading test. From the volumetric behavior of ROSs, it was noted that decreasing mean effective stress leads to an increase in the volume of the specimens (Figure 4-19). Furthermore, it was observed that the absolute permeability of the sample increases up to 28% with a decrease in effective confining stress from 7 MPa to 1 MPa (Figure 4-20).

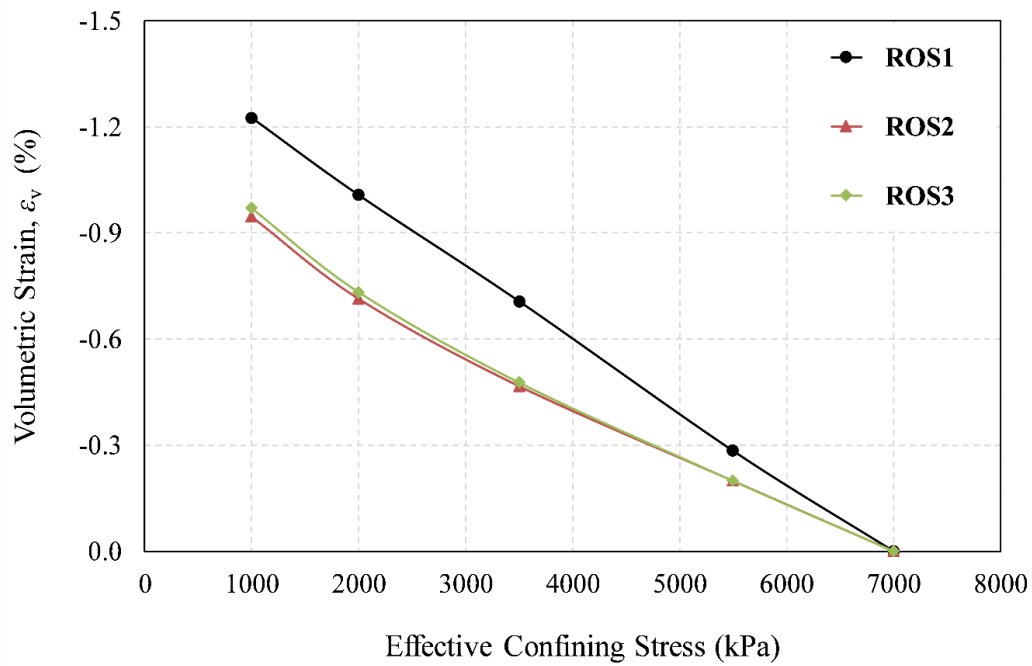


Figure 4-19 Volume change during isotropic unloading of analog sand samples

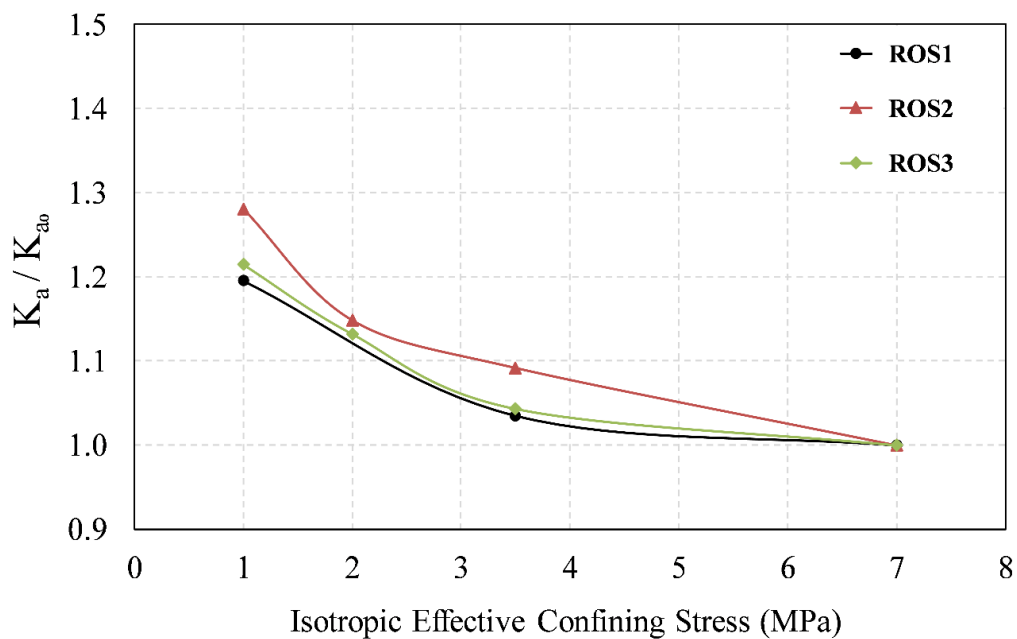


Figure 4-20 Normalized absolute permeability versus effective confining stress for analog sand samples

In view of the results presented in Figure 4-19 and Figure 4-20, it can safely be assumed that there is a direct relationship between the change in absolute permeability and the volumetric behavior

of reconstituted analog sand samples. In order to describe such a relationship, the variation of K_a with the volumetric strain (ε_v) was plotted for all specimens in Figure 4-21. It can be seen that the dilative behavior of the samples during isotropic unloading results in permeability augmentation. For instance, in the case of ROS2, the volume change of 1% in the sample increases the permeability by 20%. The most likely explanation for this phenomenon is that during isotropic unloading the sand grains slightly move apart from each other without any shearing or fabric distortion. This widens the flow channels within the samples and increases the permeability.

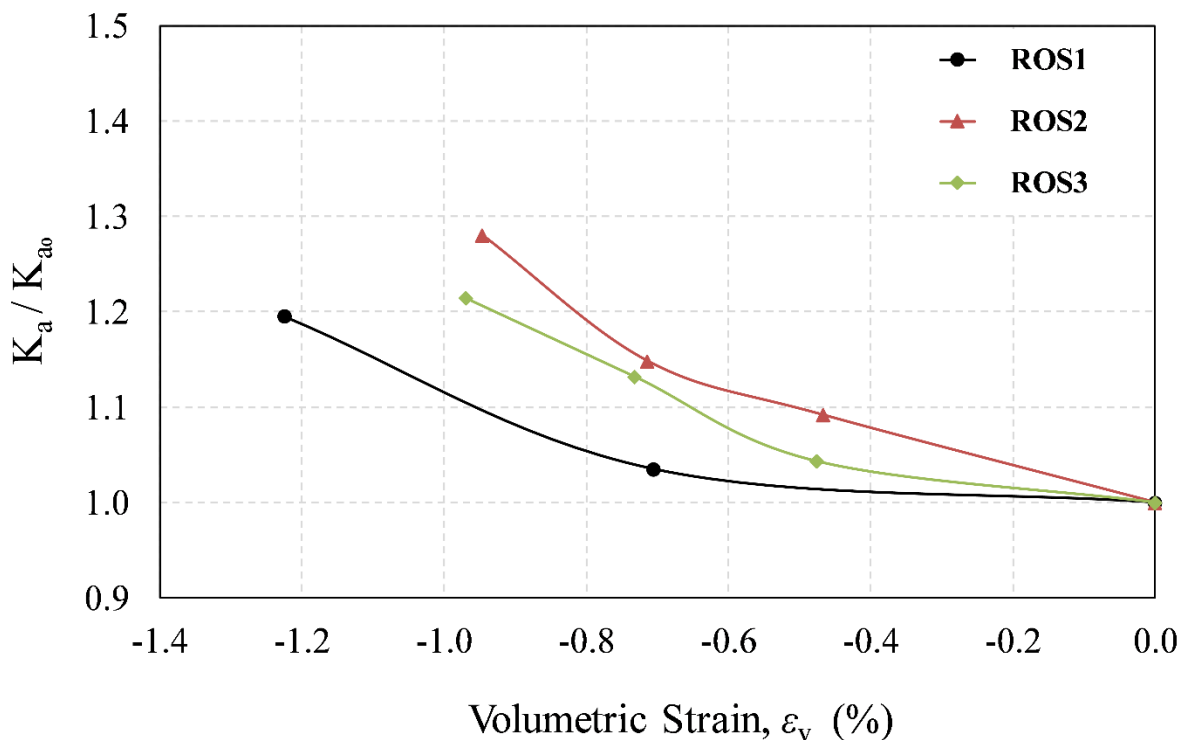


Figure 4-21 Normalized absolute permeability versus volume change for analog sand samples during isotropic unloading

The majority of previous experimental studies on oil sands established equations that relate the changes in porosity to permeability. In order to investigate the applicability of these studies, the variation of K_a with the changes in porosity is also presented here (Figure 4-22). Due to the small difference in the initial porosity value between the sand samples, the normalized porosity was used in this graph. As it was expected from the volumetric behavior of ROSs, the porosity values of these samples were increased during isotropic unloading, and this led to an increase in their

permeability values. More details on verification of the previous permeability relationships can be found in section 4.6.1.2.

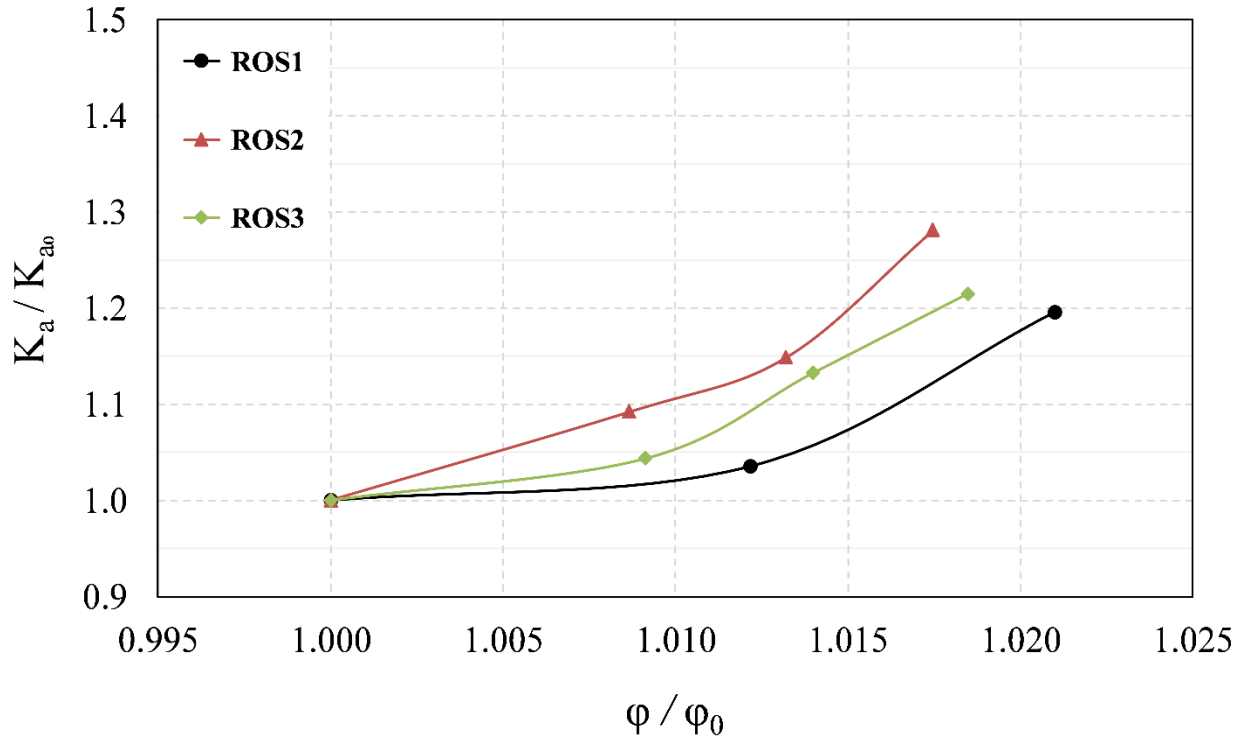


Figure 4-22 Normalized absolute permeability versus normalized porosity for analog sand samples during isotropic unloading

4.5.1.2. Permeability Changes during Triaxial Shearing

As stated before, in order to investigate the evolution of absolute permeability under the second component of SAGD-induced stress paths, a series of isotropically consolidated drained triaxial compression tests were performed on analog sand samples under effective confining stresses of 0.5, 1 and 3.5 MPa. As explained in section 3.5.5, these experiments were paused at several axial strain levels, and the permeability tests were carried out in these rest intervals.

Before investigating the permeability changes during shearing, the volumetric behavior of the samples needed to be analyzed. Section 4.4.1.2 presents the volumetric behavior of ROSs during triaxial compression tests. As illustrated in Figure 4-6, the volumetric behavior of sand samples

during shearing is dominated by the value of effective confining stress. In other words, sand samples show dilative behavior at low effective confining stresses, while presenting contractive behavior at high effective confining stresses.

Figure 4-23 shows the variations normalized absolute permeability with axial strain during triaxial shearing for all analog sand samples. It can be seen that the permeability continuously decreased throughout the shearing, except for the test on ROS3. In this test, which was performed under effective confining stress of 0.5 MPa, after the axial strain of 5%, permeability started to increase.

As can be seen in Figure 4-23, the amount of permeability reduction in ROS2 is slightly higher than ROS1 despite its lower confining stress. This is because ROS1 has a higher porosity value compared to ROS2 (Table 3-2). Likewise, other experimental studies on oil sand have shown that the samples with smaller initial porosity display greater permeability changes during shearing (Touhidi-Baghini, 1998).

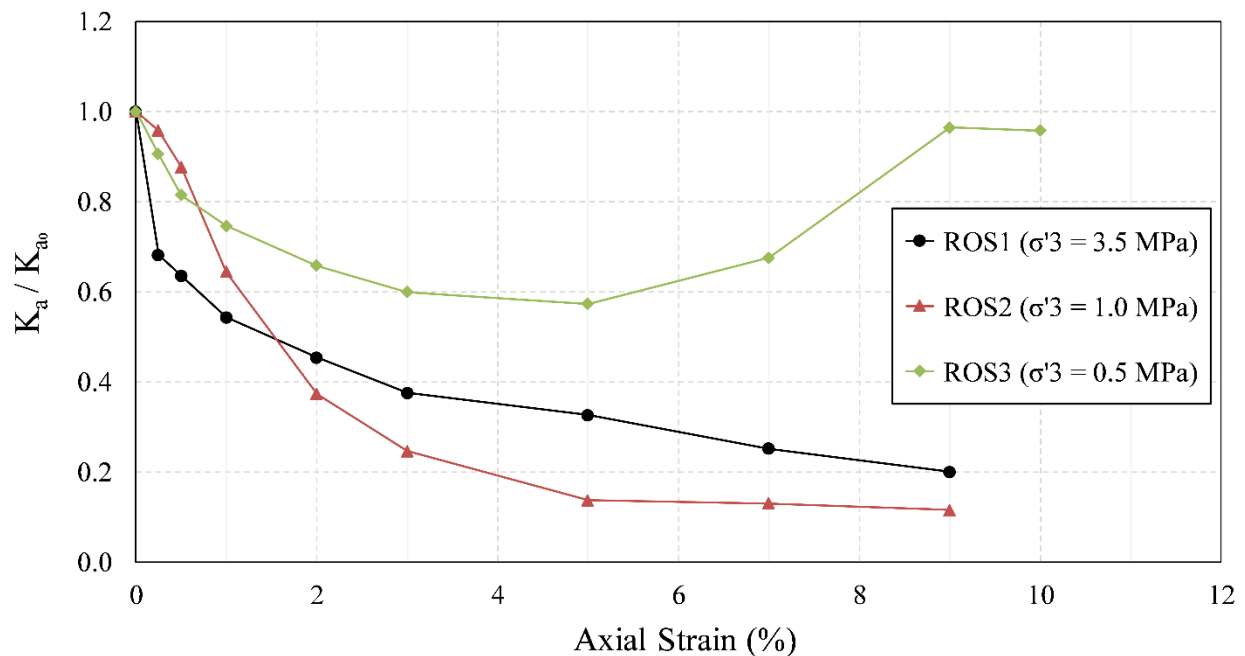


Figure 4-23 Normalized absolute permeability versus axial strain for analog sand samples during triaxial shearing

Figure 4-24 and Figure 4-25 present the variation of normalized absolute permeability with volumetric strain and porosity changes respectively. As can be seen in these graphs, during shearing, unlike

the isotropic unloading tests, the sample's dilation (or the increase in porosity value), did not necessarily translate into permeability augmentation. The final results also revealed that the positive effects of dilation on permeability are only limited to the tests at very low effective confining stresses, and the volumetric strain is required to reach a certain level.

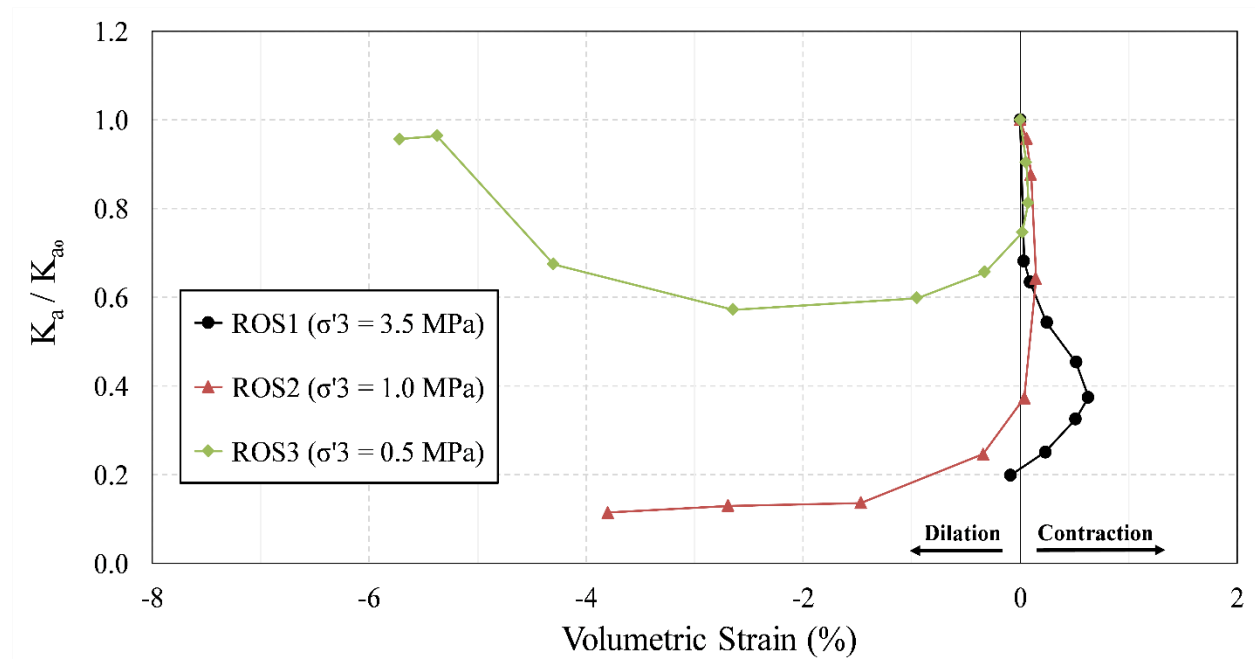


Figure 4-24 Normalized absolute permeability versus volumetric strain for analog sand samples during triaxial shearing

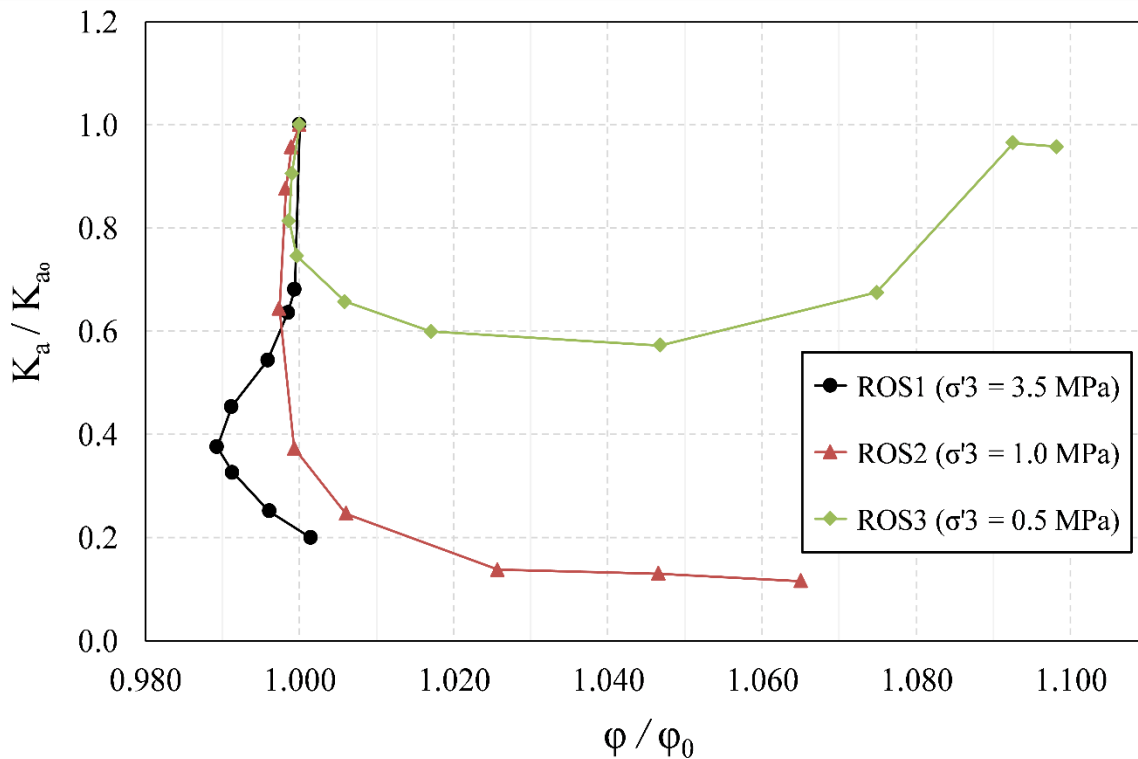


Figure 4-25 Normalized absolute permeability versus normalized porosity for analog sand samples during triaxial shearing

During shearing, several flow channels develop within the specimen potentially increasing its permeability value (Touhidi-Baghini, 1998). The sand samples test results have shown that an improvement is not noticeable at high effective confining stresses, which is likely due to the suppression of the created channels at high confining stress creating a lack of connectivity between these channels.

The other probable reasons behind this phenomenon are grain crushing and pore network distortion that occur during shearing. To illustrate, shearing a sample can significantly disturb its internal structure and grain size distribution. Therefore, shearing has major impacts on flow paths and pore space connectivity within the specimen. Such fabric distortion is, indeed, a double-edged sword. At low effective confining stresses, when the flow channels are wide, this could increase the connectivity between pore spaces and enhance permeability; at high effective confining stresses when the flow paths are tight, it can clog the existing and new flow channels and reduce permeability.

4.6. Discussion and Conclusions

4.6.1. Comparison with Previous Experimental Studies on Oil Sand

This section discusses the outcomes of previous experimental studies on oil sand cores and other reconstituted oil sand samples to ensure the resemblance between ROSs and McMurray Formation oil sands in terms of their geomechanical properties. Such analysis also provides an assurance of similarity between the sand layers of analog IHS and in situ ones, because, as explained in Chapter 2, the ROSs were used to reconstitute the analog IHS specimens.

4.6.1.1. Geomechanical Properties

4.6.1.1.1. Stress-Strain Behavior

Figure 4-26 displays the peak failure envelope from former laboratory studies on McMurray Formation oil sands with the results of this study. It can be seen that the results from ROSs (red crosses on the graph) are quite consistent with other data. Based on the Mohr-Coulomb failure criteria, the slope of the line which goes through the peak values in $s'-t$ plot is equal to the sine of the friction angles ($\tan \alpha = \sin \varphi$). Therefore, the average value of friction angle for McMurray oil sand is 40° which is very close to the value that was measured from the test performed on ROSs (37°). The minor difference that was observed in the values of friction angles might be due to the interlocking structure in the undisturbed oil sand cores. In addition, it can be concluded from this graph that, like the ROSs, the undisturbed oil sand samples have no cohesion.

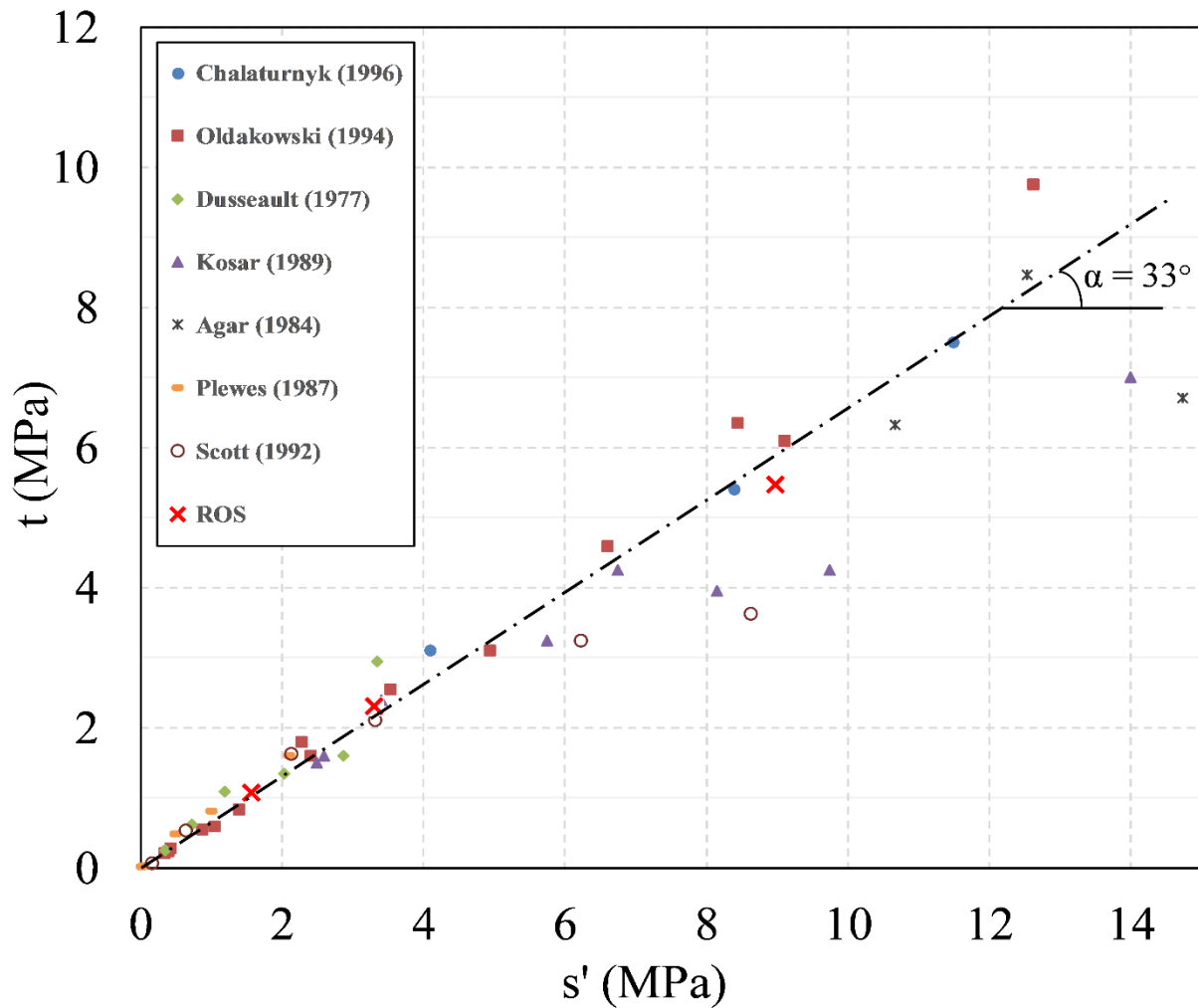


Figure 4-26 Peak failure envelope for McMurray Formation oil sands

To characterize the dilatancy behavior of McMurray Formation oil sand, several researchers such as Samieh and Wong (1997) and Touhidi-Baghini (1998) measured its dilation angle (ψ). Their results showed that the value of dilation angle decreases with the increase in effective confining stress. This behavior was completely compatible with the dilation angle trend that was observed in this study. In addition, as declared by Vermeer and de Borst (1984), after shearing to a certain degree, the dilatancy angle gradually decreases. Such a transition from peak dilation rate to residual dilation rate was also clearly noticed in the ROSs.

With regard to the stiffness of the Athabasca oil sand reservoir, several researchers investigated the elastic modulus (E) of the oil sands using their stress-strain response. Figure 4-27 illustrates

the variation of elastic modulus with effective confining stress (σ_3') from previous experimental studies on McMurray Formation oil sands as well as the results from ROSs. As can be seen in this figure, the value of E rises drastically with the increase in σ_3' . Moreover, it is noted that the elastic modulus of ROSs (red crosses on the graph) are congruous with other oil sands data, particularly at lower confining stresses. The observed discrepancy in value elastic modulus is due to the difference in the strain level at which the E was calculated, and also to the dissimilarity in the density of the tested samples.

Over the past few decades, several researchers have established equations that capture the relationship between elastic modulus and effective confining stress. Typically, a standard hyperbolic function is chosen to define the dependency E to σ_3' as follows:

$$E_i = K_E p_a \left(\frac{\sigma_3'}{p_a} \right)^n \quad \text{Equation 4-6}$$

where E_i is the modulus of elasticity at the low strain level, K_E is the modulus number, p_a is the atmospheric pressure, and n is the modulus exponent.

Byrne et al. (1987) proposed a series of guidelines for selecting K_E and n based on the type and condition of the sand masses. Using the curve fitting techniques, the hyperbolic expressions for aggregate oil sands' data and ROSs are:

$$\text{Oil sands data: } E_i = 1042 p_a \left(\frac{\sigma_3'}{p_a} \right)^{0.6} \quad \text{Equation 4-7}$$

$$\text{ROSs: } E_i = 822 p_a \left(\frac{\sigma_3'}{p_a} \right)^{0.5} \quad \text{Equation 4-8}$$

While these equations can reasonably match the experimental data at low confining stresses, they substantially underestimate E at higher values of effective confining stress. Consequently, the application of these equations should be limited to the circumstances where effective confining

stress is less than 4 MPa. As can be seen in Figure 4-27, the oil sands' elastic modulus has a better agreement, compared to Equation 4-7 Equation 4-8, with a power function which can be expressed as

$$E = 340(\sigma'_3)^{0.8} \tag{Equation 4-9}$$

Unlike the last two equations, the power function can be used for the whole range of confining stress up to 10 MPa.

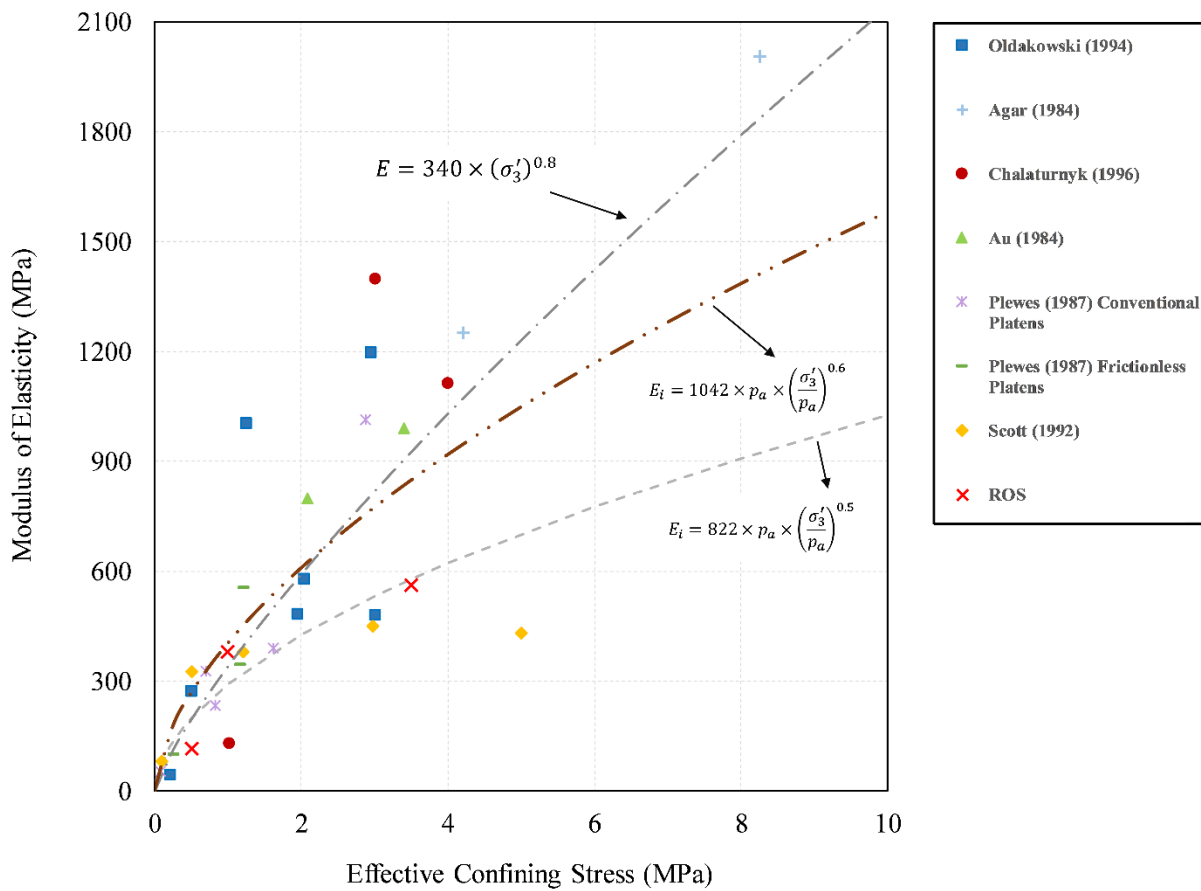


Figure 4-27 Modulus of elasticity versus effective confining stress for McMurray Formation oil sands

4.6.1.1.2. Shear Strength

As stated earlier, the value of shear strength is greatly affected by the confining stress. Therefore, to compare the shear strength of ROSs with in situ oil sand cores and other reconstituted oil sand specimens, the normalized deviatoric stresses of some of the previous studies on oil sands were plotted versus the axial strain. As can be seen in Figure 4-28, the shear strength values of the reconstituted sand samples are similar to other oil sands specimens. The minor deviations observed between different samples is probably because they have different values of initial density or porosity.

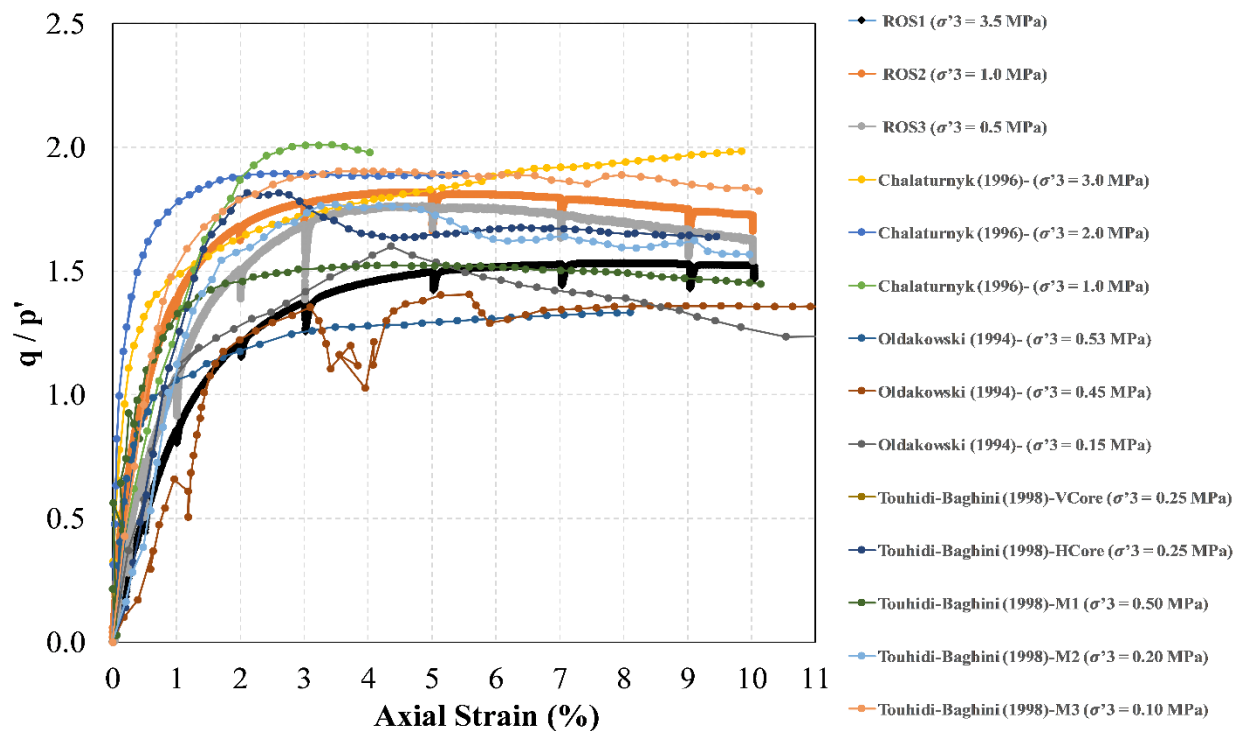


Figure 4-28 Normalized deviatoric stress versus axial strain for McMurray Formation oil sand

Considering the comparative analysis that was explained in sections 4.6.1.1 and 4.6.1.2, it can be concluded that the geomechanical properties of ROSs match in situ oil sand cores and other reconstituted oil sand samples.

4.6.1.2. *Investigating the Applicability of Previous Empirical Permeability Relationships*

During a SAGD operation, an oil sand reservoir undergoes substantial geomechanical processes that affect its porosity, pore structure, and stress state. These processes greatly impact the value of absolute permeability (K_a) and substantially influence the performance of a SAGD project. Therefore, it is important to investigate the variation of K_a when the reservoir material undergoes these SAGD-induced changes.

Over the past few decades, several researchers have established equations that represent flow through porous media. These relationships, which link the permeability to pore structure, can be used to predict the variation of K_a during a SAGD operation. This section briefly describes some of these experimental permeability expressions and also examines their applicability to the ROSs.

4.6.1.2.1. Kozeny-Carman Model

The Kozeny-Carman model is one of the first relationships developed to link the permeability of soil to its morphology. This relationship, which is particularly applicable to cohesionless sandy and silty soils, can be expressed as follows:

$$K = \frac{C n^3 D_s^2}{(1 - n)^2} \quad \text{Equation 4-10}$$

where n is the porosity, D_s is the mean particle size, and C is a function of particle shape and pore shape.

Although this relation was originally developed to estimate the initial porosity of soil, it can also be used to estimate the evolution of permeability during stress state changes and deformation. In order to do that, it was assumed that D_s and C are constant throughout the tests and only porosity varies. In this regard, the measured porosity values were substituted in the modified Kozeny-Carman's equation to calculate the permeability alteration. This equation can be expressed as,

$$\frac{K}{K_0} = \left(\frac{\varphi}{\varphi_0}\right)^3 \left(\frac{1 - \varphi_0}{1 - \varphi}\right)^2 \quad \text{Equation 4-11}$$

where K is the current absolute permeability, K_0 is the initial absolute permeability, φ is the current porosity, and φ_0 is the initial porosity.

Figure 4-29 and Figure 4-30 show the measured and predicted variation of absolute permeability using the Kozeny-Carman relation during isotropic unloading and triaxial shearing respectively. As can be seen, for all ROSs, the Kozeny-Carman equation underestimates the absolute permeability improvement during isotropic unloading. Moreover, the divergence between measured and predicted values increases with the increase in porosity.

With respect to the triaxial shearing test, a huge discrepancy was observed between predicted and measured data. This might be because the assumptions of constant mean grain size and pore shape are not valid during shearing. In fact, the grain crushing and pore structure rearrangement that happen during shearing significantly change the sample tortuosity and consequently alter the permeability value.

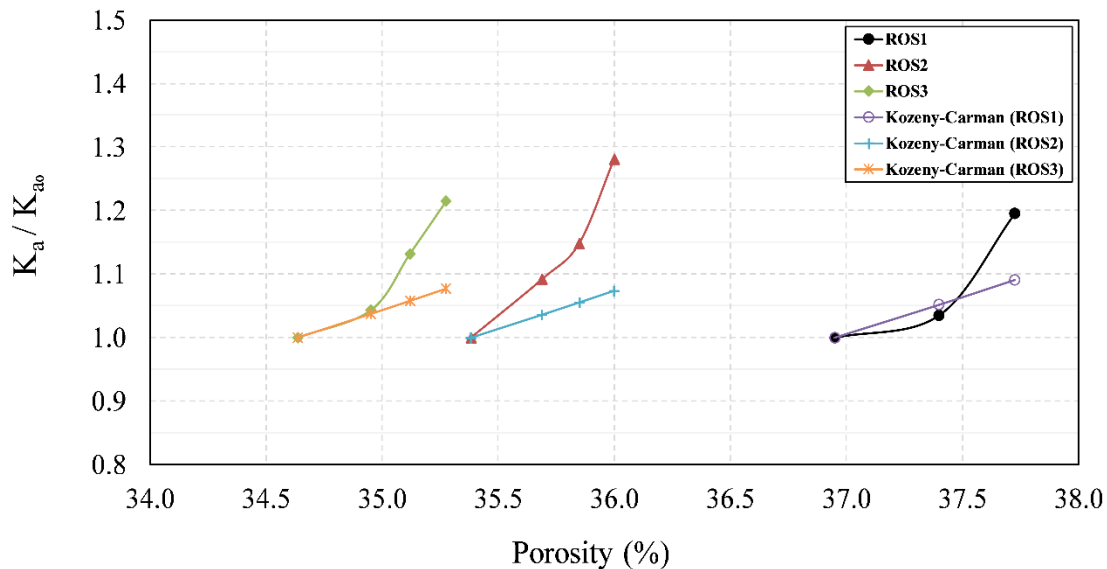


Figure 4-29 Prediction of absolute permeability alteration during isotropic unloading using the Kozeny-Carman equation

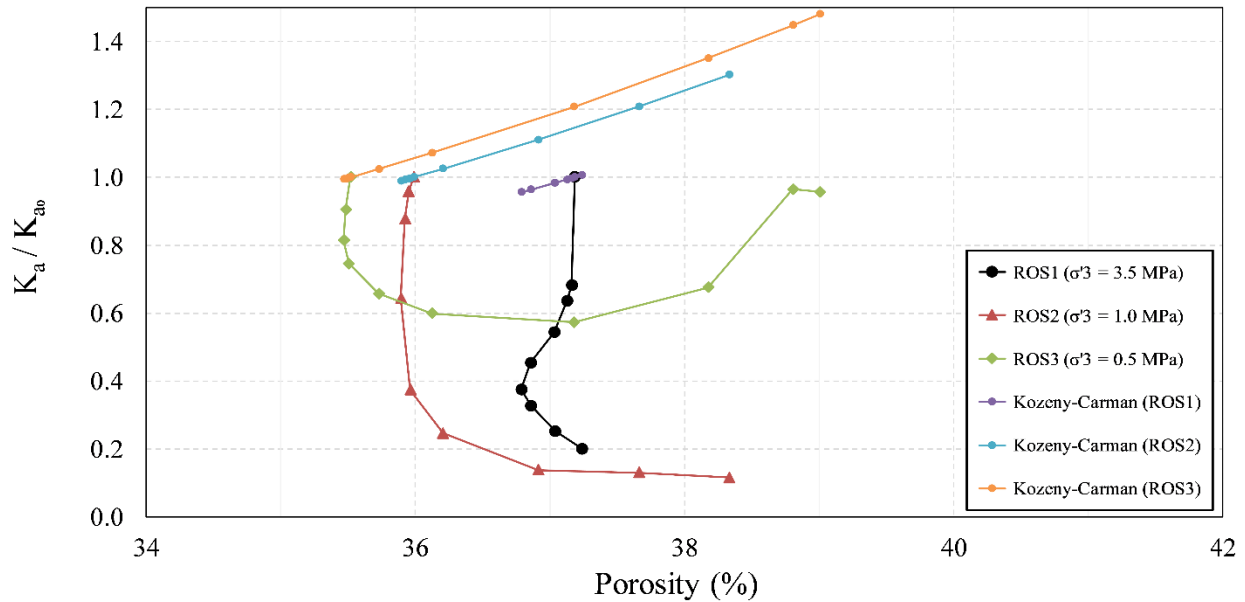


Figure 4-30 Prediction of absolute permeability alteration during triaxial shearing using the Kozeny-Carman equation

4.6.1.2.2. Chardabellas' Model

Another well-known expression that relates the permeability to pore volume was introduced by Chardabellas (Kézdi, 1974). This relationship can be expressed as follows:

$$K = Ae^B \quad \text{Equation 4-12}$$

where e is the void ratio, A is the absolute permeability at the void ratio of 1 (porosity of 50%), and B is the rate of change of permeability with the change of void ratio which ranges from 2 to 5.

Similar to Kozeny-Carman, Chardabellas' equation was originally derived to estimate the initial porosity of soil. However, it can be applied to estimate the modified permeability during the geomechanical processes. Since in this equation A and B are constant, the change in absolute permeability was calculated by substituting the measured void ratio in the equation.

Figure 4-31 displays the measured and predicted variation of absolute permeability using Chardabellas' relation for the B values of 2 and 5 during isotropic unloading. As illustrated in the graph, the correlation for $B=5$ shows a better fit with the experimental results, yet it slightly underestimates the amount of permeability enhancement due to dilation.

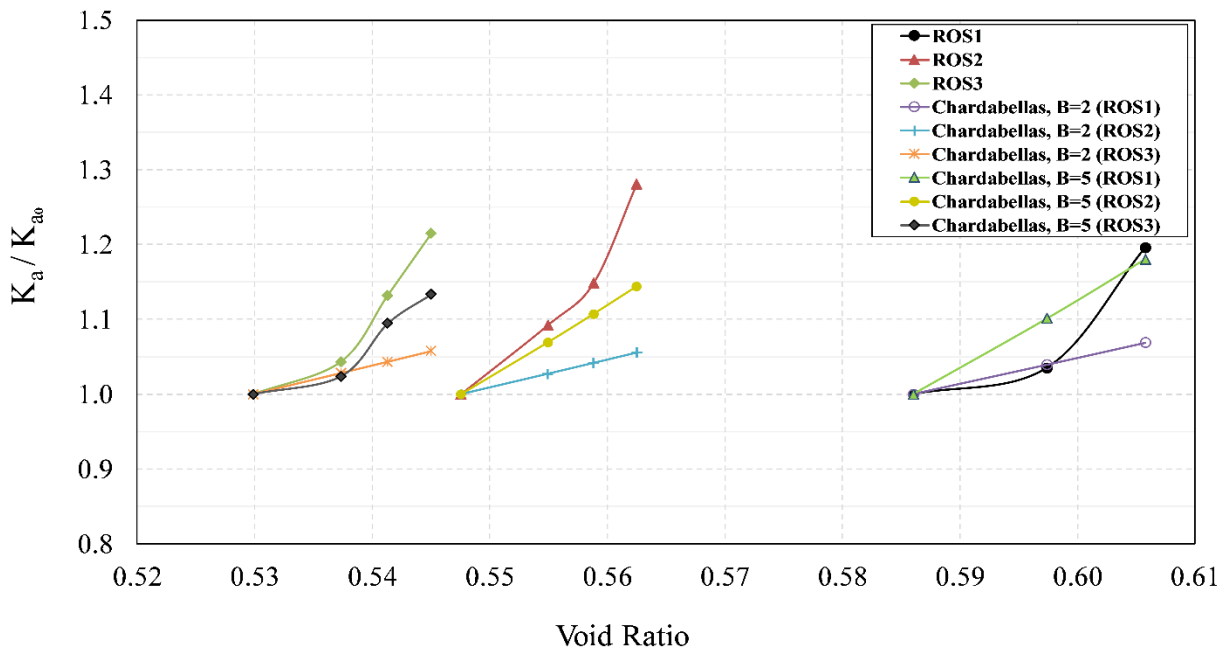


Figure 4-31 Prediction of absolute permeability alteration during isotropic unloading using Chardabellas' equation

4.6.1.2.3. Tortike's Model

In an attempt to incorporate the geomechanically-induced volumetric strain into the changes in the absolute permeability, Tortike and Farouq Ali (1991) derived the following equation based on the Kozeny-Carman model:

$$\frac{K}{K_0} = \frac{\left(1 + \frac{\varepsilon_v}{\varphi_0}\right)^3}{(1 + \varepsilon_v)} \quad \text{Equation 4-13}$$

where K is the current absolute permeability, K_0 is the initial absolute permeability, ε_v is the volumetric strain, and φ_0 is the initial porosity.

Figure 4-32 shows the measured and predicted variation of absolute permeability using Tortike's equation during isotropic unloading. It can be seen that at low dilation values, the Tortike's equation can capture the permeability changes, while at high values of volumetric expansion, it significantly underestimates the modified permeability.

Previous experimental research and the results presented in this study have shown that the application of this equation is limited to isotropic unloading process. In other words, it cannot be used to determine the modified absolute permeability in triaxial shearing tests. This is because Torike's equation, like the Kozemy-Carman equation, does not consider the variation of tortuosity that occurs during shearing.

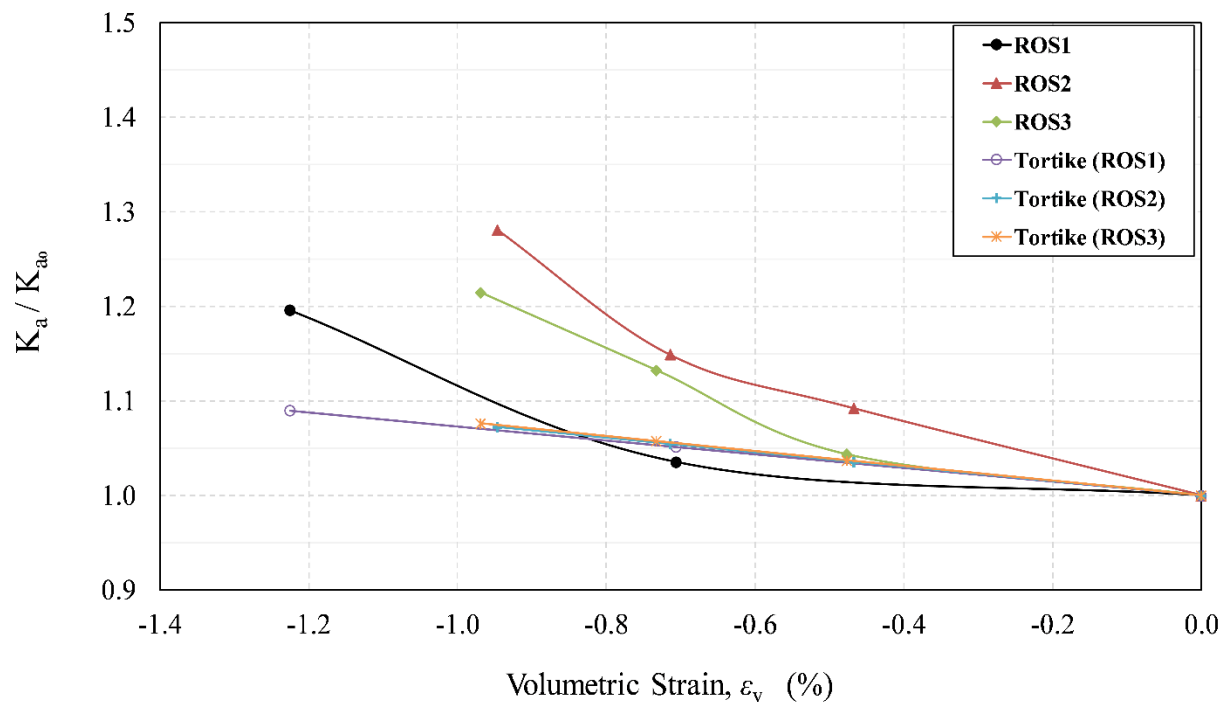


Figure 4-32 Prediction of absolute permeability alteration during isotropic unloading using Tortike's equation

4.6.1.2.4. Touhidi-Baghini's Model

In another attempt to link the variation of absolute permeability to geomechanically-induced volumetric strain, Touhidi-Baghini (1998) introduced the following linear semi-logarithmic expression for oil sands.

$$\ln \frac{K}{K_0} = C_{n_1} \varepsilon_v$$

Equation 4-14

$$C_{n_1} = \left[\frac{(1 - \varphi_0) a + b \varphi_0}{\varphi_0} \right]$$

where K is the current absolute permeability, K_0 is the initial absolute permeability, ε_v is the volumetric strain, a and b are the experimental constants, and φ_0 is the initial porosity.

By assuming $a = b = B$ (Chardabellas' term), the above equation can be rewritten as follows:

$$\ln \frac{K}{K_0} = \frac{B}{\varphi_0} \varepsilon_v$$

Equation 4-15

Figure 4-33 and Figure 4-34 display the measured and predicted variation of absolute permeability using Touhidi-Baghini's equation for B value of 5 and 7 respectively during isotropic unloading. As illustrated in the graph, the correlation for $B = 7$ generally shows a better fit with the results from ROSs.

One of the interesting aspects of Touhidi-Baghini's expression is that it shows that the sample's initial porosity is inversely proportional to the permeability alteration during a geomechanical process. The final results in this study displayed similar behavior. For instance, the ROS1, which had slightly higher porosity value compared to the ROS2 and ROS3, showed less permeability improvement during isotropic unloading.

Using Touhidi-Baghini's equation for calculating the modified absolute permeability due to shearing induces a significant error because this equation was derived based on the assumption that pore shape and particle shape do not change in the course of shearing. As explained in section 4.5.1.2, these assumptions are not valid, particularly for compression tests at high effective confining stresses.

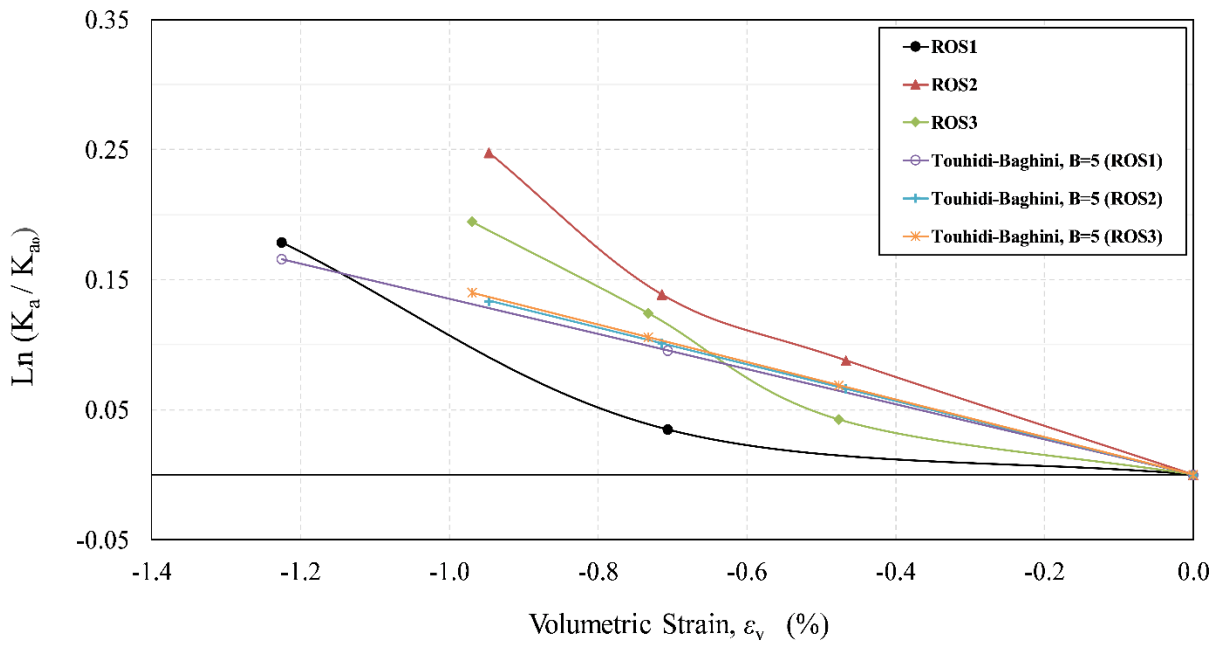


Figure 4-33 Prediction of absolute permeability alteration during isotropic unloading using Touhidi-Baghini's equation

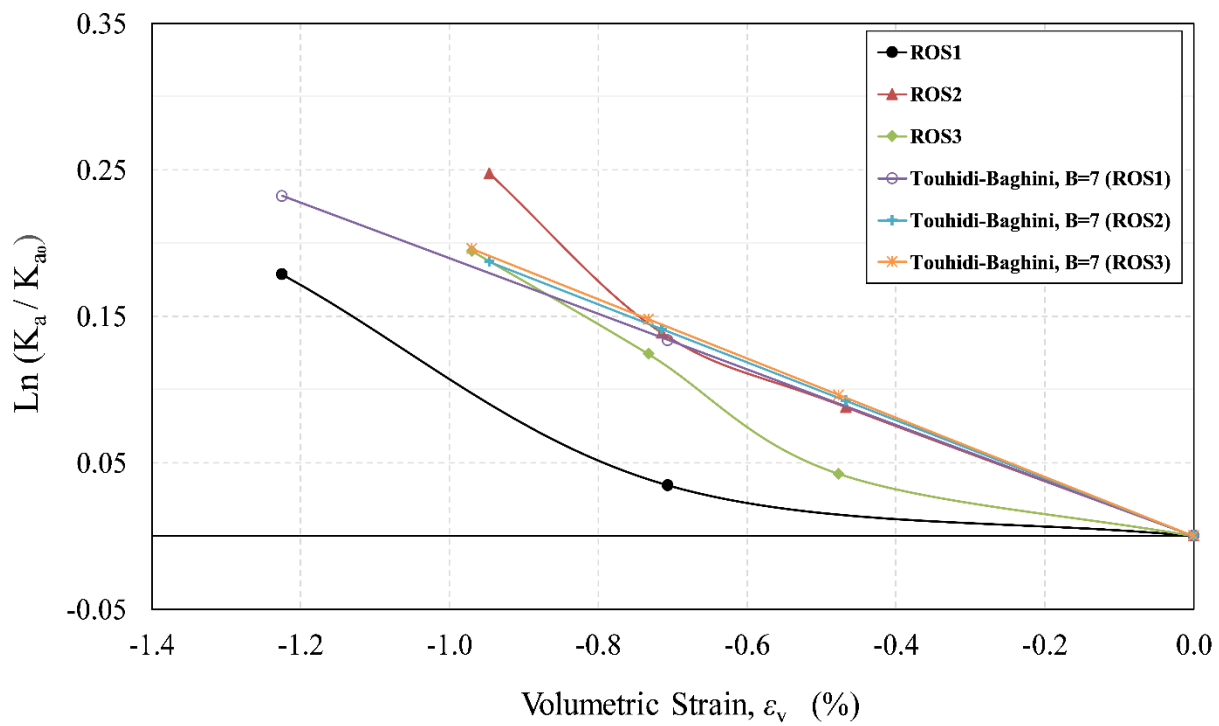


Figure 4-34 Prediction of absolute permeability alteration during isotropic unloading using Touhidi-Baghini's equation, B=7

4.7. Summary

The following summarizes the conclusions of this chapter:

- Full saturation of reconstituted sand samples was confirmed through running a series of B-tests.
- Bulk compressibility of the sand sample is a strong function of the effective confining stress, particularly at low stress levels (below 3 MPa), and the relationship between them can be expressed using a power function.
- The elastic modulus of ROSs is stress dependent. It increases with the increase in effective confining stress, and its variation with σ_3' is nonlinear.
- The dilative or contractive behavior of the sand specimens during shearing is predominantly controlled by the value of effective confining stress.
- The dilation angle of ROSs is stress dependent. It decreases with the increase in effective confining stress, and its variation with σ_3' can be described using a power function.
- The analog sand specimens were found to be cohesionless and have an effective friction angle of 37° .
- The absolute permeability of ROSs increased up to 28% with a decrease in effective confining stress from 7 MPa to 1 MPa. In addition, the absolute permeability continuously decreased throughout the shearing, except for the test on ROS3 which was performed at low effective confining stress. Therefore, during shearing, unlike the isotropic unloading tests, the sample's dilation does not necessarily translate into permeability augmentation. The final results also revealed that the positive effects of dilation on permeability are only limited to the tests at very low effective confining stresses, and the volumetric strain is required to reach a certain level.
- Comparing the measured stress-strain and strength parameters of reconstituted sand samples in this study with the previous experimental studies on oil sand cores and other reconstituted oil sand samples assured the resemblance between ROSs and McMurray Formation oil sands

in terms of their geomechanical properties. Such analysis also provided an assurance of similarity between the sand layers of analog IHS and in situ ones.

- Previous empirical permeability relationships are only applicable to calculate the modified absolute permeability due to isotropic unloading and triaxial shearing under low effective confining stresses. This is because none of these correlations take the variation of tortuosity into account. In fact, they assume that the particle size and pore shape are constant throughout the geomechanical reactions. But these assumptions are not well-founded.

5. HYDRO-MECHANICAL TESTING ON MUD LAYER

5.1. Introduction

In order to investigate the geomechanical constitutive behavior of McMurray mudstone and its permeability evolution under SAGD-induced stress paths, a series of tests was performed on reconstituted mud samples. Chapter 5 presents and analyzes the results of these experiments, which include B-test, isotropic cyclic consolidation test, drained triaxial compression test, and permeability test.

In addition, this chapter discusses the outcomes of previous experimental studies on McMurry Formation mudstone and other silt-clay mixtures to assure the resemblance between analog mud samples and in situ mudstone specimens in terms of their geomechanical properties. It also investigates the applicability of former empirical permeability relationships.

5.2. B-test

As explained in section 4.2, if the calculated B value for three consecutive B tests on a sample was quite constant, it could safely be assumed that the sample was fully saturated (Chaney et al., 1979).

Figure 5-1 shows the results of B-tests on three analog mud samples. As can be seen, the plots of undrained pore pressure increase versus isotropic confining stress increments are completely linear for all samples. This indicates that the B value is constant and independent of the magnitude of the back pressure. Therefore, according to the method suggested by Chaney et al. (1979), all mud samples are fully saturated.

The relationships between pore pressure (u) and isotropic confining stress (σ_c) for mud samples are also displayed on the graph, reconfirming a saturated value of B of unity.

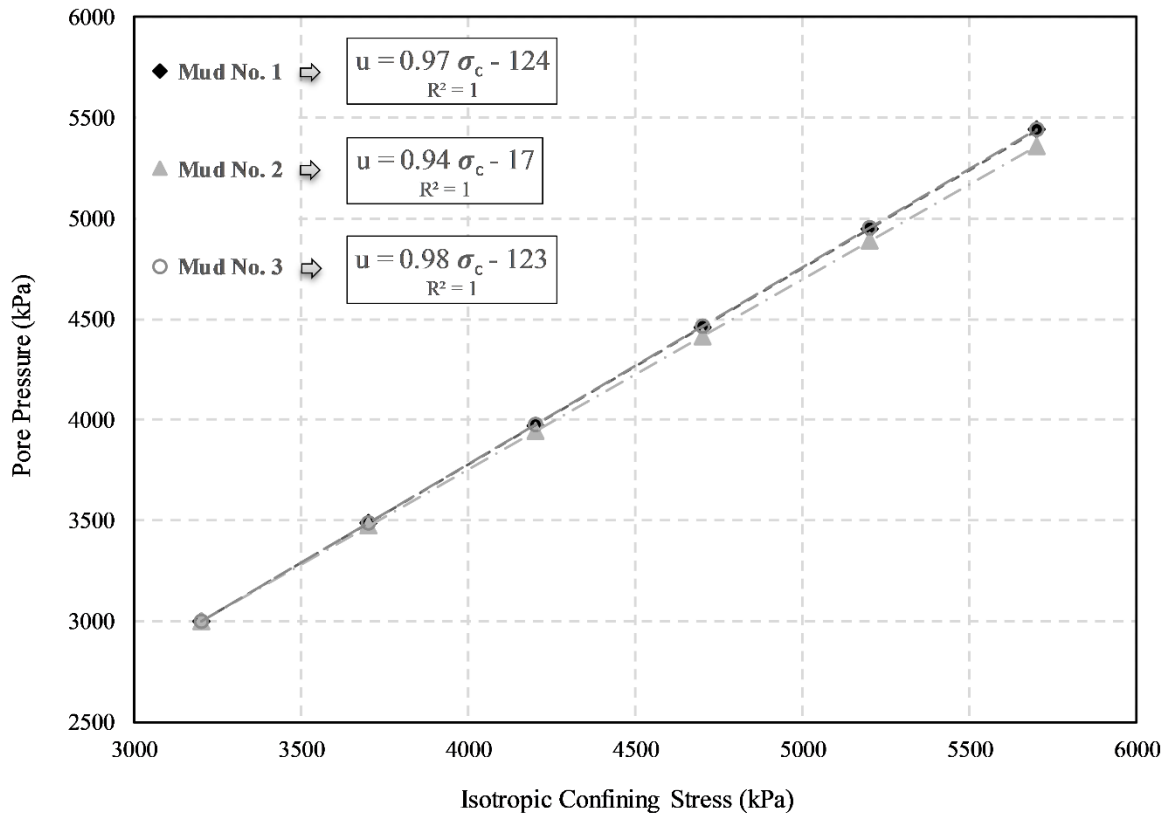


Figure 5-1 B-tests on analog mud samples

5.3. Isotropic Cyclic Consolidation Test

The isotropic cyclic consolidation test was performed on reconstituted mud samples in an attempt to measure the coefficient of bulk compressibility and recompact the specimens before drained shear tests.

As stated before, each specimen was saturated under effective isotropic confining stress of 0.2 MPa with a pore pressure of 3 MPa. Afterward, the effective confining stress was cycled two times between 0.2 MPa and 7 MPa. For a soil subjected exclusively to isotropic stress, the volume change is governed by effective stress rather than total stress. Figure 5-2 illustrates the mud samples' bulk volume changes with the effective confining stresses.

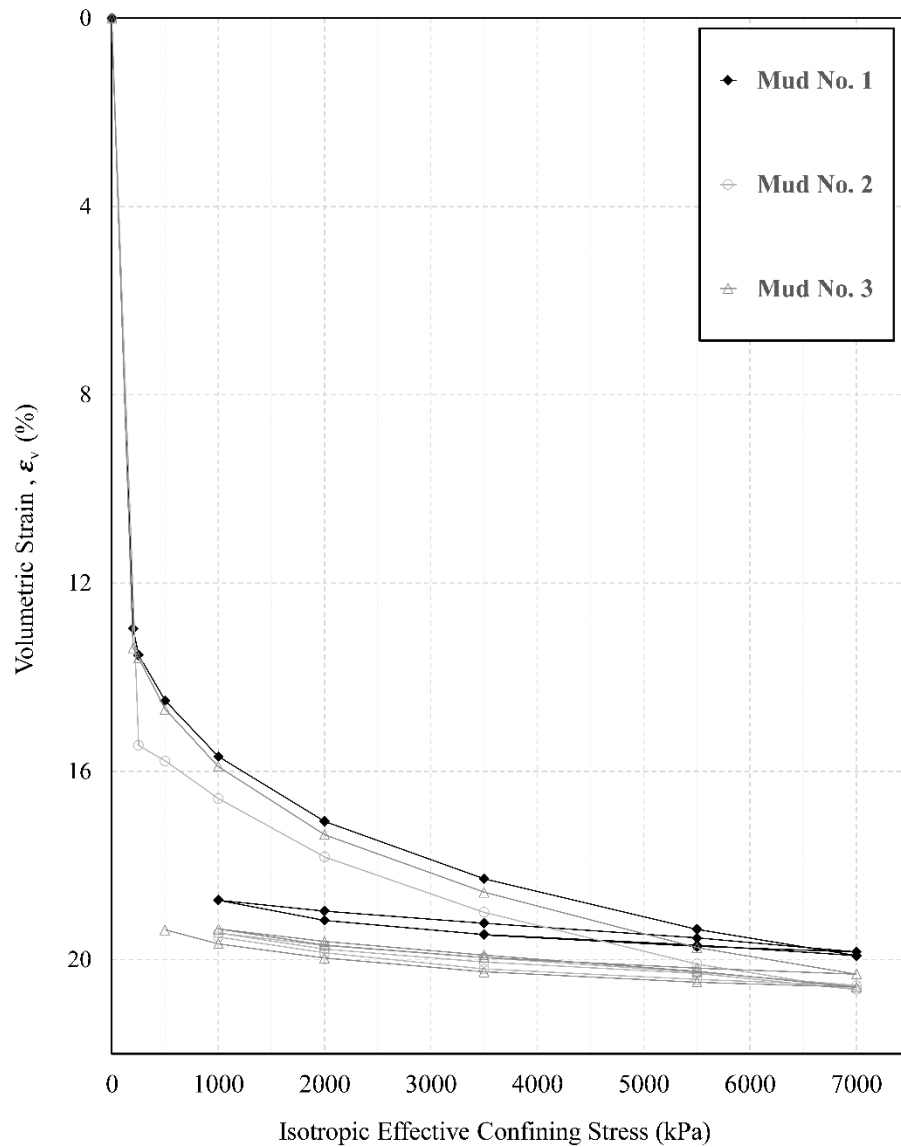


Figure 5-2 Bulk volume change of analog mud samples

As stated before, the mud samples were reconstituted using the slurry consolidation method. Therefore, during the saturation process, under confining stress of 0.2 MPa, the specimens underwent a significant amount of volume change (Figure 5-2). Moreover, some hysteresis loops can be observed in the consolidation curves between the loading, unloading, and reloading branches.

5.3.1. Isotropic Bulk Compressibility

Figure 5-3 shows the variation of the coefficient of isotropic bulk compressibility (C_b) for analog mud samples. As shown in this graph, despite the observed hysteresis in consolidation curves, the computed compressibility values for each effective confining stress are very close.

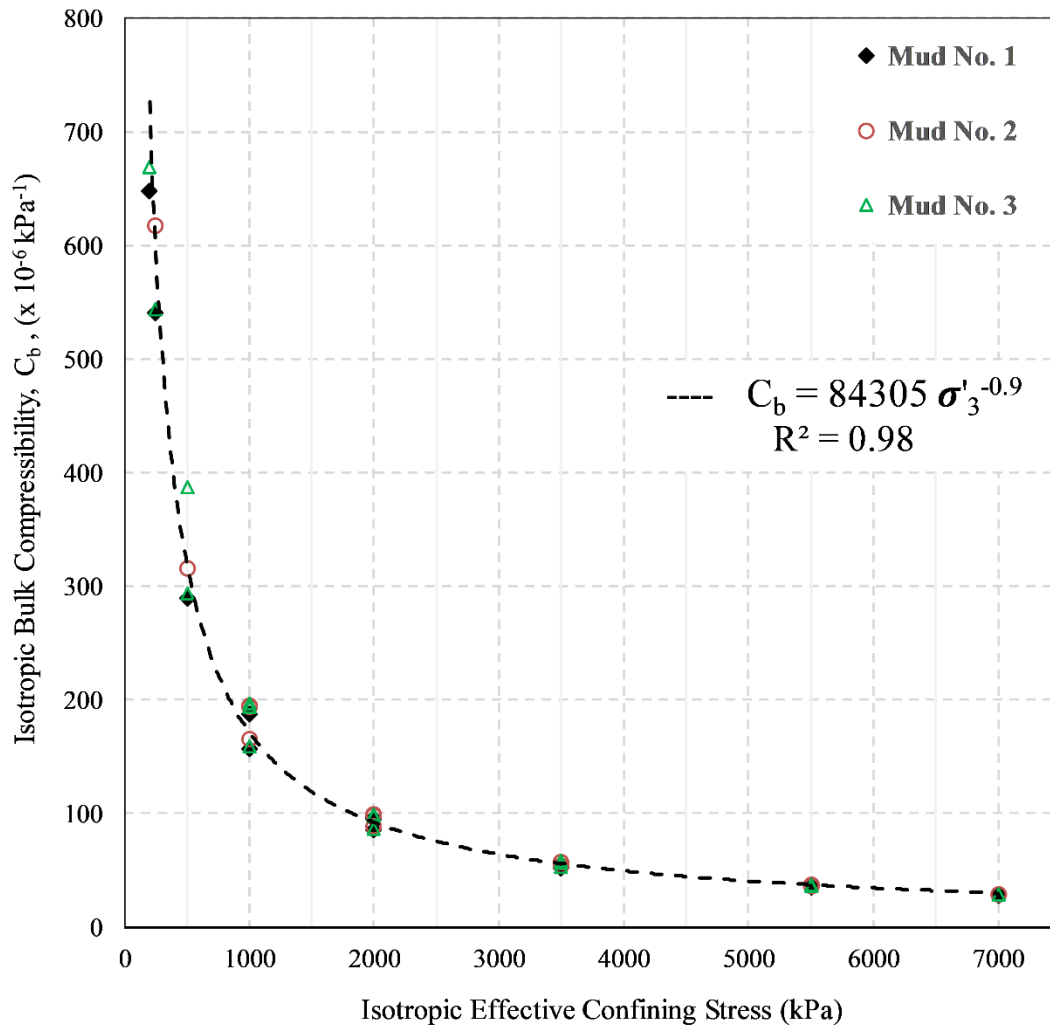


Figure 5-3 Coefficient of isotropic bulk compressibility of analog mud samples

5.3.1.1. Empirical Correlation for change in Bulk Compressibility

Analyzing the final results revealed that bulk compressibility is a strong function of effective confining stress, particularly at low stress levels (below 2 MPa). A power law function was established to capture the relationship between the compressibility and effective confining stress, which can be expressed as follows:

$$C_b = a\sigma_3'^b \quad \text{Equation 5-1}$$

where C_b is the coefficient of bulk compressibility ($\times 10^{-6} \text{ kPa}^{-1}$), σ_3' is the effective confining stress (kPa), and a and b are constants.

Using curve fitting techniques, the constants a and b can be determined for each test (and even for every single cycle of loading or unloading), but given the consistency of the constants for all tests, a single curve fit equation was developed. Figure 5-3 illustrates the power law curve fit for all data where the values of the constants a and b are 84305 and -0.9 respectively

Although the developed relationship can be used to estimate C_b based on effective confining stress levels, its applicability is limited to σ_m' ranging from 0.2 MPa to 7 MPa only. Therefore, extra caution needs to be exercised for any applications out of this range.

5.4. Drained Triaxial Compression Test

The drained triaxial compression tests were conducted with effective confining stresses of 0.5, 1, and 3.5 MPa. A total of three tests were performed on analog mud samples. The results of these isotropically consolidated drained shear tests are plotted together in Figure 5-4. As can be seen in this figure, the samples' stress-strain behavior is strongly influenced by the confining stress. At all three confining stresses, semi-ductile failure was observed. Therefore, the deviatoric stress did not drop significantly after the peak shear strength was reached.

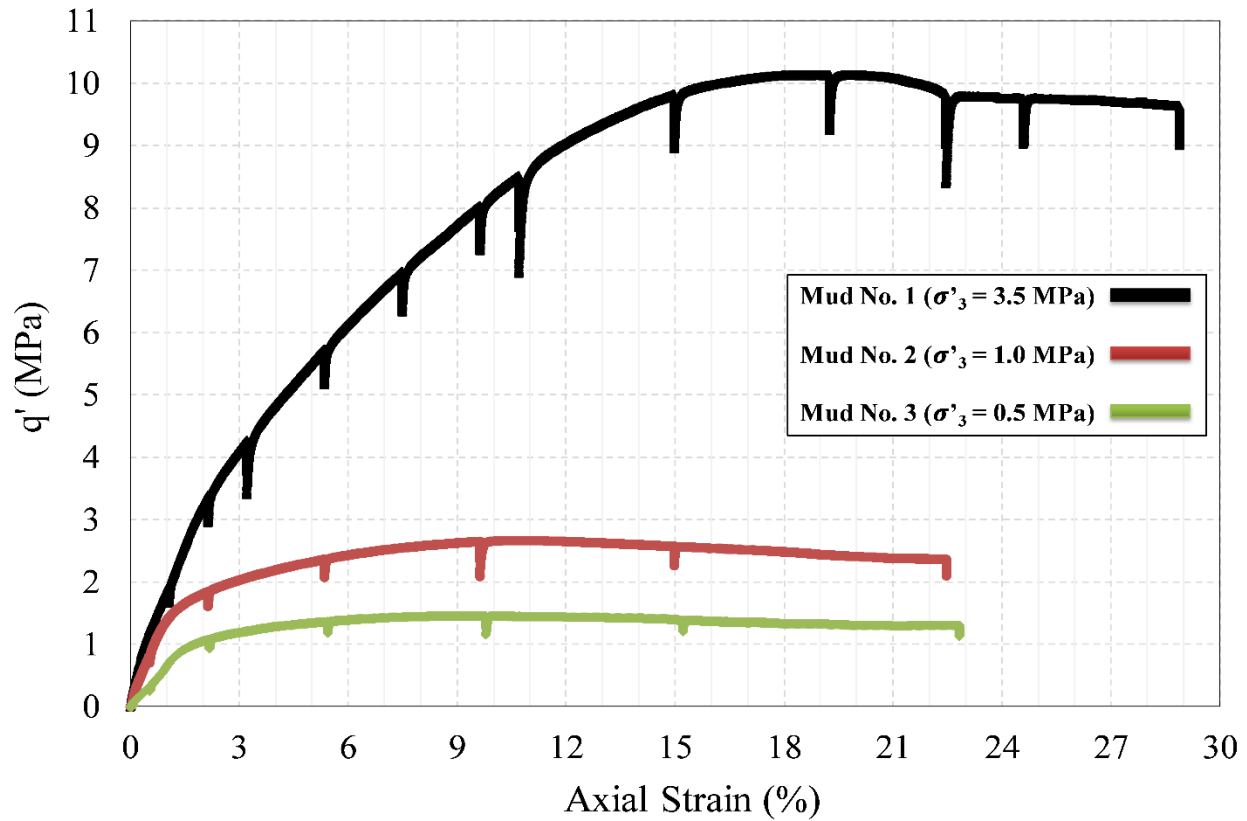


Figure 5-4 Isotropically consolidated drained triaxial compression tests on analog mud samples

5.4.1. Stress-Strain Behavior

5.4.1.1. Modulus of Elasticity

Following the same procedure explained in section 4.4.1.1, Young's modulus (E) was calculated for each mud specimen using its stress-strain curve.

Figure 5-5 shows Young's modulus changes for analog mud samples with effective confining stresses. As can be seen, the modulus of elasticity increases with the increase in effective confining stress, and its variation with σ_3' is nonlinear.

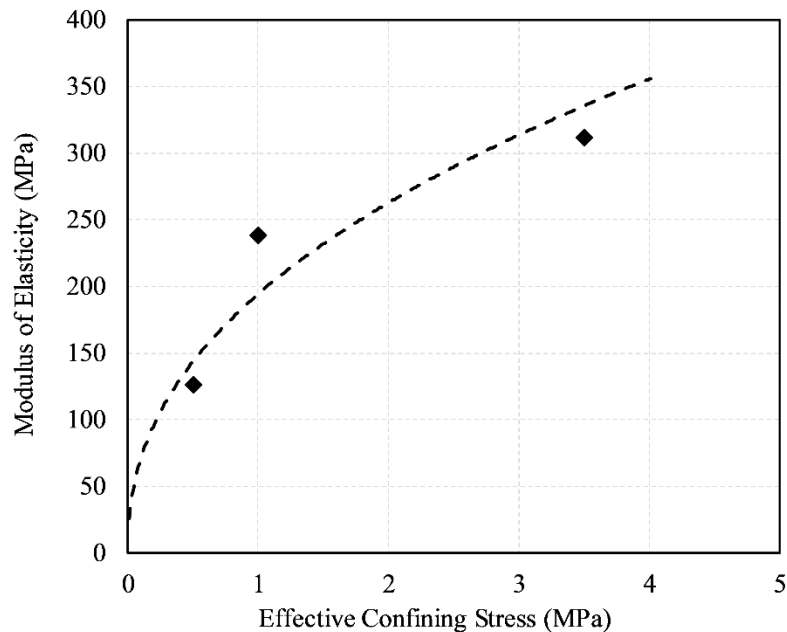


Figure 5-5 Variation of modulus of elasticity versus effective confining stress for analog mud samples

5.4.1.2. Volumetric Behavior during Shearing

Figure 5-6 illustrates the volumetric behavior during shearing for analog mud samples. It is clear from this graph that the dilative or contractive behavior of the mud specimens during shearing is predominantly controlled by the value of effective confining stress (σ_3'). In fact, all the tests displayed contraction to a certain level at the beginning of the shearing, and subsequently showed different volume changes with an increase in axial strain depending on their confining stress. It was observed that under 3.5 MPa effective confining stress, contraction continued until 13% axial strain, then the sample started to dilate in shear. But in total, the sample could not retrieve its initial volume and contracted by the end of shearing in this test. On the other hand, for the samples under effective confining stresses of 1 and 0.5 MPa, after a short period of contraction at the beginning of the tests, which stopped before the axial strain of 2%, both specimens dilated noticeably up to the end of shearing.

As stated before, all mud samples were isotropically consolidated resulting in a high pre-shear density and consequently it was expected that volumetric dilation would occur during compression

shearing. However, the results showed that their volumetric behavior is completely controlled by the effective confining stress. The reasons for this phenomenon are explained in detail in section 4.4.1.2.

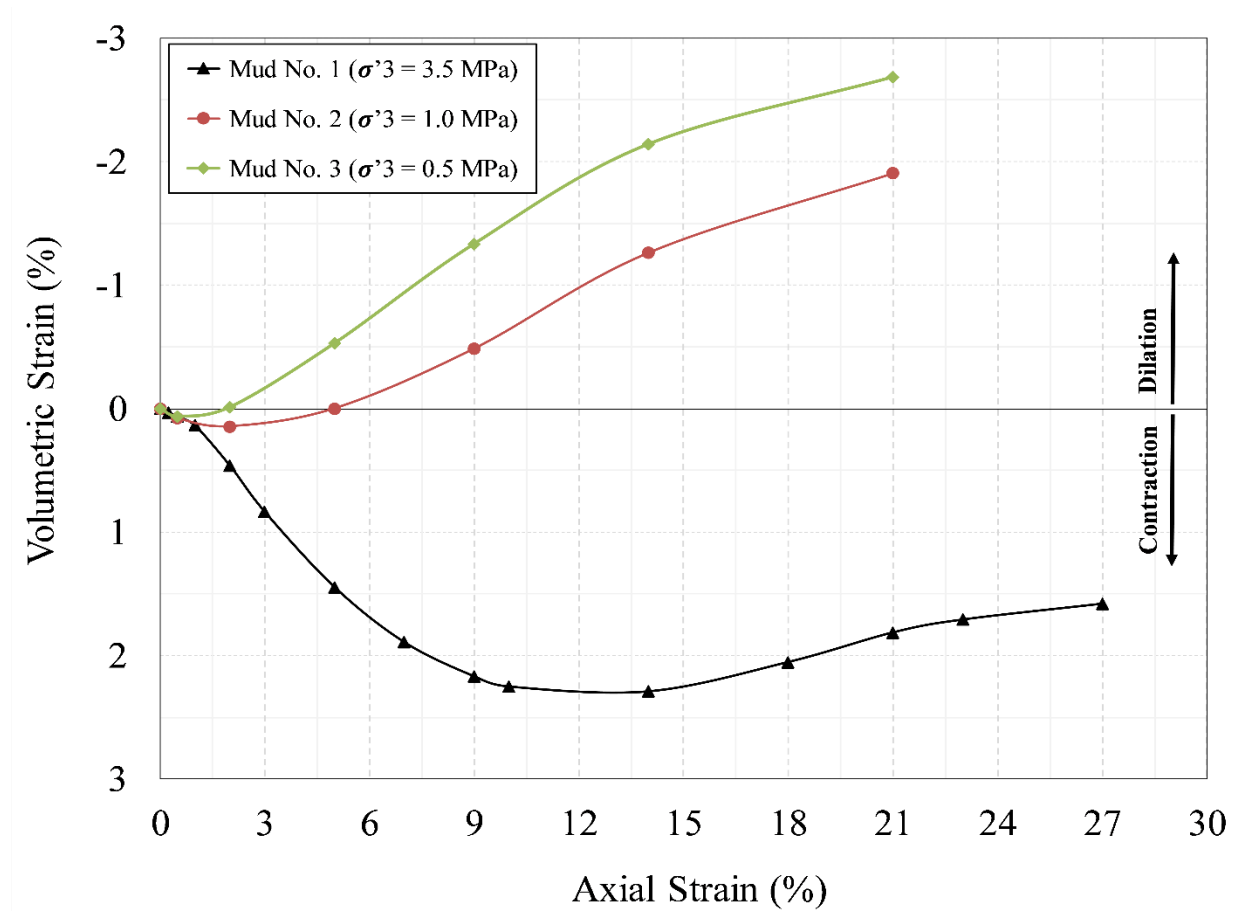


Figure 5-6 Volumetric behavior of analog mud samples during drained triaxial compression tests

5.4.1.3. Poisson's Ratio

Following the same procedure explained in section 4.4.1.1, Poisson's ratio (ν) was calculated for each mud specimen using Equation 4-2. As can be seen in Table 5-1, the calculated ν values for all mud samples are almost the same.

5.4.1.4. Dilation Angle

Following the same procedure explained in section 4.4.1.4, the dilation angle (ψ) was calculated for each mud specimen using its volumetric behavior and Equation 4-4.

Figure 5-7 presents the dilation angle changes with effective confining stress for analog mud samples. As can be seen, the ψ decreases with the increase in effective confining stress, and its variation with σ_3' can be described using a logarithmic function.

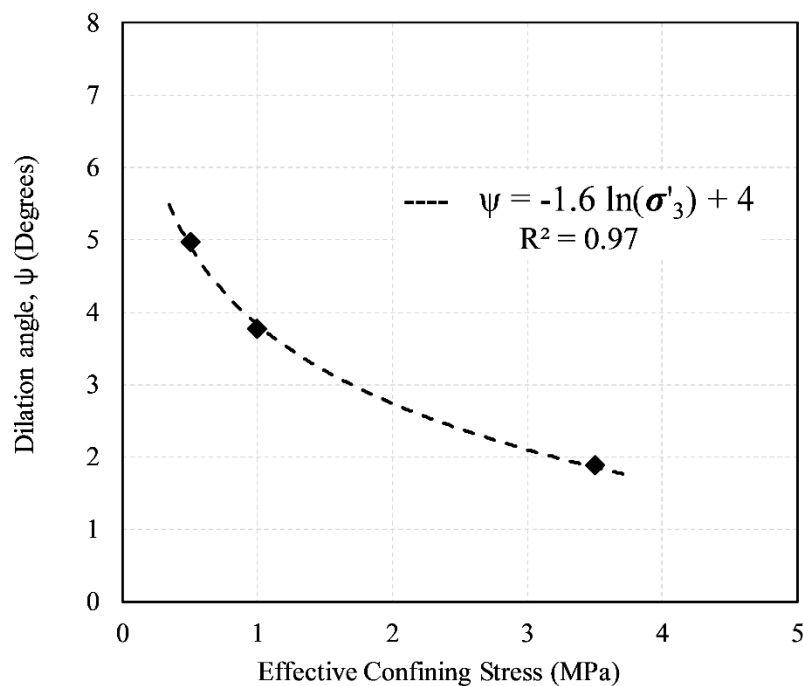


Figure 5-7 Variation of dilation angle with effective confining stress for analog mud samples

5.4.1.5. Specimens' Deformation Patterns and Mode of Failure

Following the same procedure explained in section 4.4.1.5, the mode of failure in analog mud samples was investigated. Figure 5-8 to Figure 5-10 show the mud specimens after they were triaxially failed under effective confining stresses of 3.5 , 1, and 0.5 MPa respectively. The Mud

No. 2 (σ_3' of 1MPa) was significantly disturbed during membrane removal; therefore, it could not be retrieved for CT scanning.

It is noted that the center of all three specimens substantially bulged outward, and several cracks formed on both sides of these samples. The creation of cone-shaped zones at the top and bottom of the samples was more evident in Mud No. 1 and 2 (σ_3' of 3.5 and 1 MPa). As discussed before, these cracks formed because of the friction between loading platens and mud samples. It should also be noted that upon the removal of axial and confining stresses at the end of the test, some shape rebounding might have occurred in the mud samples. Additionally, freezing the samples, and removing the Viton[®] membrane could both cause significant disturbance to the deformed shape of the sample. Therefore, extra caution needs to be exercised in analyzing these images.

By comparing the deformed shape of analog mud specimens with the deformation modes presented in Figure 4-10 and Figure 4-11, it can be concluded that the mode of failure for these samples is semi-ductile (Type IC) or ductile-faulting type. Because no clear shear failure lines were observed in the analog mud samples, obvious peaks of deviatoric stress were not observed on the stress-strain curves of these samples. It is also worth noting that the consolidation-induced volume change in the mud samples was significant; therefore, the samples showed considerable double cone type deformation during this phase (Type IC in Figure 4-9). Despite the shape rebounding that occurred upon the removal of pressures, the effects of such hydrostatic loading-induced volume changes were evident at both ends of the specimens at the end of shearing. This behavior is very similar to the case that is schematically depicted in Figure 4-12-E.



Figure 5-8 Mud sample loaded in an isotropically consolidated drained shear test under σ_3' of 3.5 MPa



Figure 5-9 Mud sample loaded in an isotropically consolidated drained shear test under σ_3' of 1 MPa

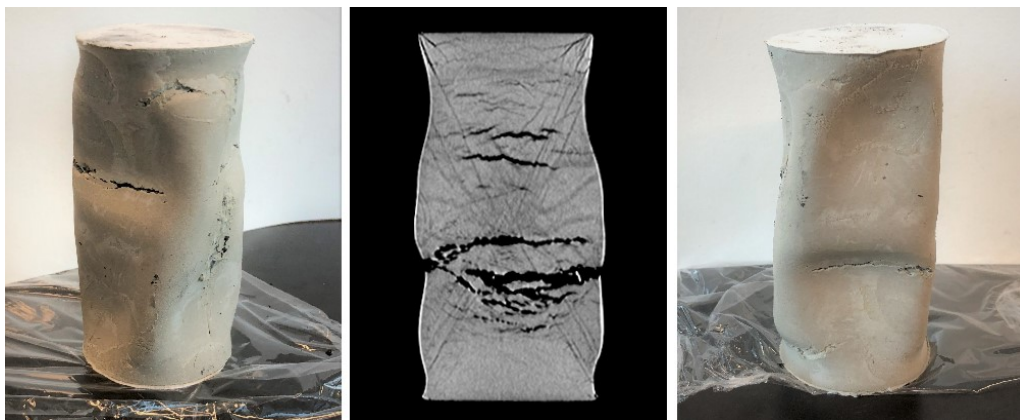


Figure 5-10 Mud sample loaded in an isotropically consolidated drained shear test under σ_3' of 0.5 MPa

5.4.2. Drained Shear Strength

From the stress-strain curves in Figure 5-4, it is noted that the shear strength of mud samples is highly dependent on the effective confining stress. Indeed, increasing the effective confining stress leads to a rise in shear strength. In addition, for all tested analog mud samples, the post-peak stress reduction was not significant. Such a minor post-peak shear strength reduction is due to the absence of an interlocking structure within the reconstituted samples, and also to the relatively high confining stresses under which the specimens were sheared.

In order to develop the failure envelope for the analog mud specimens, their stress paths were plotted in s' - t space. As demonstrated in Figure 5-11, a linear equation can capture the relationship between t and s' over the effective stress range tested.

$$t = 0.6 s' - 0.01$$

Equation 5-2

$$R^2 = 0.97$$

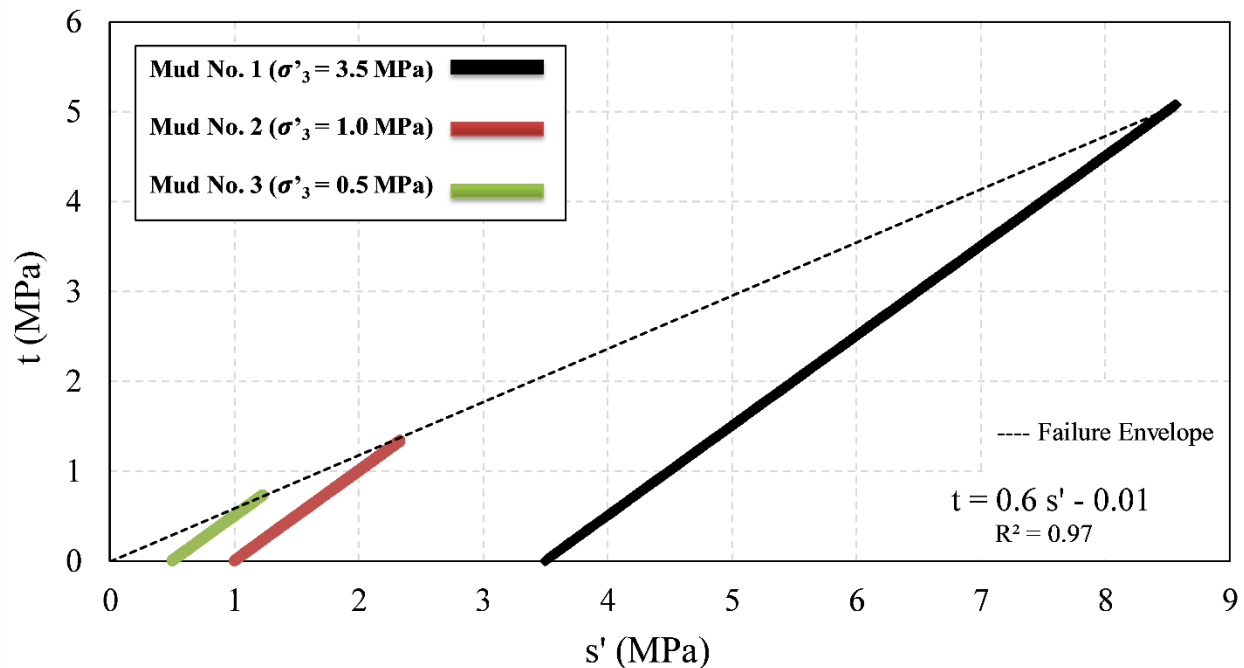


Figure 5-11 Drained triaxial compression tests stress paths and failure envelope for analog mud samples

5.4.2.1. Cohesion

From the peak failure envelope in $s'-t$ space (Figure 5-11), it can be concluded that the reconstituted analog mud sample has no cohesion. This is similar to the final results from the Athabasca Wabiskaw-McMurray succession shale and mudstone samples.

5.4.2.2. Friction Angle

Using the peak failure envelope in $s'-t$ space, a friction angle of 36° was computed for the reconstituted mud specimens. It should be noted that other researchers have reported almost the same value of friction angles for McMurray mudstone and shale samples, as well as Clearwater and Wabiskaw shale specimens (Kosar, 1989; Chalaturnyk, 1996; Suncor Energy, 2009).

5.4.2.3. Axial and Volumetric Strains at Peak Shear Strength

Figure 5-12 and Figure 5-13 show the axial and volumetric strains at peak shear strength with the effective confining stresses respectively. From these plots, it is noted that the rise in effective confining stress leads to an increase in the axial strain, while it decreases the volumetric strain. In fact, for the tests performed at low effective confining stresses, the volumetric strain at peak shear strength was negative. This means that the samples' volume increased, whereas for high effective confining stresses, the volumetric strain at peak became positive, which represents volume decrease in the specimen (Table 5-1). Therefore, the dilative or contractive behavior of mud samples is governed by the value of effective confining stress. Section 4.4.1.2 provides a detailed explanation for these volumetric reactions.

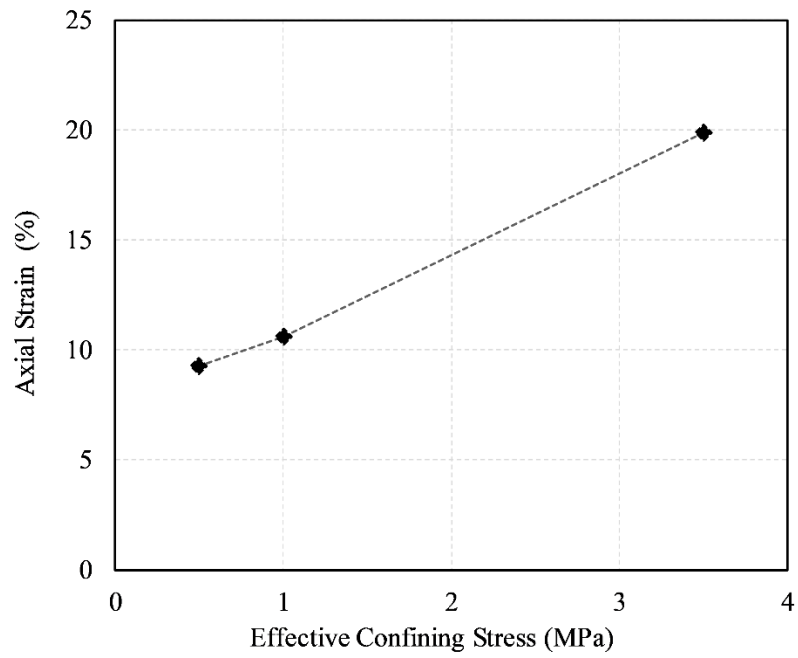


Figure 5-12 Peak axial strain for analog mud samples

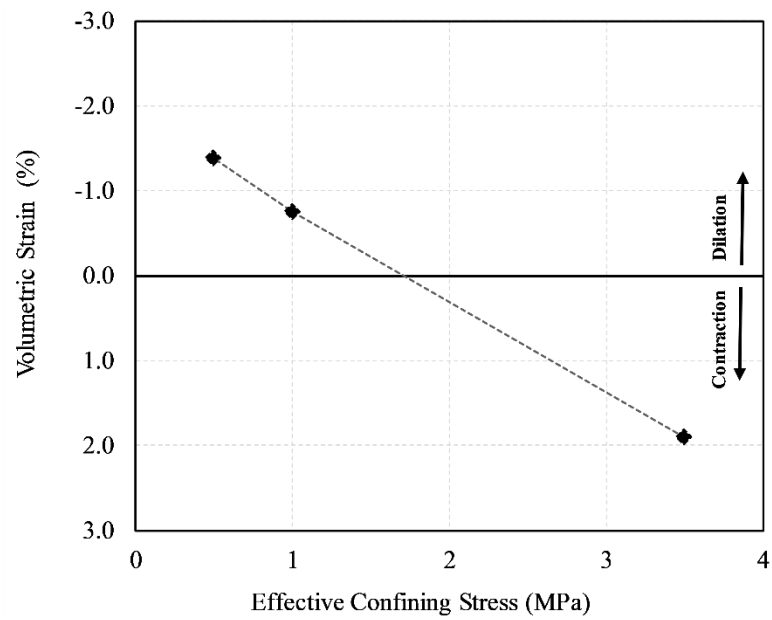


Figure 5-13 Peak volumetric strain for analog mud samples

Table 5-1 Isotropically consolidated drained triaxial compression tests data for analog mud samples

Test	Effective Confining Stress (MPa)	Back Pressure (MPa)	Deviatoric Stress at Peak Shear Strength (MPa)	Axial Strain at Peak Shear Strength (%)	Volumetric Strain at Peak Shear Strength (%)	Young Modulus @ $\varepsilon_a=1\%$ (MPa)	Young Modulus @ $\varepsilon_a=0.2\%$ (MPa)	Poisson's Ratio
Mud No. 1	3.5	3.0	10.1	19.9	1.9	198	312	0.40
Mud No. 2	1.0	3.0	2.7	10.6	-0.7	143	238	0.41
Mud No. 3	0.5	3.0	1.5	9.3	-1.4	62	126	0.43

5.5. Permeability Test

5.5.1. Absolute Permeability Evolution under SAGD Stress Paths

As delineated in section 4.5.1, a reservoir undergoes two major geomechanical reactions during a SAGD operation. These reactions are i) decreasing mean effective stress due to pore pressure injection, and ii) increasing mean and deviatoric stress due to thermal expansion. They both significantly affect the value of absolute permeability (K_a), and consequently the performance of the SAGD project.

In order to understand the effects of these geomechanical processes on absolute permeability of McMurray mudstone, a series of tests was performed on reconstituted analog mud samples. These tests were designed to simulate the stress state and pore pressure conditions of the reservoir during a SAGD operation. It should also be noted that due to the inherent geological heterogeneity and complexity of the McMurray Formation, the value of initial in situ absolute permeability for mudstone varies at different locations within the reservoir. Therefore, this study focuses on changes to the initial absolute permeability (under SAGD stress paths), rather than on calculating the true value of in situ permeability.

In addition, as explained in section 3.5.5, to calculate the permeability of mud samples, each test was performed at three different flow rates, and the differential pressure along the sample was measured using three different methods. The final results show a minimal discrepancy between different flow rates and various differential pressure measurement techniques.

5.5.1.1. Permeability Changes during Isotropic Unloading

Following the same procedure explained in section 4.5.1.1, the evolution of permeability was investigated under the first component of the SAGD-induced stress path, which is decreasing mean effective stress, because of the increase in pore pressure.

Figure 5-14, Figure 5-15, and Figure 4-20 show the variations of volumetric strain and normalized absolute permeability of analog mud samples respectively with effective confining stresses during an isotropic unloading test. From the volumetric behavior of mud samples, it is noted that decreasing mean effective stress leads to an increase in the volume of the specimens (Figure 5-14). Furthermore, it was observed that absolute permeability of the sample increases up to 29% with a decrease in effective confining stress from 7 MPa to 1 MPa (Figure 5-15).

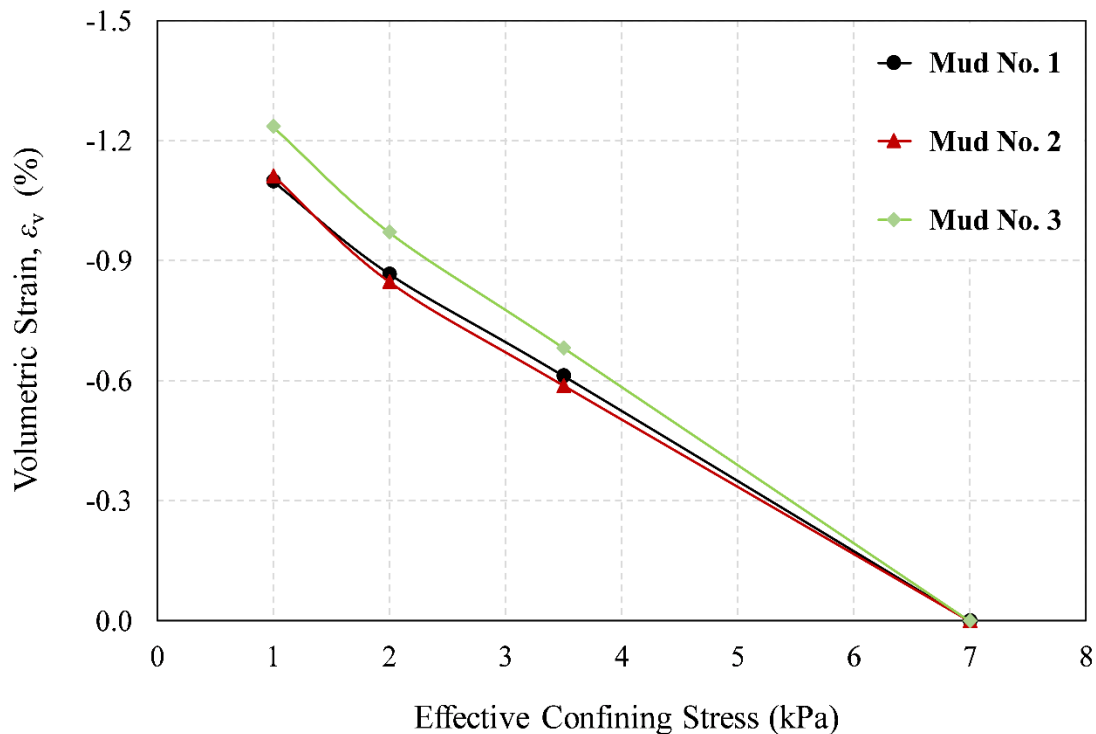


Figure 5-14 Volume change during isotropic unloading of analog mud samples

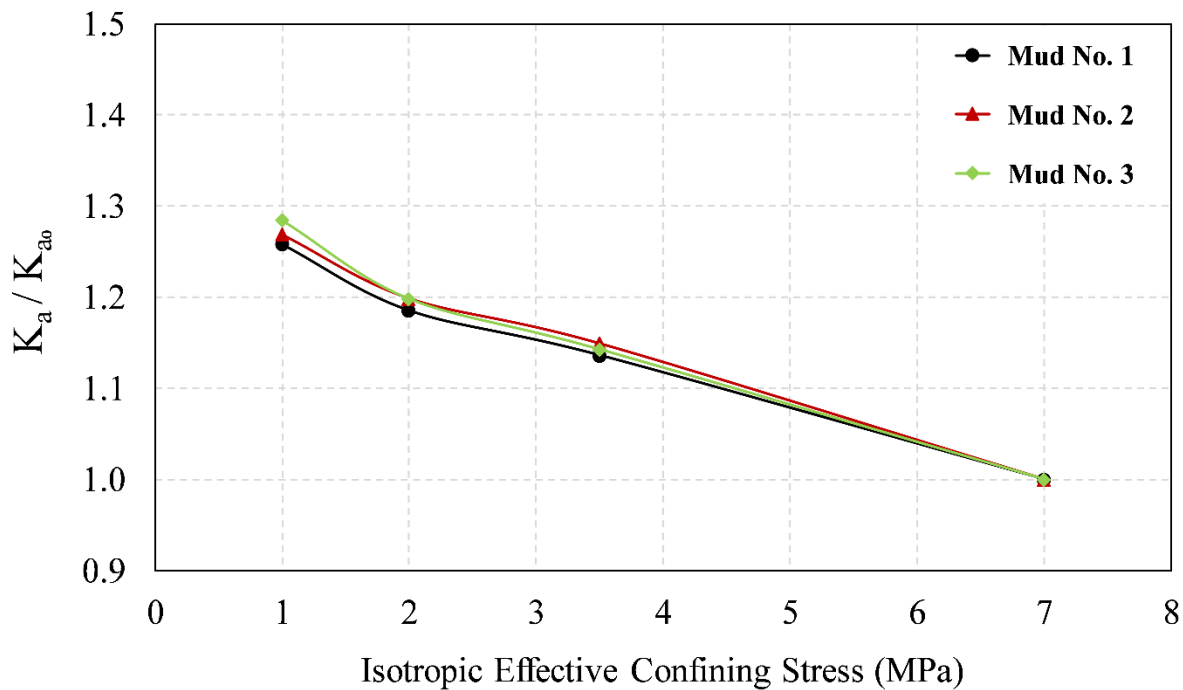


Figure 5-15 Normalized absolute permeability versus effective confining stress for analog mud samples

In view of the results presented in Figure 5-14 and Figure 5-15, it can be concluded that there is a direct relationship between the change in absolute permeability and the volumetric behavior of reconstituted analog mud samples. In order to describe such a relationship, the variation of K_a with the volumetric strain (ε_v) was plotted for all specimens in Figure 5-16. It can be seen that the dilative behavior of the samples during isotropic unloading resulted in permeability augmentation. As a case in point, for Mud No. 2, the volume change of 0.6% in the sample increased the permeability by 15%. As presented in section 4.5.1.1, during isotropic unloading the silt and clay particles move apart from each other to a small degree without any shearing or fabric distortion. This widens the flow channels within the samples and increases the permeability.

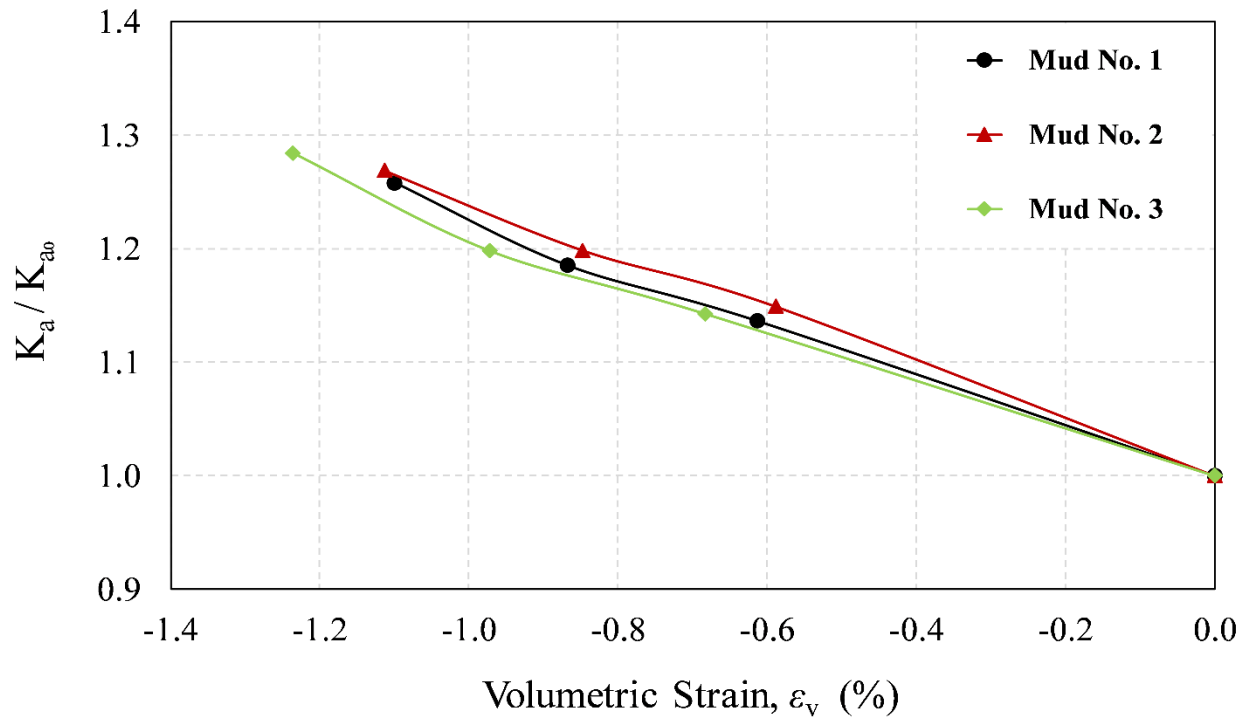


Figure 5-16 Normalized absolute permeability versus volume change for analog mud samples during isotropic unloading

Most of the former studies on mudstone, shale, and silt-clay mixtures have tried to relate the permeability development to porosity. Therefore, to examine the applicability of these studies, the variation of K_a with the changes in porosity is presented in Figure 5-17. Due to the small difference in the initial porosity value between the mud samples, the normalized porosity was used in this graph. As it was expected from the volumetric behavior of mud specimens, the porosity of the samples increased during isotropic unloading, and this led to an increase in the permeability values. More details on verifying the previous permeability relationships can be seen in section 5.6.1.2.

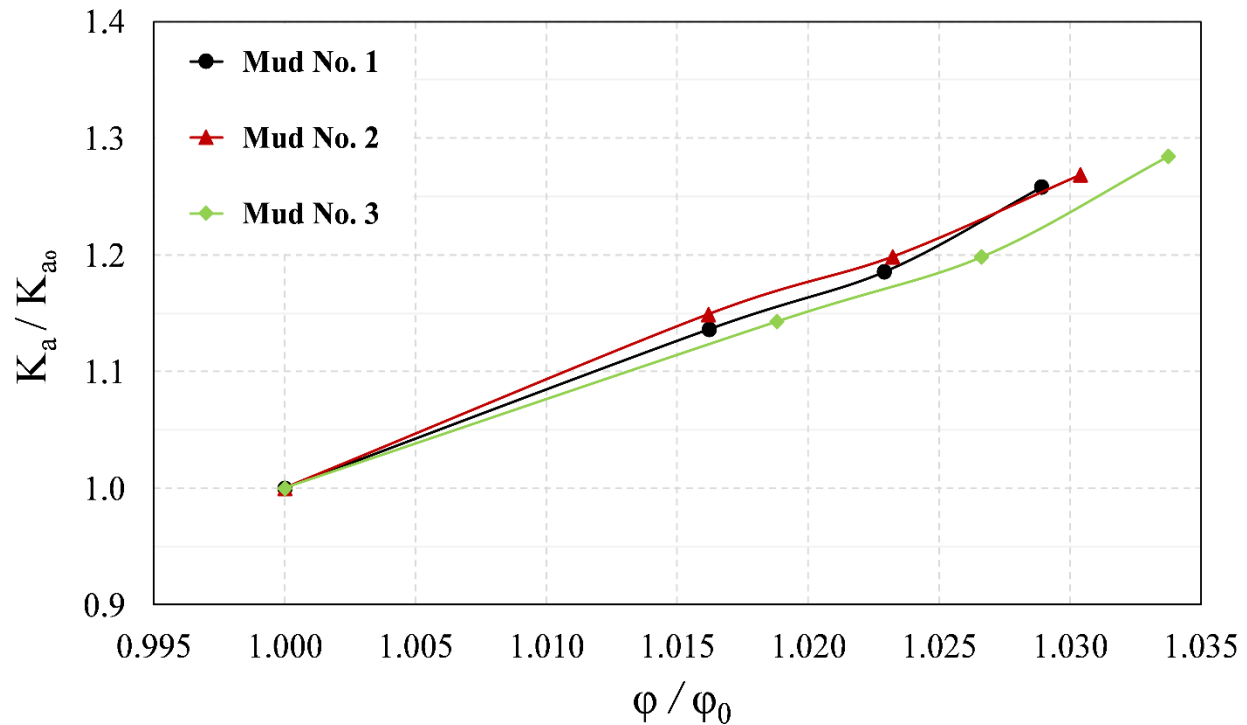


Figure 5-17 Normalized absolute permeability versus porosity for analog mud samples during isotropic unloading

5.5.1.2. Permeability Changes during Triaxial shearing

Following the same procedure explained in section 4.5.1.2, the evolution of permeability was investigated under the second component of SAGD-induced stress paths, which is increasing mean and deviatoric stresses.

As discussed before, in order to understand the permeability changes during shearing, the volumetric behavior of the samples needs to be analyzed first. Section 5.4.1.2 presents the volumetric behavior of analog mud specimens during triaxial compression tests. As illustrated in Figure 5-6, the volumetric behavior of mud samples during shearing is dominated by the value of the effective confining stress. In other words, mud samples show dilative behavior at low effective confining stresses, while they present contractive behavior at high effective confining stresses.

Figure 5-18 shows the variation of normalized absolute permeability with axial strain during triaxial shearing for all analog mud samples. It can be seen that the permeability continuously decreased throughout the shearing for the sample tested under an effective confining stress of 3.5 MPa. However, for the test performed under an effective confining stress of 1 MPa, the permeability decreased prior to the axial strain of 9%, then it started to grow until the end of shearing. In this test, despite the initial drop in the permeability value, the sample could almost retrieve its initial permeability by the end of shearing. Finally, for the test under an effective confining stress of 0.5 MPa, after a short period of permeability reduction which stopped before the axial strain of 0.5%, the permeability value continuously grew throughout the shearing. By the time that shearing was stopped for this sample, the amount of permeability augmentation was as high as 24%.

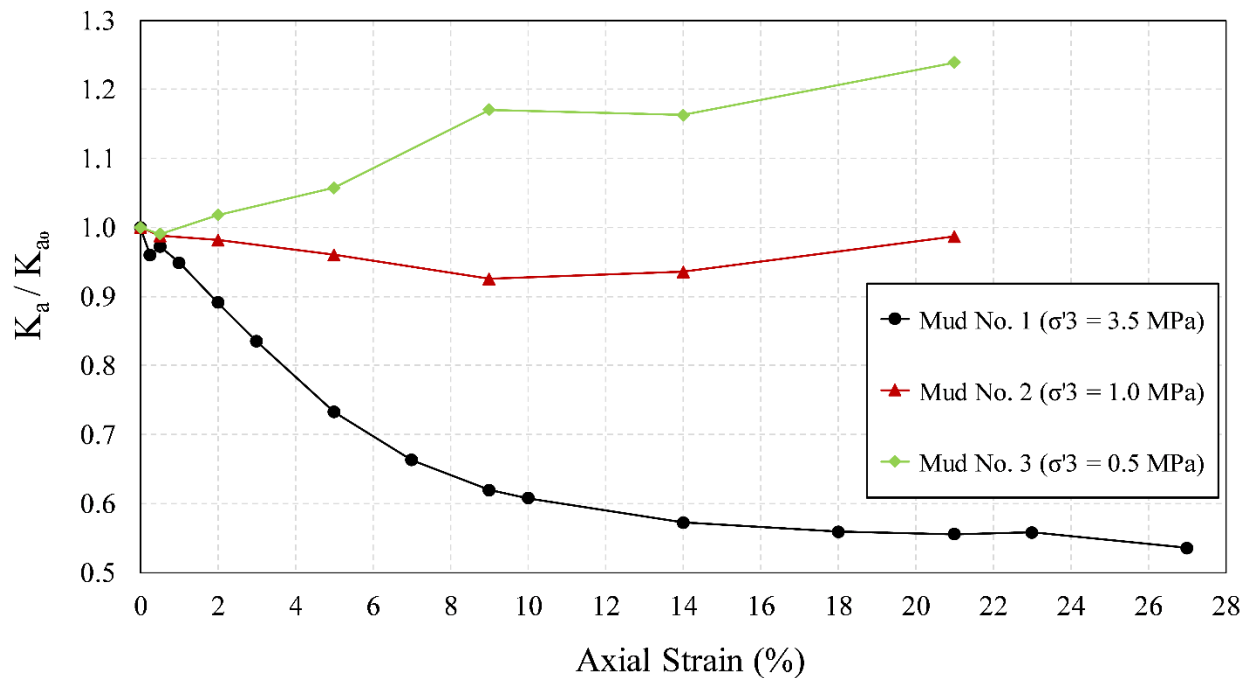


Figure 5-18 Normalized absolute permeability versus axial strain for analog mud samples during triaxial shearing

Figure 5-19 and Figure 5-20 present the variation of normalized absolute permeability with volumetric strain and porosity changes respectively. As can be seen in these graphs, unlike in the isotropic unloading tests, during shearing the sample's dilation (or the increase in porosity value) does not necessarily translate into permeability enhancement. For that to be effective, the amount of

effective confining stress needs to be low. The result also revealed that the volumetric strain was required to reach a certain level before its positive effect on permeability became noticeable. It was also observed that the contraction which happens during shearing under high effective confining stresses, could significantly decrease the value of absolute permeability in mud samples.

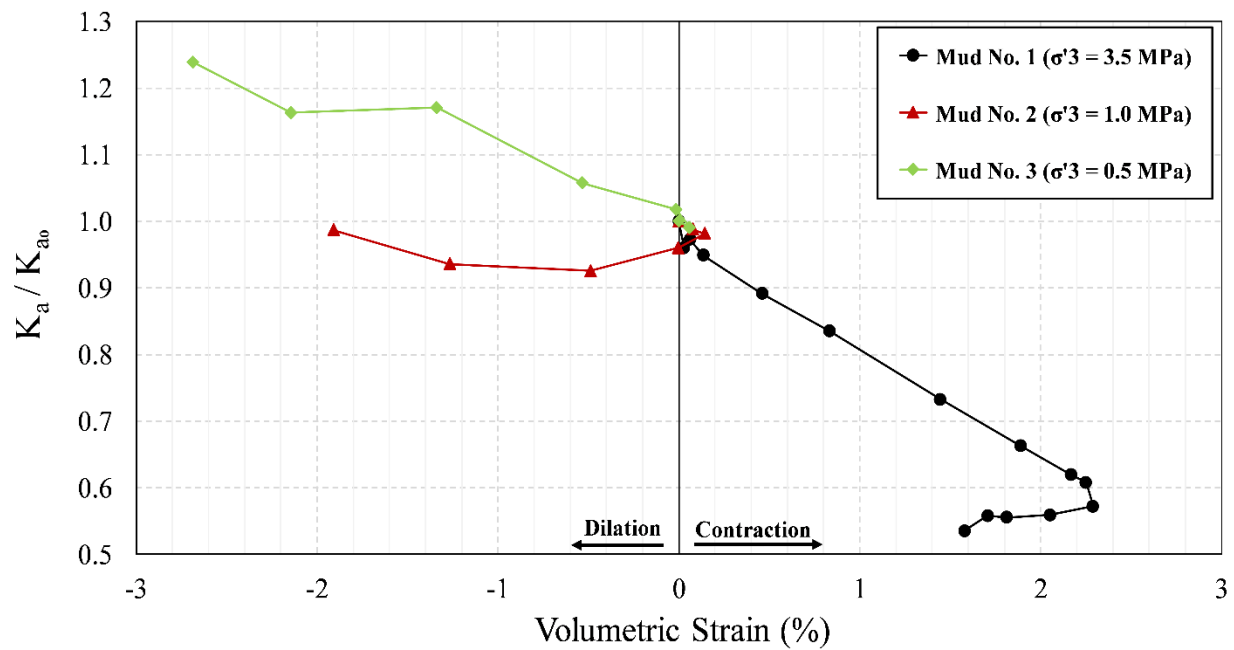


Figure 5-19 Normalized absolute permeability versus volumetric strain for analog mud samples during triaxial shearing

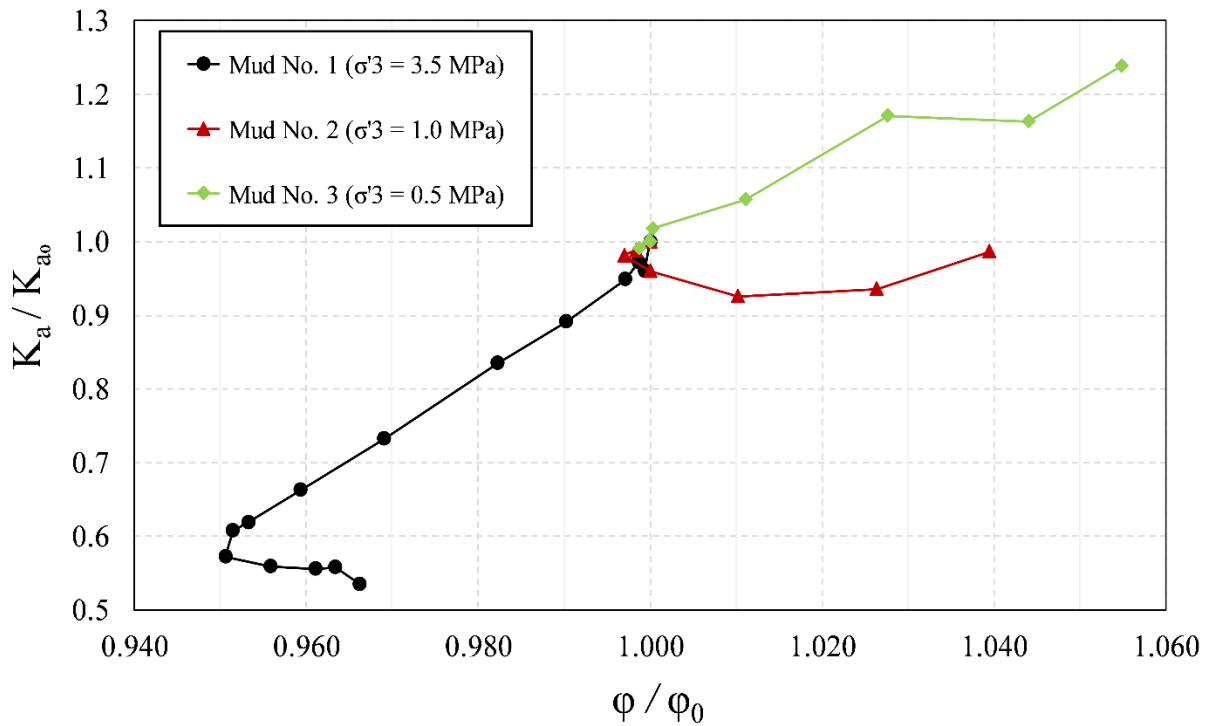


Figure 5-20 Normalized absolute permeability versus porosity for analog mud samples during triaxial shearing

As delineated in section 4.5.1.2, at low effective confining stresses, the new flow channels that were developed due to shearing could improve the sample's permeability. In contrast, at high confining stresses, these newly-formed flow paths are suppressed and lose their connectivity. Therefore, their effects on permeability become negligible. The other reason behind these phenomena is tortuosity variation during shearing. To illustrate, shearing a sample significantly disturbs its pore network and consequently changes its tortuosity value. At low effective confining stresses, when the flow channels are wide, this could decrease the tortuosity and enhance the permeability, while at high effective confining stresses, when the flow paths are tight, it could increase the tortuosity and reduce permeability.

5.6. Discussion and Conclusions

5.6.1. Comparison with Previous Experimental Studies on Shale and Silt-Clay Mixtures

This section discusses the outcomes of previous experimental studies on Clearwater Formation mudstone (including Wabiskaw Member shale), Lower and Upper McMurray Formation shale, and other reconstituted silt-clay mixtures to ensure the resemblance between analog mud samples and McMurray mudstone in terms of their geomechanical properties. Such analysis also provides an assurance of similarity between the mud layers of analog IHS and in situ ones, because, as explained in Chapter 2, these mud samples were used to reconstitute the analog IHS specimens.

5.6.1.1. Geomechanical Properties

5.6.1.1.1. Stress-Strain Behavior

Figure 5-21 displays the peak failure envelope from former laboratory studies on Clearwater shale, Wabiskaw shale, upper and Lower McMurray shale plus the results of this study. It can be seen that the results from analog mud samples (red crosses on the graph) are quite consistent with other data. As explained in section 4.6.1.1.1, the value of friction angle (ϕ) and cohesion (c) can be obtained using the failure envelope in s' - t plot. In this study, deriving average values for friction angle and cohesion of all shale types was avoided because each of these shale groups has slightly different porosity and composition. Therefore, the value of ϕ and c are reported separately for each category of specimens (Table 5-2).

Table 5-2 In situ shale cores and analog mud samples' strength parameters (Suncor Energy, 2005; Suncor Energy 2009; Chalaturnyk, 1996)

Sample Type	Friction Angle (Degree)	Cohesion (MPa)
Clearwater Shale (Triaxial Shear Test)	34	0.14
Clearwater Shale (Direct Shear Test)	32	0.10
Wabiskaw Shale (Triaxial Shear Test)	36	0.09
Wabiskaw Shale (Direct Shear Test)	35	0.01

Upper McMurray Shale	36	0.56
Lower McMurray Shale	48	0.00
Reconstituted Analog Mud	36	0.00

As can be seen in the table above, the values of friction angle and cohesion for analog mud samples are very close to the ones calculated for shale samples, particularly Wabisakaw shale. As stated earlier, the minor discrepancy observed in the results is due to the difference in the value of initial porosity (before shearing), as well as to the dissimilarity in grain size distribution and clay composition between the various types of shale cores.

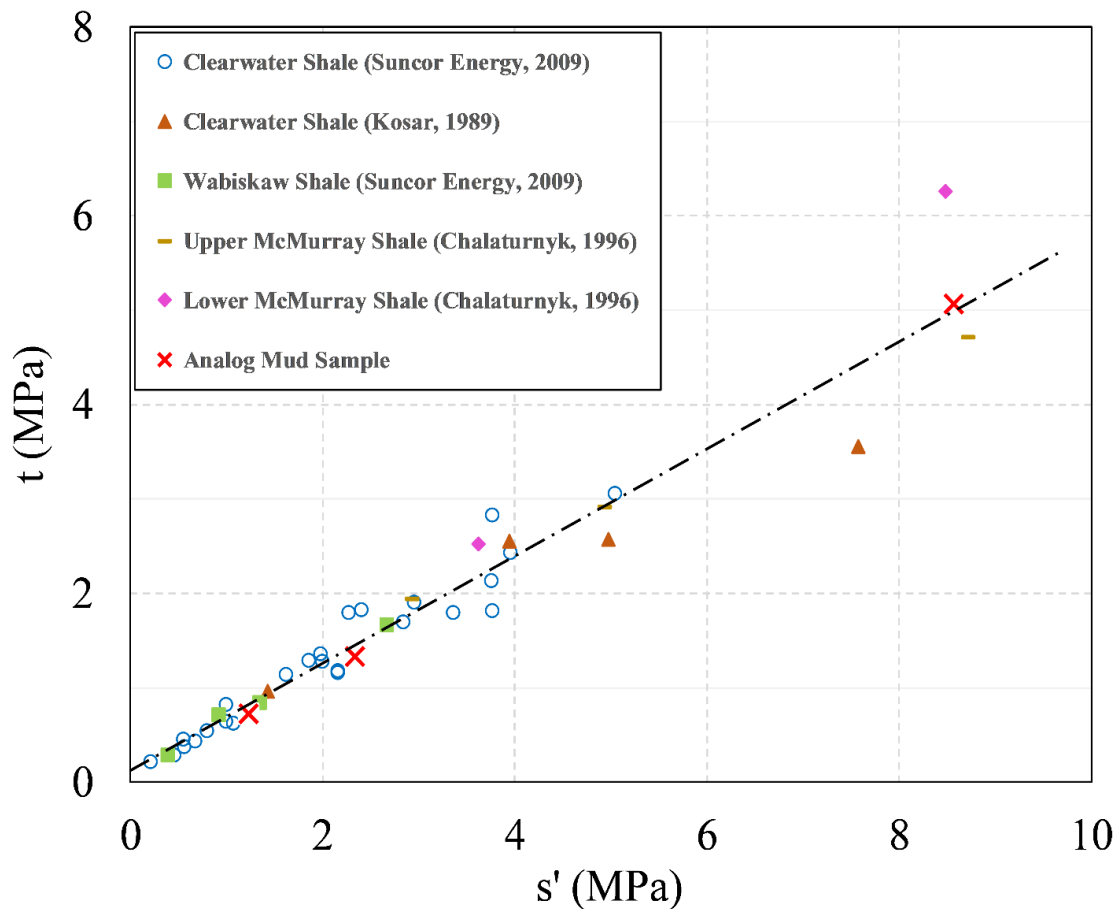


Figure 5-21 Peak failure envelope for in situ shale cores and analog mud samples

In order to investigate the dilatancy behavior of shale samples, their plastic deformation during shearing was analyzed, particularly those samples which had been tested under high effective

confining stresses or those having a lower value of initial porosity. The results showed that the value of dilatancy angle decreases with the increase in effective confining stress. This behavior was completely compatible with the dilation angle trend observed in analog mud specimens (Figure 5-7). In addition, the transition from peak dilation rate to residual dilation rate (which was explained in section 4.4.1.4) was also clearly apparent in both in situ shale cores and analog mud samples.

With the aim of comparing the stiffness of analog mud samples with in situ shale cores, the variation of their elastic modulus (E) with effective confining stresses (σ_3') was plotted in **Error! Reference source not found.** It can be seen that the value of E surges with the increase in σ_3' . Moreover, it is noted that the elastic modulus of mud samples (particularly the ones measured at the axial strain of 1%) are congruous with previous experimental studies on in situ shale samples. The observed discrepancy in the value elastic modulus is due to the difference in the strain level at which the E was calculated, and also to the dissimilarity in the density and composition of the tested samples. Due to these reasons, deriving a single equation which captures the relationship between E and σ_3' for all types of shale cores and mud samples was unfeasible.

As explained in section 4.6.1.1.1, in most cases, a standard hyperbolic function is chosen to define the dependency elastic modulus to effective confining stress (**Error! Reference source not found.**). Using the curve fitting techniques, the hyperbolic expressions for the elastic modulus of mud samples at the axial strain of 1% and 0.2% are:

$$E \text{ measured at } \varepsilon_a = 1\%: \quad E_i = 413p_a \left(\frac{\sigma_3'}{p_a} \right)^{0.4} \quad \text{Equation 5-3}$$

$$E \text{ measured at } \varepsilon_a = 0.2\%: \quad E_i = 855p_a \left(\frac{\sigma_3'}{p_a} \right)^{0.4} \quad \text{Equation 5-4}$$

While these equations can reasonably match the experimental data at low effective confining stresses, they underestimate (Equation 5-3) or overestimate (Equation 5-4) the value of E at high

effective confining stresses. Therefore, extra caution needs to be exercised for any applications out of the tested range.

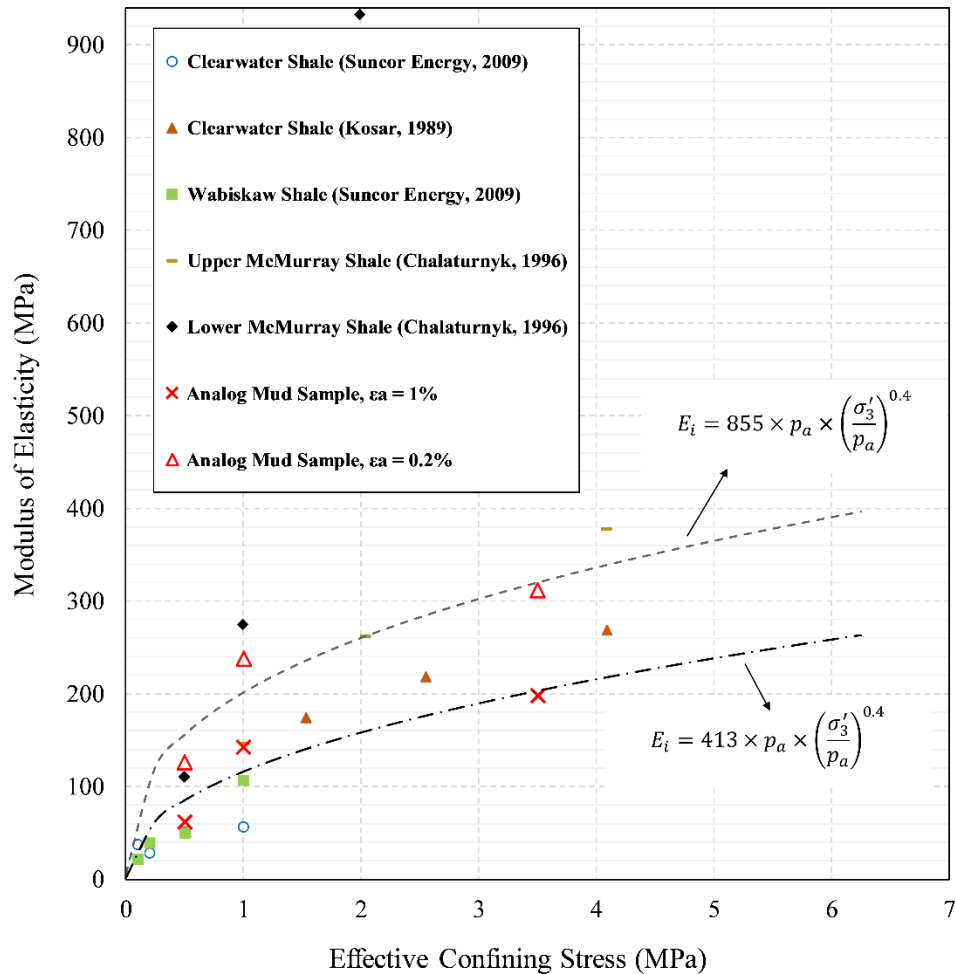


Figure 5-22 Modulus of elasticity versus effective confining stress for in situ shale cores and analog mud samples

5.6.1.1.2. Shear Strength

As shown earlier, the value of shear strength is greatly affected by the confining stress. Therefore, to compare the shear strength of analog mud samples with McMurray mudstone, the normalized deviatoric stresses of some of the previous studies on in situ shale cores were plotted versus the axial strain (Figure 5-23Figure 5-26). According to the results presented in these figures, the shear strength of the reconstituted mud samples (Figure 5-27) is similar to the other shale specimens.

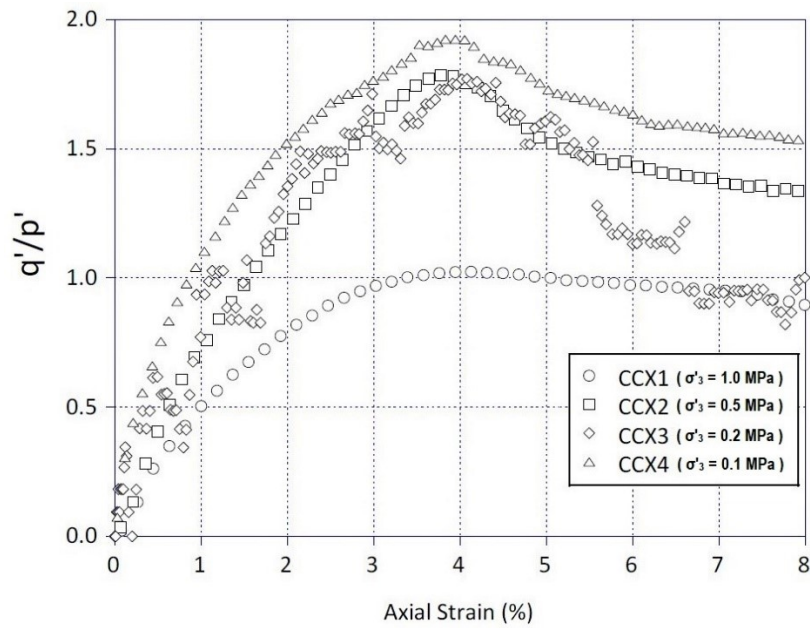


Figure 5-23 Normalized deviatoric stress versus axial strain for Clearwater shale (Suncor Energy, 2009)

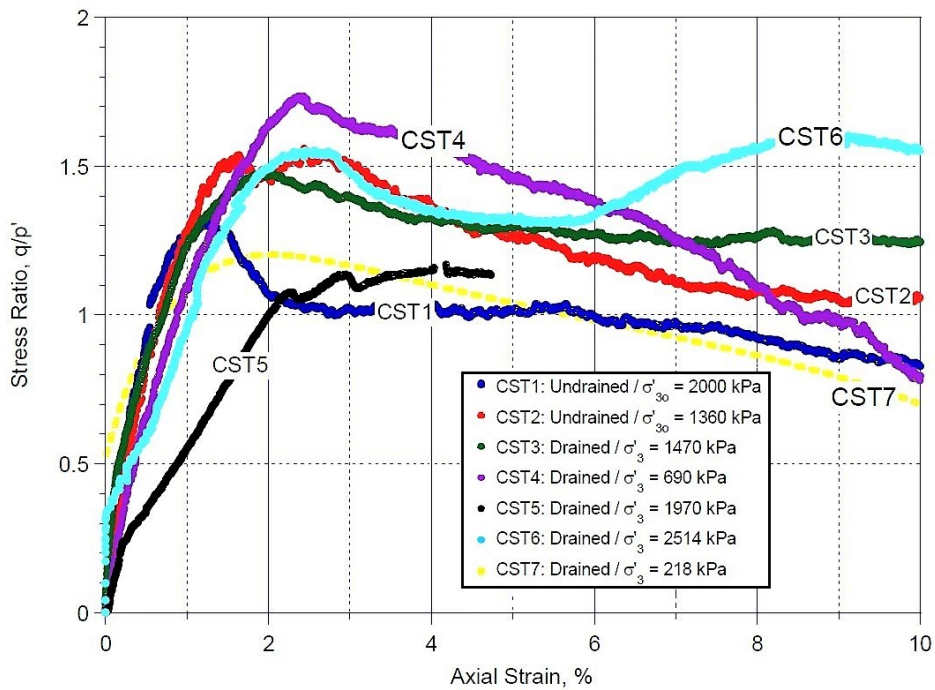


Figure 5-24 Normalized deviatoric stress versus axial strain for Wabiskaw shale (Suncor Energy, 2005)

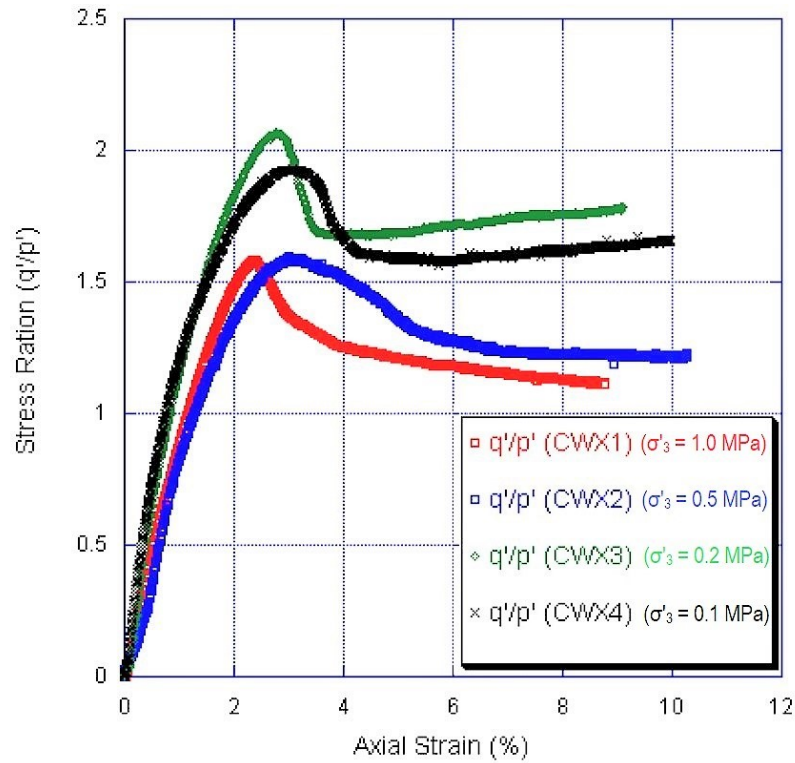


Figure 5-25 Normalized deviatoric stress versus axial strain for Wabiskaw shale (Suncor Energy, 2009)

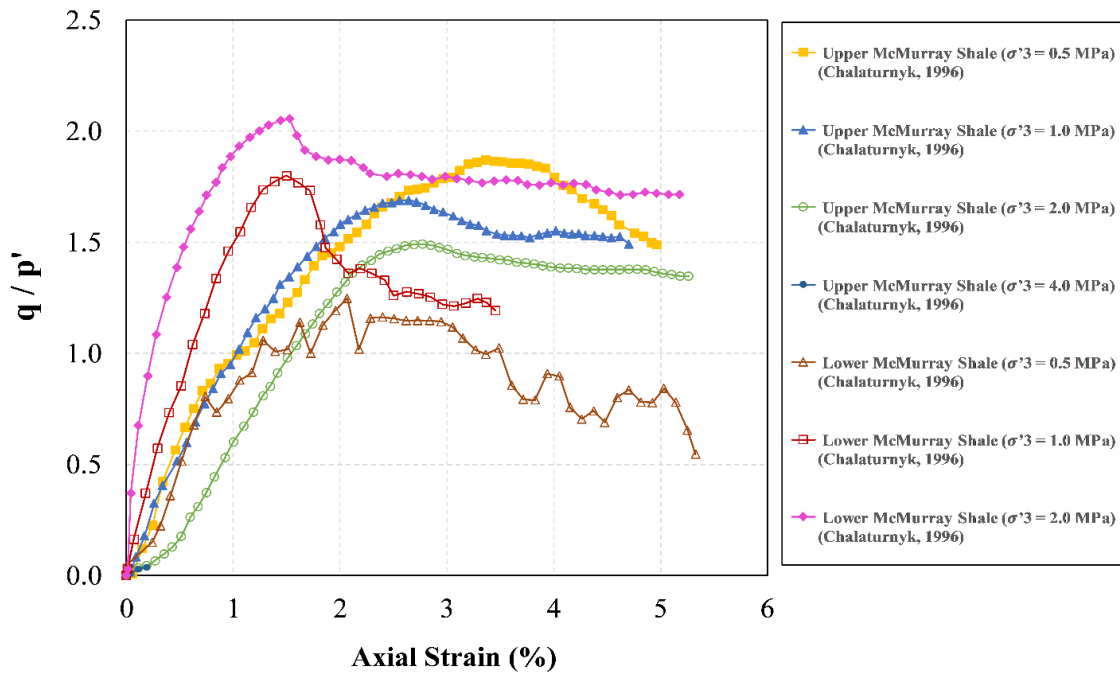


Figure 5-26 Normalized deviatoric stress versus axial strain for Upper and Lower McMurray shale (Chalaturnyk, 1996)

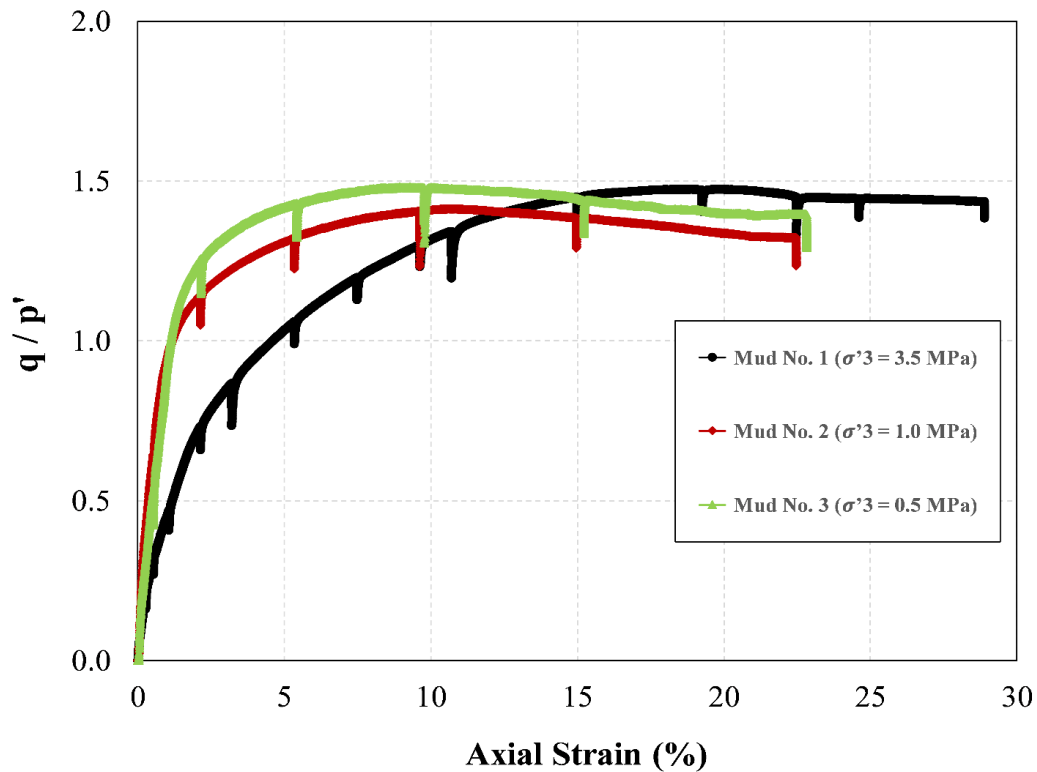


Figure 5-27 Normalized deviatoric stress versus axial strain for analog mud samples

Considering the comparative analysis explained in sections 5.6.1.1 and 5.6.1.2, it can be concluded that the geomechanical properties of analog mud samples match in situ shale and mudstone cores reasonably well.

5.6.1.2. Absolute Permeability

As explained in Chapter 2, due to the low permeability of mud layers, they typically act as a flow baffle during a SAGD operation and substantially influence the pore pressure development (or steam chamber advancement) within an IHS reservoir. Previous experimental studies on in situ shale and synthetic mudstone have shown that the initial value of absolute permeability can vary as much as several orders of magnitude, depending on the clay mineralogy and grain size distribution of the sample (Mondol, 2009; Suncor Energy, 2009). Therefore, assigning a single

value to the absolute permeability of McMurray Formation mudstone is an extremely difficult task, considering the inherent geological heterogeneity of this formation.

In an attempt to quantify the relationship between the porosity and permeability of mudstone, Mondol (2009) created several synthetic mudstones by mixing different portions of silt and clay (kaolinite). Afterward, these samples were mechanically compacted using an oedometer test setup (up to the vertical effective stress of 50 MPa), and their porosity and permeability were measured accordingly. Figure 5-28Figure 5-29 show the variation of porosity and permeability for two of Mondol's mixtures which had a somewhat similar composition to the analog mud samples. The results from analog mud specimens are also added to these graphs.

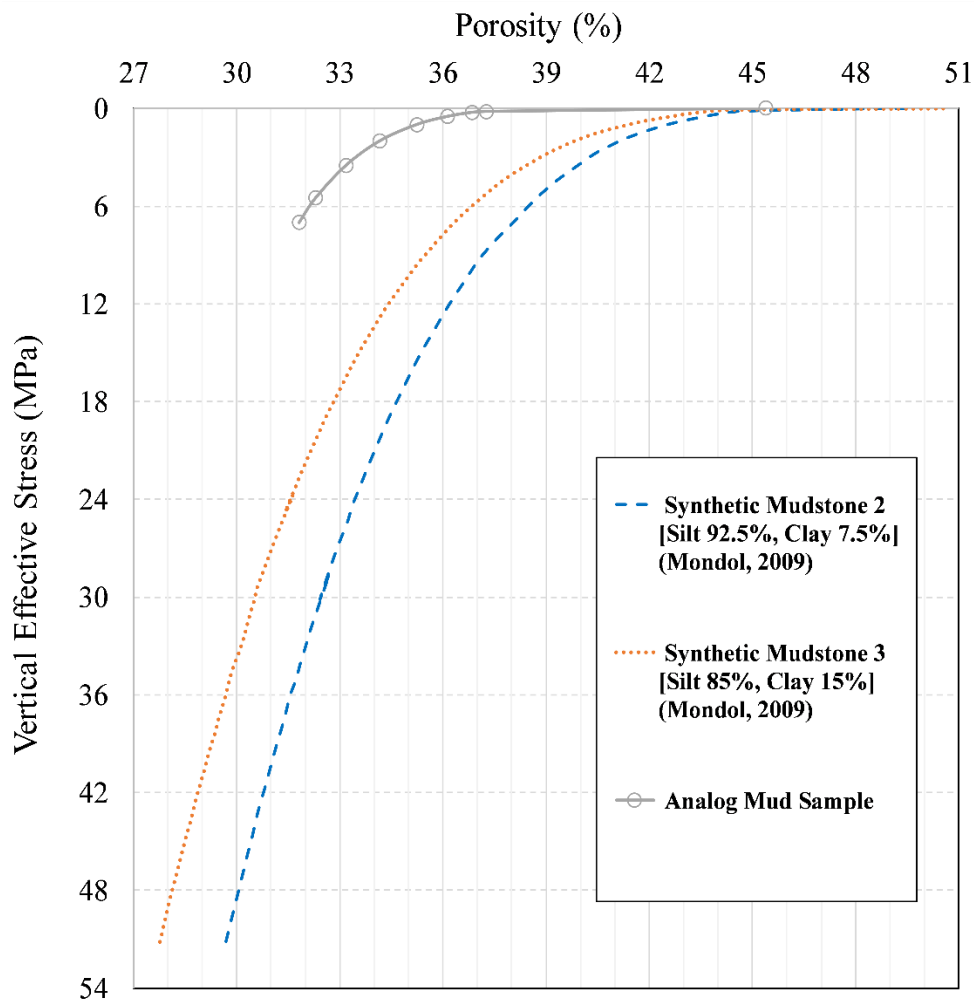


Figure 5-28 Porosity versus vertical effective stress for Mondol's synthetic mudstones and analog mud samples

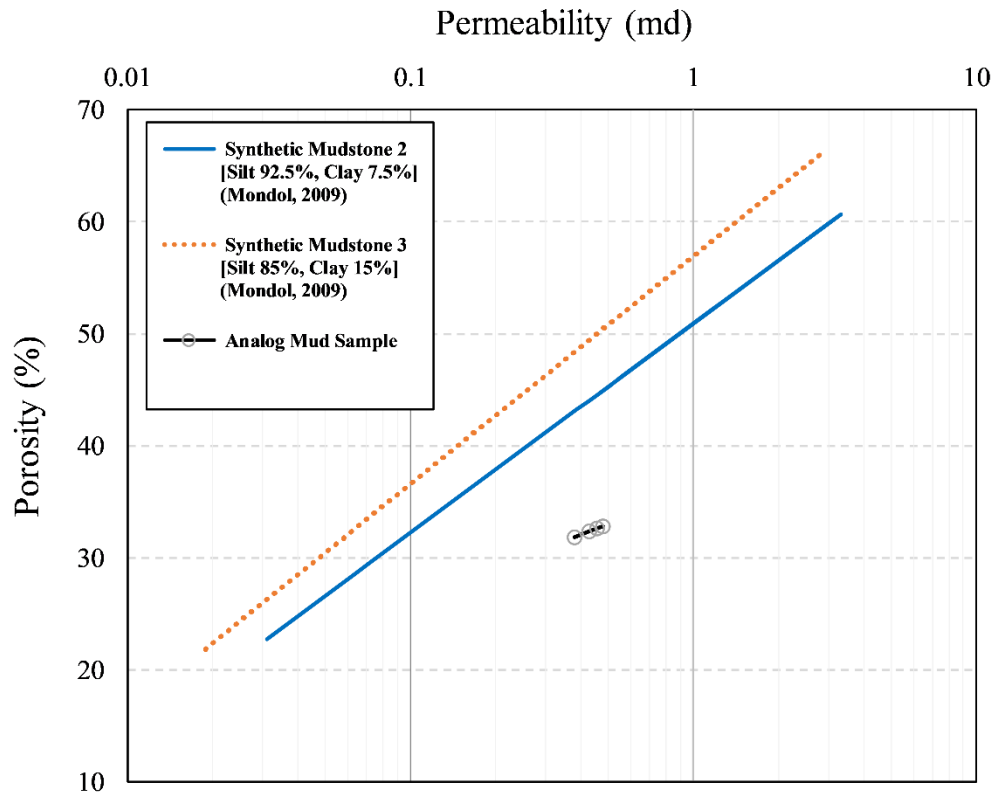


Figure 5-29 Absolute permeability versus porosity for Mondol's synthetic mudstones and analog mud samples

As can be seen in Figure 5-29, permeability rises with the increase in porosity for both synthetic mudstones and analog mud samples. However, the rate of permeability increase is slightly higher in synthetic mudstones compared to the analog mud samples. That difference is because permeability tests in the analog mud samples were performed in the second cycle of loading-unloading, while permeability was measured during the initial loading for the synthetic mudstones. Another reason for this difference might be because analog mud samples were isotropically consolidated, whereas the synthetic mudstones were uniaxially compacted.

With regard to the value of absolute permeability, it is noted that analog mud samples had moderately higher values than synthetic mudstones. This might be due to the difference in grain size distribution between the samples, and also to the dissimilarity in mineralogy and composition of used clay because, unlike synthetic mudstone, analog mud samples have a minor amount of fine-grained sand. As noted earlier, the permeability of mudstone is not a sole function of porosity;

in fact, it is very sensitive to grain size distribution and pore structure (Mondol, 2009). In other words, estimating mudstone permeability from porosity without taking into account the effects of mineralogy and pore structure could cause a significant error.

With regard to the variation of absolute permeability during shearing, an analysis of the results of Clearwater shale and Wabiskaw shale samples revealed that at high effective confining stresses the value of post shear permeability was lower than the pre-shear one. In contrast, at low effective confining stresses, the post-shear permeability was higher than the pre-shear one. Moreover, during compression, the permeability dropped noticeably for both Clearwater and Wabisakaw shale. As delineated in section 5.5.1, the same behavior was observed for analog mud samples in this study.

5.7. Summary

The following summarizes the conclusions of this chapter:

- Full saturation of reconstituted mud samples was confirmed by running a series of B-tests.
- Bulk compressibility of mud samples is a strong function of the effective confining stress, particularly at low stress levels (below 2 MPa), and the relationship between them can be expressed using a power function.
- The elastic modulus of analog mud samples is stress dependent. It increases with the increase in effective confining stress, and its variation with σ_3' can be expressed using a hyperbolic function.
- The dilative or contractive behavior of the mud specimens during shearing is predominantly controlled by the value of effective confining stress.
- The dilation angle of the analog mud samples is stress dependent. It decreases with the increase in effective confining stress, and its variation with σ_3' can be described using a logarithmic function.

- The analog mud specimens were found to be cohesionless, and have an effective friction angle of 36° .
- The absolute permeability of the sample increases up to 29% with a decrease in effective confining stress from 7 MPa to 1 MPa. Test results also revealed that the dilative behavior of the samples during isotropic unloading leads to permeability augmentation.
- The variation of absolute permeability during shearing is strongly influenced by the effective confining stress. For Mud No. 1 (σ_3' of 3.5 MPa), the permeability continuously decreased throughout the shearing. For Mud No. 2 (σ_3' of 1 MPa), despite the initial drop in the permeability value, the sample could almost retrieve its initial permeability by the end of shearing. Finally, for Mud No. 3 (σ_3' of 0.5 MPa), after a short period of permeability reduction, the permeability value continuously grew throughout the shearing (up to a 24% increase). Consequently, unlike the isotropic unloading tests, the sample's dilation during shearing did not necessarily translate into permeability augmentation. For that to be effective, the value σ_3' needs to be low and the amount of dilation must reach a certain level.
- Comparing the measured stress-strain and strength parameters and absolute permeability values of reconstituted mud samples in this study with previous experimental studies on shale cores and other reconstituted silt-clay mixtures assured the resemblance between analog mud samples and McMurray mudstone in terms of their hydro-geomechanical properties. Such analysis also provided an assurance of similarity between the mud layers of analog IHS and in situ ones.

After characterizing both constituent layers of IHS (sand and mud), the following chapter will discuss the hydro-geomechanical properties of analog IHS.

6. HYDRO-MECHANICAL TESTING ON IHS SPECIMEN¹

6.1. Introduction

In order to investigate the geomechanical constitutive behavior of McMurray IHS and its permeability evolution under SAGD-induced stress paths, a series of tests was performed on reconstituted analog IHS samples. Chapter 6 presents and analyzes the results of these experiments, which include B-test, isotropic cyclic consolidation test, drained triaxial compression test, and permeability test.

In addition, this chapter compares the hydro-geomechanical properties of the IHS specimens with their constituent layers (i.e. sand and mud samples). Finally, it investigates the applicability of former empirical permeability relationships and proposes a new correlation that relates the absolute permeability of IHS to its stress state, deformation, and degree of bioturbation.

6.2. B-test

As explained in section 4.2, it can safely be assumed that a sample is fully saturated if the calculated B value for three consecutive B-tests on the sample was fairly constant (Chaney et al., 1979).

Figure 6-1 shows the results of B-tests on four analog IHS samples. As can be seen, the plots of undrained pore pressure increase versus isotropic confining stress increments are completely linear for all samples. This indicates that the B value is constant and independent of the magnitude of the back pressure. Therefore, according to the method suggested by Chaney et al. (1979), all IHS samples are fully saturated.

The relationships between pore pressure (u) and isotropic confining stress (σ_c) for IHS samples are also displayed on the graph, reconfirming a saturated value of B of unity.

¹ Part of the chapter 6 has been published in the SPE ATCE 2019: <https://doi.org/10.2118/195968-MS>

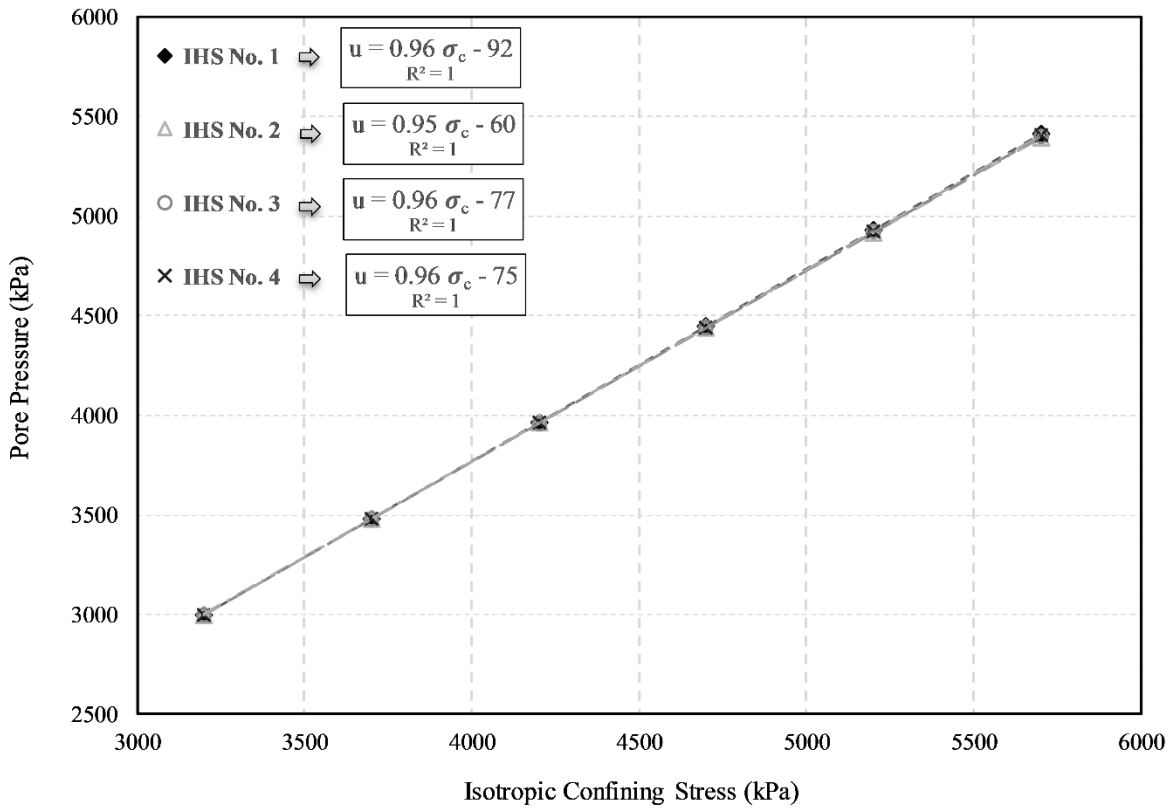


Figure 6-1 B-tests on analog IHS samples

6.3. Isotropic Cyclic Consolidation Test

The isotropic cyclic consolidation test was performed on reconstituted IHS samples in an attempt to measure the coefficient of bulk compressibility and recompact the specimens before drained shear tests.

As stated before, each specimen was saturated under an effective isotropic confining stress of 0.2 MPa with a pore pressure of 3 MPa. Afterward, the effective confining stress was cycled two times between 0.2 MPa and 7 MPa. For a soil specimen subjected exclusively to isotropic stress, the volume change is governed by effective stress, not total stress. Figure 6-2 illustrates the IHS samples' bulk volume changes with the effective confining stresses.

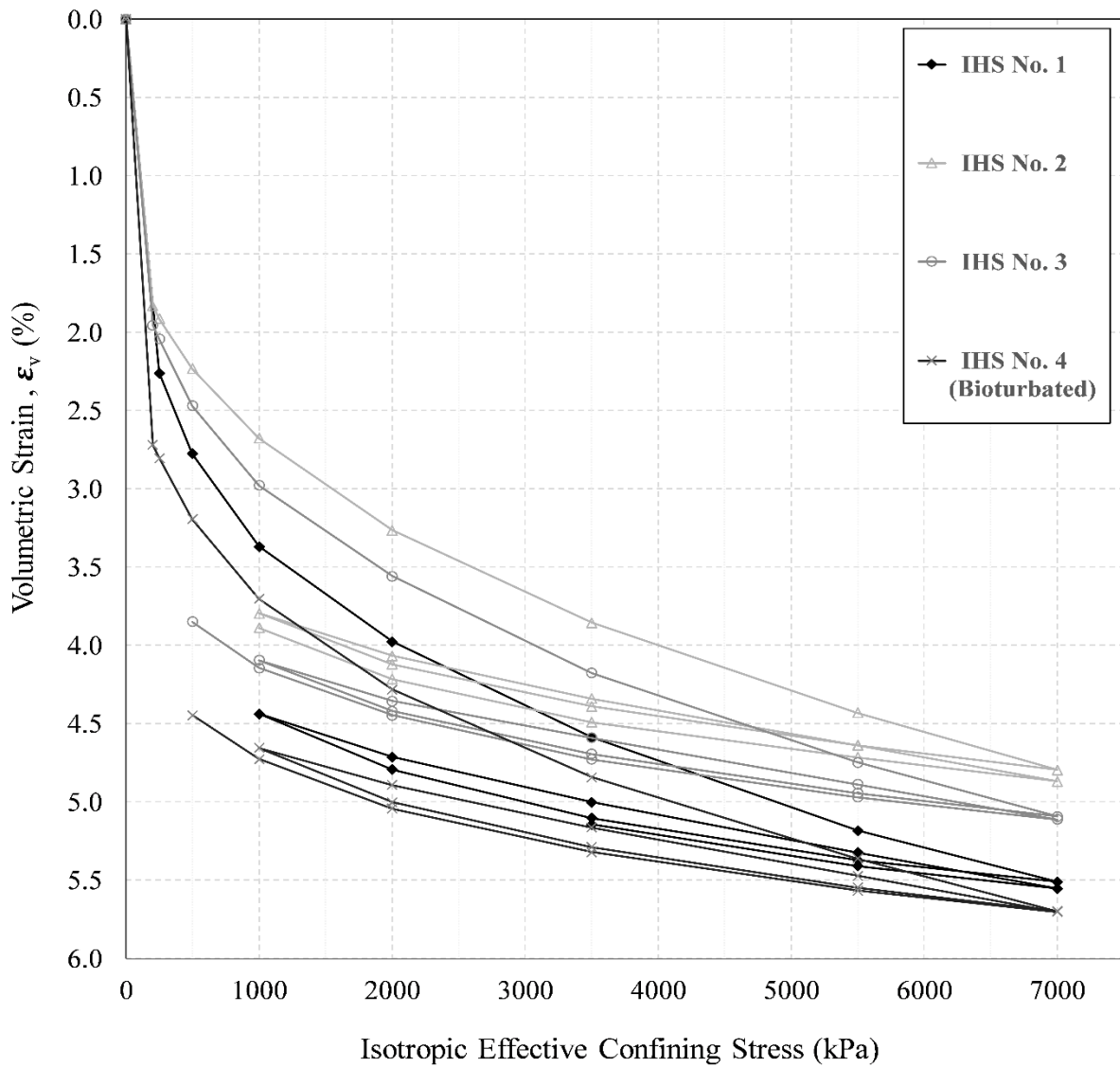


Figure 6-2 Bulk volume change of analog IHS samples

The initial loading produced a significant amount of volume change as result of initial grain rearrangement and the high initial porosity of the mud layers. Moreover, some hysteresis loops can be observed in the consolidation curves between loading, unloading, and reloading branches. Such hysteresis was expected, considering the silt and clay content of the samples.

6.3.1. Isotropic Bulk Compressibility

Figure 6-3 shows the variation of the coefficient of isotropic bulk compressibility (C_b) for analog IHS. Despite the observed hysteresis in the consolidation curves, it is noted that the computed compressibility values for each effective confining stress are very close, especially at higher values of effective confining stresses. In addition, at confining stresses lower than 2 MPa, the bioturbated sample showed slightly higher compressibility values compared to the non-bioturbation samples.

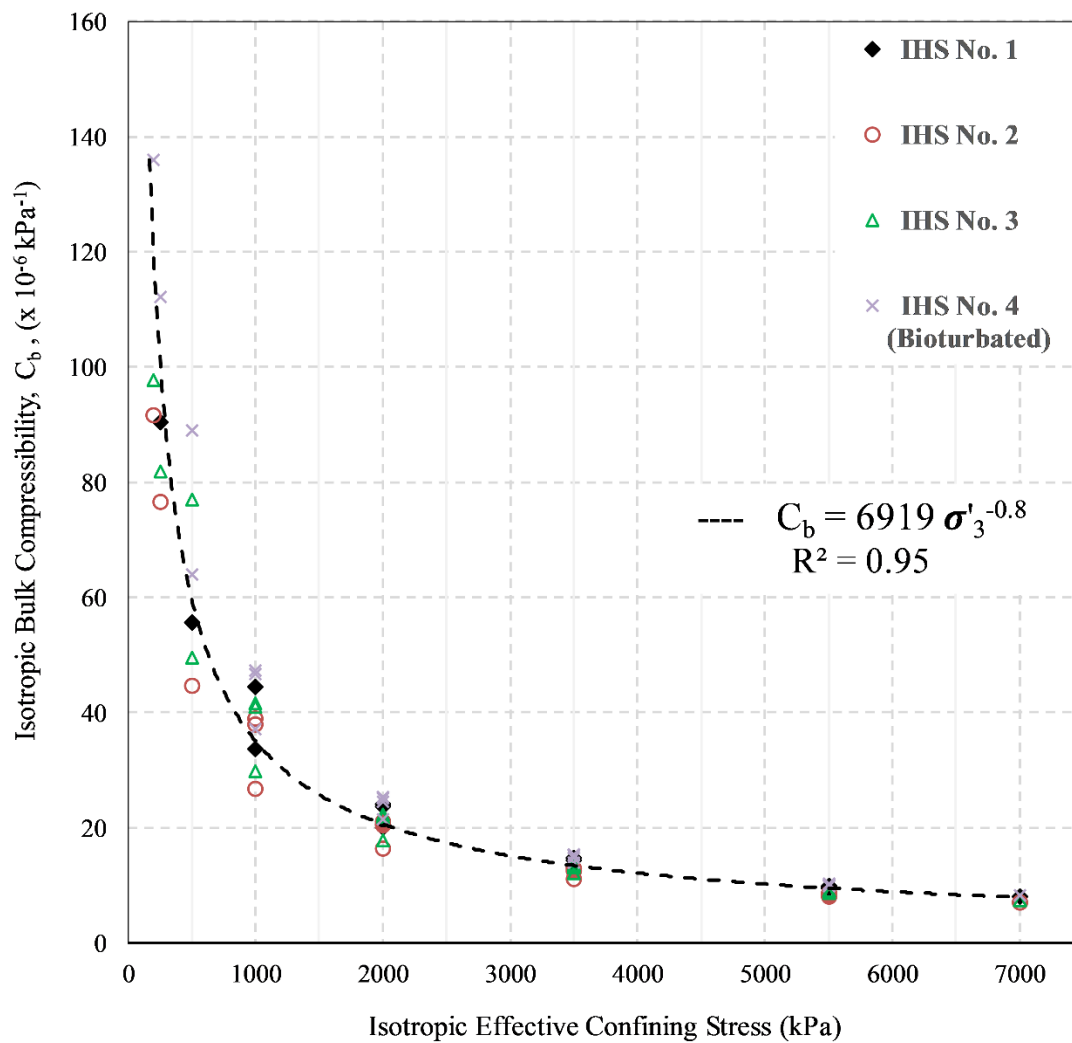


Figure 6-3 Coefficient of isotropic bulk compressibility of analog IHS samples

6.3.1.1. Empirical Correlation for change in Bulk Compressibility

Analyzing the final results revealed that bulk compressibility is a strong function of effective confining stress, particularly at low stress levels (below 3 MPa). A power law function was established to capture the relationship between the compressibility and effective confining stress, which can be expressed as follows:

$$C_b = a\sigma_3'^b \quad \text{Equation 6-1}$$

where C_b is the coefficient of bulk compressibility ($\times 10^{-6}$ kPa⁻¹), σ_3' is the effective confining stress (kPa), and a and b are constants.

Using curve fitting techniques, the constants a and b can be determined for each test (and even for every single cycle of loading or unloading), but given the consistency of the constants for all tests, a single curve fit equation was developed. Figure 6-3 illustrates the power law curve fit for all data where the values of the constants a and b are 6919 and -0.8 respectively.

Although the developed relationship can be used to estimate C_b based on effective confining stress levels, its applicability is limited to σ_3' ranging from 0.2 MPa to 7 MPa only. Therefore, extra caution needs to be exercised for any applications out of this range.

6.4. Drained Triaxial Compression Test

The drained triaxial compression tests were conducted with effective confining stresses of 0.5, 1, and 3.5 MPa. A total of four tests were performed on analog IHS samples. The results of these isotropically consolidated drained shear tests are plotted together in Figure 6-4. As can be seen in this figure, the samples' stress-strain behavior is strongly influenced by the confining stress. At all three confining stresses, semi-ductile failure was observed. Therefore, the deviatoric stress did not drop significantly after the peak shear strength was reached.

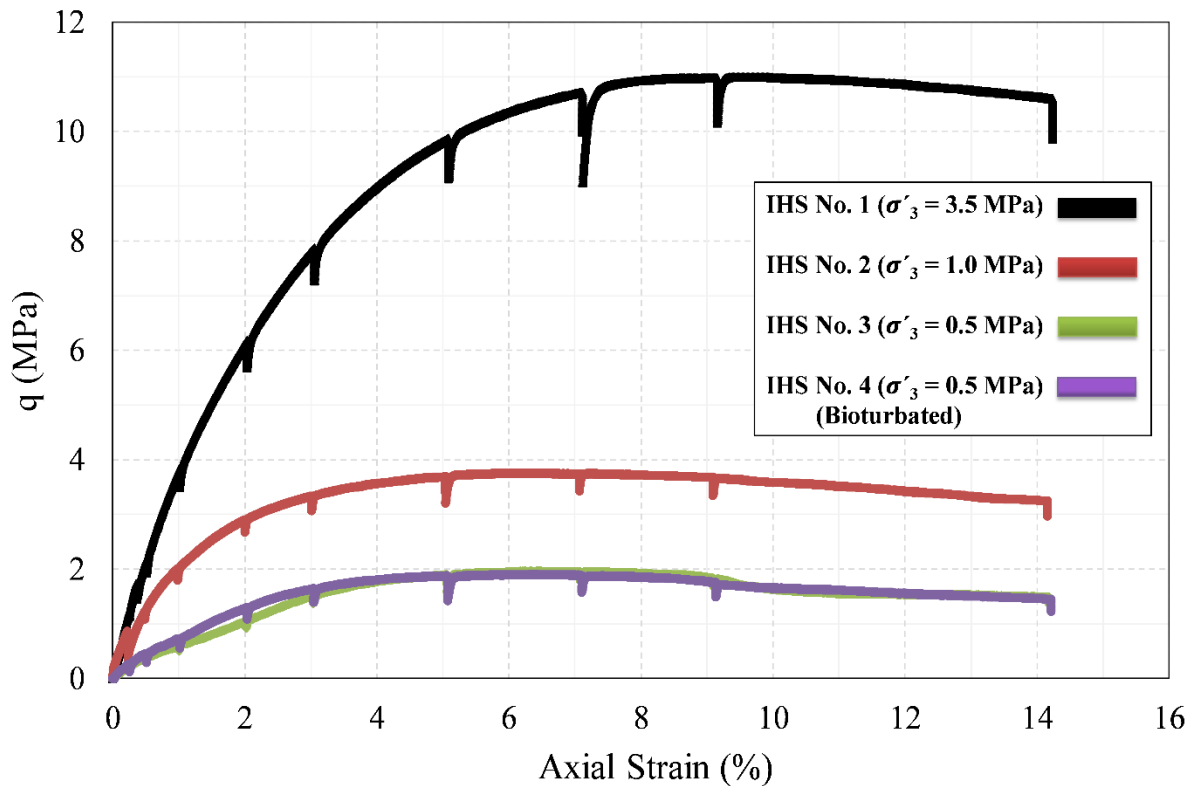


Figure 6-4 Isotropically consolidated drained triaxial compression tests on analog IHS samples

6.4.1. Stress-Strain Behavior

6.4.1.1. Modulus of Elasticity

Following the same procedure that was explained in section 4.4.1.1, Young's modulus (E) was calculated for each IHS specimen using its stress-strain curve.

Figure 6-5 displays Young's modulus of analog IHS samples with effective confining stresses. It is noted that the modulus of elasticity increases drastically with the increase in effective confining stress, and its variation with σ_3' is nonlinear. As explained in section 4.6.1.1.1, a standard hyperbolic function is typically chosen to define the dependency E to σ_3' (Equation 4-6). Therefore, using curve fitting techniques, the following equation was obtained for analog IHS samples:

$$E_i = 684p_a \left(\frac{\sigma_3'}{p_a} \right)^{0.6} \quad \text{Equation 6-2}$$

where E_i is the modulus of elasticity at the low strain level, σ_3' is the effective confining stress, and p_a is atmospheric pressure. In addition, as illustrated in Figure 6-5, the value of Young's modulus was not significantly affected by bioturbation in the mud layers.

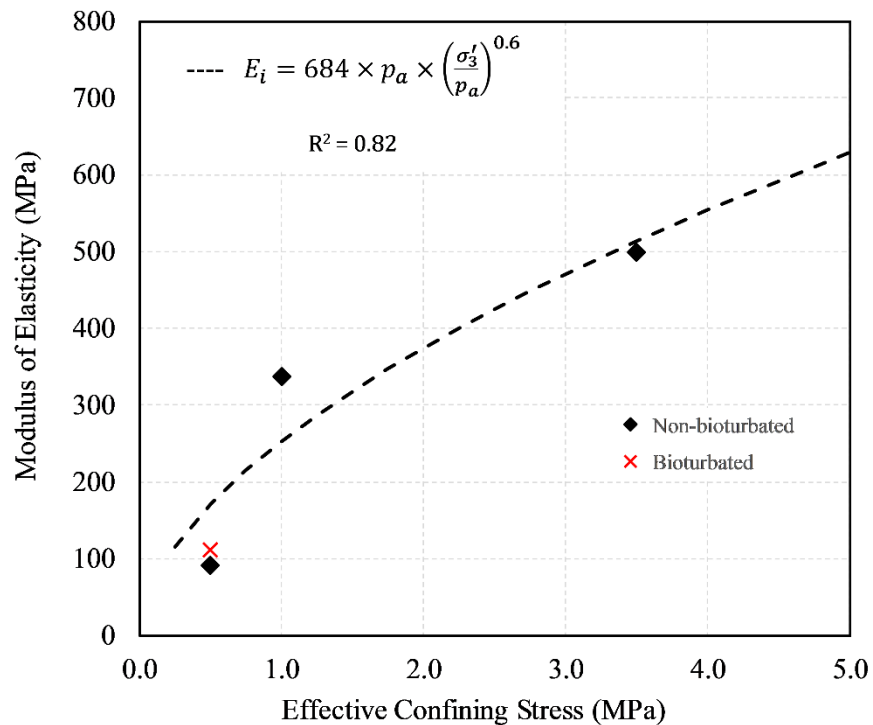


Figure 6-5 Variation of modulus of elasticity versus effective confining stress for analog IHS samples

6.4.1.2. Volumetric Behavior during Shearing

Figure 6-6 illustrates the volumetric behavior during shearing for analog IHS samples. It is clear from this graph that the dilative or contractive behavior of the IHS specimens during shearing was predominantly controlled by the value of the effective confining stress (σ_3'). In fact, all the tests displayed contraction to a certain level at the beginning of the shearing; subsequently, different volume changes with an increase in axial strain depended on their confining stress. It is observed that under 3.5 MPa effective confining stress, contraction continued until 5% axial strain, then the

sample started to dilate in shear. But in total no significant volume changes occurred throughout the shearing in this test. On the other hand, for the samples under effective confining stresses of 1 and 0.5 MPa, after a short period of contraction at the beginning of the tests (which stopped before the axial strain of 1%) all three specimens dilated noticeably up to the end of shearing. The final results also revealed that the volumetric behavior of bioturbated and nonbioturbated samples were almost the same.

As stated before, all IHS samples were isotropically consolidated resulting in a high pre-shear density, and consequently it was expected that volumetric dilation would occur during compression shearing. Drawing from his research on oil sands, Scott (1992) declared that such behavior is due to the particles rolling and crushing, which occurs in the course of shearing. According to his theory, at low effective confining stresses the sand and silt grains can roll over each other during shearing causing a volume expansion, yet at higher σ_3' values they cannot overcome the confining stress to roll over each other and inevitably will be broken by the shear force. As a result, these small, broken particles plus finer silt and clay grains will fill the voids inside the specimen which could not be filled before shearing. Consequently, volume contraction occurs in the sample. This influence on permeability is discussed subsequently.

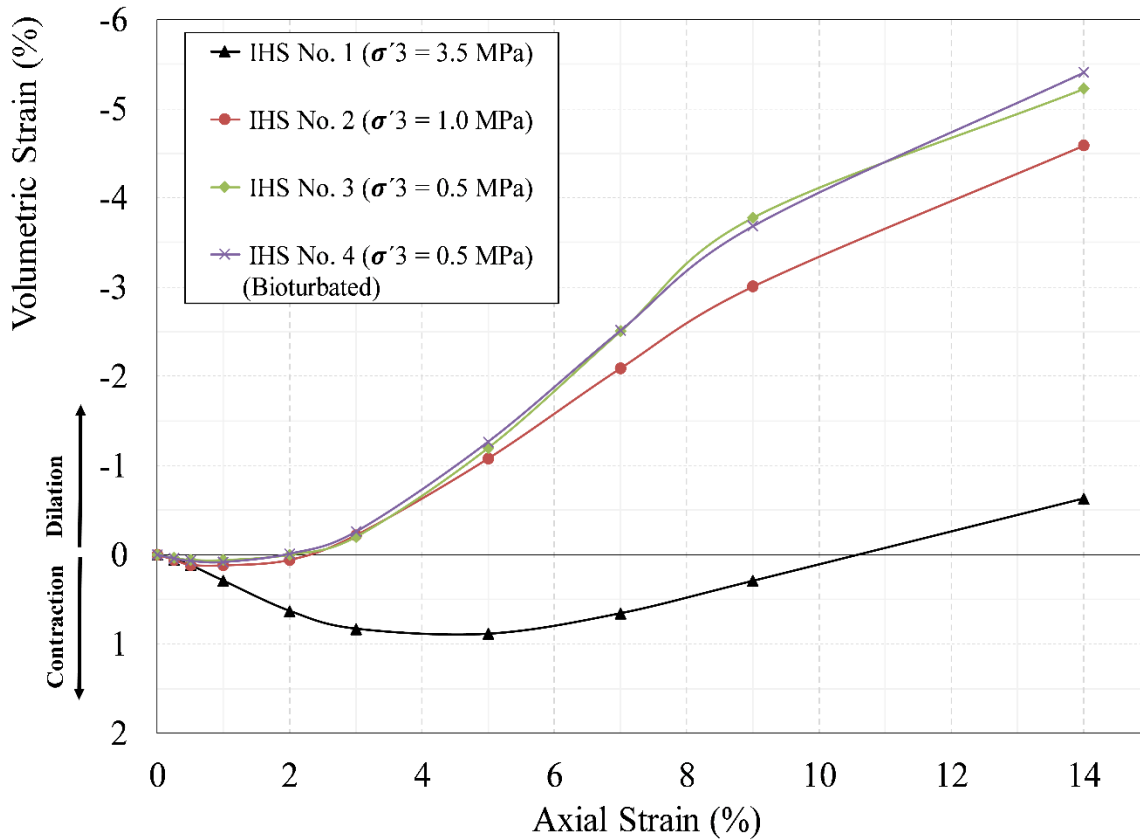


Figure 6-6 Volumetric behavior of analog IHS samples during drained triaxial compression tests

6.4.1.3. Poisson's Ratio

Following the same procedure that was explained in section 4.4.1.1, Poisson's ratio (ν) was calculated for each IHS specimen using Equation 4-2. As presented in Table 6-1, the samples which were sheared at lower confining stresses show slightly higher ν values. Furthermore, the values of the Poisson's ratio for bioturbated and nonbioturbated samples were almost the same.

6.4.1.4. Dilation Angle

Following the same procedure that was explained in section 4.4.1.4, the dilation angle (ψ) was calculated for each IHS specimen using its volumetric behavior and Equation 4-4.

Figure 6-7 presents the dilation angle changes with effective confining stresses for analog IHS samples. As can be seen, the ψ decreases with the increase in effective confining stress, and its variation with σ_3' can be described using a linear function.

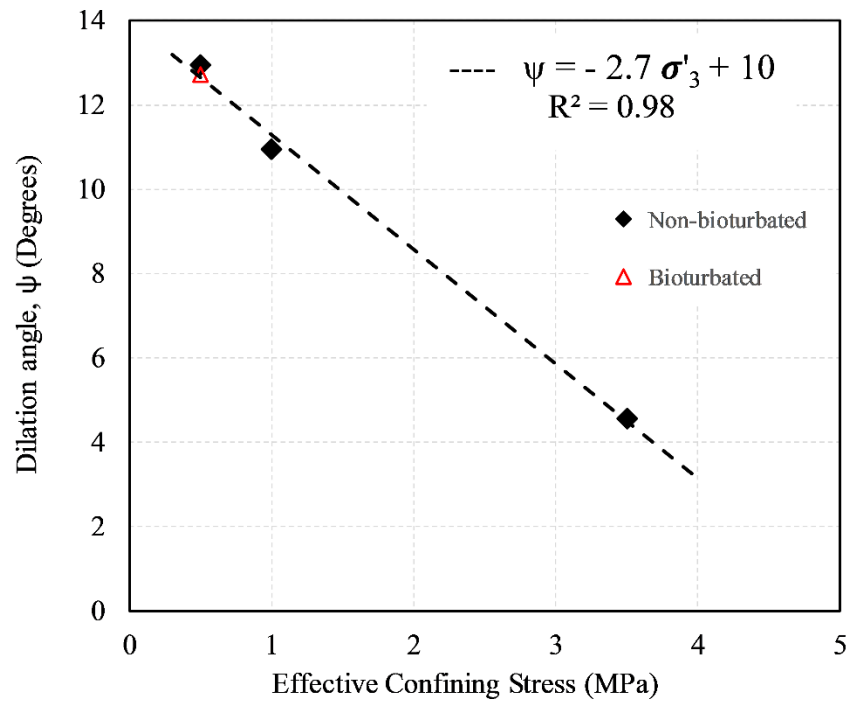


Figure 6-7 Variation of dilation angle with effective confining stress for analog IHS samples

As illustrated in Figure 6-7, the dilation angle values for bioturbated and non-bioturbated IHS samples were almost the same.

6.4.1.5. Specimens' Deformation Patterns and Mode of Failure

Following the same procedure explained in section 4.4.1.5, the mode of failure in analog IHS samples was investigated. Figure 6-8 Figure 6-11 show the IHS specimens after they were triaxially failed under effective confining stresses of 3.5, 1, and 0.5 MPa respectively.

It is noted that the center of all four specimens moderately bulged outward and several cracks formed in both sides and along the length of these samples. While such cracks are not detectable

in digital photos of the samples, they manifest themselves clearly in the CT scan images. The creation of cone-shaped zones at the top and bottom of the samples is more evident in IHS No. 3 and 4 (σ_3' of 0.5). As discussed before, the creation of these zones is due to the friction between loading platens and the IHS samples. It should also be noted that some shape rebounding usually occurs in a sample upon the removal of axial and confining stresses, and this would mask some of the cracks created within the samples.

By comparing the deformed shapes of analog IHS specimens with the deformation modes presented in Figure 4-10 and Figure 4-11, it can be concluded that the mode of failure for these samples is semi-ductile (Type IC) or ductile-faulting type. Because no clear shear failure lines were observed in the IHS samples, obvious peaks of deviatoric stress were not observed on the stress-strain curves of these samples. It is also worth noting that the isotropic consolidation-induced volume change in IHS samples was not significant; therefore, the samples did not show considerable deformation during this phase. However, upon the start of shearing, the specimen deformed downward axially and outward radially under the influence of increased deviatoric stress.



Figure 6-8 IHS sample loaded in an isotropically consolidated drained shear test under σ_3' of 3.5 MPa



Figure 6-9 IHS sample loaded in an isotropically consolidated drained shear test under σ_3' of 1 MPa



Figure 6-10 IHS sample loaded in an isotropically consolidated drained shear test under σ_3' of 0.5 MPa



Figure 6-11 Bioturbated IHS sample loaded in an isotropically consolidated drained shear test under σ_3' of 0.5 MPa

6.4.2. Drained Shear Strength

From the stress-strain curves in Figure 6-4, it is noted that the shear strength of IHS samples is highly dependent on the effective confining stress. Indeed, increasing the effective confining stress leads to a rise in shear strength. In addition, for all specimens, the post-peak stress reduction was not significant. Such a minor post-peak shear strength reduction is due to the relatively high confining stresses under which these specimens were tested, and also to the absence of interlocking structures within the reconstituted samples.

As stated earlier, the failure envelope describes the generalized stress state under which material will fail. Therefore, to develop the failure envelope for the analog IHS specimens, their stress paths were plotted in s' - t space. As demonstrated in Figure 6-12, a polynomial equation can capture the relationship between t and s' over the effective stress range tested.

$$t = -0.007 s'^2 + 0.7 s' + 0.003$$

Equation 6-3

$$R^2 = 0.96$$

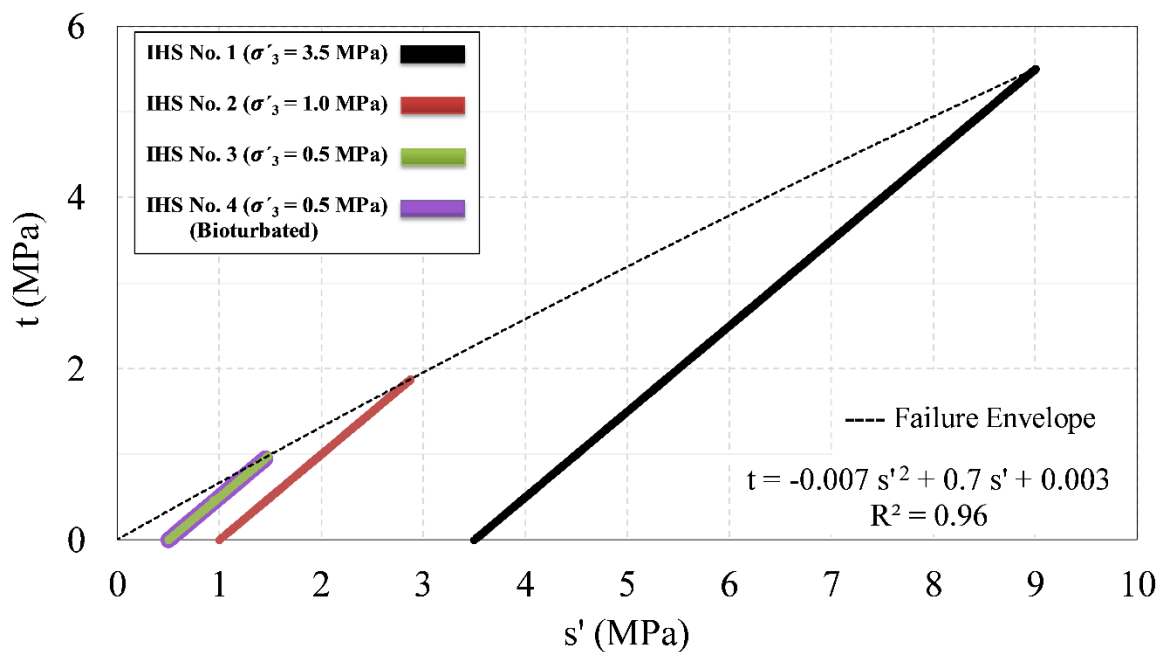


Figure 6-12 Drained triaxial compression tests stress paths and failure envelope for analog IHS samples

The stress path of the bioturbated sample is not visible in Figure 6-12 because it is masked by the one for IHS No. 3. Indeed, the stress paths for IHS samples No. 3 and 4 are nearly identical (Figure 6-13). Therefore, it can be concluded that the existence of bioturbation does not have a significant effect on the shear strength of the IHS samples.

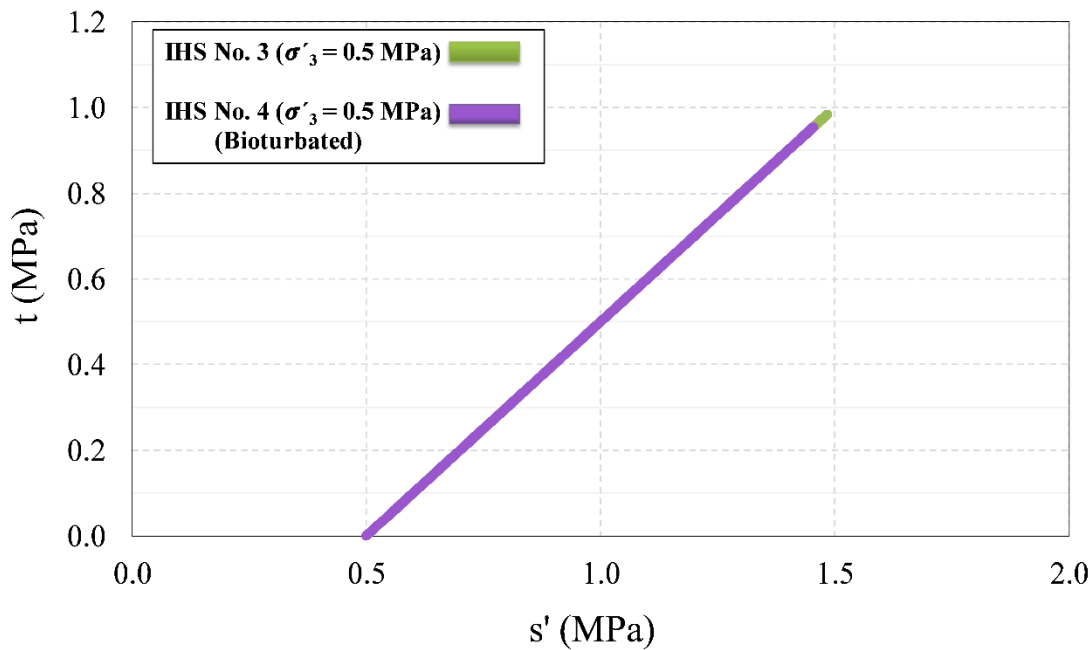


Figure 6-13 Drained triaxial compression tests stress paths for bioturbated and non-bioturbated analog IHS samples

6.4.2.1. Cohesion and Friction Angle

From the peak failure envelope in s' - t space (Figure 6-12), it can be concluded that the values of cohesion and effective friction angle for the reconstituted analog IHS sample are equal to 0.15 MPa and 37° respectively. Some of the previous experimental studies on oil sands have shown that the friction angle has direct relationships with relative density and effective confining stress. In fact, the peak friction angle increases with the increase in relative density, and the decrease in effective confining stress (Scott, 1992; Touhidi-Baghini, 1998). Regarding the IHS samples, the slight curvature observed in the failure envelope could imply a mild reduction in the effective friction angle with an increase in the effective confining stress.

6.4.2.2. Axial and Volumetric Strains at Peak Shear Strength

Figure 6-14 and Figure 6-15 show the axial and volumetric strains at peak shear strength with the effective confining stresses respectively. From these plots, it is noted that the rise in effective confining stress leads to an increase in the axial strain, while it decreases the volumetric strain. In fact, for the tests performed at low effective confining stresses, the volumetric strain at peak shear strength was negative. This means the samples' volume increased, whereas for high effective confining stresses, the volumetric strain at peak became positive, which represents volume decrease in the specimen (Table 6-1).

Therefore, at low confining stresses dilation is dominant, and at high effective stresses contraction is dominant. It is expected that an IHS reservoir exhibits the same volumetric behavior during a SAGD operation when the reservoir undergoes shearing. As delineated before, the reasons behind this phenomenon could be particles crushing and rolling at high and low effective confining stresses respectively.

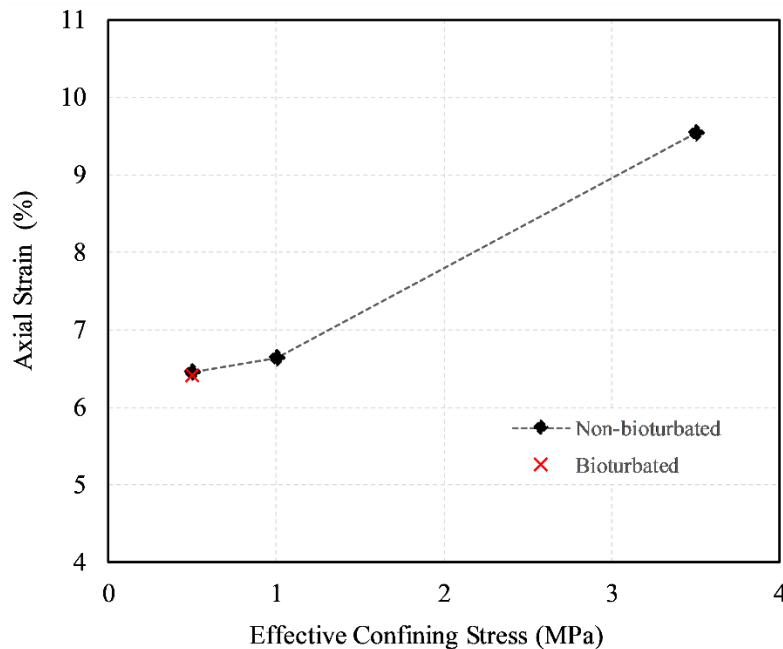


Figure 6-14 Peak axial strain for analog IHS samples

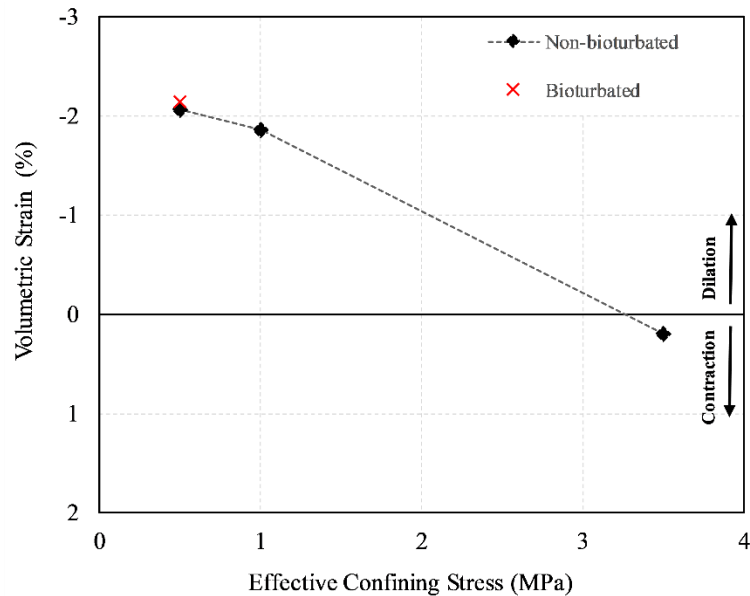


Figure 6-15 Peak volumetric strain for analog IHS samples

Table 6-1 Isotropically consolidated drained triaxial compression tests data for analog IHS samples

Test	Effective Confining Stress (MPa)	Back Pressure (MPa)	Deviatoric Stress at Peak Shear Strength (MPa)	Axial Strain at Peak Shear Strength (%)	Volumetric Strain at Peak Shear Strength (%)	Young Modulus @ $\varepsilon_a=1\%$ (MPa)	Young Modulus @ $\varepsilon_a=0.2\%$ (MPa)	Poisson's Ratio
IHS No. 1	3.5	3.0	11.0	9.5	0.2	389	499	0.39
IHS No. 2	1.0	3.0	3.8	6.6	-1.9	220	337	0.39
IHS No. 3	0.5	3.0	2.0	6.5	-2.1	64	91	0.42
IHS No. 4	0.5	3.0	1.9	6.4	-2.1	75	112	0.42

6.5. Permeability Test

6.5.1. Absolute Permeability Evolution under SAGD Stress Paths

As described in section 4.5.1, a reservoir undergoes two major geomechanical reactions during a SAGD operation: i) decreasing mean effective stress due to pore pressure injection, and ii) increasing mean and deviatoric stress due to thermal expansion. These reactions both substantially affect the value of absolute permeability (K_a), and consequently the performance of the SAGD project.

In order to understand the effects of these geomechanical processes on absolute permeability of McMurray IHS, a series of tests was performed on reconstituted analog IHS samples. These tests were designed to simulate the stress state and pore pressure conditions of the reservoir during a SAGD operation. It should also be noted that due to the inherent geological heterogeneity and complexity of the McMurray Formation, the value of initial in situ absolute permeability for IHS varies at different locations within the reservoir. Therefore, this study focuses on the changes to the initial absolute permeability (under SAGD stress paths), rather than on calculating the true value of in situ permeability.

As explained in section 3.5.5, in order to calculate the permeability of IHS samples each test was performed at three different flow rates, and the differential pressure along the sample was measured using three different methods. The final results show a minimal discrepancy between different flow rates and various differential pressure measurement techniques.

6.5.1.1. Permeability Changes during Isotropic Unloading

In order to investigate the evolution of absolute permeability under the first component of SAGD-induced stress paths, the isotropic unloading test was paused at different effective confining stresses to perform permeability tests.

Figure 6-16 and Figure 6-17 show the variations of volumetric strain and normalized absolute permeability of the IHS samples respectively, with effective confining stresses during isotropic unloading tests. From the volumetric behavior of the specimens, it is noted that decreasing mean effective stress leads to an increase in the volume of the specimens (Figure 6-16). Furthermore, it was observed that absolute permeability increases up to 40% for non-bioturbated samples, and 140% for the bioturbated sample with a decrease in effective confining stress from 7 MPa to 1 MPa (Figure 6-17).

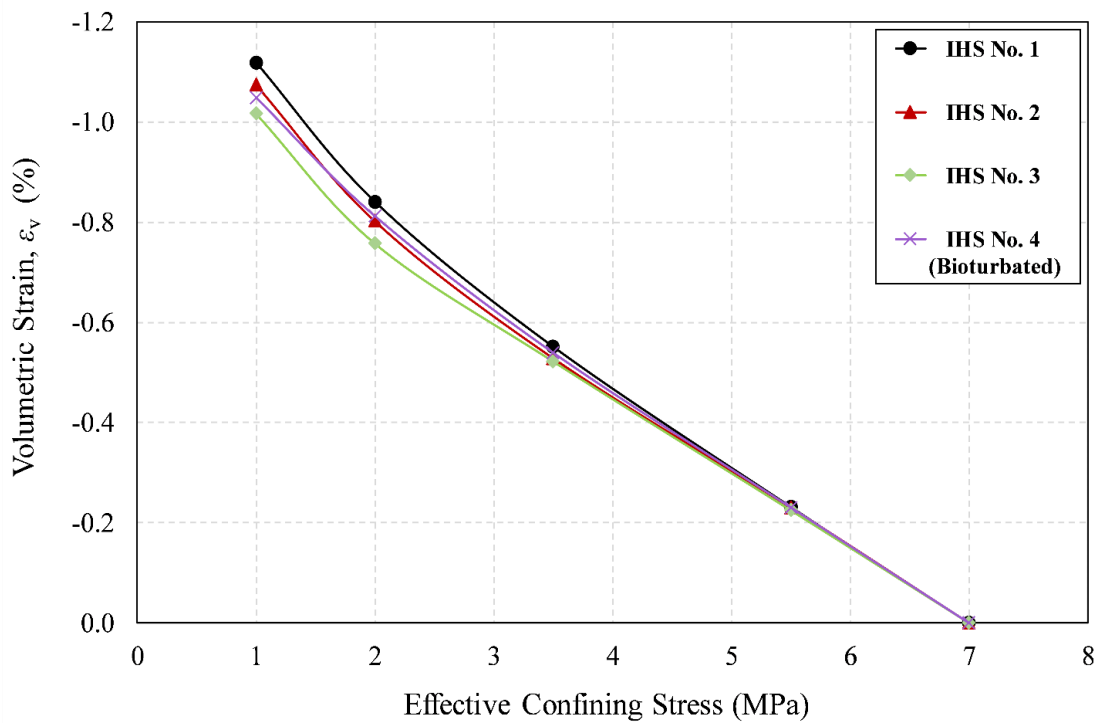


Figure 6-16 Bulk volume change during isotropic unloading of analog IHS samples

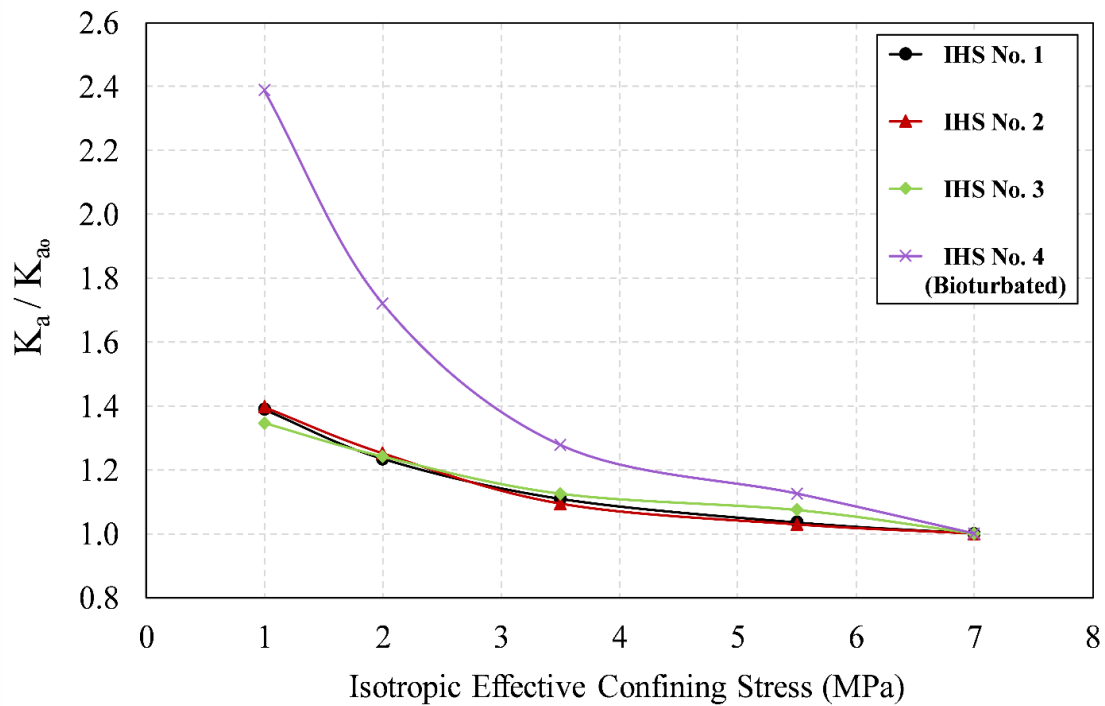


Figure 6-17 Normalized absolute permeability versus effective confining stress for analog IHS samples

In view of results presented in Figure 6-16Figure 6-17, it can safely be assumed that there is a direct relationship between the change in absolute permeability and the volumetric behavior of reconstituted analog IHS samples. In order to describe such a relationship, the variation of K_a with the volumetric strain (ε_v) was plotted for all specimens in Figure 6-18. It can be seen that the dilative behavior of the samples during isotropic unloading results in permeability enhancement. For instance, in the case of IHS No. 2, the volume change of 0.8% in the sample increased the permeability by 25%. This might be because during isotropic unloading, the soil particles slightly move apart from each other without any shearing or fabric distortion. This widens the flow channels within the samples and increases permeability.

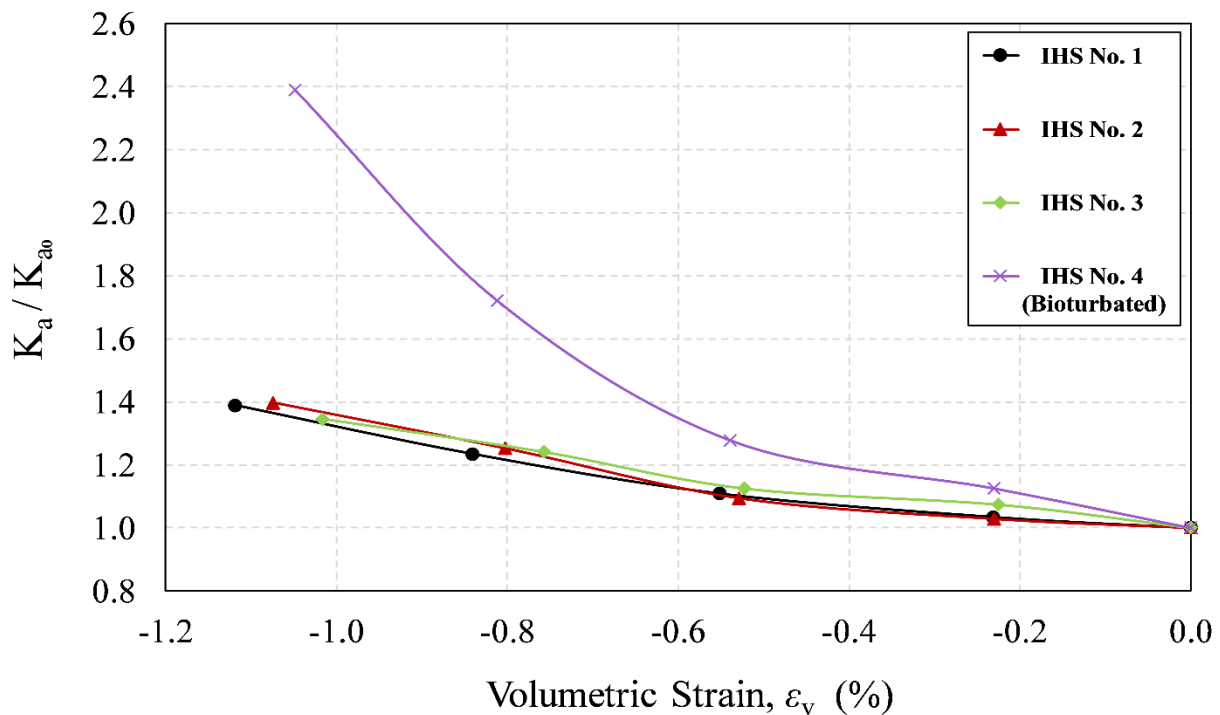


Figure 6-18 Normalized absolute permeability versus volume change for analog IHS samples during isotropic unloading

This graph also shows that the rate of permeability augmentation increases after expansion to a certain level. In other words, there is a dilation threshold (0.5% for IHS samples), and when it is passed, the rate of permeability improvement with volumetric strain increases noticeably. Therefore, the relationship between normalized absolute permeability and volumetric expansion

in an isotropic unloading test on an IHS sample can be approximated by a bilinear curve fit model that represents the primary and secondary permeability augmentation rate regions (Figure 6-19).

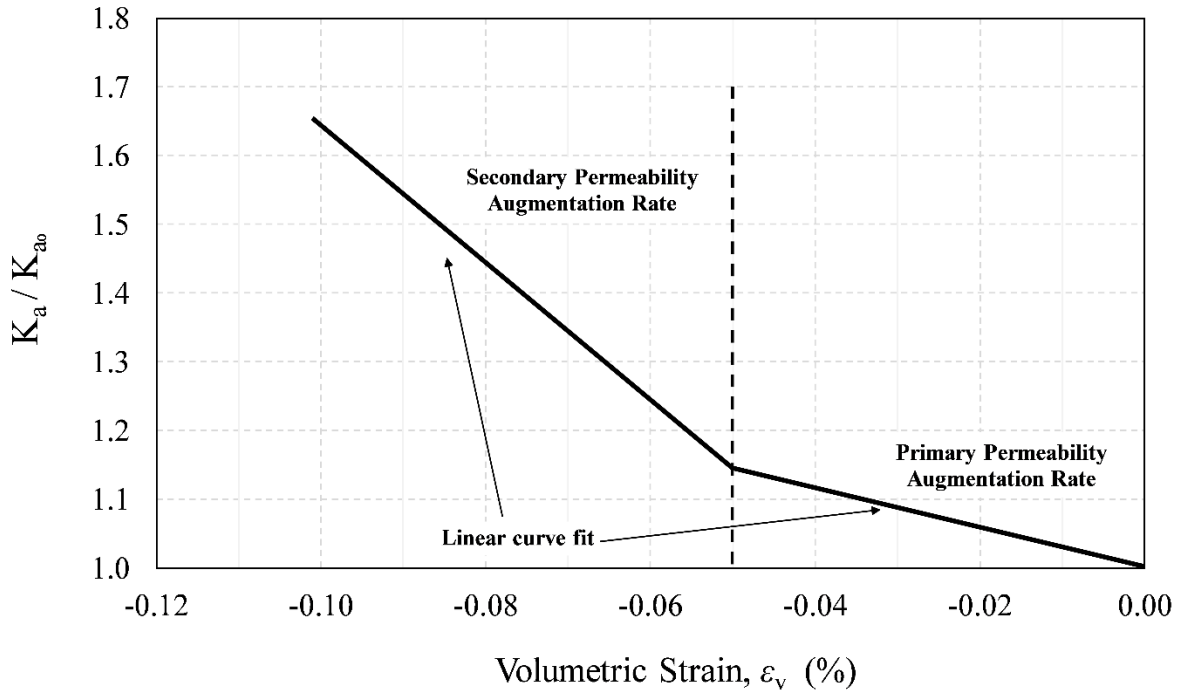


Figure 6-19 Typical normalized absolute evolution for an analog IHS sample during isotropic unloading

The most probable explanation for this phenomenon is that in the primary region only the existing flow channels are widened, while in the secondary region several new flow channels are created together with the widening of existing flow channels. In fact, when the volumetric expansion reaches this threshold, the fluid will be able to flow through channels (pore throats) which were impassable previously due to their tightness.

The other significant observation is that the amount of permeability enhancement in the bioturbated sample is substantially higher than in the non-bioturbated ones, particularly in the secondary region. This might be because some of these newly-developed flow channels are located within the bioturbated area of the mud layer.

The majority of previous experimental studies on oil sands established equations that link the changes in porosity to permeability. In order to investigate the applicability of these studies, the

variation of K_a with the changes in porosity is also presented here (Figure 6-20). Due to the small difference in the initial porosity value between the IHS samples, the normalized porosity was used in this graph. As it was expected from the volumetric behavior of IHS, the porosity of these samples increased during isotropic unloading, and this led to an increase in the permeability values.

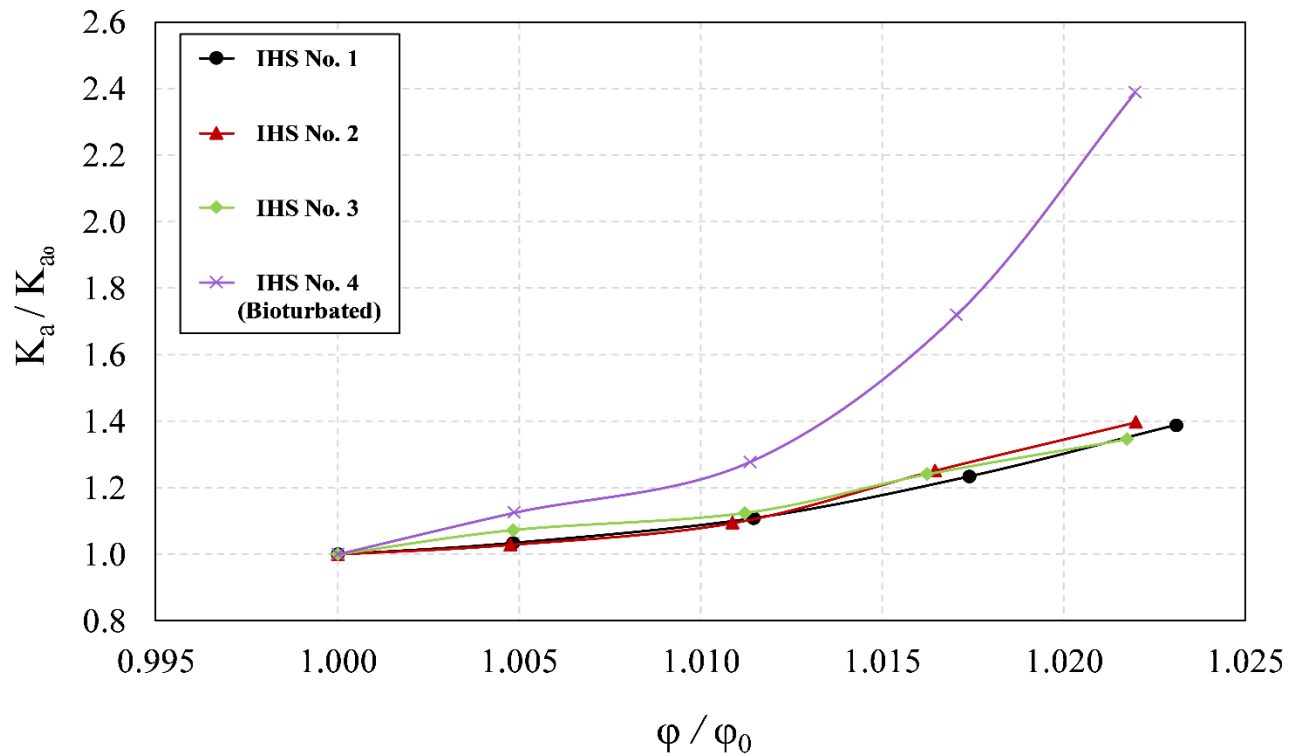


Figure 6-20 Normalized absolute permeability versus normalized porosity for analog IHS samples during isotropic unloading

6.5.1.2. Permeability Changes during Triaxial Shearing

Following the same procedure explained in section 4.5.1.2, the evolution of absolute permeability was investigated under the second component of SAGD-induced stress paths, which is increasing mean and deviatoric stresses.

Before investigating the permeability changes during shearing, the volumetric behavior of the samples needed to be analyzed. As depicted in Figure 6-6 and explained previously, the volumetric behavior of IHS samples during shearing is dominated by the value of the effective confining

stress. In other words, IHS samples show dilative behavior at low effective confining stresses, while present contractive behavior at high effective confining stresses.

Figure 6-21 shows the variations of normalized absolute permeability with axial strain during triaxial shearing for all analog IHS samples. It can be seen that the permeability continuously decreased throughout shearing for the sample tested under the effective confining stress of 3.5 MPa. However, for the tests performed under the effective confining stresses of 1 and 0.5 MPa on non-bioturbated samples, the permeability decreased prior to the axial strain of 7%, then it started to grow until the end of shearing. In these tests, despite the final increases in the permeability value, the samples could not retrieve their initial permeability by the end of shearing. Finally, for the test under the effective confining stress of 0.5 MPa on the bioturbated sample, after a short period of permeability fluctuation which stopped before the axial strain of 2%, the permeability of the sample continuously diminished until the end of shearing.

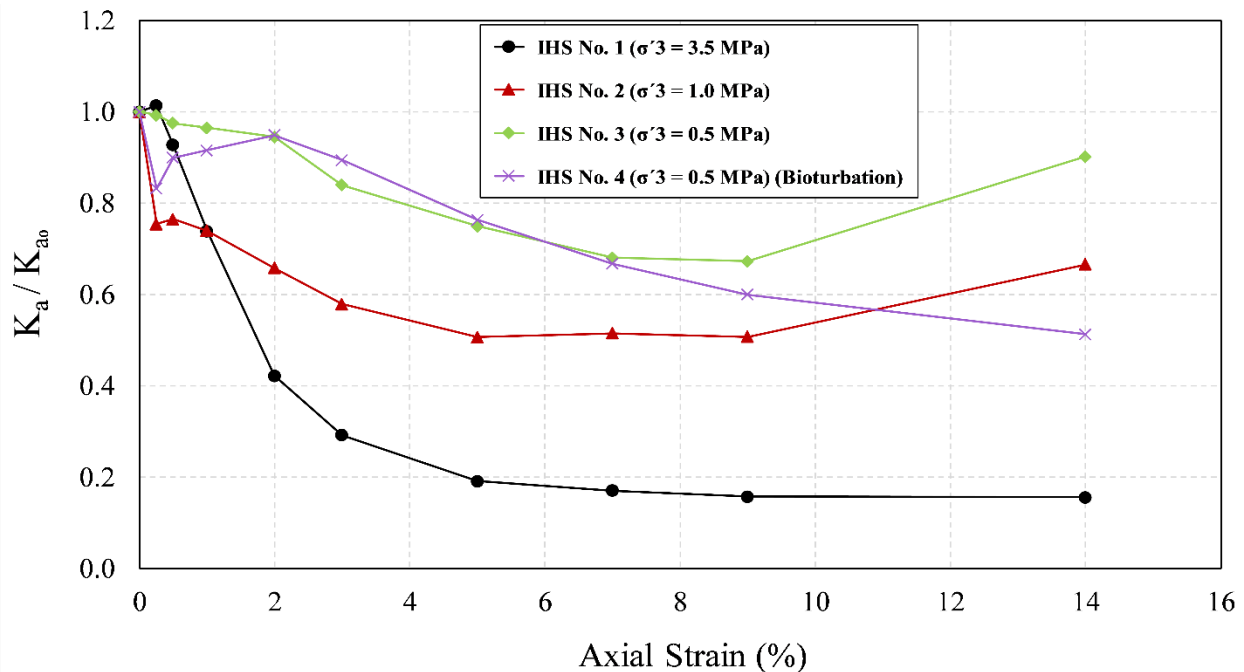


Figure 6-21 Normalized absolute permeability versus axial strain for analog IHS samples during triaxial shearing

Figure 6-22 and Figure 6-23 present the variation of normalized absolute permeability with volumetric strain and porosity changes respectively. As can be seen in these graphs, unlike the results of the isotropic unloading tests, during shearing the sample's dilation (or the increase in porosity value)

does not necessarily translate into permeability augmentation. The final results also revealed that the positive effects of dilation on permeability are only limited to the tests at very low effective confining stresses, and they require the volumetric strain to reach a certain level. It was also observed that the contraction which happens during shearing under high effective confining stresses could significantly decrease the value of absolute permeability in the IHS samples.

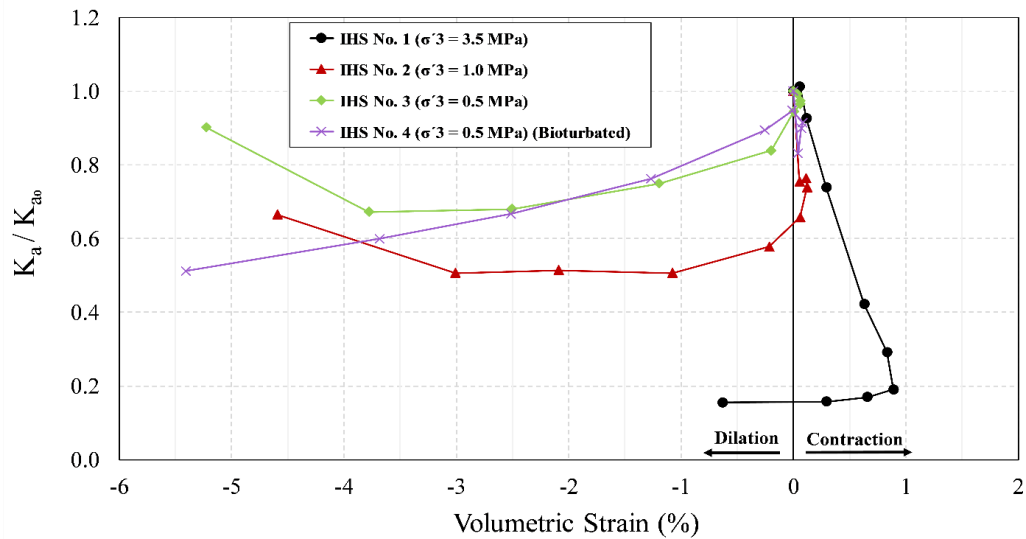


Figure 6-22 Normalized absolute permeability versus volumetric strain for analog IHS samples during triaxial shearing

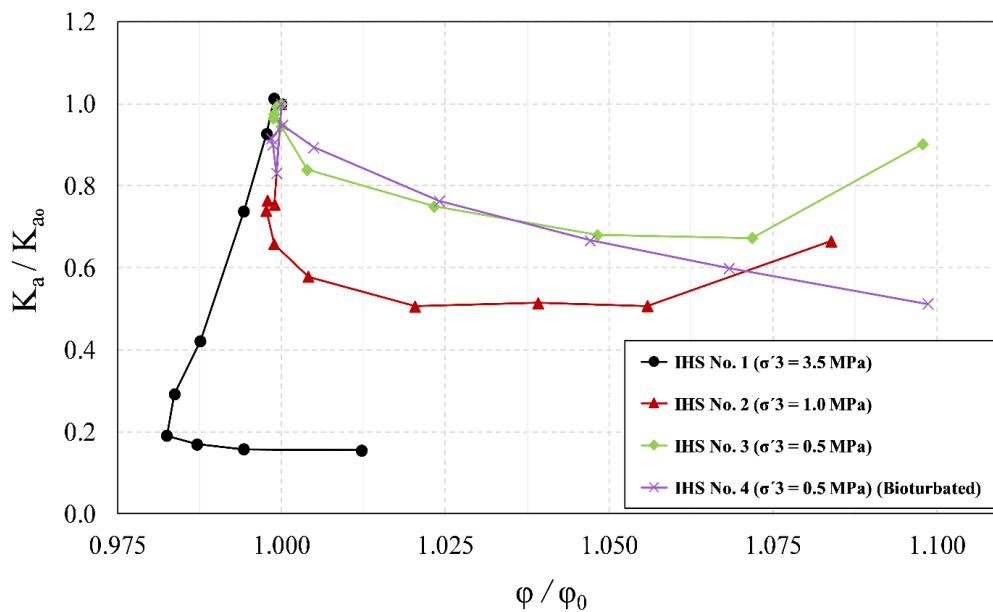


Figure 6-23 Normalized absolute permeability versus normalized porosity for analog IHS samples during triaxial shearing

As presented in sections 4.5.1.2 and 5.5.1.2, during shearing, several flow channels develop within the specimen that could increase the permeability value (Touhidi-Baghini, 1998). However, the positive effect of these newly-developed channels on permeability is contingent on the amount of effective confining stress (σ_c'). At low σ_c' values, these channels could improve permeability; at high σ_c' value, they are suppressed, they lose their connectivity, and their effects on permeability become negligible.

The other important factor which imparts a substantial influence on permeability evolution during shearing is tortuosity and its variation. To illustrate, shearing a sample could severely disturb its pore network and consequently change its tortuosity value. At low effective confining stresses when the flow channels are wide, this could decrease tortuosity and enhance permeability; at high effective confining stresses, when the flow paths are tight, this could increase tortuosity and reduce the permeability value.

With regard to the bioturbated sample (IHS No. 4), it was observed that despite the high value of dilation at the final stages of shearing under σ_3' of 0.5 MPa, permeability continued to decrease. This is probably caused by the silt and clay migration that occurs during permeability tests. In fact, due to the high permeability of bioturbated samples compared to non-bioturbated ones, the flow rates used for permeability tests on IHS No. 4 were an order magnitude higher than the ones used for non-bioturbated specimens. Therefore, there is a strong chance that such high flow rates triggered the silt and clay migration, and these fine-grained particles clogged some of the potential flow paths within the bioturbated area of the sample. This phenomenon could increase tortuosity and consequently reduce permeability.

6.6. Discussion and Conclusions

This section compares the hydro-geomechanical properties of IHS specimens with their constituent layers (analog sand and mud sample). It also investigates the applicability of former empirical permeability relationships on analog IHS and proposes a new correlation that relates the absolute permeability of IHS to its stress state, deformation, and degree of bioturbation.

6.6.1. Sand-Mud-IHS Comparison

6.6.1.1. *Compressibility*

In view of the results presented in Figure 4-3, Figure 5-3, Figure 6-3, it can be concluded that the IHSs' compressibility value is higher than sand but lower than mud. Furthermore, the difference in C_b values between IHS, sand, and mud samples increases with a decrease in effective confining stresses. Such behavior was expected, considering the IHS constituent layers' composition and the fact that the mud samples are far more compressible than the sand specimens.

6.6.1.2. *Shear Strength*

Figure 6-24, Figure 6-26 show the results of drained triaxial compression tests on analog sand, mud and IHS samples together under effective confining stresses of 3.5, 1, and 0.5 MPa respectively. By comparing the shear strength of IHS samples with sand and mud specimens, it was concluded that the shear strength of sand-dominated IHS is lower than sand but higher than mud. The results also revealed that increasing the effective confining stress under which the sample is sheared decreases the percentage of shear strength difference between IHS, sand, and mud. It was also observed that the axial strains at which the IHS samples reach their peak shear strength are lower than mud specimens but higher than sand samples, regardless of the effective confining stress under which the samples were sheared.

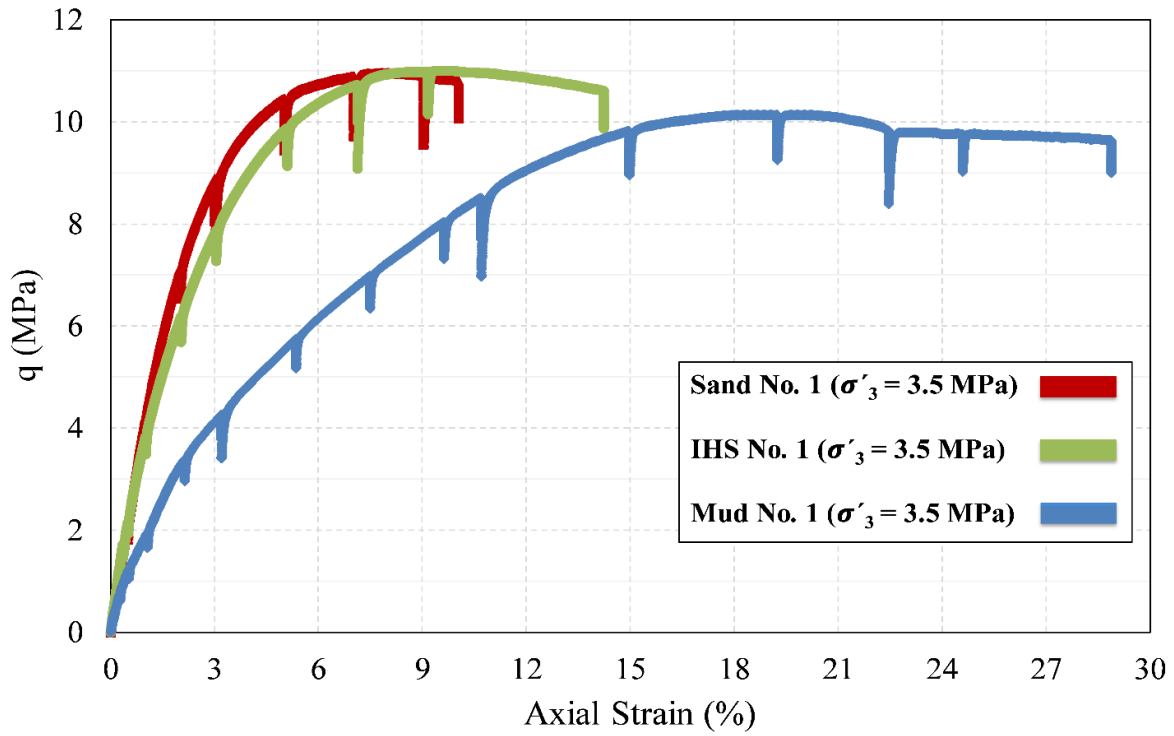


Figure 6-24 Stress-strain curves of analog sand, mud, and IHS samples under σ_3' of 3.5 MPa

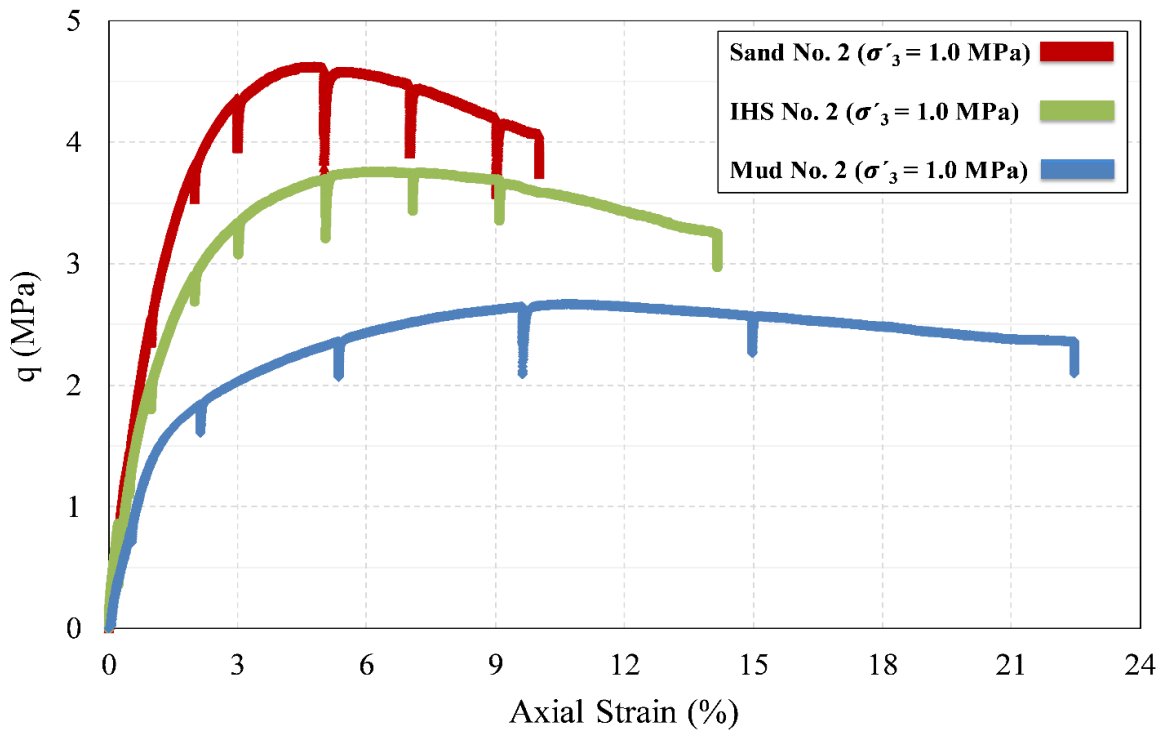


Figure 6-25 Stress-strain curves of analog sand, mud, and IHS samples under σ_3' of 1 MPa

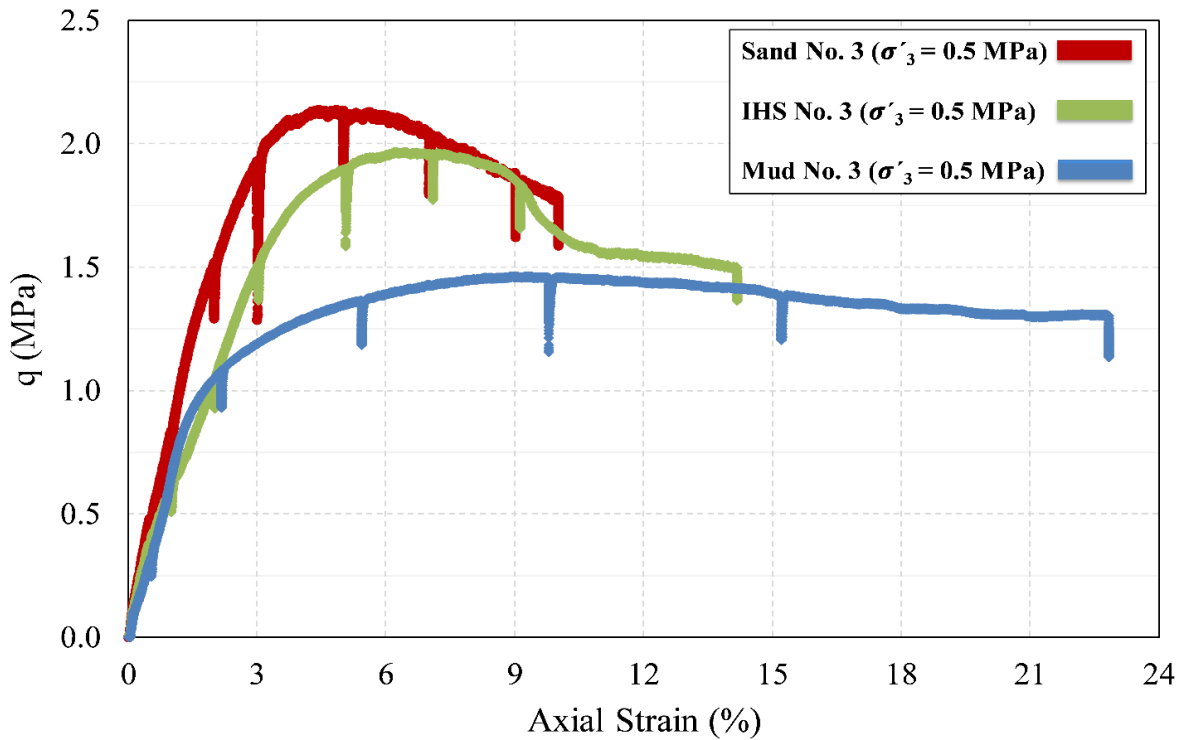


Figure 6-26 Stress-strain curves of analog sand, mud, and IHS samples under σ'_3 of 0.5 MPa

6.6.1.3. Modulus of Elasticity

In view of the results presented in Figure 4-5, Figure 5-5, Figure 6-5, it can be concluded that the value of elastic modulus in sand-dominated IHS is slightly lower than sand, but significantly higher than mud. Such behavior was expected, considering the high sand content of the IHS specimens, and the fact that the sand samples have higher stiffness values compared to the mud specimens.

Despite the different E values that were calculated for the sand, mud and IHS samples, the general trend of Young's modulus changes with effective confining stress is the same in all three sample types. In other words, the value of E grows with the increase in effective confining stress, and its variation with σ'_3 is nonlinear.

6.6.1.4. *Poisson's Ratio, Cohesion, and Friction Angle*

In view of the results displayed in Table 4-1, Table 5-1, Table 6-1, it can be concluded that the value of Poisson's ratio in sand-dominated IHS is slightly lower than mud. The results also revealed that at high confining stresses the value of ν is nearly the same in analog sand and IHS samples; however, at low confining stresses, IHS samples showed slightly higher ν values compared to sand specimens. Despite the different ν values that were computed for sand, mud and IHS samples, the general trend of Poisson's ratio changes with effective confining stress is the same in all three sample types. In other words, the value of ν moderately grows with a decrease in effective confining stress.

In addition, by comparing the failure envelopes of sand, mud and IHS samples (Figure 4-16, Figure 5-11, Figure 6-12), it was inferred that the values of effective friction angle are relatively similar in all three sample types. Finally, it was observed that sand and mud samples are cohesionless, but IHS specimens showed a very small amount of cohesion.

6.6.1.5. *Volumetric Behavior and Dilation Angle*

Figure 6-27 to Figure 6-29 show the shear-induced volumetric behavior of analog sand, mud and IHS samples together under effective confining stresses of 3.5, 1, and 0.5 MPa respectively. As illustrated in these figures, over the effective stress range tested, the volumetric strain curves of the IHS samples sit between the ones for the sand and mud specimens. It should also be noted that the IHS curves have a strong inclination toward the sand curves. Such behavior was anticipated, considering the fact that a significant portion of sand-dominated IHS samples are made of sand layers.

In addition, it is noted that the mud samples display significantly higher contraction and lower dilation compared to the sand and IHS specimens at all three effective confining stresses. Such behavior is more noticeable when comparing the dilation angles of these samples (Figure 4-8, Figure 5-7, Figure 6-7). This is probably due to the difference in grain size distribution between these

samples. In fact, the larger soil grains in the sand samples could create more volume when they roll over each other compared to silt and clay. On the other hand, the finer-grained particles in mud samples could fill the samples' voids more easily during shearing, compared to the large sand grains.

Despite the different ψ values that were computed for sand, mud, and IHS samples, the general trend of dilation angle variation with effective confining stress is the same in all three sample types. In other words, the value of ψ nonlinearly declines with the increase in effective confining stress.

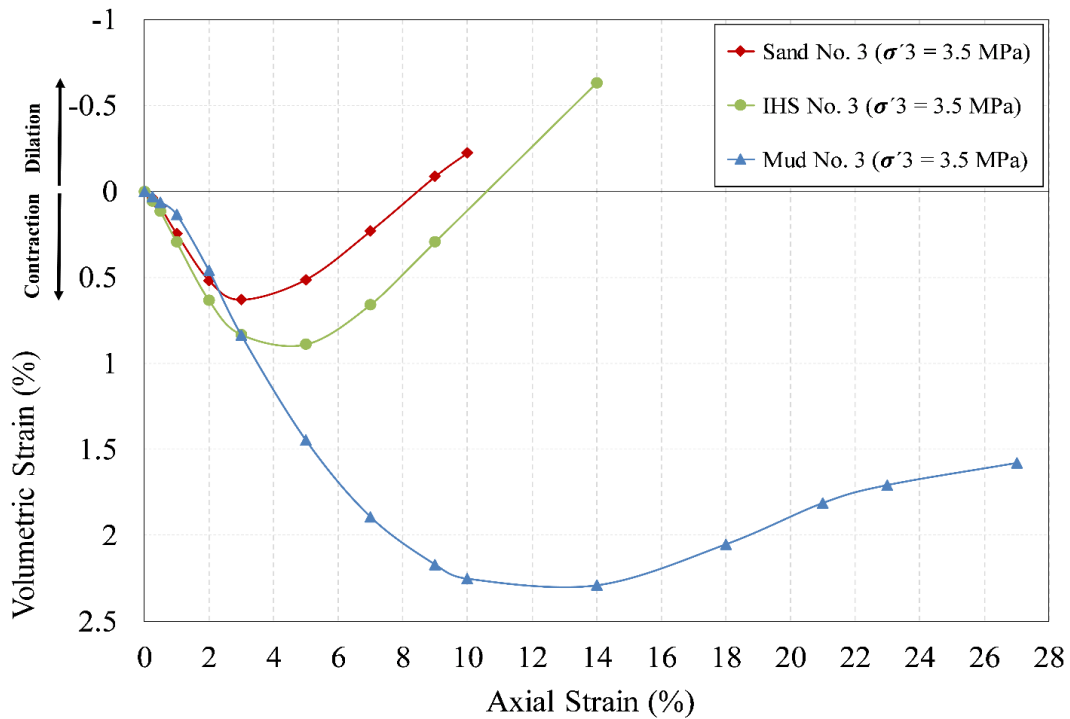


Figure 6-27 Volumetric behavior of analog sand, mud, and IHS samples during drained triaxial shearing under σ'_3 of 3.5 MPa

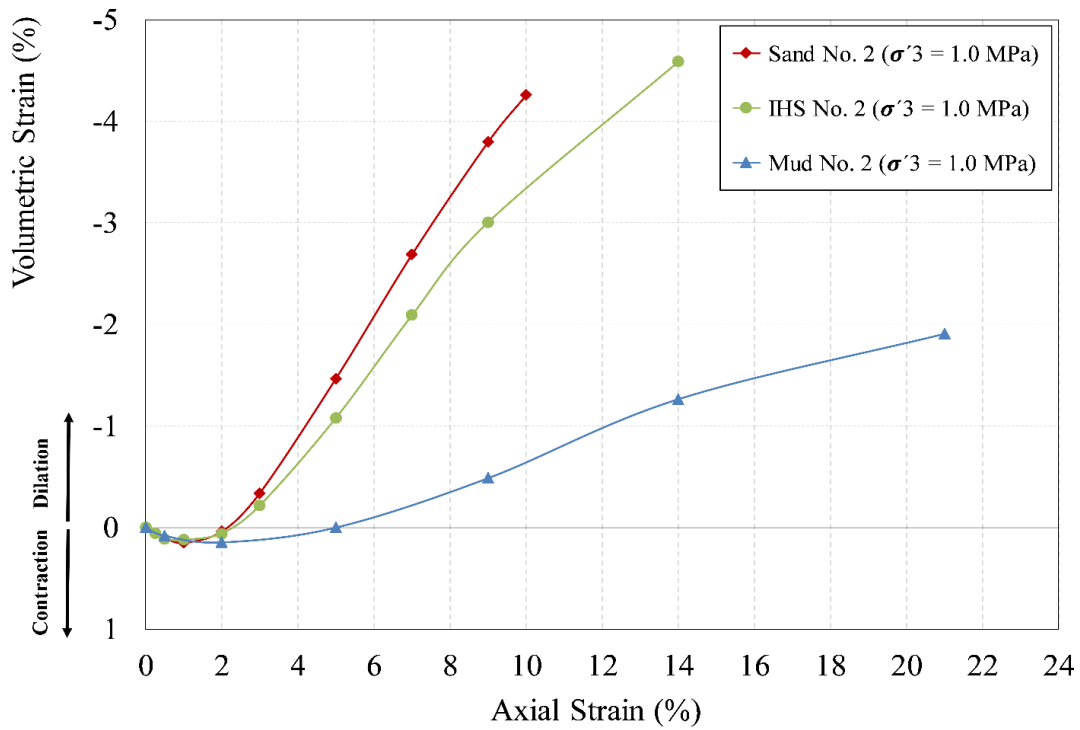


Figure 6-28 Volumetric behavior of analog sand, mud, and IHS samples during drained triaxial shearing under σ'_3 of 1 MPa

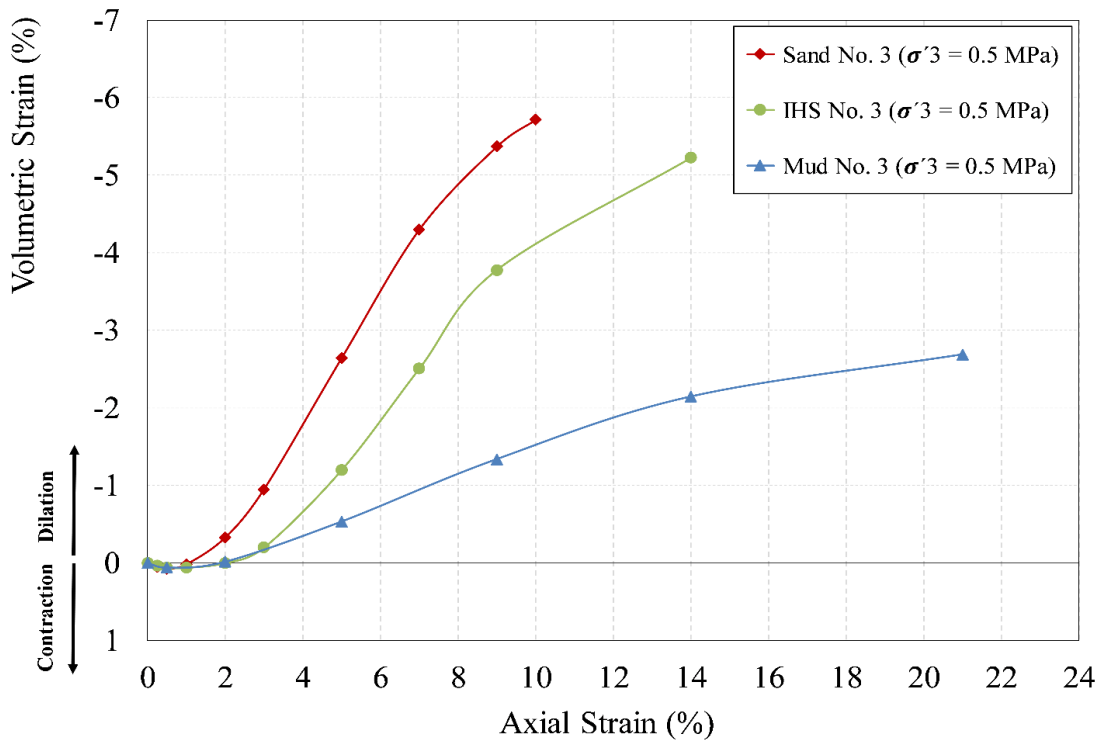


Figure 6-29 Volumetric behavior of analog sand, mud, and IHS samples during drained triaxial shearing under σ'_3 of 0.5 MPa

6.6.1.6. *Permeability Evolution under SAGD Stress Paths*

By comparing the results presented in sections 4.5, 5.5, and 6.5, it can be concluded that in all three sample types (sand, mud, and IHS), volumetric expansion during isotropic unloading results in permeability enhancement, and shear-induced contraction leads to a diminution in permeability value. The results also revealed that shear-induced dilation does not always improve permeability, and for that to be effective the confining stress needs to be low and the value of dilation must reach a certain level. More details on the geomechanically-induced permeability alteration for each sample type can be found in the corresponding chapters.

6.6.2. Investigating the Applicability of Previous Empirical Permeability Relationships

As delineated before, during a SAGD operation in an IHS reservoir, the porosity, pore structure, and stress state of the reservoir change considerably. These changes have strong effects on the value of absolute permeability (K_a) and substantially influence the performance of the SAGD project. Therefore, it is important to evaluate the variation of K_a when the reservoir material experiences these SAGD-induced changes.

As explained in Chapter 4, over the past few decades, several experimental and analytical relationships were developed to capture the fluid flow through porous media. Section 4.6.1.2 described some of these relationships that could be used to calculate the geomechanically-induced permeability alteration. This section examines the applicability of these permeability expressions to the analog IHS.

6.6.2.1. *Kozeny-Carman Model*

Following the same procedure explained in section 4.6.1.2.1, the evolution of absolute permeability was investigated using the Kozeny-Carman equation. Figure 6-30 shows the measured and predicted variation of absolute permeability using the Kozeny-Carman relation

during isotropic unloading. As can be seen, for all IHS samples, the Kozeny-Carman equation underestimates the absolute permeability improvement during isotropic unloading. Moreover, the divergence between measured and predicted values grows with the increase in porosity changes.

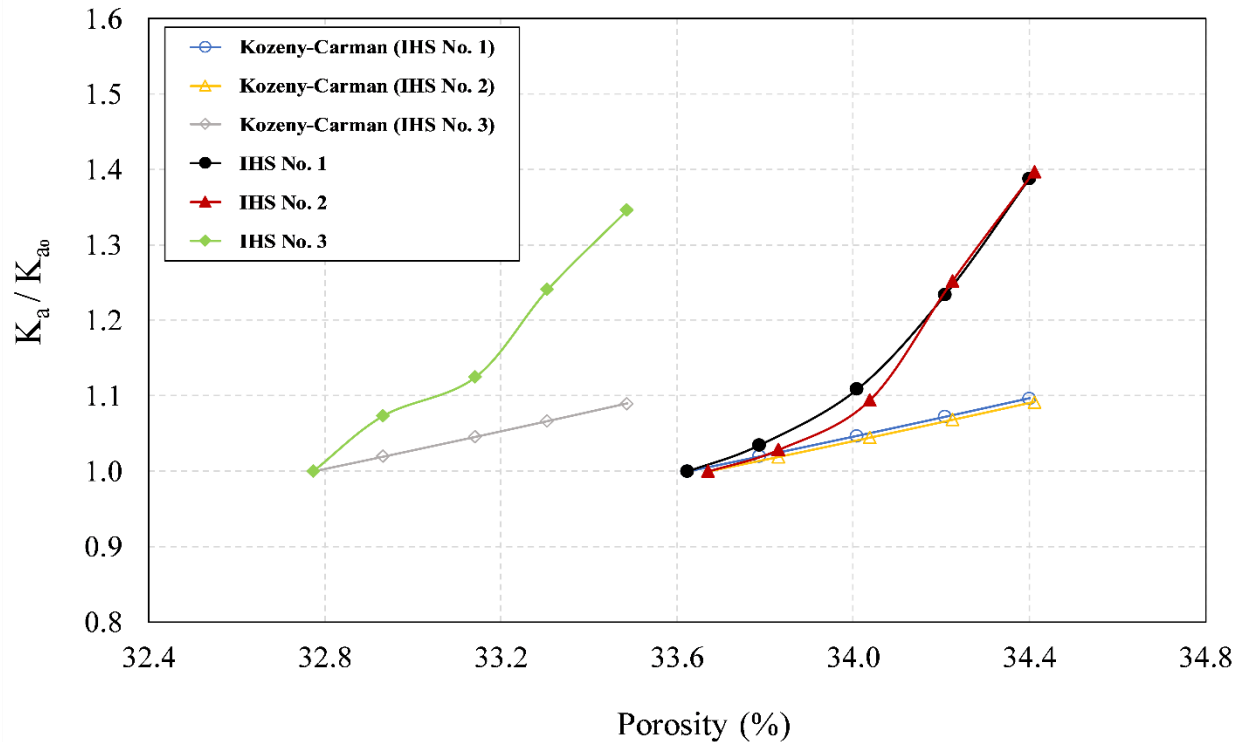


Figure 6-30 Prediction of absolute permeability alteration of IHS during isotropic unloading using the Kozeny-Carman equation

6.6.2.2. Chardabellas' Model

Following the same procedure explained in section 4.6.1.2.2, the permeability alteration was investigated using the Chardabellas' model. Figure 6-31 displays the measured and predicted variation of absolute permeability using the Chardabellas relation for the B values of 2 and 5 during isotropic unloading. As illustrated in the graph, the correlation for $B=5$ shows a better fit with the experimental results, yet it still underestimates the amount of permeability enhancement due to dilation.

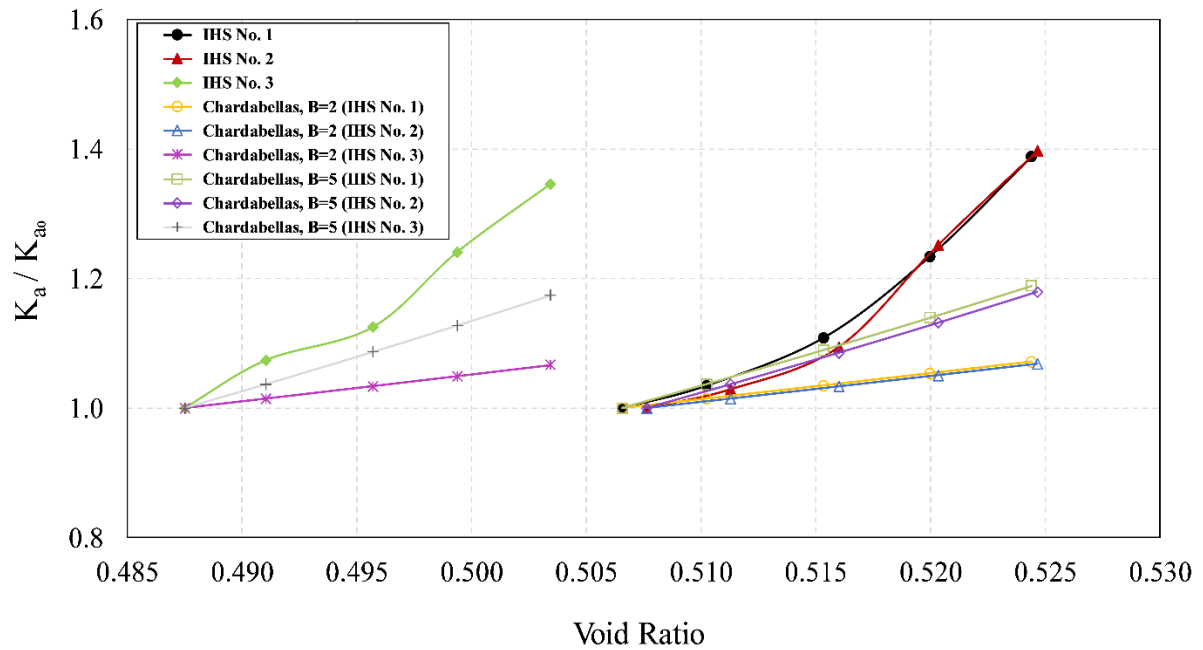


Figure 6-31 Prediction of absolute permeability alteration of IHS during isotropic unloading using Chardabellas' equation

6.6.2.3. Tortike's Model

Following the same procedure explained in section 4.6.1.2.3, the evolution of absolute permeability was investigated using Tortike's model. Figure 6-32 shows the measured and predicted variation of absolute permeability using Tortike's equation during isotropic unloading. It can be seen that Tortike's equation underestimates the absolute permeability improvement during isotropic unloading. Moreover, the divergence between measured and predicted values increases with an increase in the dilation value.

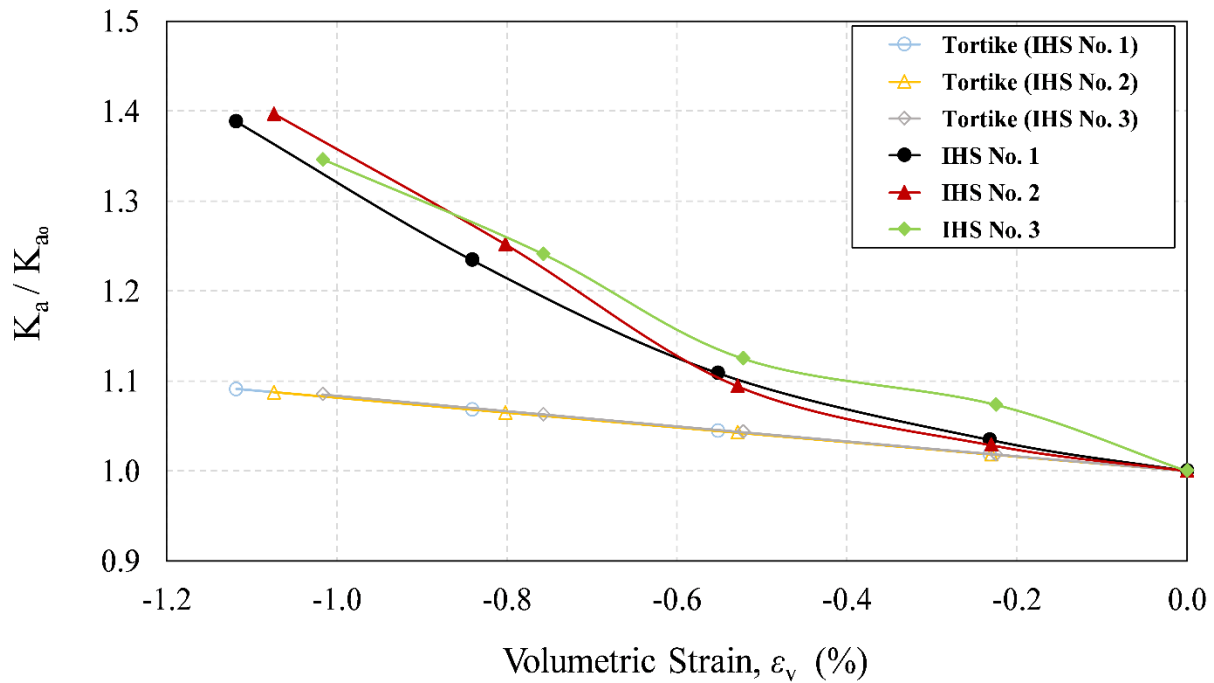


Figure 6-32 Prediction of absolute permeability alteration of IHS during isotropic unloading using Tortike's equation

6.6.2.4. *Touhidi-Baghini's Model*

Following the same procedure explained in section 4.6.1.2.4, the permeability alteration was investigated using Touhidi-Baghini's model. Figure 6-33 displays the measured and predicted variation of absolute permeability using Touhidi-Baghini's equation for the B value of 5 during isotropic unloading. It can be seen that at low dilation values, Touhidi-Baghini's equation can capture the permeability changes, while at high values of volumetric expansion, it significantly underestimates the modified permeability.

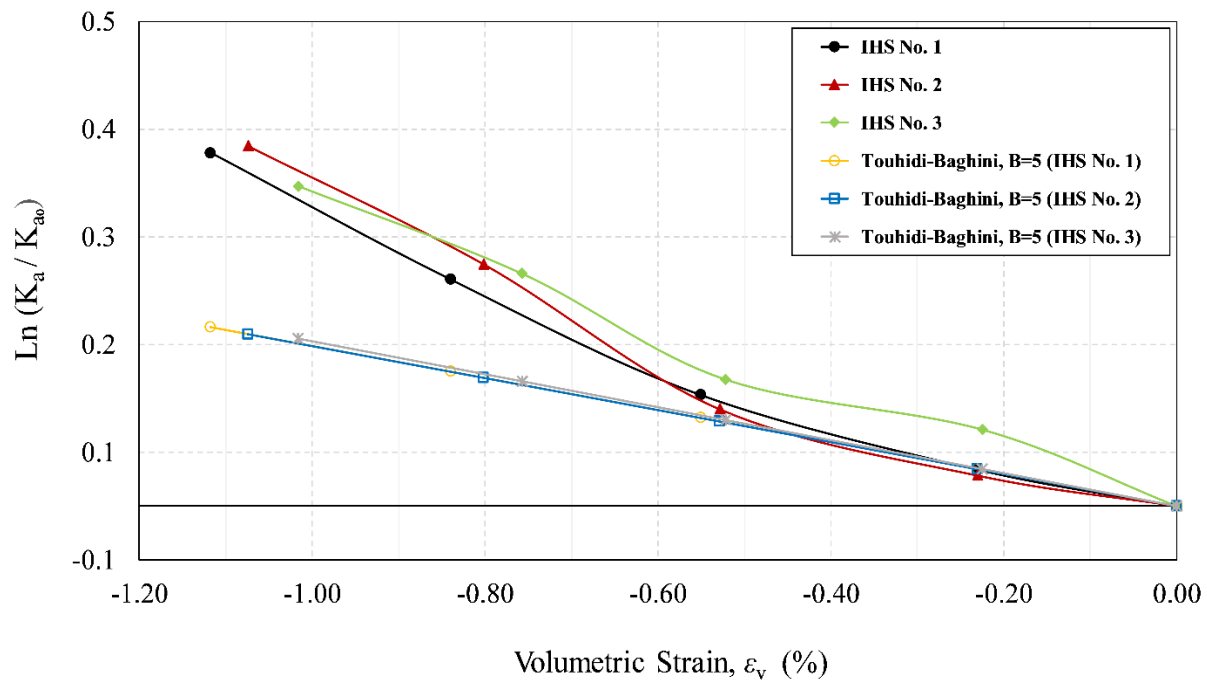


Figure 6-33 Prediction of absolute permeability alteration of IHS during isotropic unloading using Touhidi-Baghini's equation

Using any of the above-mentioned equations for calculating the modified absolute permeability due to shearing induces a significant error, because all of these relationships were derived based on the assumptions that pore shape, particle shape, and particle size do not change in the course of shearing. As shown earlier, these assumptions are not valid. In fact, the grain crushing, fine-grained soil migration, and pore structure rearrangement that occur during shearing significantly change the sample tortuosity and consequently alter the permeability value. In addition, all of these equations underestimate the amount of permeability improvement due to dilation. Such underestimations are more severe in the secondary permeability augmentation region, and also for the bioturbated sample.

6.6.3. Empirical Correlations for Changes in Absolute Permeability

As explained earlier, the final results revealed that the evolution of permeability during isotropic unloading is twofold (Figure 6-34 and Figure 6-35). Additionally, it was observed that a linear semi-logarithmic relationship could reasonably capture the permeability changes during a

geomechanically-induced volumetric expansion (at least in the primary region). Therefore, using the curve fitting techniques, the following correlations were obtained for non-bioturbated samples in the primary and secondary regions respectively:

$$\begin{aligned} \text{Non-Bioturbated IHS - Primary Region: } \ln\left(\frac{K}{K_0}\right) &= -0.19 \varepsilon_v \\ R^2 &= 0.95 \end{aligned} \quad \text{Equation 6-4}$$

$$\begin{aligned} \text{Non-Bioturbated IHS - Secondary Region: } \ln\left(\frac{K}{K_0}\right) &= -0.40 \varepsilon_v - 0.11 \\ R^2 &= 0.95 \end{aligned} \quad \text{Equation 6-5}$$

The same type of correlations were developed for bioturbated samples as follows:

$$\begin{aligned} \text{Bioturbated IHS - Primary Region: } \ln\left(\frac{K}{K_0}\right) &= -0.45 \varepsilon_v \\ R^2 &= 0.96 \end{aligned} \quad \text{Equation 6-6}$$

$$\begin{aligned} \text{Bioturbated IHS - Secondary Region: } \ln\left(\frac{K}{K_0}\right) &= -1.22 \varepsilon_v + 0.43 \\ R^2 &= 0.95 \end{aligned} \quad \text{Equation 6-7}$$

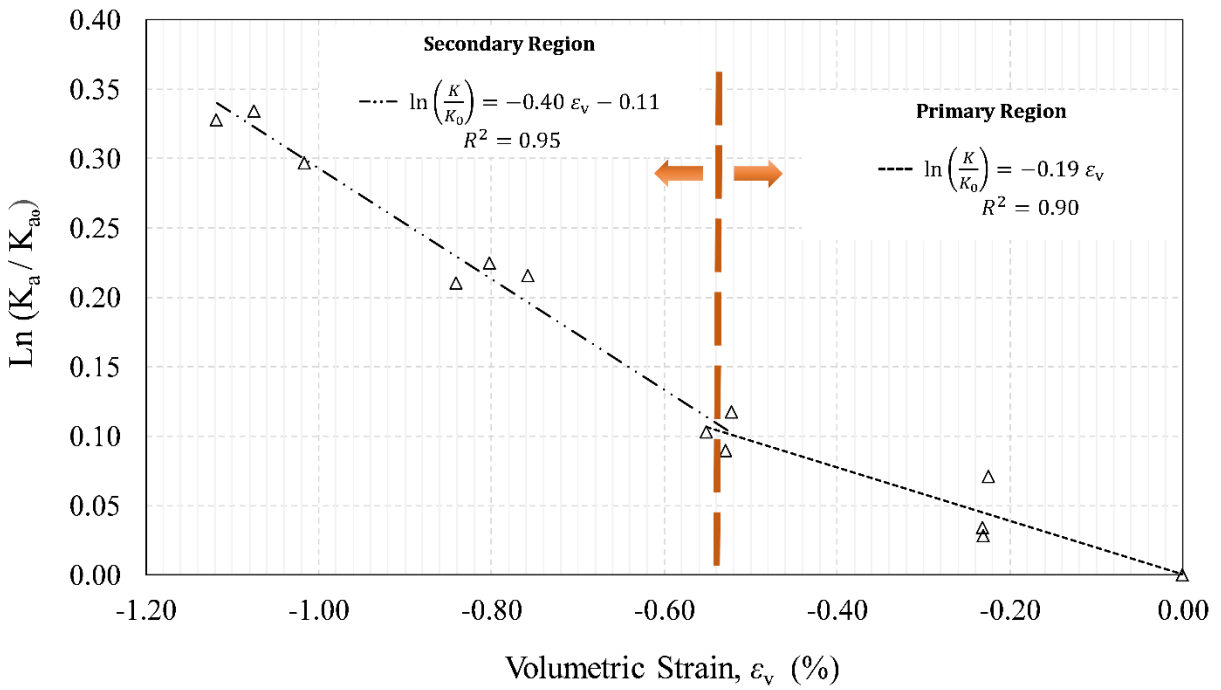


Figure 6-34 Normalized absolute permeability correlation for non-bioturbated IHS samples

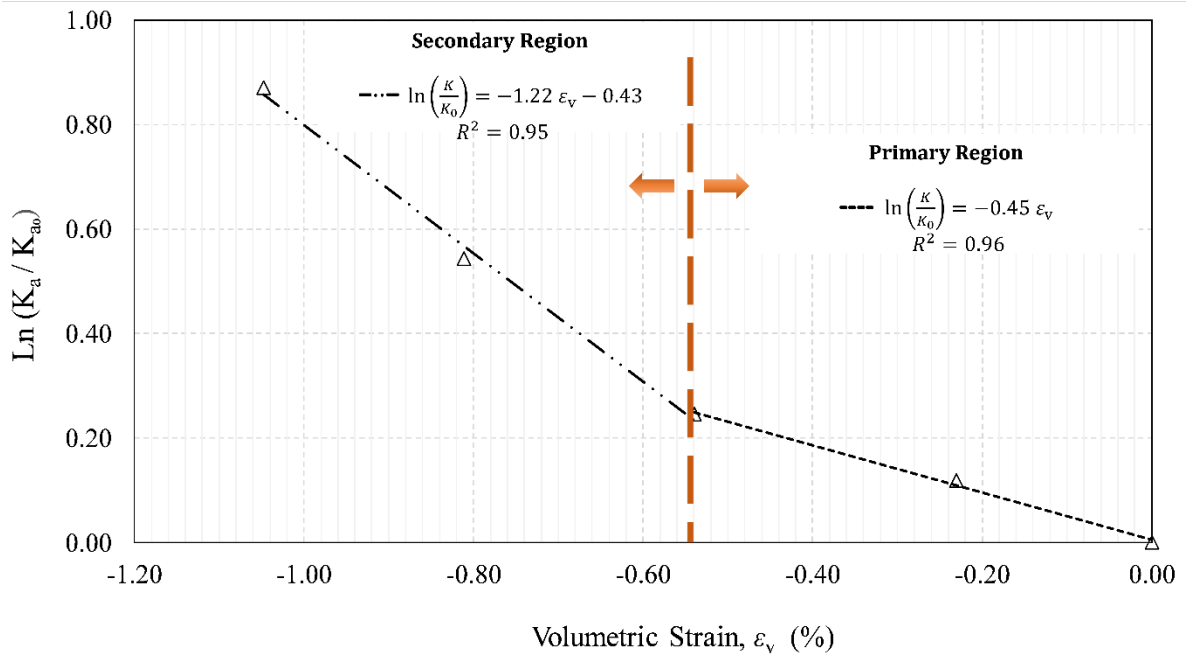


Figure 6-35 Normalized absolute permeability correlation for bioturbated IHS samples

As shown in Figure 6-34 and Figure 6-35, the vertical dashed line defines a volumetric dilation threshold of 0.54% for transitioning from the primary region to the secondary region in both non-

bioturbated and non-bioturbated IHS specimens. It is also worth noting that the coefficient of ε_v in the above-mentioned correlations (slope of the lines) corresponds to C_{nl} in Touhidi-Baghini's expression.

6.7. Summary

The following summarizes the conclusions of this chapter:

- Bulk compressibility of IHS is a strong function of the effective confining stress, particularly at low stress levels (below 3 MPa), and the relationship between them can be expressed using a power function.
- The elastic modulus of analog IHS increases with the increase in effective confining stress, and its variation with σ_3' can be captured using a hyperbolic function.
- The dilative or contractive behavior of the IHS specimens during shearing is predominantly controlled by the value of effective confining stress (σ_c'). In fact, the dilation angle of IHS decreases with the increase in effective confining stress, and its variation with σ_c' can be described using a linear function.
- The analogue IHS specimens were found to have an effective cohesion of 0.15 MPa and an effective friction angle of 37° .
- Comparing the measured stress-strain and strength parameters of the bioturbated IHS specimen with non-bioturbated samples assured that the existence of bioturbation imparts a negligible influence on the mechanical properties of the IHS.
- The absolute permeability of non-bioturbated IHS increases up to 40% with the decrease in effective confining stress from 7 MPa to 1 MPa. The amount of such an increase in the bioturbated sample was 140%. The test results also revealed that the dilative behavior of the samples during isotropic unloading leads to this permeability augmentation. It should also be noted that the initial value of absolute permeability for the bioturbated sample was an order of magnitude larger than that of the non-bioturbated samples.

- The variation of absolute permeability during shearing is a function of both effective confining stress and degree of bioturbation. For IHS No. 1 (σ_3' of 3.5 MPa), the permeability continuously decreased throughout the shearing. For IHS No. 2 and 3 (σ_3' of 1 and 0.5 MPa), the permeability was reduced prior to the axial strain of 7%, then it rose until the end of shearing. Despite the final increases in the permeability value, the initial permeability of the samples was not retrieved by the end of shearing. Finally, for IHS No. 4 (σ_3' of 0.5 MPa and bioturbated), after a short period of permeability fluctuation, the permeability of the sample continuously lowered until the end of shearing. This phenomenon was probably due to the fine-grained soil migration that occurred in this sample.
- Considering the volumetric behavior of the IHS samples during triaxial compression tests, it can be concluded that, unlike the isotropic unloading tests, the sample's dilation during shearing does not necessarily translate into permeability augmentation. For that to be effective, the value σ_3' needs to be low, and the amount of dilation is required to reach a certain level.
- The results showed that the rate of permeability evolution during isotropic unloading is not constant. In fact, after dilation to a certain degree, this rate increases significantly. Therefore, a bilinear curve fit model was used to capture such behavior. Moreover, two linear semi-logarithmic correlations were developed to link the absolute permeability variation to geomechanically-induced volumetric dilation in the primary and secondary permeability augmentation regions.
- Previous empirical permeability relationships are only applicable to calculate the modified absolute permeability due to isotropic unloading in the primary region and the triaxial shearing under low effective confining stresses when the dilation value is high. This is because none of these correlations take the variation of tortuosity or creation of microcracks within the sample into account. In fact, the underlying assumptions of unchanged pore shape and particle size in these equations are not well founded.
- Comparing the hydro-geomechanical properties of IHS with its constituent layers showed that sand-dominated analog IHS specimens reflect the characteristics of both analog sand and mud samples. However, their behavior is heavily influenced by the sand rather than the mud.

7. NUMERICAL SIMULATION OF IHS GEOMECHANICAL BEHAVIOR

7.1. Introduction

In order to numerically simulate the geomechanical constitutive behavior of sand-dominated IHS, a representative geomechanical model is needed. To obtain this model, the laboratory testing results on sand, mud, and IHS specimens were analyzed and simulated using FLAC3D™ software. Chapter 7 describes the numerical simulator, constitutive model, and material properties that were used in building this geomechanical model.

In addition, this chapter compares the results of numerical experiments on sand, mud, and IHS samples with the outcomes of laboratory tests on these specimens. These comparisons include characteristics such as drained shear strength, stress-strain behavior, mode of failure, and volumetric behavior during shearing.

7.2. FLAC3D™

FLAC3D™ (Fast Lagrangian Analysis of Continua 3 Dimensions) is a three-dimensional explicit Lagrangian finite-difference program that can be used to simulate the behavior of structures made of soil, rock, or other materials displaying path-dependent behavior. The basis of FLAC3D™ codes is a numerical formulation used by the two-dimensional program FLAC™. While FLAC™ has the capability of analyzing engineering mechanics in two dimensions, FLAC3D™ extends this capability into three dimensions (Itasca, 2017).

In FLAC3D™, materials are represented by polyhedral elements within a three-dimensional grid, and the user has the capability of adjusting the grid in order to fit the shape of the object that needs to be modeled. When forces or boundary restraints are applied to the material, its elements behave according to a prescribed linear or nonlinear stress or strain law. Also, if the stresses are high

enough to cause the material to yield and flow, the grid can deform (in large-strain mode) and move with the material that is represented (Itasca, 2017).

In order to model the plastic collapse and flow of the material, FLAC3D™ uses the explicit Lagrangian calculation scheme and the mixed-discretization zoning technique. This permits large three-dimensional calculations without excessive memory requirements since no matrices are formed. It is also worth noting that the explicit formulation has its own disadvantages such as a small timestep limitation and the issue of required damping. These drawbacks are overcome by the benefits of automatic damping and automatic inertia scaling, which minimize the effects on the path to plastic yielding (Itasca, 2017).

FLAC3D™ has nineteen built-in constitutive models available that allow the simulation of the highly nonlinear irreversible response of geologic materials. Among them is Plastic Hardening which was introduced in the latest version of the software. This software also has its own built-in programming language, FISH, which is the short form of FLAC-ISH. This scripting language gives the user powerful control over almost every aspect of the program's operation. Therefore, FLAC3D™ offers an analysis tool to solve three-dimensional problems in geotechnical engineering, particularly in soil testing. Finally, it should be noted that in this study, FLAC3D™ version 6 was used (Itasca, 2017).

7.3. Constitutive Model

Considering the laboratory test results on sand, mud and IHS samples which display mainly a plastic hardening behavior with very little to no shear softening, the Plastic Hardening (PH) constitutive model was chosen to simulate and analyze the geomechanical behavior of the specimens. This model, which is specially developed to simulate soil behavior, is a shear and volumetric hardening constitutive model.

As explained by Duncan and Chang (1970) in their “hyperbolic-soil” model, during a conventional drained triaxial compression test, when a soil specimen is subjected to deviatoric stress, it shows

a decrease in stiffness which is associated with irreversible deformation. Therefore, in the majority of cases, such as the ones presented for the samples in chapters 4 to 6, the plot of deviatoric stress versus axial strain can be approximated by a hyperbola.

The formulation framework for the PH constitutive model is hardening plasticity (Schanz et al., 1999). Furthermore, the PH model has several notable features such as i) hyperbolic stress-strain relationship during drained axial compression, ii) shear hardening or plastic strain in mobilizing friction, iii) volumetric hardening or plastic strain in primary compression, iv) stress-dependent elastic stiffness, and v) Mohr-Coulomb failure criterion (Itasca, 2017). These features, as well as the straightforward process for calibrating the PH model, enabled this model to be utilized to simulate and characterize the geomechanical behavior of tested soil specimens.

As stated before, in order to describe the elastic behavior, the PH model adopts hypo-elasticity. In fact, in addition to the Young's Modulus, this model uses an additional stiffness criterion, E_{50} . As displayed in Figure 7-1, this measure can be defined as the initial slope of the hyperbolic stress-strain curve, and can be expressed as follows:

$$E_{50} = E_{50}^{ref} Z^m \quad \text{Equation 7-1}$$

$$Z = \frac{c \cot \varphi - \sigma_3}{c \cot \varphi + p^{ref}} \quad \text{Equation 7-2}$$

where E_{50}^{ref} is a material parameter (that could be estimated from a set of triaxial compression tests), p^{ref} is reference pressure, c is cohesion, and m is a user-defined function that needs to be calibrated through series of lab tests.

In the PH model, the following shear yield function is used to detect the start and development of shear hardening.

$$f^s = \frac{E_{ur}}{E_i} \times \frac{q_a q}{(q_a - q)} - q - \frac{E_{ur} \gamma^p}{2} = 0 \quad \text{Equation 7-3}$$

where γ^p is the shear hardening parameter, q is deviatoric stress ($\sigma_1 - \sigma_3$), and E_{ur} is unloading-reloading Young's modulus. The E_i and q_a in the above formula can be calculated using the Equation 7-5/Equation 7-6 respectively.

$$E_i = \frac{2E_{50}}{(2 - R_f)} \quad \text{Equation 7-4}$$

$$q_a = \frac{q_f}{R_f} = K_{qa}(c \cot \varphi - \sigma_3) \quad \text{Equation 7-5}$$

$$K_{qa} = \frac{1}{R_f} \times \frac{2 \sin \varphi}{1 - \sin \varphi} \quad \text{Equation 7-6}$$

The R_f in these equations is the failure ratio which can be defined as the ratio of q_f to q_a ; therefore, its value is always smaller than one. In the PH model, the ultimate deviatoric stress can be computed using the following expression, which is consistent with the Mohr-Coulomb failure criterion:

$$q_f = \frac{2 \sin \varphi (c \cot \varphi - \sigma_3)}{1 - \sin \varphi} \quad \text{Equation 7-7}$$

The relationship between axial strain (ε_1) and deviatoric stress (q) in a drained triaxial test can be expressed using Equation 7-8. This equation is also displayed in Figure 7-1 with the cut-off at q_f .

$$\varepsilon_1 = \frac{q_a q}{E_i(q_a - q)} \quad \text{Equation 7-8}$$

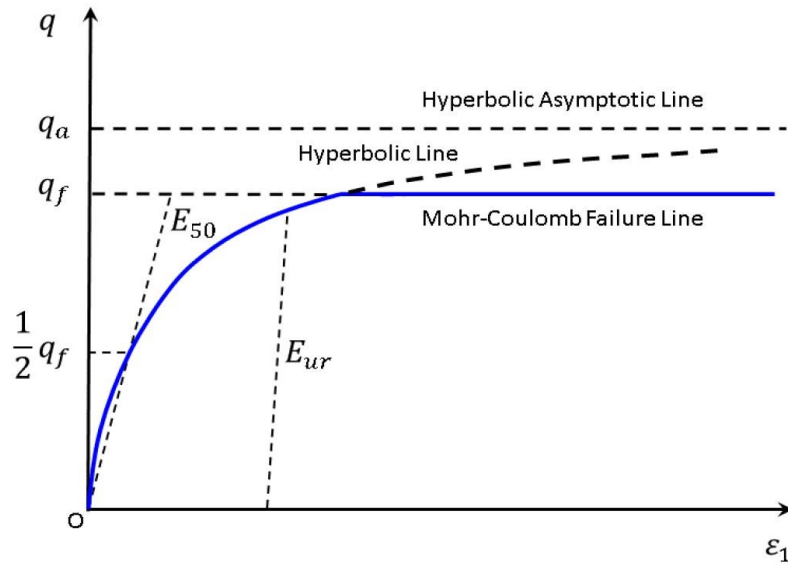


Figure 7-1 Hyperbolic stress-strain relation (Itasca, 2017)

The shear hardening parameter γ^p , which is used in shear yield function, can be defined in its incremental form as follows:

$$\Delta\gamma^p = -(\Delta\varepsilon_1^p - \Delta\varepsilon_2^p - \Delta\varepsilon_3^p) \quad \text{Equation 7-9}$$

When the shear hardening parameter increases, the shear yield surface expands to its ultimate surface. This ultimate shear yield surface is defined by a conventional Mohr-Coulomb failure criterion. Consequently, when the material undergoes ultimate shear failure, the Mohr-Coulomb failure criteria are triggered.

In the PH model, the relationship between the volumetric and shear plastic strains can be expressed using the following flow rule in which $\sin(\psi_m)$ is the mobilized dilation angle.

$$\Delta\varepsilon_v^p = \sin \psi_m \Delta\gamma^p \quad \text{Equation 7-10}$$

It should also be noted that the mobilized dilation angle should be smaller or equal to the user-defined ultimate dilation angle. More details on this constitutive model, its capabilities, and its material properties' calibration process can be found in the FLAC3D™ user manual.

7.4. Numerical Analysis

In this study, a total of nine numerical experiments were performed, including three tests on sand samples, three tests on mud samples, and three tests on IHS samples. The approach taken in this study was to perform these numerical experiments under the same testing conditions as those applied in the laboratory. The testing conditions comprise stress and displacement boundary conditions, material properties, and applied stress path.

As stated before, FLAC3D™ version 6 was used as a geomechanical simulator in this study, and the Plastic Hardening constitutive model was applied in all tests. The constitutive model parameters and other required input data were extracted from the triaxial tests described in chapters 4 and 5. The numerical experiment approach was employed to match the laboratory test results, which included drained shear strength, stress-strain behavior, mode of failure, and volumetric behavior during shearing.

As explained in Chapter 4, in this study, strain-control shearing was chosen to fail the samples in the laboratory. Therefore, in numerical experiments, the axial loading was applied through increments of vertical displacement (vertical velocity). The rate of loading could cause an inertia effect. To minimize such an effect, very low vertical velocities with a high number of steps were used to shear the samples. The vertical velocities were chosen so that the specimens would experience 10% axial strain in 400,000 steps.

Unlike FLAC, FLAC3D™ allows the full cylinder to be modeled in the numerical experiments. This is particularly needed in the case of IHS samples in which the sand and mud layers are not axisymmetric. Figure 7-2 shows the grid systems that were used for all numerical experiments. It can be seen that the same grid system ($7 \times 10 \times 7 \times 4 = 1960$ blocks) was applied in all numerical experiments on sand and mud samples. However, a grid system with a higher number of blocks ($7 \times 100 \times 7 \times 4 = 19600$ blocks) was applied for the IHS specimens. In light of the effects of the grid system on the simulation result, it was found that the grid system of 19600 blocks could minimize the gridding effect, and also capture the geometry of sand and mud layers in IHS samples reasonably well.

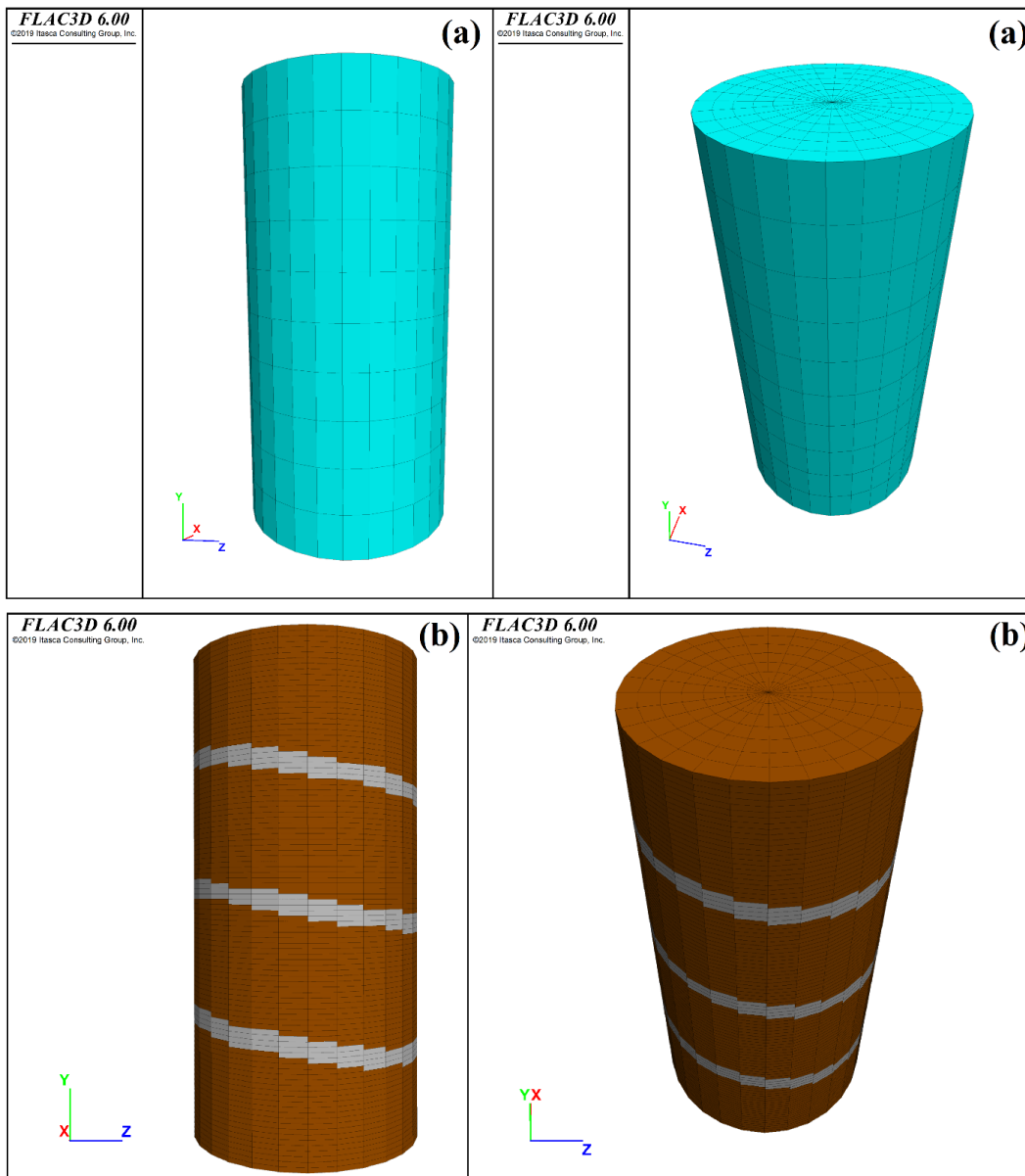


Figure 7-2 Geometry of the problems and the assumed grid sizes for sand (a), mud (a), and IHS (b) samples

7.4.1. FLAC3DTM Numerical Experiments of Laboratory Tests on Sand Layer

In the numerical simulation of sand samples, the conventional triaxial compression test stress path was applied to all specimens. A total of three numerical experiments was performed under

effective confining stresses of 0.5, 1, and 3.5 MPa. Figure 7-3 shows the deviatoric stress versus axial strain behavior followed in the numerical simulations and the actual experiments.

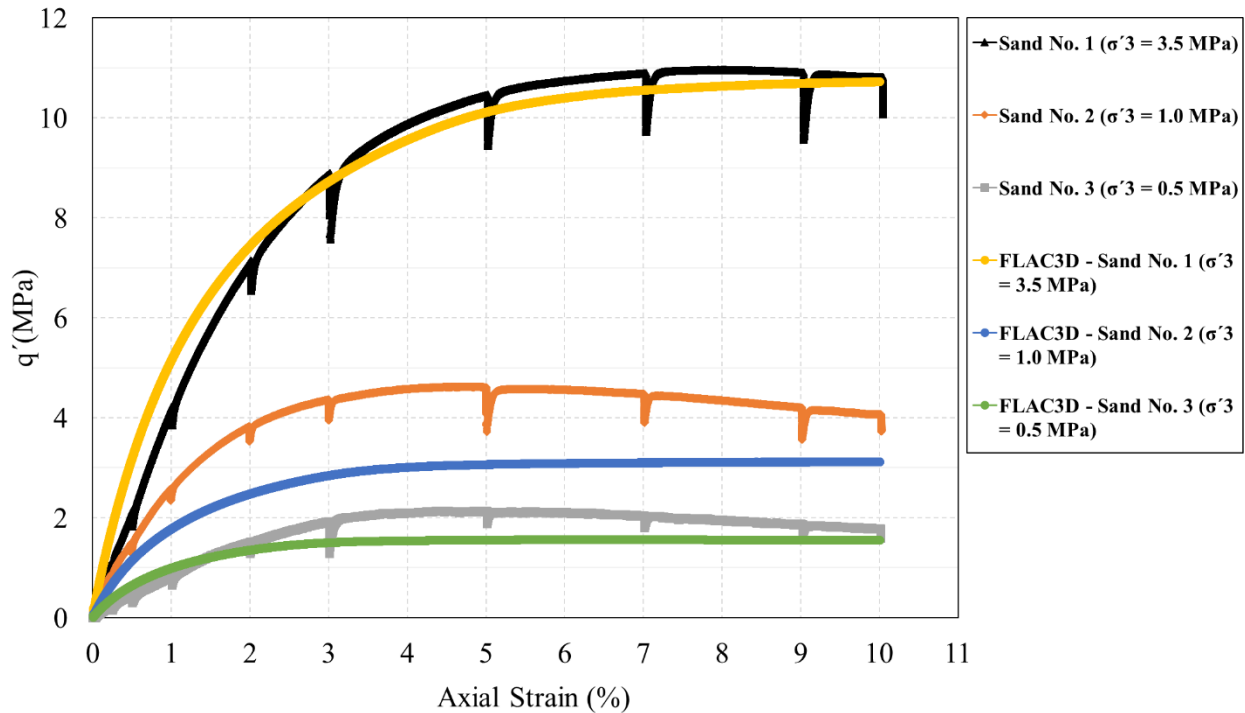


Figure 7-3 Deviatoric stress versus axial strain for sand samples (Lab tests simulated by FLAC3D™)

As can be seen in Figure 7-3, the stress-strain relationships in both laboratory tests and numerical simulations show the same trend for all samples. With regard to numerical values, the shear strength of Sand No.1 is 2% higher in the experimental study compared to numerical simulation. However, for Sands No. 2 and No. 3, there are minor deviations between the simulated shear strength and the experimental results. Such discrepancy is because the used friction angle in the model was the same in all three sand samples, which was not the case in the actual experiments. In fact, the true value of the friction angle is a function of the density of the sample and the effective confining stress under which the sample is sheared. As explained in Chapter 4, increasing the effective confining stress and decreasing the density of a sample could both lead to a decrease in friction angle. Therefore, considering the lower values of effective confining stresses for Sands No. 2 and 3, and also the slightly higher density value (lower porosity) for these samples compared to Sand No. 1, it can be concluded that the actual friction angles of these two samples are higher than the one used in the model. Consequently, it would be more appropriate to use a series of input

functions for the friction angle that represents the changes in the friction angle under various effective confining stresses and/or dry densities.

The predicted volumetric strain versus axial strain behavior for the three sand samples are shown together in Figure 7-4. It can be seen that the volumetric behaviors in both laboratory tests and numerical simulations show the same trend for all sand samples. For example, the difference in the peak dilation rate (refer to Figure 4-7) between experimental and numerical results for Sand No. 2 is 5%. The minor deviation observed in the contraction part of Sand No. 1 is because the compressibility of the sand samples is not constant. In fact, as explained in Chapter 4, the value of compressibility decreases with the increase in effective confining stress, and its variation is not linear.

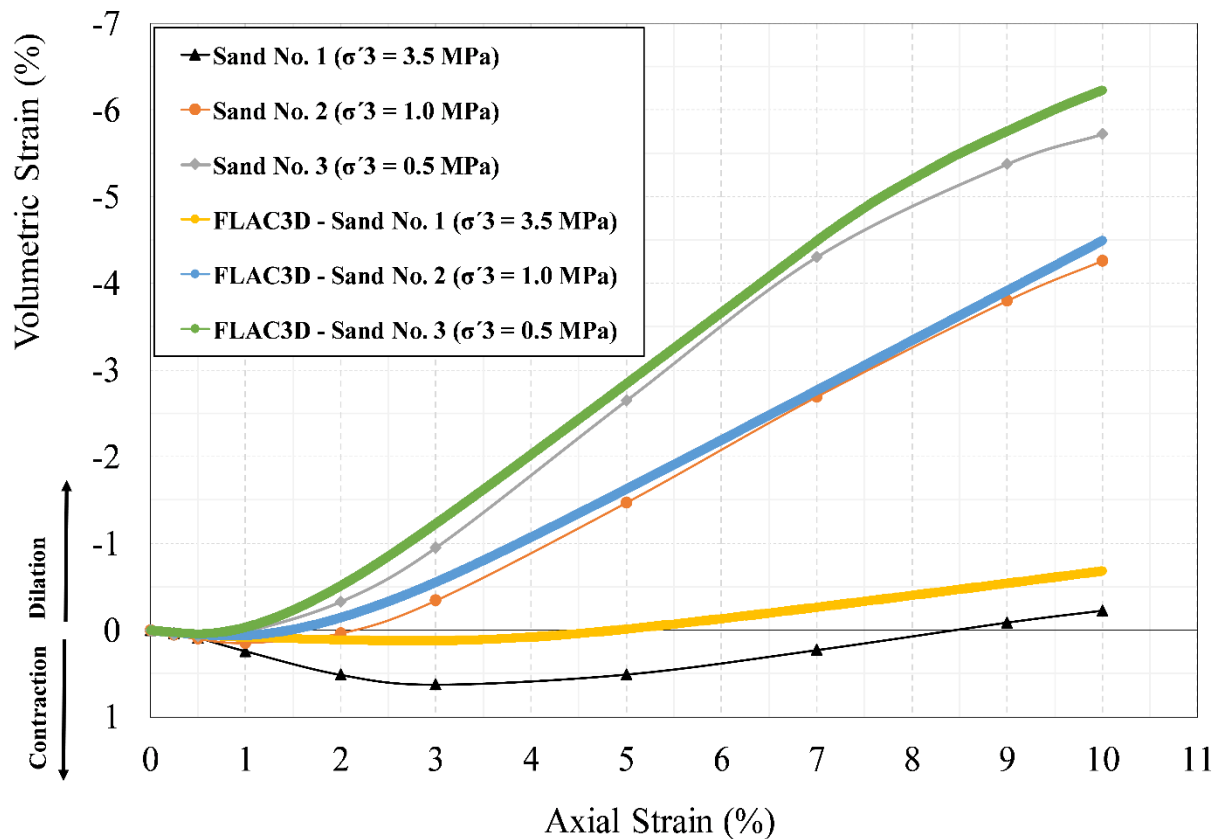


Figure 7-4 Volumetric strain versus axial strain for sand samples (Lab tests simulated by FLAC3D™)

As explained in section 4.4.1.5, one of the qualitative methods that can be used to determine the mode of failure in a shear test is investigating the state of a sample at the end of shearing. The other methods are using the stress-strain curve and the amount of stress drop after peak shear stress (Mercier et al., 2003; Schöpfer et al., 2013). In this numerical study, in order to analyze the shape of failed specimens, the contours of volumetric and shear strains of the failed sand samples under effective confining stresses of 3.5, 1 and 0.5 MPa together with CT images of the sheared samples are plotted in Figure 7-5 Figure 7-7 respectively.

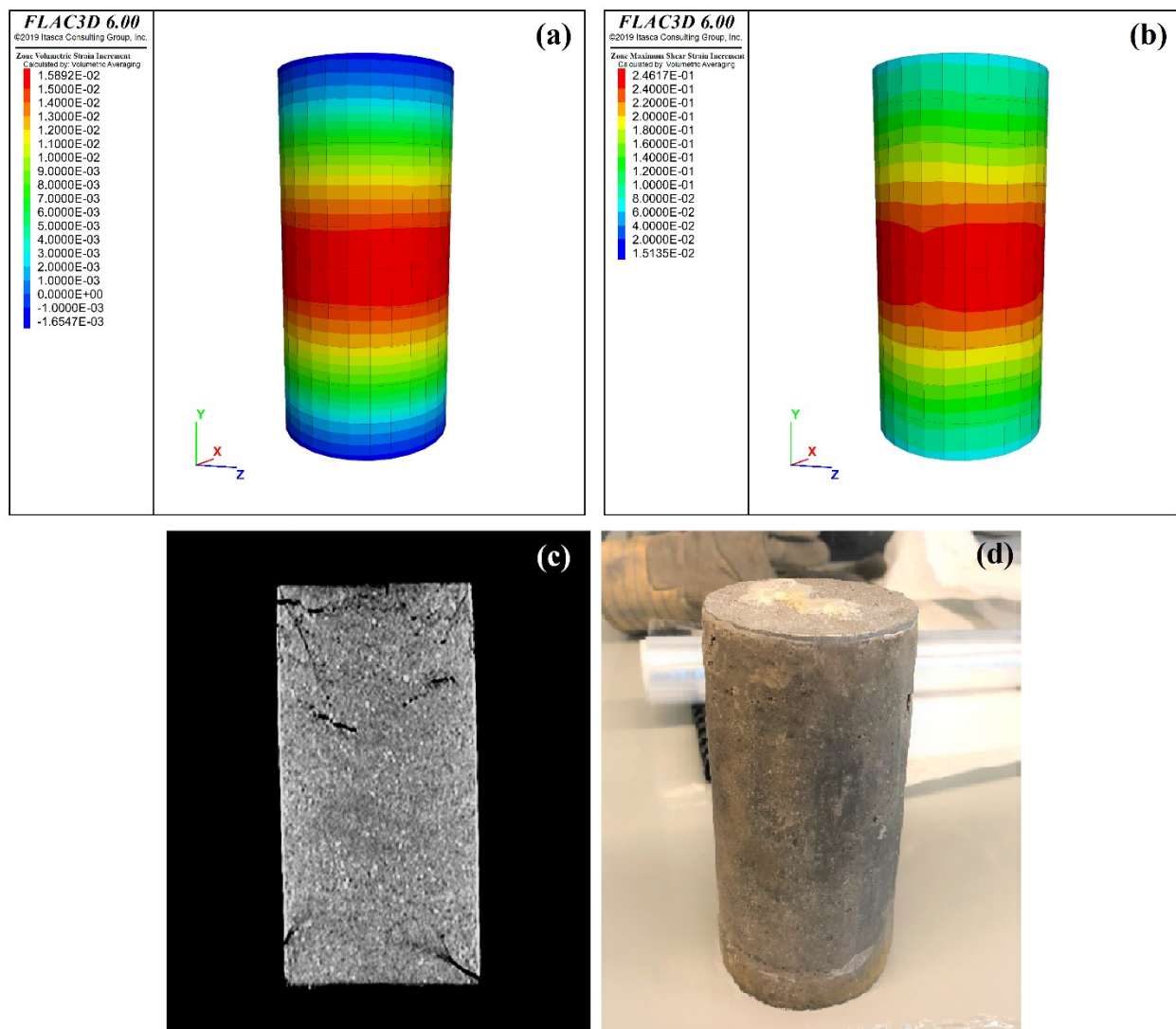


Figure 7-5 Contours of volumetric strain (a), contours of shear strain (b), CT Scan (c), and digital image (d) of Sand No. 1 ($\sigma'_3 = 3.5$ MPa)

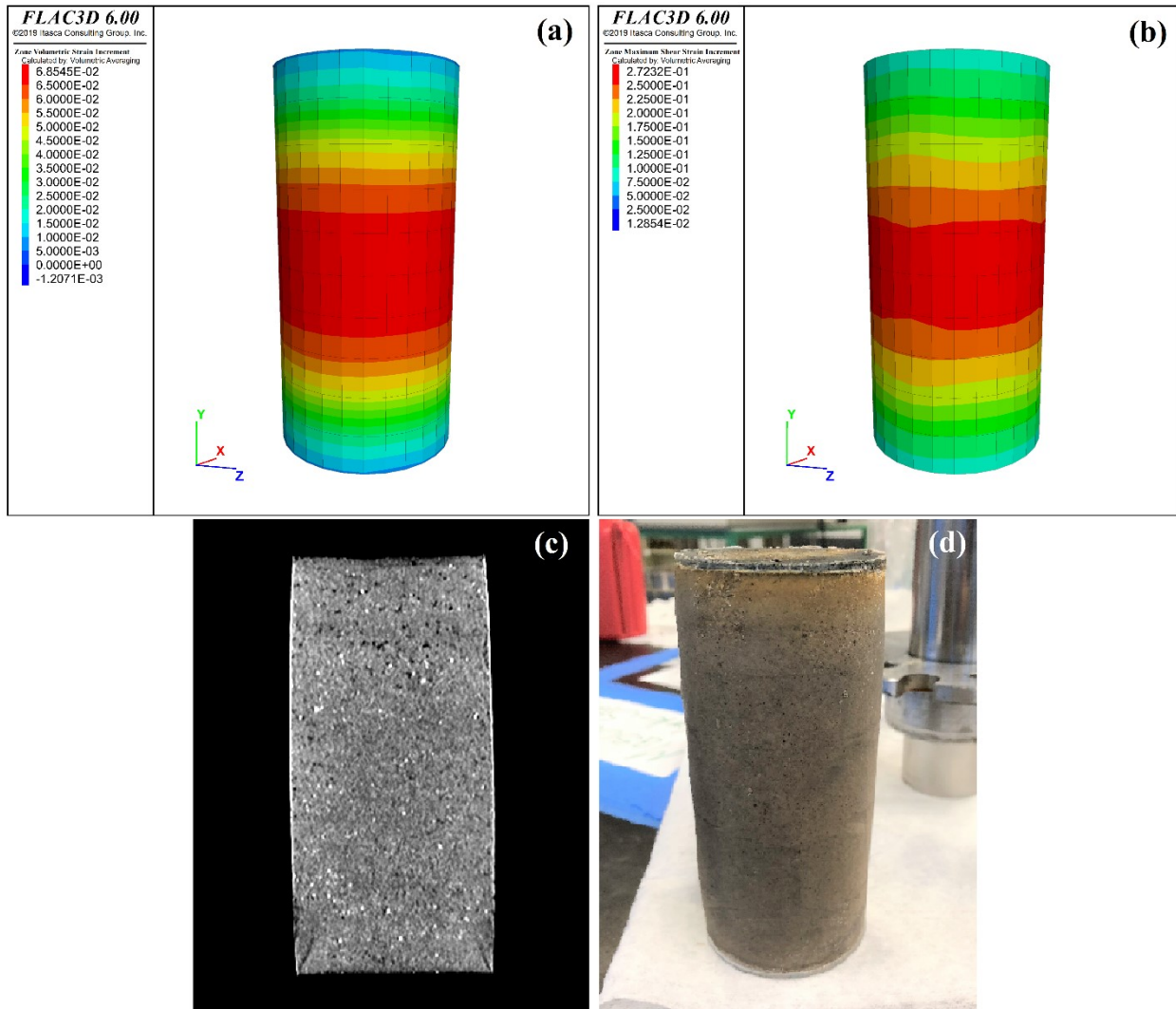


Figure 7-6 Contours of volumetric strain (a), contours of shear strain (b), CT Scan (c), and digital image (d) of Sand No. 2 ($\sigma_3' = 1$ MPa)

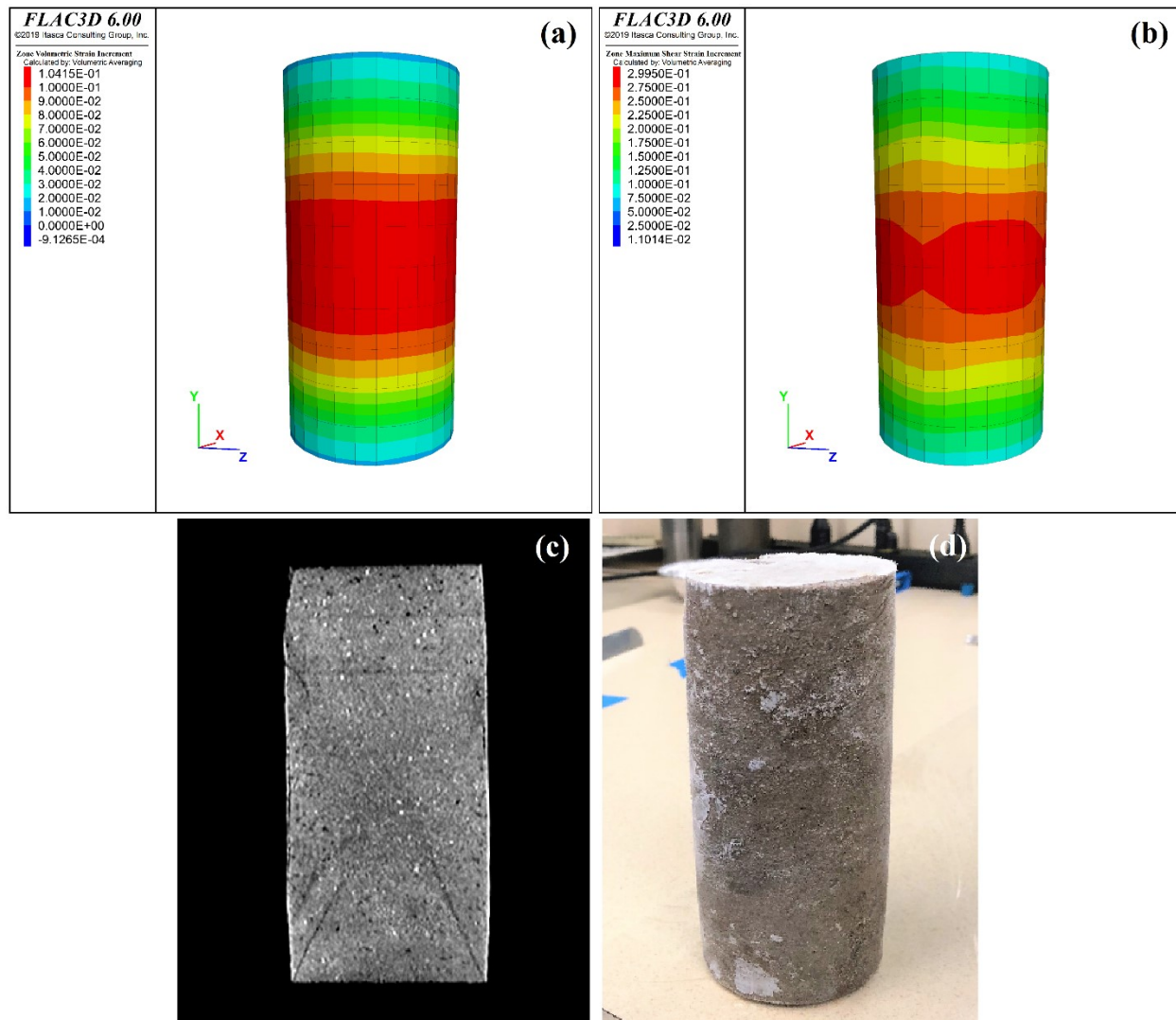


Figure 7-7 Contours of volumetric strain (a), contours of shear strain (b), CT Scan (c), and digital image (d) of Sand No. 3 ($\sigma'_3 = 0.5$ MPa)

It can be seen that within all three sand samples, the deformation was not uniform. Indeed, the concentrations of volumetric dilation and shear deformation occurred in the middle of the specimens, with their ends remaining relatively unaffected. This implies an outward bulging of the middle region of the specimens, which is consistent with the behavior observed in the CT scan images of the sand samples.

In addition, in view of the result presented in Figure 7-3, it can be concluded that the three tested sand samples have shown a large amount of plastic deformation, with no obvious peaks in

deviatoric stress. Such behavior was expected, considering the fact that no clear shear band developed within these samples during shearing. Therefore, it can be concluded that the mode of failure for sand samples is ductile type failure with a bulge in the middle, or barreling failure. It is also worth noting that, unlike the lab tests, no cracks were observed at the top or bottom of the sheared samples. This might be due to the absence of end-cap friction in the numerical experiments.

7.4.2. FLAC3DTM Numerical Experiments of Laboratory Tests on Mud Layer

In the numerical simulation of mud samples, the conventional triaxial compression test stress path was applied to all specimens. A total of three numerical experiments were performed under effective confining stresses of 0.5, 1, and 3.5 MPa. The match obtained with experimental data for the stress-strain relationship as a function of axial strain is shown in Figure 7-8.

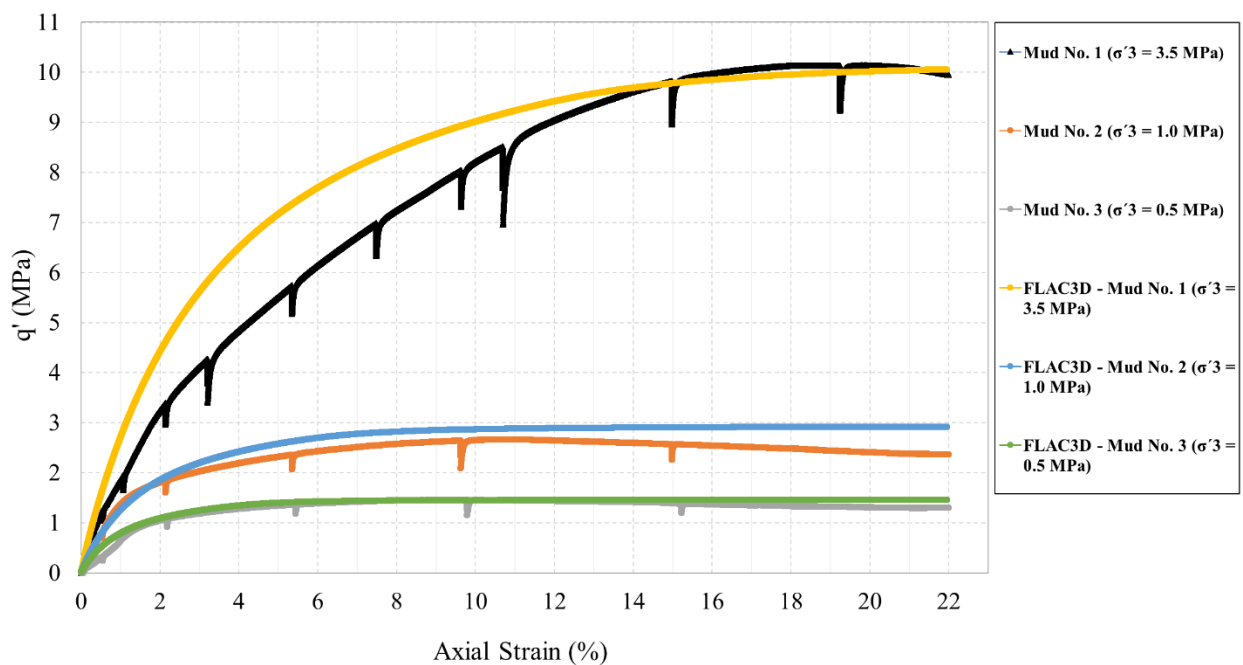


Figure 7-8 Deviatoric stress versus axial strain for mud samples (Lab tests simulated by FLAC3DTM)

As can be seen in Figure 7-8, the stress-strain relationships in both laboratory tests and numerical simulations show the same trend for the mud samples. For example, the difference in the peak

shear strength between experimental and numerical results for Mud No. 3 is 2%. There is a minor deviation between the simulated stress-strain curve and the experimental result for Mud No. 1. Such discrepancy is because the shear test on this sample was paused many times before the peak shear strength to run the permeability tests; these rest intervals might have caused creep and subsequent softening of the specimen. It is also apparent that the values of shear strength in all three mud samples were captured well in the simulations.

The predicted volumetric strain versus axial strain curves for the mud samples are shown together in Figure 7-9. It can be seen that the volumetric behaviors in both laboratory tests and numerical simulations show the same trend for all Mud samples. For instance, the difference in the peak dilation rate (refer to Figure 4-7) between experimental and numerical results for Mud No. 2 is 7%. The deviation that is observed in the contraction part of Mud No. 1 is because the compressibility of the mud samples is not constant. In fact, as explained in Chapter 5, the value of mud compressibility decreases with the increase in effective confining stress, and its variation is not linear.

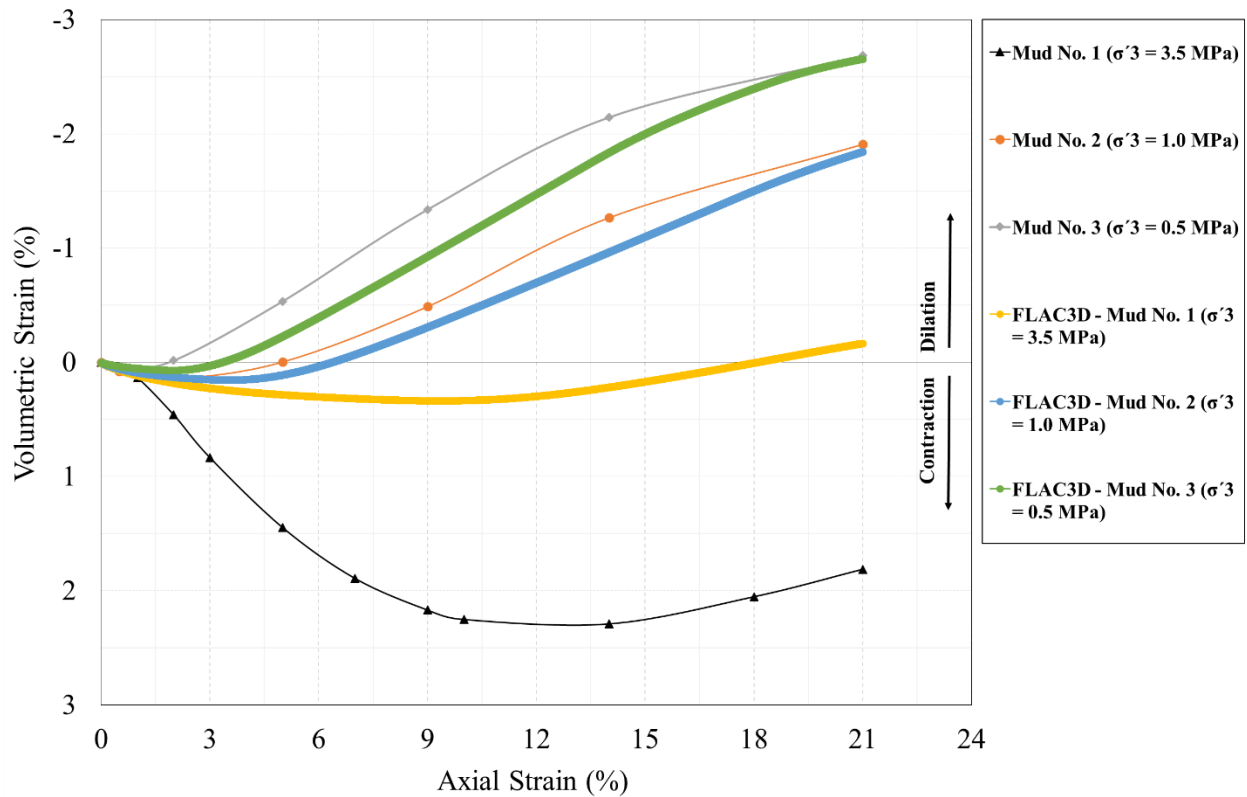


Figure 7-9 Volumetric strain versus axial strain for mud samples (Lab tests simulated by FLAC3D™)

Following the same procedure explained in section 7.4.1, the mode of failure in the analog mud samples was investigated. Figure 7-10Figure 7-12 show the contours of volumetric and shear strains of the failed mud samples, together with CT images of the sheared samples under effective confining stresses of 3.5, 1 and 0.5 MPa respectively. As described in section 5.4.1.5, Mud No. 2 was significantly disturbed during membrane removal; therefore, it could not be retrieved for CT scanning.

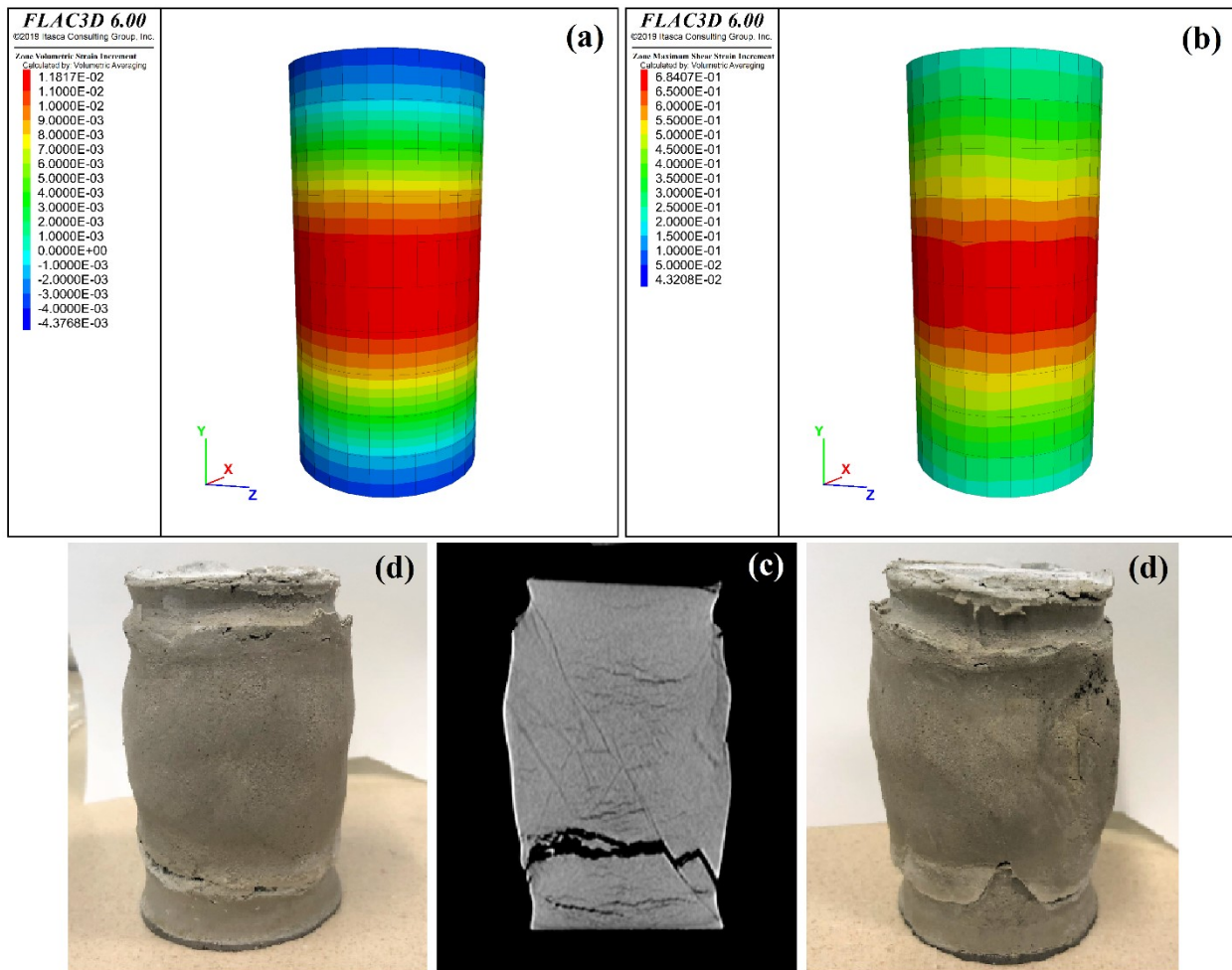


Figure 7-10 Contours of volumetric strain (a), contours of shear strain (b), CT Scan (c), and digital image (d) of Mud No. 1 ($\sigma_3' = 3.5$ MPa)

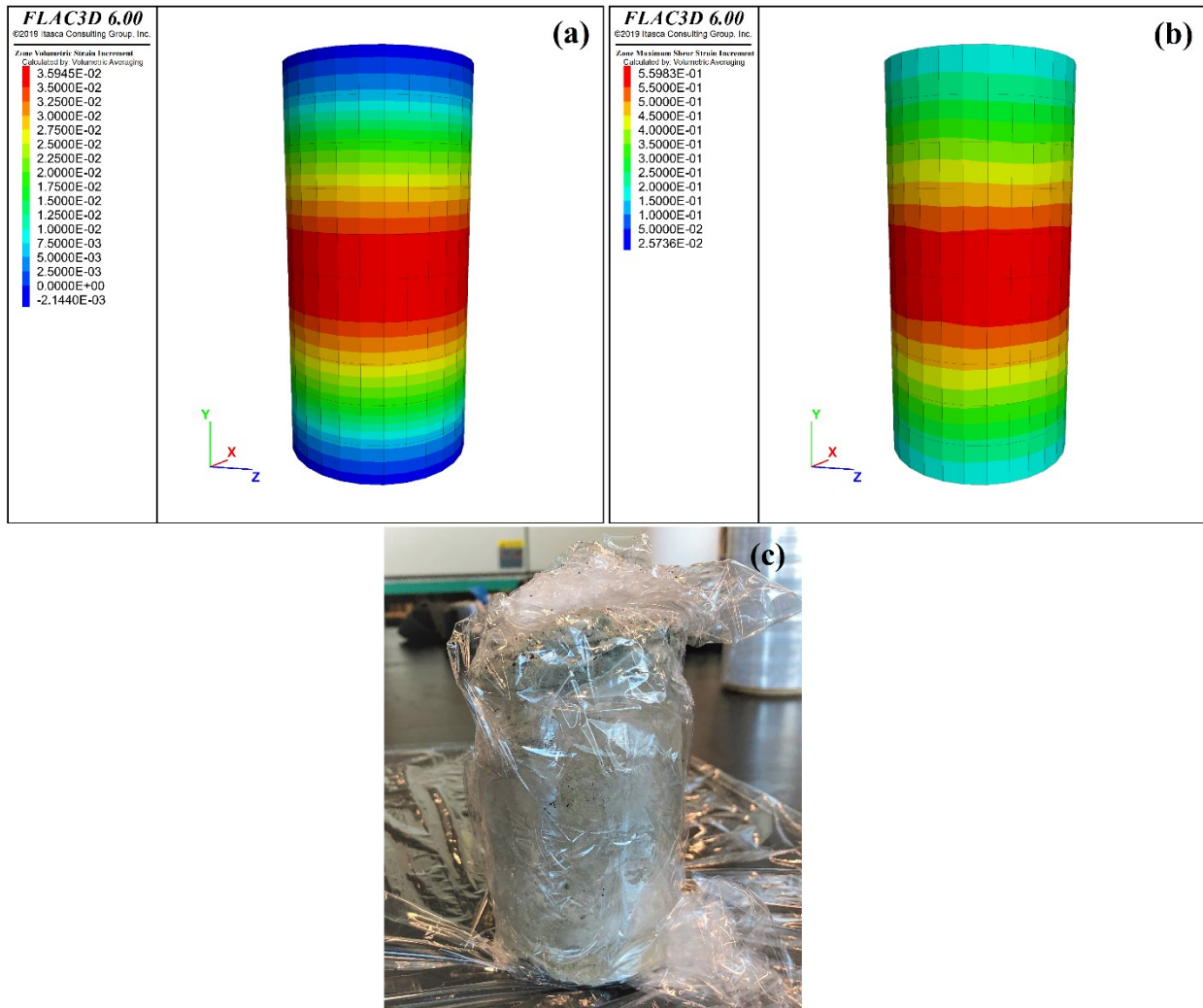


Figure 7-11 Contours of volumetric strain (a), contours of shear strain (b), and digital image (c) of Mud No. 1 ($\sigma'_3 = 1$ MPa)

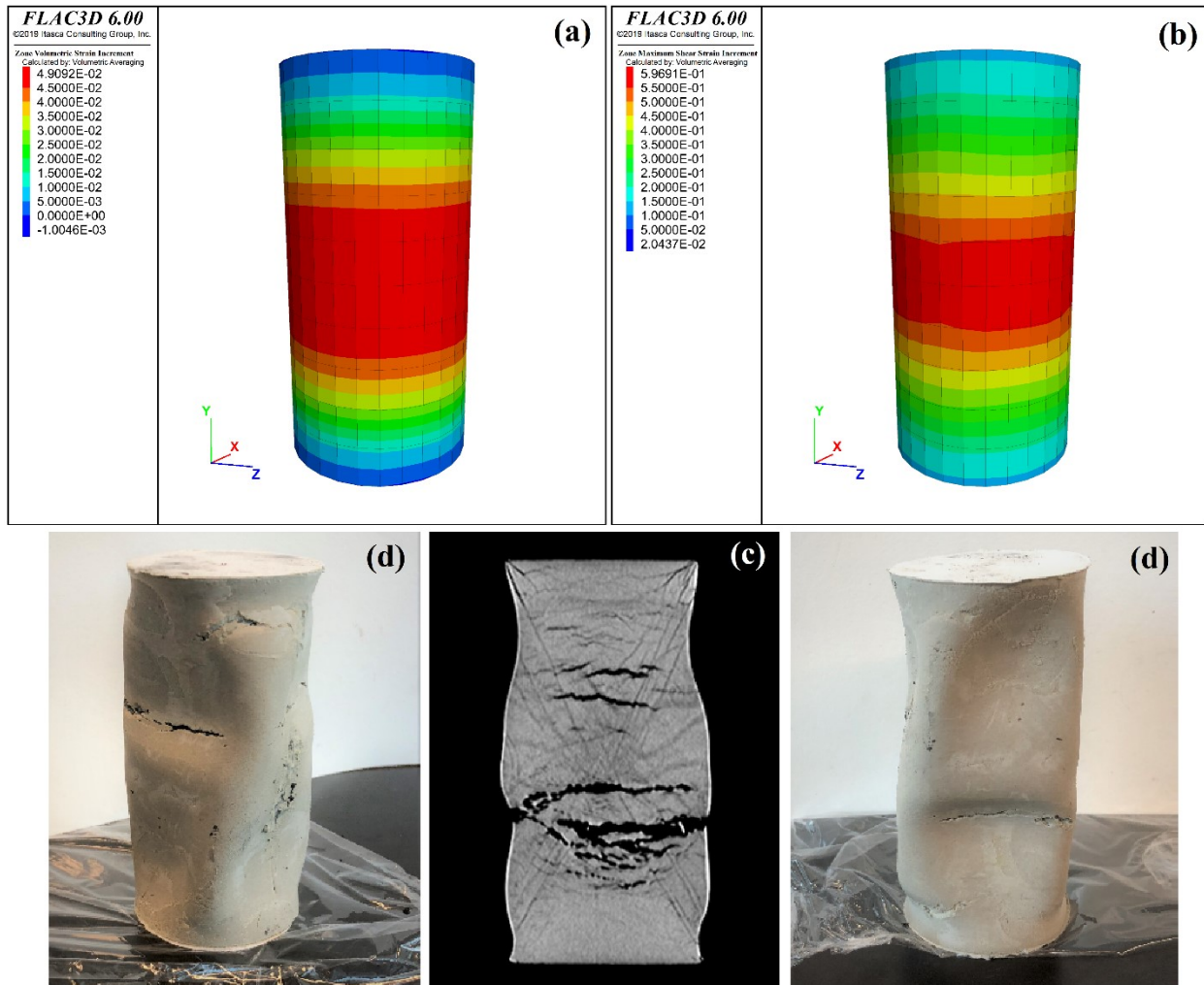


Figure 7-12 Contours of volumetric strain (a), contours of shear strain (b), CT Scan (c), and digital image (d) of Mud No. 3 ($\sigma_3' = 0.5$ MPa)

It can be seen that within all three mud samples, the deformation was not uniform. Indeed, the concentrations of volumetric dilation and shear deformation were in the middle of the specimens, and the samples' ends remained relatively unaffected. This implies the outward bulging of the middle region of the specimens, which is consistent with the behavior that was observed in CT scan images of the mud samples.

In addition, in view of the result presented in Figure 7-8, it can be concluded that the three mud samples tested have shown a large amount of plastic deformation, with no obvious peaks in deviatoric stress. Such behavior was expected considering the fact that no clear shear band

developed within the samples during shearing. Therefore, it can be concluded that the mode of failure for mud samples is ductile type failure with a bulge in the middle, or barreling failure. It is also worth noting that, unlike the lab tests, no cracks were observed at the top or bottom of the sheared samples. This might be due to the absence of end-cap friction in the numerical experiments.

7.4.3. FLAC3D™ Numerical Experiments of Laboratory Tests on IHS

As explained in section 7.4 and depicted in Figure 7-2-b, the geometry of the problem in the numerical simulation of an IHS sample is comprised of sand and mud layers. Since these layers have different material properties, two distinct sets of constitutive model parameters were used in the IHS model. The model was built for a sand-dominated IHS with three layers of mud (12% of the sample's volume). The angle of inclination for sand–mud contact is 10° in this model.

Considering the reasonable match between the numerical and laboratory experiments on the sand and mud samples (discussed in sections 7.4.1 and 7.4.2), the required input data for the sand and mud layers in the IHS model were extracted from the triaxial tests performed on the sand and mud samples respectively.

In the numerical simulation of the IHS samples, the conventional triaxial compression test stress path was applied to all specimens. A total of three numerical experiments were performed under the effective confining stresses of 0.5, 1, and 3.5 MPa. Figure 7-13 shows the deviatoric stress versus axial strain behavior followed in the numerical simulations and the actual experiments.

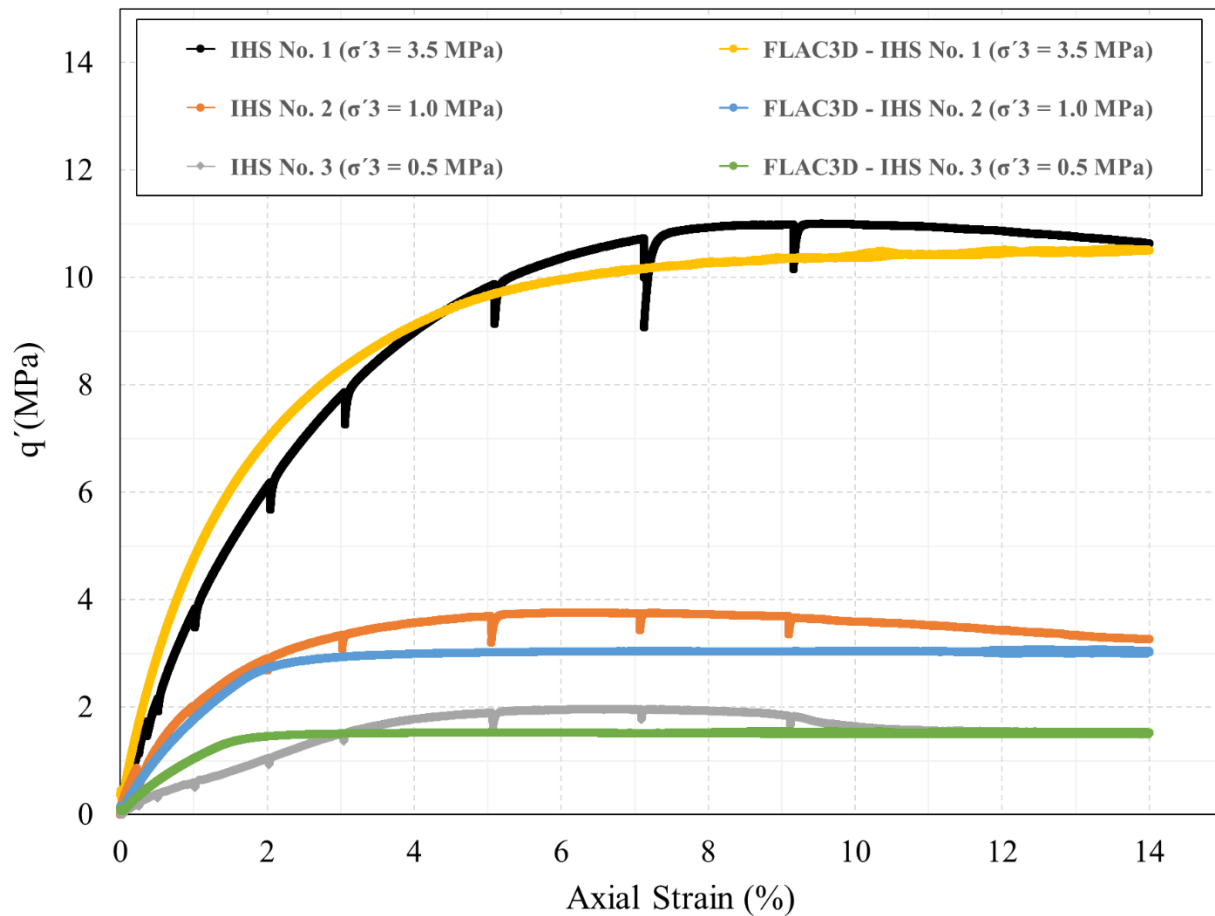


Figure 7-13 Deviatoric stress versus axial strain for IHS samples (Lab tests simulated by FLAC3D™)

As can be seen in Figure 7-13, the stress-strain relationships in both laboratory tests and numerical simulations show the same trend for all IHS samples. For example, the difference in the peak shear strength between experimental and numerical results for IHS No. 1 is 4%. Although the values of shear strength in all three IHS samples were captured reasonably well, there are minor deviations between the simulated shear strength and the experimental results. As explained in section 7.4.1, such discrepancy is because the friction angles which were used for the model's sand and mud layers were the same in all three IHS samples, which was not the case in the actual experiments.

The predicted volumetric strain versus axial strain curves for the three IHS samples are shown together in Figure 7-14. It can be seen that the volumetric behaviors in both laboratory tests and numerical simulations show the same trend for all IHS samples. For instance, the difference in the

peak dilation rate (refer to Figure 4-7) between experimental and numerical results for IHS No. 2 is 2%. The minor deviation that is observed in the contraction part of IHS No. 1 is because the compressibility of the IHS sample (and its constituent layers) is not constant. In fact, as explained in Chapter 6, the value of compressibility decreases with the increase in effective confining stress, and its variation is not linear.

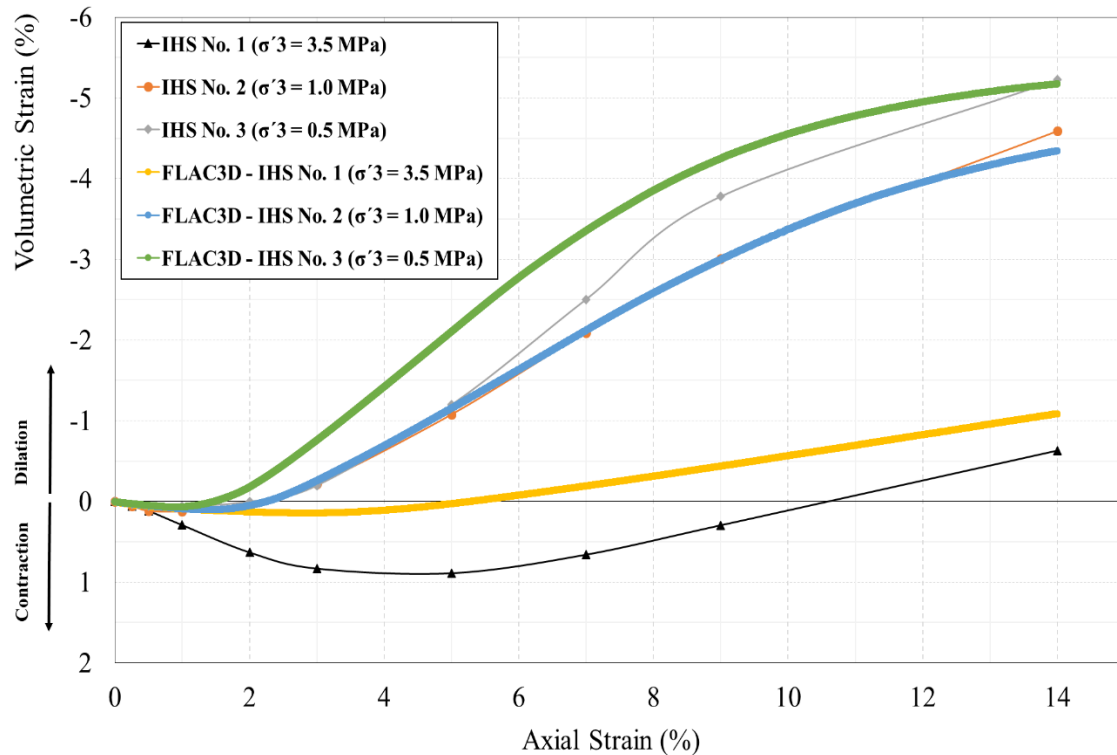


Figure 7-14 Volumetric strain versus axial strain for IHS samples (Lab tests simulated by FLAC3D™)

Following the same procedure explained in section 7.4.1, the mode of failure in analog IHS samples was investigated. Figure 7-15Figure 7-17 show the contours of volumetric and shear strains of the failed IHS samples, together with CT images of the sheared samples under effective confining stresses of 3.5, 1 and 0.5 MPa respectively.

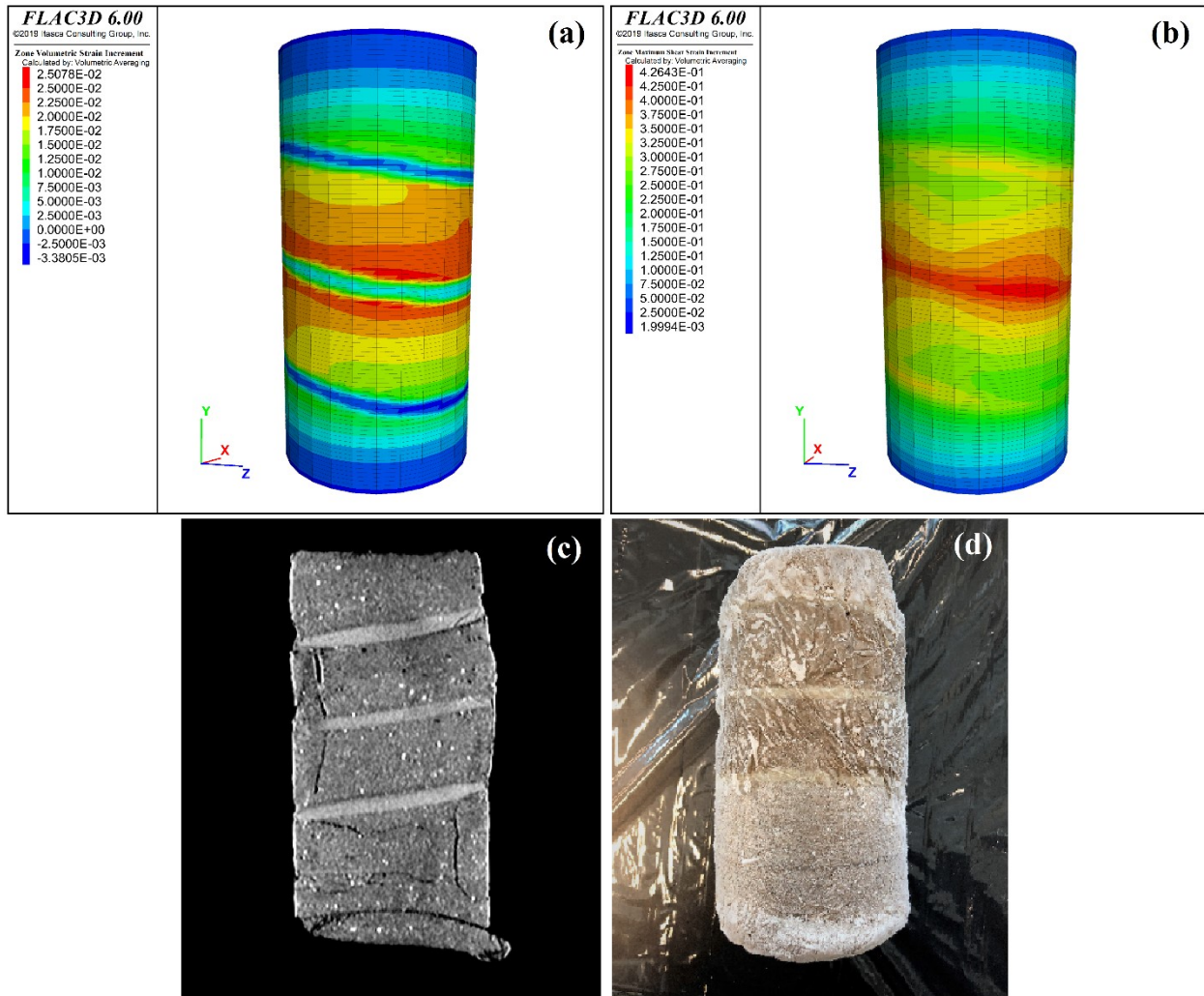


Figure 7-15 Contours of volumetric strain (a), contours of shear strain (b), CT Scan (c), and digital image (d) of IHS No. 1 ($\sigma_3' = 3.5$ MPa)

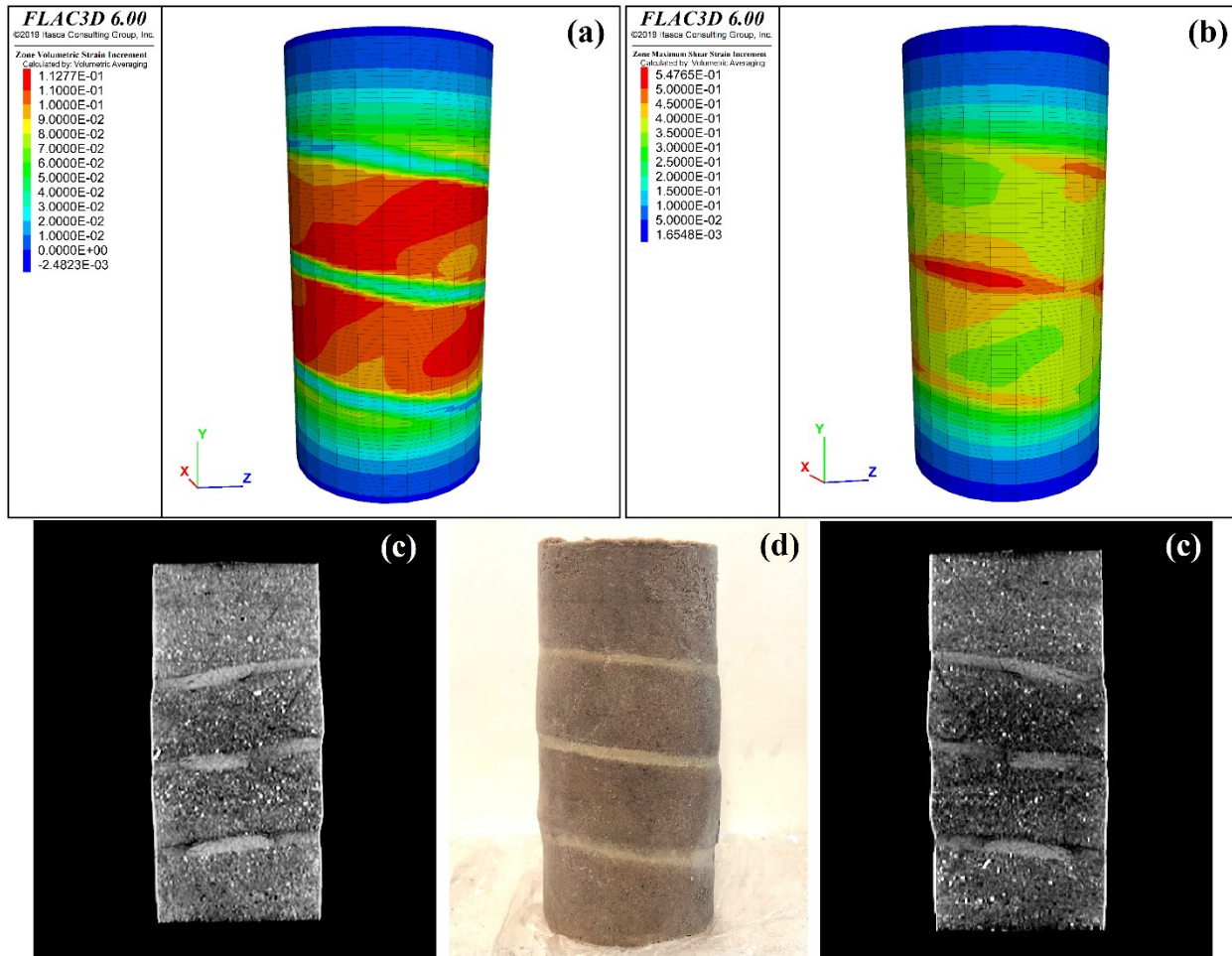


Figure 7-16 Contours of volumetric strain (a), contours of shear strain (b), CT Scan (c), and digital image (d) of IHS No. 2 ($\sigma_3' = 1$ MPa)

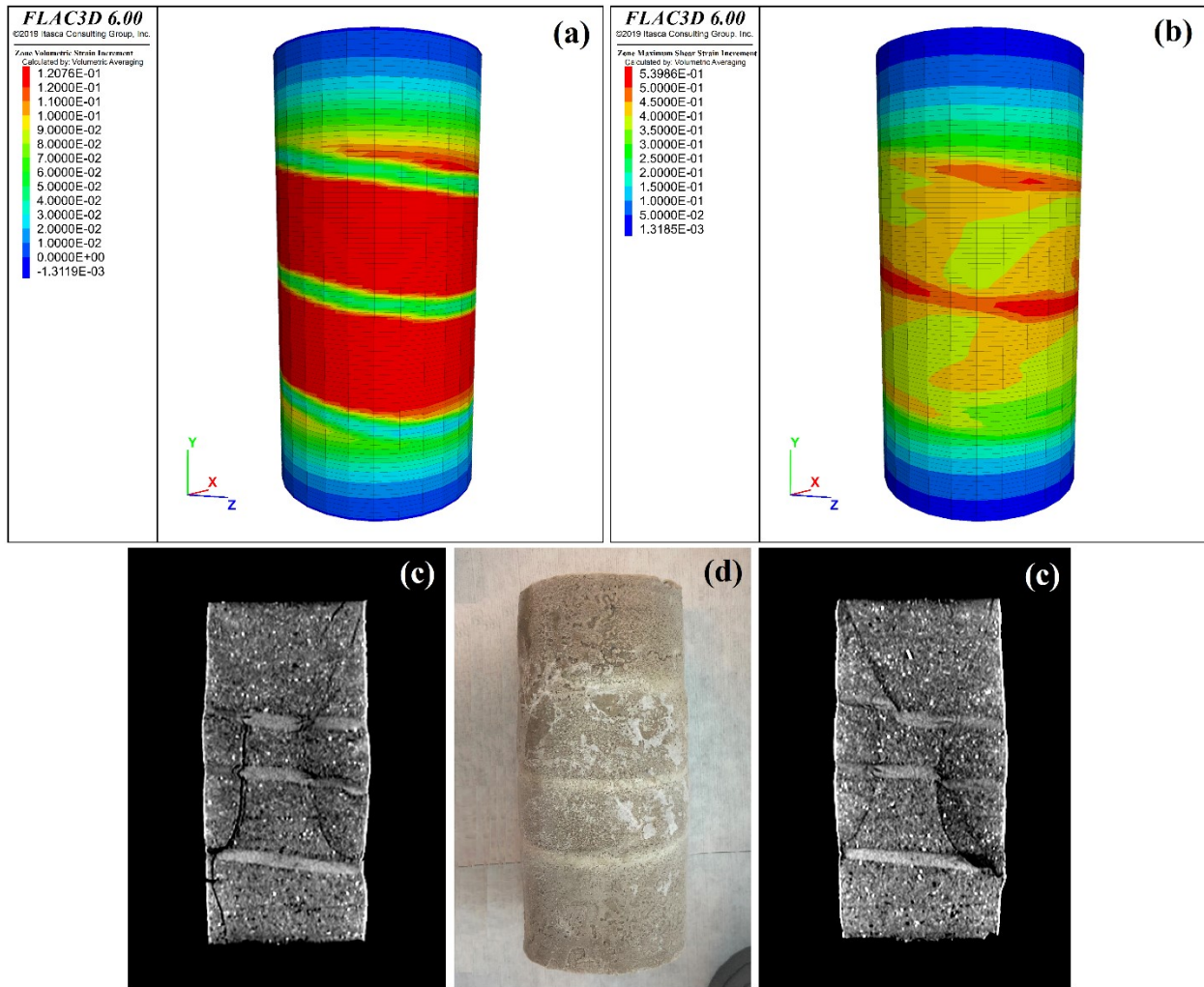


Figure 7-17 Contours of volumetric strain (a), contours of shear strain (b), CT Scan (c), and digital image (d) of IHS No. 3 ($\sigma_3' = 0.5$ MPa)

It can be seen that within all three IHS samples, the deformation was not uniform. Indeed, the concentrations of volumetric dilation and shear deformation were in the middle of the specimens, and the samples' ends remained relatively unaffected. This implies the outward bulging of the middle region of the specimens, which is consistent with the behavior observed in CT scan images of the IHS samples.

An interesting observation from the volumetric strain contours is that the sand layers, particularly the ones in the middle of the samples, show more dilative behavior compared to the adjacent mud layers. This is probably due to the higher value of dilation angle in the sand layers compared to

the mud layers. Another thought-provoking finding is that while all three samples bulge in the middle, the value of shear strain is more pronounced in the mud layers, especially at lower confining stresses. This might be due to the lower value of shear modulus in the mud layers compared to the sand ones.

In addition, in view of the results presented in Figure 7-13, it can be concluded that the three IHS samples tested have shown a large amount of plastic deformation, with no obvious peaks in deviatoric stress. Such behavior was expected, considering the fact that no clear shear band developed within the samples during shearing. Therefore, it can be concluded that the mode of failure for IHS samples is ductile type failure with a bulge in the middle, or barreling failure. It is also worth noting that, unlike the lab tests, no cracks were observed at the top or bottom of the sheared samples. This might be due to the absence of end-cap friction in the numerical experiments.

7.4.3.1. Geomechanical Model of IHS

Given the reasonable match between the numerical and laboratory experiments on the IHS samples, it can be concluded that the geomechanical model applied in the FLAC3DTM simulation can be a representative model for IHS. In this numerical model, the Plastic Hardening constitutive model was used, with two separate sets of parameters for the sand and mud layers. The required parameters for this geomechanical model can be obtained through a series of triaxial tests on sand and mud specimens.

Although the developed model can be used to characterize the geomechanical behavior of IHS, its applicability is limited to the tested geometry (configuration of layers) and the effective confining stresses ranging from 0.5 MPa to 3.5 MPa. Therefore, extra caution needs to be exercised for any applications out of the tested stress range, and for any other IHS geometries.

7.5. Summary

The following summarizes the conclusions of this chapter:

- The objective of this chapter was to find a representative model to numerically simulate the geomechanical behavior of sand-dominated IHS by using a Plastic Hardening constitutive model with FLAC3D™.
- Several material input functions are necessary in order to simulate the plastic hardening model with FLAC3D™. Results of high-quality triaxial tests on sand and mud samples were used to provide the required input data.
- Nine numerical experiments were performed to match the corresponding laboratory data, including three tests on sand samples, three tests on mud samples, and three tests on IHS samples. The numerical experiments were performed with the same testing conditions as those applied in the laboratory. Therefore, in all simulations, the stress path of conventional triaxial compression was followed.
- For the sand, mud, and IHS samples, the stress-strain relationships in both laboratory tests and numerical simulations show the same trend. However, there are minor deviations between the simulated shear strength and the experimental results. Such discrepancies are because the actual friction angle of the samples, which is a function of effective confining stress and density of the sample, was not captured in the model. Therefore, it would be more appropriate to use a series of input functions for the friction angle that represents the changes in the friction angle under various effective confining stresses and/or densities.
- The predicted volumetric behavior during shearing matches with the experimental data in all three sample types (sand, mud, and IHS). However, for the tests performed under the effective confining stress of 3.5 MPa, minor deviations were observed in the contraction part of the curves. This is because the compressibility of the samples is not constant. Indeed, the value of compressibility decreases with the increase in effective confining stress, and its variation is not linear.

- Investigating the shape of failed specimens in the numerical experiments revealed that within all three sample types the deformation pattern is not uniform. Indeed, the concentrations of volumetric dilation and shear deformation were in the middle of the specimens, and the samples' ends remained relatively unaffected. Furthermore, the stress-strain curves of the sand, mud, and IHS specimens showed a large amount of plastic deformation, with no obvious peaks in deviatoric stress. Therefore, it was concluded that the mode of failure in all three sample types is ductile type failure with a bulge in the middle, or barreling failure.
- The developed model can be used to characterize the geomechanical behavior of IHS; however, its applicability is limited to the tested geometry and the effective confining stresses ranging from 0.5 MPa to 3.5 MPa. Consequently, extra caution needs to be exercised for any applications out of the tested stress range, and for any other IHS geometries.

8. CONCLUSIONS AND RECOMMENDATIONS

8.1. Summary

A sizeable portion of the Athabasca oil sand reservoir is classified as Inclined Heterolithic Stratification lithosomes, which has a significant capacity of recoverable crude bitumen. However, due to the significant heterogeneity of IHS in terms of sand and mud layer thickness, percentage, and inclination, as well as the contrasting and complex behavior of these layers, very few experimental investigations of the hydro-mechanical behavior of this type of lithology have been carried out so far. In fact, having too many changeable parameters makes undisturbed in situ IHS samples (cores) unsuitable for laboratory testing. Therefore, the development of a technique to reconstitute analog IHS specimens becomes a necessity for any kind of experimental study on this type of lithology.

This research introduced the concept of IHS from sedimentological and ichnological perspectives. It also explained the geological position of IHS facies with respect to the Athabasca oil sand reservoir. Furthermore, it illuminated the need for and role of reservoir geomechanical studies on IHS. The main objectives of this research were investigating the geomechanical constitutive behavior of IHS and linking its geological and mechanical characteristics to its hydraulic behavior in order to estimate the permeability evolution of IHS during a SAGD operation.

To that end, a detailed methodology for the reconstitution of analog IHS specimens was developed, and a microscopic comparative study was conducted between analog and in situ IHS samples. It should also be noted that the experimental protocol which was used to create analog IHS includes reconstitution of analog sand and mud specimens. Therefore, before using the analog sand and mud samples as the constituent layers of analog IHS, its hydro-geomechanical behavior was investigated through a series of laboratory tests. In addition, the outcomes of previous experimental studies on McMurray Formation oil sand and mudstone were discussed to ensure the resemblance between the analog sand and mud samples and the in situ oil sand and mudstone specimens respectively.

In this study, the SAGD-induced stress paths were experimentally simulated by running isotropic cyclic consolidation and drained triaxial shearing tests on analog sand, mud, and IHS samples. Both series of experiments were performed in conjunction with permeability tests at different strain levels, flow rates, and stress states. Additionally, an analog IHS sample with bioturbation was tested to examine the hydro-geomechanical effects of bioturbation. Lastly, the hydro-mechanical characteristics of analog IHS were compared with their constituent layers (sand and mud).

The applicability of former empirical permeability relationships was also investigated in this research, and a new correlation was proposed that relates the absolute permeability of IHS to its stress state and deformation. Finally, a representative model was found to numerically simulate the geomechanical behavior of sand-dominated IHS by using the Plastic Hardening constitutive model with FLAC3D™ version 6.

8.2. Conclusions

The following are conclusions regarding the stated objectives of this thesis.

8.2.1. Sand, Mud, and IHS Samples Preparation

- The analog sand samples were reconstituted using a modified combination of moist tamping and wet vibration methods. The porosity values and grain size distribution of these samples matched other reconstituted sand samples and in situ oil sand cores.
- The analog mud samples were reconstituted using the slurry molding method, which is an improved version of what was called the “slurry consolidation approach” by Wang et al. (2011). The grain size distribution and porosity values of these reconstituted samples are similar to the mud layer of IHS and with the McMurray Formation mudstone.
- The analog IHS samples were reconstituted following the experimental protocol developed in this study. The microscopic study, which was conducted on these samples, showed that the

reconstituted analog IHS specimens have a satisfactory resemblance to in situ IHS, in terms of grain composition and layers integration.

8.2.2. Geomechanical Properties of Sand, Mud, and IHS

- Running isotropic cyclic consolidation tests on the sand, mud, and IHS samples revealed that the bulk compressibility of these samples is a strong function of the effective confining stress. A series of power law functions were established to capture the relationship between compressibility and effective confining stress which can be expressed as follows:

$$C_b = a\sigma_3'^b \quad \text{Equation 8-1}$$

- The value of constants a and b for different sample types can be found in Table 8-1. It should also be noted that the applicability of this equation is limited to σ_3' ranging from 0.2 MPa to 7 MPa only. Therefore, extra caution needs to be exercised for any applications out of this range.

Table 8-1 Compressibility equation constants

Sample Type	Sand	Mud	IHS
a	541	84305	6919
b	-0.6	-0.9	-0.8

- The elastic modulus of the sand, mud, and IHS samples significantly increases with the increase in effective confining stress. Typically, a standard hyperbolic function is chosen to define the dependency E to σ_3' as follows:

$$E_i = K_E p_a \left(\frac{\sigma_3'}{p_a} \right)^n \quad \text{Equation 8-2}$$

- The values of modulus number (K_E) and modulus exponent (n) for the different types of sample can be found in Table 8-2.

Table 8-2 Modulus number and modulus exponent for different types of sample

Sample Type	Sand	Mud	IHS
K_E	1042	413	684
n	0.6	0.4	0.6

- With regard to the volumetric behavior of the specimens during shearing, it was observed that the value of effective confining stress (σ_c') controls the dilative or contractive responses of the samples. As a matter of fact, the dilation angle (ψ) of all three sample types decreased with the increase in effective confining stress. The following relationships can be used to estimate the variation of ψ with σ_c' for the sand, mud, and IHS samples respectively.

$$\text{Sand: } \psi = 11\sigma_c'^{0.8} \quad \text{Equation 8-3}$$

$$\text{Mud: } \psi = -1.6 \ln \sigma_c' + 4 \quad \text{Equation 8-4}$$

$$\text{IHS: } \psi = -2.7\sigma_c' + 10 \quad \text{Equation 8-5}$$

- The following are the failure envelope relationships in $s'-t$ space for the sand, mud, and IHS samples respectively.

$$\text{Sand: } t = -0.01 s'^2 + 0.7 s' - 0.02 \quad \text{Equation 8-6}$$

$$\text{Mud: } t = 0.6 s' - 0.01 \quad \text{Equation 8-7}$$

$$\text{IHS: } t = -0.007 s'^2 + 0.7 s' + 0.003 \quad \text{Equation 8-8}$$

- From the peak failure envelopes, it can be concluded that the analog sand and mud samples are both cohesionless materials that have effective friction angles of 37° and 36° respectively. Moreover, analog IHS specimens were found to have an effective cohesion of 0.15 MPa and an effective friction angle of 37° . It is also worth noting that the failure envelopes of the sand and IHS samples have a slight curvature, which implies a mild reduction in the effective friction angle with an increase in the effective confining stress.
- Comparing the measured stress-strain and strength parameters of ROSs with the previous experimental studies on McMurray Formation oil sand cores and other reconstituted oil sand

samples assured the resemblance between analog sand samples and McMurray Formation oil sands in terms of their geomechanical properties. Similarly, the results from analog mud samples were compared with previous experimental studies on McMurray Formation shale cores and other reconstituted silt-clay mixtures. This comparative analysis showed that the geomechanical properties of analog mud samples match in situ shale and mudstone cores reasonably well. Such in-depth analysis also provided an assurance of similarity between the constituent layers of analog IHS and in situ one.

- The numerical study performed in this thesis showed that the geomechanical model applied in the FLAC3D™ simulation can be a representative model for IHS. In this numerical model, the Plastic Hardening constitutive model was used, with two separate sets of parameters for the sand and mud layers. The required parameters for this geomechanical model were obtained through a series of triaxial tests on sand and mud specimens. Although this model can be used to characterize the geomechanical behavior of IHS, its applicability is limited to the tested geometry (configuration of layers) and the effective confining stresses ranging from 0.5 MPa to 3.5 MPa. Therefore, extra caution needs to be exercised for any applications out of the tested stress range, and for any other IHS geometries.
- Using the developed geomechanical model, nine numerical experiments were performed on the sand, mud, and IHS samples (three tests on each sample type). The numerical results matched with experimental data in terms of drained shear strength, stress-strain behavior, mode of failure, and volumetric behavior during shearing.
- It is worth noting that the developed geomechanical model has its own limitation, which can cause some deviations between the simulated and experimental results. For example, the actual friction angle of the samples, which is a function of effective confining stress and density, was not captured in this model. Therefore, it would be more appropriate to use a series of input functions for friction angle that represents the changes in the friction angle under various effective confining stresses and/or densities.

8.2.3. Absolute Permeability Changes of Sand, Mud, and IHS

- The results of permeability tests on the sand, mud, and IHS samples revealed that the dilative behavior of the specimens during isotropic unloading leads to a permeability augmentation. For example, the absolute permeability of ROSs increased up to 28% with a decrease in effective confining stress from 7 MPa to 1 MPa. The amount of such increase in the mud samples was 29%, in the non-bioturbated IHS it was 40%, and in the bioturbated IHS it was 140%. This might be because during isotropic unloading, the soil particles slightly move apart from each other without any shearing or fabric distortion. This widens the flow channels within the samples and increases the permeability. It should also be noted that the initial value of absolute permeability for the bioturbated IHS was an order of magnitude larger than that for the non-bioturbated one.
- Running the permeability tests at different strain levels and stress states showed that the variation of absolute permeability during shearing in all three sample types is a function of both effective confining stresses, and the amount of volumetric strain. In the IHS samples, the degree of bioturbation could also play an important role in permeability evolution during shearing. To illustrate, in tests performed under the effective confining stress of 3.5 MPa, the permeability continuously decreased throughout the shearing, regardless of the sample type. However, for the tests performed under lower effective confining stresses (1 and 0.5 MPa), permeability was reduced prior to a specific axial strain level, then it rose until the end of shearing. In some cases, despite the initial drop in the permeability value, samples could almost retrieve their initial permeability value or even improve it by the end of shearing.
- Considering the volumetric behavior of the samples during triaxial compression tests, it can be concluded that the effect of the samples' volume change on permeability is contingent on the stress state and stress path. In other words, unlike the isotropic unloading tests, the sample's dilation during shearing does not necessarily translate into permeability augmentation. For that to be effective, the value σ_3' needs to be low, and the amount of dilation must reach a certain level.
- The tests performed on bioturbated and non-bioturbated IHS samples revealed that the existence of bioturbation dramatically improves the permeability of IHS in comparison to

equivalent non-bioturbated specimens, but has negligible effects on their mechanical properties, which remain similar to non-bioturbated specimens. The results also showed that bioturbation has minimal impact on permeability changes during shearing.

- The permeability test results on the IHS samples showed that the rate of permeability evolution during isotropic unloading is not constant. Indeed, after a certain degree of dilation, this rate increases significantly. Therefore, the relationship between normalized absolute permeability and volumetric expansion in the IHS samples was approximated using a bilinear curve fit model that represented the primary and secondary permeability augmentation rate regions. The most probable explanation for this phenomenon is that in the primary region, only the existing flow channels are widened, while in the secondary region several new flow channels are created together with the widening of existing flow channels. In fact, when the volumetric expansion reaches the dilation threshold, which is 0.54% in analog IHS samples, the fluid will be able to flow through channels (pore throats) which were impassable before due to their tightness. In order to capture such behavior, and also to link the IHS absolute permeability variation to geomechanically-induced volumetric dilation in primary and secondary permeability augmentation regions, two linear semi-logarithmic correlations were developed as follows:

$$\text{Non-Bioturbated IHS - Primary Region: } \ln\left(\frac{K}{K_0}\right) = -0.19 \varepsilon_v \quad \text{Equation 8-9}$$

$$\text{Non-Bioturbated IHS - Secondary Region: } \ln\left(\frac{K}{K_0}\right) = -0.40 \varepsilon_v - 0.11 \quad \text{Equation 8-10}$$

- In an effort to investigate the applicability of former empirical permeability relationships, it was found that these relationships are only applicable to calculate the modified absolute permeability due to isotropic unloading in the primary region and the triaxial shearing under very effective confining stresses when the dilation value is high. This is because none of these correlations take the variation of tortuosity or creation of microcracks within the sample into account. In fact, the underlying assumptions of unchanged pore shape and particle size in these equations are not well-founded.

- Comparing the hydro-geomechanical properties of IHS with its constituent layers showed that sand-dominated analog IHS specimens reflect the characteristics of both analog sand and mud samples. However, their behavior is heavily influenced by the sand rather than mud. Such behavior was rightly expected, considering the high percentage of sand layers in these samples.

8.3. Recommendations for Future Research

The following identifies the areas of further research on IHS:

- In order to better understand the heterogeneity of IHS and its impact on hydro-geomechanical responses of the reservoir during SAGD operations, the developed methodology to reconstitute analog IHS needs to be advanced to include different degrees of bioturbation and bitumen saturation. It also must include alterations in the thickness and inclination of the sand and mud layers.
- The effects of temperature on the geomechanical and hydraulic properties of IHS needs to be investigated by conducting a series of hydro-mechanical tests at elevated temperatures (up to 300°C).
- IHS samples' relative permeability to oil and water should be analyzed with different degrees of bitumen saturation. Furthermore, the evolution of relative permeability should be investigated under SAGD induced stress paths as a function of temperature.
- In order to simulate the geomechanical behavior of IHS more accurately, a more complex geomechanical model is needed. Such a model should have a series of input functions for friction and dilation angles which represents the changes in these parameters under various confining stresses, densities, and shear strain levels. This model should also account for the viscoelastic behavior of soil samples during shearing.
- One of the issues associated with CT scan analysis is the shape-rebounding which occurs in samples upon the removal of axial and confining stresses. This could disturb the post-shear geometry and mask some of the created cracks. In order to overcome this problem, it is

recommended that a simultaneous real-time CT triaxial test system is used. This system includes a special frame design and integrated X-ray CT system, and is suitable for a wide range of analysis of pore size, pore fluid, and material like soils and rocks. Using this system sample's porosity, any pore fluids exchange, pre-yield and post-yield geometry, and crack propagation could be monitored in situ during testing.

- During a SAGD operation, the stress path which is followed by different parts of the reservoir is not the same. In fact, the true stress path for each section of the reservoir depends on its distance from the injection or production well and the value of water or steam mobility within that section of the reservoir. Therefore, further study is recommended on the hydro-geomechanical behavior of IHS over a wider range of stress paths.

REFERENCES

- Abdallah, K. B. (2013). *Steam Assisted Gravity Drainage (SAGD): Influence of Geomechanical Processes on Absolute Permeability*. A Thesis presented for the Master Degree, Department of Civil and Environmental Engineering, University of Alberta, Edmonton, Canada.
- Agar, J. G. (1984). *Geotechnical behaviour of oil sands at elevated temperatures and pressures*. A Thesis presented for the PhD Degree, Department of Civil Engineering, University of Alberta, Edmonton, Canada.
- Agar, J. G., Morgenstern, N. R., & Scott, J. D. (1987). Shear strength and stress-strain behaviour of Athabasca oil sand at elevated temperatures and pressures. *Canadian Geotechnical Journal*, 24(1), 1-10.
- Aherne, A., & Maini, B. (2008). Fluid Movement in the SAGD Process: A Review of the Dover Project. *Journal of Canadian Petroleum Technology*, 47(01), 31-37. doi:<https://doi.org/10.2118/08-01-31>
- Alberta Energy Regulator. (2015). *Alberta's Energy Reserves 2014 and Supply/Demand Outlook 2015–2024*. Calgary: Alberta Energy Regulator. Retrieved from <https://www.aer.ca/documents/sts/ST98/ST98-2015.pdf>
- Alberta Energy Regulator. (2017, July 6). *Statistical Reports*. Retrieved from The Alberta Energy Regulator: <https://www.aer.ca/data-and-publications/statistical-reports>
- Asghari, E., Toll, D. G., & Haeri, S. M. (2004). Effect of Cementation on the Shear Strength of Tehran Gravelly Sand Using Triaxial Tests. *Journal of Sciences, University of Tehran*, 15(1), 65-71.
- ASTM International. (2006). ASTM D2434-68: Standard Test Method for Permeability of Granular Soils. In *Annual book of ASTM standards 2006*. West Conshohocken, PA: American Society for Testing and Materials.

- ASTM International. (2016). ASTM D7181-11: Method for Consolidated Drained Triaxial Compression Test for Soils. In *Annual book of ASTM standards 2016*. West Conshohocken, PA: American Society for Testing and Materials.
- ASTM International. (2016). D7012-10: Standard Test Method for Compressive Strength and Elastic Moduli of Intact Rock Core Specimens under Varying States of Stress and Temperatures. In *Annual book of ASTM standards 2016*. West Conshohocken, PA: American Society for Testing and Materials.
- Bagheri, M., & Settari, A. (2007, March). Methods for Modelling Full Tensor Permeability in Reservoir Simulators. *Journal of Canadian Petroleum Technology*, 46(03), 31-38.
- Bailleul, J., Delhay-Prat, V., & Parize, O. (2006). Facies Analysis and Architectural Elements Within a Fluvio-Estuarine Sedimentary System: The Lower Cretaceous Bituminous Sandstones of the McMurray Formation, Alberta (Canada). *SPE Annual Technical Conference and Exhibition*. San Antonio, Texas: Society of Petroleum Engineers.
- Bechtel, D., Yuill, C., Ranger, M., & Pemberton, S. (1994). Ichnology of Inclined Heterolithic Stratification in the McMurray Formation, Northeastern Alberta. *Western Canadian and International Expertise* (p. 362). Calgary: Canadian Society of Petroleum Geologists. Retrieved from http://archives.datapages.com/data/meta/cspg_sp/data/CSPG-SP-016/016001/pdfs/362_firstpage.pdf
- Belheine, N., Plassiard, J. P., Donzé, F. V., Darve, F., & Seridi, A. (2009). Numerical simulation of drained triaxial test using 3D discrete element modeling. *Computers and Geotechnics*, 36(1-2), 320-331. doi:<https://doi.org/10.1016/j.compgeo.2008.02.003>
- Bharatha, S., Chan, M., Yee, C., & Lee, D. (2004). Two-Dimensional Permeability of Breccia Facies in the Athabasca Oil Sands. *Canadian International Petroleum Conference*. Calgary: Petroleum Society of Canada.
- Bishop, A. W., & Henkel, D. J. (1962). *The measurement of soil properties in the triaxial test*. London: E. Arnold Publication LTD.

- Byrne, P. M., Cheung, H., & Yan, L. (1987). Soil parameters for deformation analysis of sand masses. *Canadian Geotechnical Journal*, 24(3), 366-376. doi:<https://doi.org/10.1139/t87-047>
- Canadian Association of Petroleum Producers . (2017, June 4). *Publications and Statistics*. Retrieved from The Canadian Association of Petroleum Producers (CAPP): <https://www.capp.ca/publications-and-statistics>
- Canadian Energy Research Institute. (2017, July 5). *Crude Oil*. Retrieved from The Canadian Energy Research Institute (CERI): <https://www.ceri.ca/market-updates/crude-oil>
- Carrigy, M. A. (1959). *Geology of the McMurray Formation. Part III, General geology of the McMurray area*. Memoir 01, Alberta Research Council, 130 p. Retrieved from https://ags.aer.ca/document/MEM/MEM_01.pdf
- Cenovus FCCL Ltd. (2013). *Geology and Geophysics*. Calgary: Public report, Volume 1, Section 4, Cenovus FCCL Ltd. Retrieved from <https://open.alberta.ca/publications/6082834>
- Chalaturnyk, R. J. (1996). *Geomechanics of the steam assisted gravity drainage process in heavy oil reservoirs*. A Thesis presented for the PhD Degree, Department of Civil Engineering, University of Alberta, Edmonton, Canada.
- Chandler Engineering. (2017, April 3). *QX Series*. Retrieved from CHANDLER ENGINEERING: <http://www.chandlereng.com/products/reservoiranalysis/core-flow/quixix-precision-pumps/qxseries>
- Chaney, R. C., Stevens, E., & Sheth, N. (1979). Suggested Test Method for Determination of Degree of Saturation of Soil Samples by B Value Measurement. *Geotechnical Testing Journal*, 2(3), 158-162.
- Choo, J., & Suna, W. (2018). Coupled phase-field and plasticity modeling of geological materials: From brittle fracture to ductile flow. *Computer Methods in Applied Mechanics and Engineering*, 330(1), 1-32. doi:<https://doi.org/10.1016/j.cma.2017.10.009>

- Ciammetti, G., Ringrose, P. S., Good, T. R., Lewis, J. M., & Sorbie, K. S. (1995). Waterflood Recovery and Fluid Flow Upscaling in a Shallow Marine and Fluvial Sandstone Sequence. *SPE Annual Technical conference & Exhibition*. Dallas: Society of Petroleum Engineers.
- Dabek, L., Shad, S., Dalir, A., & Knepp, R. (2014). Correlation of Permeability and Volume of Shale in Oil Sands: Improving Predictability in Low Permeability Zones of the McMurray Formation, Alberta, Canada. *SPE Heavy Oil Conference-Canada*. Alberta: Society of Petroleum Engineers.
- Dahl, M. B., Suter, J. R., Hubbard, S. M., & Leckie, D. A. (2010). Impact of Inclined Heterolithic Stratification on Oil Sands Reservoir Delineation and Management: An Outcrop Analog from the Late Cretaceous Horseshoe Canyon Formation, Willow Creek, Alberta. *GeoCanada 2010 – Working with the Earth*. Calgary: Geological Association of Canada.
- Delage, P., Hong, D., Nauroy, J. F., & Tang, A.-M. (2013). Compression Behavior of Canadian Oil Sands. *Journal of Geotechnical and Geoenvironmental Engineering*, 139(6), 969-974.
- Deutsch, C. (1989). Calculating Effective Absolute Permeability in Sandstone/Shale Sequences. *SPE Formation Evaluation*, 4(03), 343-348. doi:<https://doi.org/10.2118/17264-PA>
- Deutsch, C. (2010, December). Estimation of Vertical Permeability in the McMurry Formation. *Journal of Canadian Petroleum Technology*, 49(12), 10-18.
- Duncan, J. M., & Chang, C. Y. (1970). Nonlinear Analysis of Stress and Strain in Soils. *Journal of the Soil Mechanics and Foundations Division*, 96(5), 1629-1653.
- Dusseault, M. B. (1977). *The geotechnical characteristics of the Athabasca Oil Sands*. A Thesis presented for the PhD Degree, Department of Civil Engineering, University of Alberta, Edmonton, Canada.
- Dusseault, M. B., & Morgenstem, N. R. (1978). Shear Strength of Athabasca Oil Sands. *Canadian Geotechnical Journal*, 15(2), 216-218. doi:<https://doi.org/10.1139/t78-021>

- Edmunds, N. R. (1987). *UTF Gravity drainage process development. Advances in Petroleum Recovery and Upgrading Technology*. AOSTRA, Edmonton, Alberta, 11 p.
- Ehrgott, J. Q. (1970). Calculation of Stress and Strain from Triaxial Test Data on Undrained Soil Specimens. *Eric H. Wang Symposium on Protective Structure Technology*. New Mexico: U. S. Army Engineer Waterways Experiment Station.
- Flach, P. D. (1984). *Oil sands geology - Athabasca deposit north*. ARC/AGS Bulletin 46, Alberta Research Council, 47 p. Retrieved from https://ags.aer.ca/document/BUL/BUL_046.pdf
- Government of Alberta. (2017). *Oil Sand Facts and Statistics*. Retrieved May 2017, 4, from Government of Alberta: <https://www.alberta.ca/about-oil-sands.aspx>
- Gu, F., Chan, M., & Fryke, R. (2011). Geomechanical Data Acquisition, Monitoring and Applications in SAGD. *Journal of Canadian Petroleum Technology*, 50(06). doi:<https://doi.org/10.2118/145402-PA>
- Hassanpour, R. M. (2009). *A Review of McMurray Formation Geology in Athabasca Oil Sands*. Annual Report 11, Centre for Computational Geostatistics, University of Alberta, Edmonton. Retrieved from http://www.ccgaberta.com/ccgresources/report11/2009-201_mcmurray_formation_geology.pdf
- Hatibu, N., & Hettiaratchi, D. R. (1993, April). The Transition From Ductile Flow to Brittle Failure in Unsaturated Soils. *Journal of Agricultural Engineering Research*, 54(4), 319-328.
- Head, K. H., & Epps, R. J. (2006). *Manual of Soil Laboratory Testing* (Vols. III - Effective Stress Tests 3rd edition). Whittles Publishing.
- Hein, F. J., & Cotterill, D. K. (2006). The Athabasca oil sands - a regional geological perspective Fort McMurray area, Alberta, Canada. *Natural Resources Research*, 15(2), 85-102.

- Hein, F. J., Cotterill, D. K., & Rice, R. (2006). *Subsurface Geology of the Athabasca Wabiskaw-McMurray Succession: Lewis-Fort McMurray Area, Northeastern Alberta (NTS 74D/74E)*. Edmonton: Alberta Energy and Utilities Board/Alberta Geological Survey.
- Holly, C., Mader, M., Soni, S., & Toor, J. (2016). *Oil Sand Production Profile 2004-2014*. Alberta Energy- Energy Technical Services Resource Development Policy Division, Edmonton. Retrieved from <https://open.alberta.ca/dataset/cd892173-c37f-4c68-bf5d-f79ef7d49e72/resource/ebd6b451-dfda-4218-b855-1416d94306fd/download/initiativeospp.pdf>
- Instron®. (2017, January 17). *5980 Floor Model Systems for High-Capacity Universal Testing*. Retrieved from INSTRON: <http://www.instron.us/en-us/products/testing-systems/universal-testing-systems/electromechanical/5900/5980-floor-model>
- Itasca. (2017). *FLAC3D© 6.0 Theory and Background*. ©Itasca Consulting Group, Inc.
- Jablonski, B. V. (2012). *Process Sedimentology and Three-Dimensional Facies Architecture of a Fluvially Dominated, Tidally Influenced Point Bar: Middle McMurray Formation, Lower Steepbank River Area, Northeastern Alberta, Canada*. A Thesis presented for the Master Degree, Department of Geological Science and Geological Engineering, Queen's University, Kingston, Ontario, Canada.
- Jablonski, B., & Dalrymple, R. (2016). Recognition of strong seasonality and climatic cyclicity in an ancient, fluvially dominated, tidally influenced point bar: Middle McMurray Formation, Lower Steepbank River, Lower Steepbank River. *International Association of Sedimentologists*, 63(3), 552-585. doi:<https://doi.org/10.1111/sed.12228>
- Kézdi, Á. (1974). *Handbook of soil mechanics* (Vol. 1). (I. Lazányi, Trans.) Amsterdam: Elsevier Scientific Publishing Company.
- Kosar, K. M. (1989). *Geotechnical Properties of Oil Sands and Related Strata*. A Thesis presented for the PhD Degree, Department of Civil Engineering, University of Alberta, Edmonton, Canada.

- Kuerbis, R., & Vaid, Y. P. (1988). Sand sample preparation- the slurry deposition method. *Soils and Foundations*, 28(4), 107-118.
- Lettley, C. D., & Pemberton, S. G. (2004). *Speciation of McMurray Formation Inclined Heterolithic Strata: Varying Depositional Character Along a Riverine Estuary System*. Calgary: CSPG/CSEG GeoConvention.
- Li, P. (2006). *Numerical Simulation of the SAGD Process Coupled With Geomechanical Behavior*. A Thesis presented for the PhD Degree, Department of Civil and Environmental Engineering, University of Alberta, Edmonton, Canada.
- Li, P., & Chalaturnyk, R. J. (2006). Permeability Variations Associated With Shearing and Isotropic Unloading During the SAGD Process. *Journal of Canadian Petroleum Technology*, 45(1), 54-81.
- Manchuk, J. G., Garner, D. L., & Deutsch, C. V. (2015). Estimation of Permeability in the McMurray Formation Using High-Resolution Data Sources. *PETROPHYSICS*, 56(02), 125–139.
- McKay, J. (1989). *Undisturbed Oil Sand Sampling and Sample Quality Evaluation*. A Thesis presented for the PhD Degree, Department of Civil Engineering, University of Alberta, Edmonton, Canada.
- Mercier, J. P., Zambelli, G., & Kurz, W. (2003). *Introduction to Materials Science*. Elsevier Science. doi:<https://doi.org/10.1016/C2009-0-29148-3>
- Mondol, N. H. (2009). Porosity and permeability development in mechanically compacted silt-kaolinite mixtures. Houston, Texas: Society of Exploration Geophysicists.
- Morgenstern, N., Vick, S., Viotti, C., & Watts, B. (2016). *Report on the Immediate Causes of the Failure of the Fundão Dam*. Fundão Tailings Dam Review Panel. Retrieved from <http://fundaoinvestigation.com/>

- Mossop, G. (1980). Geology of the Athabasca oil sands. *Science*, 207(11), 145-152.
- Nandanwar, M. R. (2015). *Measurement and Simulation of Triaxial Compression Tests*. A Thesis presented for the Master Degree, Department of Biosystems Engineering, University of Manitoba, Winnipeg, Canada.
- Oldakowski, K. (1994). *Stress induced permeability changes of Athabasca oil sands*. Edmonton: A Thesis presented for the Master Degree, Department of Civil Engineering, University of Alberta, Edmonton, Canada.
- Plewes, H. D. (1987). *Undrained strength of Athabasca oil sands*. A Thesis presented for the Master Degree, Department of Civil Engineering, University of Alberta, Edmonton, Canada.
- Protulipac, D. (1991). *Comparing strength characteristics of St. Peter sandstone and oil saturated McMurray sand*. A Thesis presented for the Master Degree, Department of Civil and Environmental Engineering, University of Waterloo, Waterloo, Ontario, Canada.
- Ranger, M. J., & Gingras, M. K. (2003). *Geology of the Athabasca Oil Sands – Field Guide and Overview*. Calgary: Canadian Society of Petroleum Geologists.
- Ranger, M. J., & Pemberton, S. G. (1992). *The sedimentology and Ichnology of estuarine point bars in the McMurray Formation of the Athabasca Oil Sands deposit, northeastern Alberta, Canada*. SEPM Society for Sedimentary Geology. doi:<https://doi.org/10.2110/cor.92.01.0401>
- Ranger, M. J., Gingras, M. K., & Pemberton, S. G. (2008). The Role of Ichnology in the Stratigraphic Interpretation of the Athabasca Oil Sands. *American Association of Petroleum Geologists Hedberg Conference*. Banff, Alberta: American Association of Petroleum Geologists.
- Ranger, M. J., Pemberton, S. G., & Lettley, C. D. (2012). The Sedimentology and Ichnology of Estuarine Point Bars in The McMurray Formation of Athabasca Oil Sand Deposits,

- Northeastern Alberta, Canada. Applications of Ichnology to Petroleum Exploration. *Applications of Ichnology to Petroleum Exploration*, 401-415.
- Ray, S., Coddling, D., Skold, O., Henden, T., & Strobl, R. (2004). Process of Clastic Reservoir Facies Modelling Using Formation Micro-Images and 3D Visualisation Tools. *Canadian International Petroleum Conference*. Calgary: Petroleum Society of Canada.
- Rottenfusser, B. A., Dexter, S., & Alwast, N. K. (1988). *Initial analyses of cores from UTF Phase A*. Alberta Research Council report submitted to AOSTRA.
- Samieh, A. M., & Wong, R. C. (1997). Deformation of Athabasca oil sand at low effective stresses under varying boundary conditions. *Canadian Geotechnical Journal*, 34(6), 985-990. doi:<https://doi.org/10.1139/t97-048>
- Schanz, T., & Vermeer, P. A. (1996). Angles of friction and dilatancy of sand. *Geotechnique*, 46(No. 1), 145-151.
- Schanz, T., Vermeer, P. A., & Bonnier, P. G. (1999). The hardening soil model: Formulation and verification. *International symposium, Beyond 2000 in computational geotechnics; 1999; Amsterdam* (pp. 281-296). Rotterdam: Balkema.
- Schöpfer, M. P., Childs, C., & Manzocchi, T. (2013). Three-dimensional failure envelopes and the brittle-ductile transition. *Journal of Geophysical Research: Solid Earth*, 118(4), 1378–1392. doi:<https://doi.org/10.1002/jgrb.50081>
- Scott, J. D. (1992). *Geomechanical characterization of oil sand reservoir materials: constitutive behavior of Cold Lake oil sands*. Edmonton: AOSTRA University Research Program (Agreement 820), Report Number 6, University of Alberta, Edmonton. Canada.
- Scott, J. D., Proskin, S. A., & Adhikary, D. P. (1994). Volume and Permeability Changes Associated with Steam Stimulation in Oil Sands Reservoirs. *Journal of Canadian Petroleum Technology*, 33(7), 44-52.

- Shivam Tar Products. (2017, July 6). *What Is Bitumen?* Retrieved from Shivam Tar Products: http://www.shivamtarproducts.com/index.php?option=com_content&view=article&id=55&Itemid=74
- Siiron, P. (2002). *Characteristic grain-size distribution patterns of tidally-influenced coastal plain estuarine sediments based on comparative studies of Cretaceous McMurray Formation in Alberta, Canada and the Miocene Pebas/Solimoes formation in Western Amazonia, Peru.* A Thesis presented for the Master Degree, Department of Geography and Geology, University of Turku, Turku, Finland.
- Stewart, G. A., & MacCallum, G. T. (1978). *Athabasca oil sands guide book.* Calgary: Canadian Society of Petroleum Geologists.
- Strausz, O. P., & Lown, E. (2003). *The chemistry of Alberta oil sands, bitumens and heavy oils.* Calgary, Alberta: Alberta Energy Research Institute.
- Strobl, R., Wightman, D. M., Muwais, W. K., Cotterill, D. K., & Yuan, L. (1997). Application of Outcrop Analogues and Detailed Reservoir Characterization to the AOSTRA Underground Test Facility, McMurray Formation, North Eastern Alberta. *Canadian Society of Petroleum Geologist*, 4(18), 375-391.
- Strobl, R., Wightman, D. M., Muwais, W. K., Cotterill, D. K., & Yuan, L. (1997). Geological Modelling of McMurray Formation Reservoirs Based on Outcrop and Subsurface Analogues. In *Petroleum Geology of the Cretaceous Mannville Group* (Vol. 2, pp. 292-311). Canadian Society of Petroleum Geologists.
- Suncor Energy. (2005). *McKay River Thermal Project-Laboratory Program: Properties of Clearwater Formation Shale and McMurray Formation Oil Sands.* Edmonton: Suncor Energy.
- Suncor Energy. (2009). *McKay River Thermal Project-Geomechanics Laboratory Program: Clearwater and Wabiskaw Formations.* Edmonton: Suncor Energy.

- Taylor, A. M., & Goldring, R. (1993). Description and analysis of bioturbation and ichnofabric. *Journal of the Geological Society*, 150(1), 141-148.
- Teledyne ISCO®. (2017, March 16). *260D Syringe Pump*. Retrieved from Teledyne Isco: <http://www.teledyneisco.com/en-us/pumpproducts/Pages/260D.aspx>
- Thomas, R. G., Smith, D. G., Wood, J. M., Visser, J., Calverley-Range, A., & Koster, E. H. (1987). Inclined Heterolithic Stratification -Terminology, Description, Interpretation and Significance in Sedimentary Geology. *Sedimentary Geology*, 53(2), 123-179.
- Tortike, W. S., & Farouq Ali, S. M. (1991). Prediction of oil sand failure due to steam-induced stresses. *Journal of Canadian Petroleum Technology*, 30(01), 87-96. doi:<https://doi.org/10.2118/91-01-08>
- Touhidi-Baghini, A. (1998). *Absolute Permeability of McMurray Formation Oil Sands at Low Confining Stresses*. A Thesis presented for the PhD Degree, Department of Civil Engineering, University of Alberta, Edmonton, Canada.
- Vaid, Y. P., & Negussey, D. (1984). Relative density of pluviated sand samples. *Soils and Foundations*, 24(2), 101-105.
- Vermeer, P., & Borst, R. D. (1984). Non-Associated Plasticity for Soils, Concrete and Rock. *HERON*, 29(No. 3), 3-62.
- Wang, J. Y., Gates, I. D., & Su, Y. (2013). SAGD Pad Performance in an Ultra-Defined Athabasca Point Bar Deposit . *SPE Heavy Oil Conference*. Calgary : Society of Petroleum Engineers.
- Wang, S., Luna, R., & Stephenson, R. W. (2011). A Slurry Consolidation Approach to Reconstitute Low-Plasticity Silt Specimens for Laboratory Triaxial Testing. *Geotechnical Testing Journal*, 34(No. 4), 288-296. doi:<https://doi.org/10.1520/GTJ103529>

- Wightman, D., Rottenfusser, B., Kramers, J., & Harrison, R. (1989). *Geology of the Alberta oil sands deposits, AOSTRA technical handbook on oil sands, bitumens and heavy oils*. AOSTRA Technical Publication, Edmonton, Canada, p 9.
- Yaich, E. (2008). *The effect of Stress Paths and Shear Failure on the Permeability of Unconsolidated Sands*. Austin: A Thesis presented for the Master Degree, Department of Petroleum and Geosystems Engineering, University of Texas at Austin, Austin, USA.
- Yin, S., Towler, B., Dusseault, M. B., & Rothenburg, L. (2009). Numerical Experiments on Oil Sands Shear Dilation and Permeability Enhancement in a Multiphase Thermoporoelastoplasticity Framework. *Journal of Petroleum Science & Engineering*, 69(3/4), 219-226.